ANL-77-34 ANL-77-34

2 ~~#6~~ 27

8-15-77

25 cp. to NTIS

LIGHT-WATER-REACTOR SAFETY RESEARCH PROGRAM: QUARTERLY PROGRESS REPORT

January—March 1977

U of C-AUA-USERDA

GONNE NATIONAL LABORATORY, ARGONNE, ILLINOIS

Prepared for the U. S. NUCLEAR REGULATORY COMMISSION
Office of Nuclear Regulatory Research

The facilities of Argonne National Laboratory are owned by the United States Government. Under the terms of a contract (W-31-109-Eng-38) between the U. S. Energy Research and Development Administration, Argonne Universities Association and The University of Chicago, the University employs the staff and operates the Laboratory in accordance with policies and programs formulated, approved and reviewed by the Association.

MEMBERS OF ARGONNE UNIVERSITIES ASSOCIATION

The University of Arizona
Carnegie-Mellon University
Case Western Reserve University
The University of Chicago
University of Cincinnati
Illinois Institute of Technology
University of Illinois
Indiana University
Iowa State University
The University of Iowa
Kansas State University
The University of Kansas
Loyola University
Marquette University
Michigan State University
The University of Michigan
University of Minnesota
University of Missouri
Northwestern University
University of Notre Dame
The Ohio State University
Ohio University
The Pennsylvania State University
Purdue University
Saint Louis University
Southern Illinois University
The University of Texas at Austin
Washington University
Wayne State University
The University of Wisconsin

NOTICE

This report was prepared as an account of work sponsored by the United States Government. Neither the United States nor the United States Energy Research and Development Administration, nor any of their employees, nor any of their contractors, subcontractors, or their employees, makes any warranty, express or implied, or assumes any legal liability or responsibility for the accuracy, completeness or usefulness of any information, apparatus, product or process disclosed, or represents that its use would not infringe privately-owned rights. Mention of commercial products, their manufacturers, or their suppliers in this publication does not imply or connote approval or disapproval of the product by Argonne National Laboratory or the U. S. Energy Research and Development Administration.

Printed in the United States of America
Available from
National Technical Information Service
U. S. Department of Commerce
5285 Port Royal Road
Springfield, Virginia 22161
Price: Printed Copy $6.00; Microfiche $3.00

Distribution Categories:
Water Reactor Safety Research–
Fuel Behavior (NRC-3)
Water Reactor Safety Research–
Analysis Development (NRC-4)

ANL-77-34

ARGONNE NATIONAL LABORATORY
9700 South Cass Avenue
Argonne, Illinois 60439

LIGHT-WATER-REACTOR SAFETY RESEARCH PROGRAM: QUARTERLY PROGRESS REPORT

January–March 1977

Robert G. Sachs, Laboratory Director
Jack A. Kyger, Associate Laboratory Director

June 1977

Previous reports in this series:

ANL-76-49	January–March 1976
ANL-76-87	April–June 1976
ANL-76-121	July–September 1976
ANL-77-10	October–December 1976

THIS PAGE

WAS INTENTIONALLY

LEFT BLANK

TABLE OF CONTENTS

Page

ABSTRACT xvi

I. LOSS-OF-COOLANT ACCIDENT RESEARCH: HEAT TRANSFER AND FLUID DYNAMICS 1

A. Transient Critical Heat Flux 1

1. Calibration of Break Orifices 1
2. Flow and Fluid Temperature Measurements 1
3. Transient CHF Results 4

B. LOCA Heat-transfer Analysis 37

C. Reflood Tests 39

References 43

II. TRANSIENT FUEL RESPONSE AND FISSION-PRODUCT RELEASE PROGRAM 44

A. Modeling of Fuel-Fission-product Behavior 45

1. Modeling of Fission-gas Behavior during Steady-state Conditions 45
   a. Sensitivity Analyses 45
   b. Formulation of Models to Describe Grain-boundary Separation 52
2. Modeling of Fission-gas Behavior during Transient Conditions 53

B. Experimental Program 60

1. Transient-heating Tests 60
   a. Test Conditions 60
   b. Fission-gas Release during Transient Heating 61
2. Temperature Measurement and Calculation 63
   a. Surface-temperature Measurement 63
   b. Radial Temperature-profile Calculation 64
3. ANL-EG&G Cross-check Program 65
   a. Fuel Characterization 65
   b. DEH Testing 70

References 70

III. MECHANICAL PROPERTIES OF ZIRCALOY CONTAINING OXYGEN 71

A. Summary 71

TABLE OF CONTENTS

Page

B. Mechanical Properties of As-received Zircaloy 72

1. Flow Stress and Ductility of Zircaloy-4 in Temperature Interval 25-700°C 72
2. Work-hardening Analysis of Zircaloy-4 73
3. Effect of Texture on the Work-hardening Rate 75
4. Fine-grain Zircaloy-4 76
5. Work-hardening Analysis of Transformed β-phase Zircaloy-4. 76
6. Relationship between Work-hardening Rate and Dynamic Strain Aging. 79
7. Correlation between Superplasticity and Work-hardening Rate 81

C. Mechanical Properties of Zircaloy-Oxygen Alloys. 84

1. Homogeneous Oxygen Distribution 84
   a. Beta-phase Zircaloy-2 84
   b. Alpha-phase Zircaloy-4. 85
   c. Beta-phase Zircaloy-4 86
2. Composite Specimens with Nonuniform Oxygen Distribution 88

D. Biaxial Deformation and Rupture Characteristics of Zircaloy-4 Cladding. 93

1. Effect of Specimen Length on Rupture Characteristics of Zircaloy-4 Cladding 93
2. Burst Characteristics of Zircaloy-4 Cladding Axially Constrained by Al_2O_3 Pellets. 93
3. Analysis of Local Fracture Strain and Development of a Strain-localization Parameter. 98

E. Embrittlement of Zircaloy-4 Cladding by Oxidation 104

1. Embrittlement Tests in Air Atmosphere 104
2. Interpretation of Embrittlement-test Results 104
   a. F_W Criterion. 108
   b. Equivalent-cladding-reacted (ECR) Criterion 109
   c. Fractional β-phase Saturation (FBS) Criterion 110
   d. $F_{0.65}$ Criterion. 110
3. Future Embrittlement Studies 111

References 112

TABLE OF CONTENTS

Page

IV. STEAM-EXPLOSION STUDIES 113

A. Vapor Explosive Behavior at Elevated Ambient Pressure 113

B. Combined Physical-Chemical Explosions. 119

References 120

LIST OF FIGURES

No.	Title	Page
I.1.	Horizontal Break-line Assembly	1
I.2.	Calibration Results for Break Orifices	2
I.3.	Fluid Temperature and Flow Measurement Early in Transient	3
I.4.	Comparison between Discharge-break Flow Rate and Turbine-flowmeter Measurement	3
I.5.	Steady-state Wall-temperature Profile in DB-113	5
I.6.	Steady-state Wall-temperature Profile in DB-114	5
I.7.	Steady-state Wall-temperature Profile in DB-115	6
I.8.	Steady-state Wall-temperature Profile in DB-117	6
I.9.	Steady-state Wall-temperature Profile in DB-118	7
I.10.	Steady-state Wall-temperature Profile in DB-119	7
I.11.	System Pressure during Test DB-113	8
I.12.	Differential Pressure across Test Section during Test DB-113	8
I.13.	Differential Pressure across Break Orifice during Test DB-113	9
I.14.	Turbine-flowmeter Measurement during Test DB-113	9
I.15.	Fluid Temperature during Test DB-113	10
I.16.	Wall-thermocouple Measurement during Test DB-113	10
I.17.	System Pressure during Test DB-114	12
I.18.	Differential Pressure across Test Section during Test DB-114	13
I.19.	Differential Pressure across Break Orifice during Test DB-114	13
I.20.	Turbine-flowmeter Measurement during Test DB-114	14
I.21.	Fluid Temperature during Test DB-114	14
I.22.	Wall-thermocouple Measurement during Test DB-114	15
I.23.	System Pressure during Test DB-115	17
I.24.	Differential Pressure across Test Section during Test DB-115	17
I.25.	Differential Pressure across Break Orifice during Test DB-115	18
I.26.	Turbine-flowmeter Measurement during Test DB-115	18

LIST OF FIGURES

No.	Title	Page
I.27.	Fluid Temperature during Test DB-115	19
I.28.	Wall-thermocouple Measurement during Test DB-115	19
I.29.	System Pressure during Test DB-117	21
I.30.	Differential Pressure across Test Section during Test DB-117	22
I.31.	Differential Pressure across Break Orifice during Test DB-117	22
I.32.	Turbine-flowmeter Measurement during Test DB-117	23
I.33.	Fluid Temperature during Test DB-117	23
I.34.	Wall-thermocouple Measurement during Test DB-117	24
I.35.	System Pressure during Test DB-118	26
I.36.	Differential Pressure across Test Section during Test DB-118	26
I.37.	Differential Pressure across Break Orifice during Test DB-118	27
I.38.	Turbine-flowmeter Measurement during Test DB-118	27
I.39.	Fluid Temperature during Test DB-118	28
I.40.	Wall-thermocouple Measurement during Test DB-118	28
I.41.	System Pressure during Test DB-119	30
I.42.	Differential Pressure across Test Section during Test DB-119	31
I.43.	Differential Pressure across Break Orifice during Test DB-119	31
I.44.	Turbine-flowmeter Measurement during Test DB-119	32
I.45.	Fluid Temperature during Test DB-119	32
I.46.	Wall-thermocouple Measurement during Test DB-119	33
I.47.	Influence of System Pressure on Critical Heat Flux	36
I.48.	Saturated-steam Heat-transfer Coefficient Based on Measured Pressure and Core-inlet Velocity	37
I.49.	Calculated and Measured Heater-thermocouple Response for TH-D5-29 after CHF	38
I.50.	Calculated and Measured Heater-thermocouple Response for TH-F6-08E after CHF	38

LIST OF FIGURES

No.	Title	Page
I.51.	Integrated Energy Release during Rewet as a Function of Surface Quenching Time	39
I.52.	Typical Temperature-vs-Time Curve during Reflood of a Vertical Stainless Steel Pipe	40
I.53.	Quenching Temperature vs Axial Distance along Test Section	41
I.54.	Quenching Time vs Initial Temperature of Test Section for Thermocouple 18	41
I.55.	Amplitude of Output from Differential Pressure Transducer vs Time: Run No. 9	42
I.56.	Amplitude vs Frequency at Two Different Intervals Obtained by Using an Analog Spectrum Analyzer: Run No. 9	42
I.57.	Amplitude of Output from Differential Pressure Transducer vs Time: Run No. 7	42
I.58.	Amplitude vs Frequency at Two Different Intervals Obtained by Using an Analog Spectrum Analyzer: Run No. 7	42
I.59.	Peak Amplitude Frequency and Peak Amplitude vs Initial Temperature of Test Section	43
II.1.	GRASS-calculated Fractional Fission-gas Release as a Function of Fuel Temperature and Burnup from 10-μm Grains with 200°C/cm Radial Temperature Gradient	48
II.2.	GRASS-calculated Fission-gas Release as a Function of Fuel Temperature and Burnup from 10- and 30-μm Grains with 200°C/cm Radial Temperature Gradient	49
II.3.	Fuel-surface and Centerline Temperature Histories during LOCA for Hottest 0.25 m of a ~4-m (12-ft) Fuel Rod	54
II.4.	GRASS-calculated Pretransient Radial Distributions of Retained Gas	55
II.5.	GRASS-calculated Radial Distributions of Retained Gas after Reflood	55
II.6.	GRASS-calculated Evolution of Grain-boundary Channel Formation during LOCA	56
II.7.	GRASS-calculated Fission-gas Release during LOCA for a Variety of Fuel Microstructures	57
II.8.	Fractional Xenon Release vs Energy Input for DEH Tests at Nominal 25°C/s (4 W/s)	62

LIST OF FIGURES

No.	Title	Page
II.9.	Transverse Section through Robinson Fuel Pellet Transient-tested to Central Melting in Test 26	62
II.10.	Transverse Section through SLF Rod 844 at ~0.72 m (28 in.) above Rod Bottom	67
II.11.	Transverse Section at a Level Just above Film-boiling Boundary in Rod 007 from Test PBF IE-1	67
II.12.	Detailed View of Grain-boundary Separation in Unmelted Region of Section Shown in Fig. II.11	68
II.13.	Grain-boundary Separation in Vicinity of Radial Crack in Section Shown in Fig. II.11	68
II.14.	Transverse Section at a Level Just below Film-boiling Region in Rod 008 of Test PBF IE-1	68
II.15.	Transverse Section at a Level Just above Film-boiling Region in Rod 008 of Test PBF IE-1	68
II.16.	Grain-boundary Separation in Vicinity of Cracks near Edge of Section Shown in Fig. II.15	69
II.17.	Grain-boundary Separation in Vicinity of Large Radial Cracks in Section Shown in Fig. II.15.	69
II.18.	General View of Grain-boundary Separation in Section Shown in Fig. II.15	69
III.1.	Ultimate Tensile Strength of Zircaloy-4 at Three Strain Rates over Temperature Interval 23-700°C.	73
III.2.	Uniform Strain and Total Strain for Zircaloy-4 Specimens as a Function of Deformation Temperature at Three Strain Rates over Temperature Interval 23-700°C.	73
III.3.	Work-hardening Exponent of Zircaloy-4 as a Function of Temperature at Four Strain Rates	74
III.4.	Temperature Dependence of Parameter k for Zircaloy-4 at Three Strain Rates	74
III.5.	Variation of σ_0 with Temperature for Zircaloy-4 at Three Strain Rates	75
III.6.	Work-hardening Exponent as a Function of Temperature for Zircaloy-4 Specimens with Three Textures	75
III.7.	Total Strain as a Function of Temperature for 5-μm Grain-size Zircaloy-4 Specimens at Three Strain Rates over Temperature Interval 23-700°C	76

LIST OF FIGURES

No.	Title	Page
III.8.	Work-hardening Exponent of Fine Grain-size Zircaloy-4 as a Function of Temperature at Three Strain Rates	76
III.9.	Temperature Dependence of Work-hardening Exponent of Various Transformed β-phase Zircaloy-4 Structures	78
III.10.	Work-hardening Exponent of Basketweave Structure of Zircaloy-4 as a Function of Temperature at Two Strain Rates	79
III.11.	Strain-rate Dependence of Work-hardening Exponent of Zircaloy at 700°C	79
III.12.	Engineering-stress/Engineering-strain Curves for Zircaloy-4 at 750°C after Various Heat Treatments	81
III.13.	Strain Dependence of Strain-rate Sensitivity of Zircaloy-4 at 750°C after Two Heat Treatments	82
III.14.	Strain-rate Dependence of Work-hardening Exponent of Zircaloy-4 at 850°C	82
III.15.	Uniform and Total Strain as a Function of Oxygen Concentration for Zircaloy-2 Specimens at 1300 and 1400°C	84
III.16.	Oxygen-concentration Dependence of Yield Stress and UTS of Zircaloy-2 at 1300 and 1400°C	84
III.17.	Total Strain, Uniform Strain, Yield Stress, and UTS of Zircaloy-2 at 1300°C as a Function of Oxygen Concentration	85
III.18.	Effect of Oxygen on UTS of Zircaloy-4 at Several Temperatures between 200 and 750°C	85
III.19.	Oxygen-concentration Dependence of Uniform Strain of Zircaloy-4 at 200, 400, and 750°C	85
III.20.	Total Strain of Zircaloy-4 as a Function of Oxygen Concentration at 200, 400, and 750°C	86
III.21.	Work-hardening Exponent of Zircaloy-4 at 1000°C as a Function of Oxygen Concentration	86
III.22.	Oxygen-concentration Dependence of Work-hardening Exponent of Zircaloy-4 at 1100°C	86
III.23.	Effect of Oxygen Concentration on Work-hardening Exponent of Zircaloy-4 at 1200°C	87
III.24.	Variation of Work-hardening Exponent of Zircaloy-4 at 1300°C with Oxygen Concentration	87

LIST OF FIGURES

No.	Title	Page
III.25.	Work-hardening Exponent of Zircaloy-4 at 1400°C as a Function of Oxygen Concentration	87
III.26.	Temperature Dependence of Work-hardening Exponent of Zircaloy-4 with Several Oxygen Concentrations	87
III.27.	Microstructure of Zircaloy-4/Oxide Composite Specimen Deformed at 800°C, Showing Cracks in Oxide and α Layers	89
III.28.	Microstructure of Zircaloy-4/Oxide Composite Specimen Deformed at 1100°C, Showing No Cracks in α Layer	89
III.29.	Oxygen-concentration Dependence of Yield Stress of Zircaloy-4/Oxide Composites at Several Temperatures	90
III.30.	Ultimate Tensile Strength of Zircaloy-4/Oxide Composites as a Function of Oxygen Concentration at Several Temperatures	90
III.31.	Effect of Oxygen Concentration on Uniform Strain of Zircaloy-4/Oxide Composites at Several Temperatures	90
III.32.	Variation of Total Strain of Zircaloy-4/Oxide Composites with Oxygen Concentration at Several Temperatures	90
III.33.	Temperature Dependence of Work-hardening Exponent of Zircaloy-4/Oxide Composites with Several Oxygen Concentrations	92
III.34.	Comparison of Maximum Circumferential Strain vs Burst Temperature for 153- and 300-mm-long Axially Constrained Cladding at Heating Rate of 115°C/s In Vacuo	93
III.35.	Comparison of Maximum Circumferential Strain vs Burst Temperature for 153- and 300-mm-long Axially Constrained Cladding at Heating Rates of 5, 55, and 115°C/s in Steam	94
III.36.	Schematic Diagram of Cladding Tube Containing Alumina Pellets	94
III.37.	Nonuniform Brightness of Cladding Specimen Containing Al_2O_3 Pellets due to Axial and Circumferential Temperature Variations during Heating at 45°C/s	95
III.38.	Temperature and Internal Pressure as a Function of Time for Cladding Specimen Described in Fig. III.37	95
III.39.	Cladding Constrained by Pellets after Burst	95
III.40.	Maximum Circumferential Strain vs Maximum Burst Temperature in Steam at Heating Rate of 5°C/s for Cladding Constrained by Pellets	96

LIST OF FIGURES

No.	Title	Page
III.41.	Maximum Circumferential Strain vs Maximum Burst Temperature in Steam at Heating Rate of 45°C/s for Cladding Constrained by Pellets	96
III.42.	Maximum Circumferential Strain vs Maximum Burst Temperature in Steam at Heating Rate of 115°C/s for Cladding Constrained by Pellets	97
III.43.	Comparison of Maximum Circumferential Strain vs Initial Internal Pressure for Unconstrained and Mandrel- and Pellet-constrained Cladding at Heating Rate of 5°C/s in Steam.	97
III.44.	Comparison of Maximum Circumferential Strain vs Initial Internal Pressure for Mandrel- and Pellet-constrained Cladding at Heating Rate of 45°C/s in Steam	97
III.45.	Comparison of Maximum Circumferential Strain vs Initial Internal Pressure for Unconstrained and Mandrel- and Pellet-constrained Cladding at Heating Rate of 115°C/s in Steam	98
III.46.	Effect of Initial Internal Pressure and Heating Rate in Steam on Maximum Circumferential Strain for Zircaloy-4 Cladding Constrained by Pellets	98
III.47.	True Fracture Radial Strain vs Maximum Burst Temperature for Unconstrained and Mandrel-constrained Zircaloy-4 Cladding Burst in Steam at Heating Rates of 5, 55, and 115°C/s . . .	99
III.48.	True Fracture Radial Strain vs Maximum Burst Temperature for Unconstrained and Mandrel- and Pellet-constrained Cladding Burst in Steam at Heating Rate of 5°C/s.	99
III.49.	True Fracture Radial Strain vs Maximum Burst Temperature for Unconstrained and Mandrel- and Pellet-constrained Cladding Burst in Steam at Heating Rate of 40-60°C/s.	100
III.50.	Calculation of Ratio of True Local Radial Strain to True Fracture Radial Strain at Different Tangential Angles in Cross Section of Maximum Circumferential Strain	101
III.51.	Method of Determining Radial-strain-localization Parameter W from Plots of Ratio of True Local Radial Strain to True Fracture Radial Strain as a Function of Normalized Tangential Angle	101
III.52.	Maximum Circumferential Strain vs Radial-strain-localization Parameter for α-phase Cladding Burst under Different Test Conditions at Temperatures between 700 and 850°C	102

LIST OF FIGURES

No.	Title	Page
III.53.	Radial-strain-localization Parameter as a Function of Maximum Circumferential Temperature Difference for Cladding Burst in Steam at Temperatures near 800°C Strain Maximum. .	103
III.54.	Capability of Zircaloy-4 Cladding to Withstand "Normal Handling" at Room Temperature without Fracture after Oxidation in Air at Temperatures between 1000 and 1450°C for Various Times.	107
III.55.	Failure Map for Zircaloy Cladding under "Normal Handling" at Room Temperature in Terms of Fractional Thickness of Transformed β Region F_W and Oxidation Temperature in Air. .	108
III.56.	Failure Map for Zircaloy Cladding under "Normal Handling" at Room Temperature in Terms of Equivalent-cladding-reacted Parameter ECR and Oxidation Temperature in Air . . .	109
III.57.	Failure Map for Zircaloy Cladding under "Normal Handling" at Room Temperature in Terms of Fractional Saturation of Central β-phase Region and Oxidation Temperature in Air	110
III.58.	Failure Map for Zircaloy Cladding under "Normal Handling" at Room Temperature in Terms of Fraction of Original Cladding Thickness Containing <0.65 wt % Oxygen and Oxidation Temperature in Air	111
IV.1.	Inertial and Thermal Bubble-growth Behavior for Water at 15.5 MPa	113
IV.2.	Inertial and Thermal Bubble-growth Behavior for Water at 0.1 MPa	116
IV.3.	Transition Radius and Capture Diameters for Freon-22	117
IV.4.	Internal Fragmentation of Liquid Droplets by Inertial Bubble Growth	117

LIST OF TABLES

No.	Title	Page
I.1.	Steady-state Test Conditions in Test Section II	4
I.2.	Other Parameters during Blowdown	4
I.3.	Equivalent Water Conditions during Steady-state Conditions	4
I.4.	Description of Test Conditions	40
II.1.	GRASS Calculations for Fractional Fission-gas Release for a Fission Rate of 1×10^{13} f/cm^3·s and a Temperature Gradient of 200°C/cm	46
II.2.	GRASS Calculations for Fractional Fission-gas Release from 10-μm Grains for a Fission Rate of 1.3×10^{12} f/cm^3·s	47
II.3.	Dependence of Fractional Gas Release on Temperature and Grain Size	48
II.4.	Dependence of Fractional Gas Release on Temperature Gradient	49
II.5.	Dependence of Fractional Gas Release on Fission Rate	49
II.6.	Dependence of Gas Release on Temperatures That Decrease Slowly with Time	50
II.7.	Dependence of Gas Release on Temperatures That Stabilize Early in Life	50
II.8.	Grain-boundary Channel Formation for Table II.1	51
II.9.	Conditions of Interrupted DEH Transient-heating Tests of Robinson Fuel	60
II.10.	Fission Gas Collected during DEH Tests Conducted at Nominal 25°C/s Heating Rates	61
II.11.	Summary of Pellet-stack Electrical-conductivity Parameters	65
II.12.	Gas Analysis of Rod 843	66
III.1.	Least-squares Work-hardening Constants for Deformation Stages of 5-μm Grain-size Zircaloy-4, $\dot{\varepsilon} = 3.3 \times 10^{-2}$ s^{-1}	77
III.2.	Least-squares Work-hardening Constants for Deformation Stages of 5-μm Grain-size Zircaloy-4, $\dot{\varepsilon} = 3.3 \times 10^{-3}$ s^{-1}	77
III.3.	Least-squares Work-hardening Constants for Deformation Stages of 5-μm Grain-size Zircaloy-4, $\dot{\varepsilon} = 3.3 \times 10^{-4}$ s^{-1}	78
III.4.	Least-squares Work-hardening Constants of Longitudinal Zircaloy-2 Specimens Deformed at 700°C and Various Strain Rates	80

LIST OF TABLES

No.	Title	Page
III.5.	Least-squares Work-hardening Constants for 5-μm Grain-size Zircaloy-4 Specimens Deformed at 700°C and Various Strain Rates	80
III.6.	Least-squares Work-hardening Constants for 11-μm Grain-size Zircaloy-4 Specimens Deformed at 700°C and Various Strain Rates	80
III.7.	Least-squares Work-hardening Constants for 11-μm Grain-size Zircaloy-4 Specimens Deformed at 750°C after Various Heat Treatments, $\dot{\varepsilon} = 3.3 \times 10^{-3}\ s^{-1}$	82
III.8.	Least-squares Work-hardening Constants for 5-μm Grain-size Zircaloy-4 Specimens Deformed at 850°C and Various Strain Rates	83
III.9.	Least-squares Work-hardening Constants for 11-μm Grain-size Zircaloy-4 Specimens Deformed at 850°C and Various Strain Rates	83
III.10.	Least-squares Work-hardening Constants for 55-μm Grain-size Zircaloy-4 Deformed at 850°C and Several Strain Rates	83
III.11.	Least-squares Work-hardening Constants for Zircaloy-4 Oxide Composite Specimens, $\dot{\varepsilon} = 3.3 \times 10^{-3}\ s^{-1}$	91
III.12.	Summary of Embrittlement Test Conditions, Cladding-phase Thicknesses, and Various Calculated Oxidation Parameters	105
III.13.	Summary of Diffusion Coefficients and Equilibrium Phase-boundary Concentrations of Oxygen in Zircaloy-4	107
IV.1.	Homogeneous Nucleation of Water at 15.5 MPa	114
IV.2.	Transition Radius and Time	118

ABSTRACT

This progress report summarizes the Argonne National Laboratory work performed during January, February, and March 1977 on water-reactor-safety problems. The following research and development areas are covered: (1) Loss-of-coolant Accident Research: Heat Transfer and Fluid Dynamics; (2) Transient Fuel Response and Fission-product Release Program; (3) Mechanical Properties of Zircaloy Containing Oxygen; and (4) Steam-explosion Studies.

I. LOSS-OF-COOLANT ACCIDENT RESEARCH: HEAT TRANSFER AND FLUID DYNAMICS

Responsible Section Managers:
H. K. Fauske, R. E. Henry, and P. A. Lottes, RAS

A. Transient Critical Heat Flux (J. C. Leung and R. E. Henry, RAS)

1. Calibration of Break Orifices

The break line, which consisted of an air-operated valve and an orifice assembly, is sketched in Fig. I.1. The sharp-edged orifice was calibrated with water using a weighing tank and a mercury manometer, and the following formula is used to calculate the orifice discharge coefficient C_D

$$Q = C_D A_o \sqrt{\frac{2\Delta P}{\rho}}, \tag{1}$$

where Q is the measured volumetric flow rate and A_o is the flow area of the orifice. The calibration results are shown in Fig. I.2. For a small diameter ratio, the discharge coefficient has a nominal value of 0.61,[1] which to a certain extent depends on the location of the pressure taps. Figure I.2 illustrates close agreement with the literature and the independence of the coefficient at high Reynolds number.

2. Flow and Fluid Temperature Measurements

Upon initiation of depressurization, the flow in the test section reverses from upflow to downflow. Early in the transient, part of the liquid in the lower channel still remains subcooled, as was true in DB-113, -114 and -115. A finite time is required for the ejection of this subcooled liquid slug,

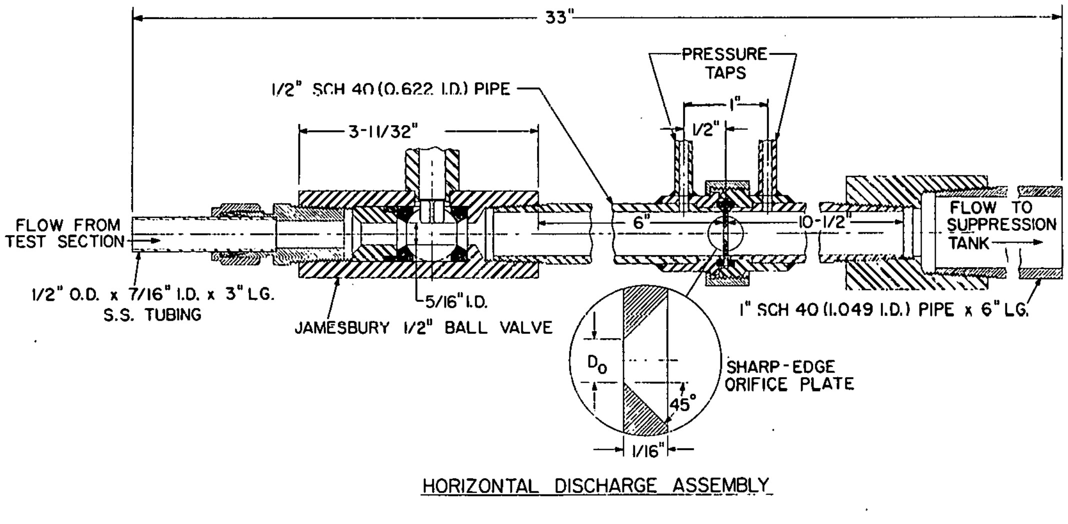

Fig. I.1. Horizontal Break-line Assembly. Conversion factor: 1 in. = 2.54 cm. ANL Neg. No. 900-77-474.

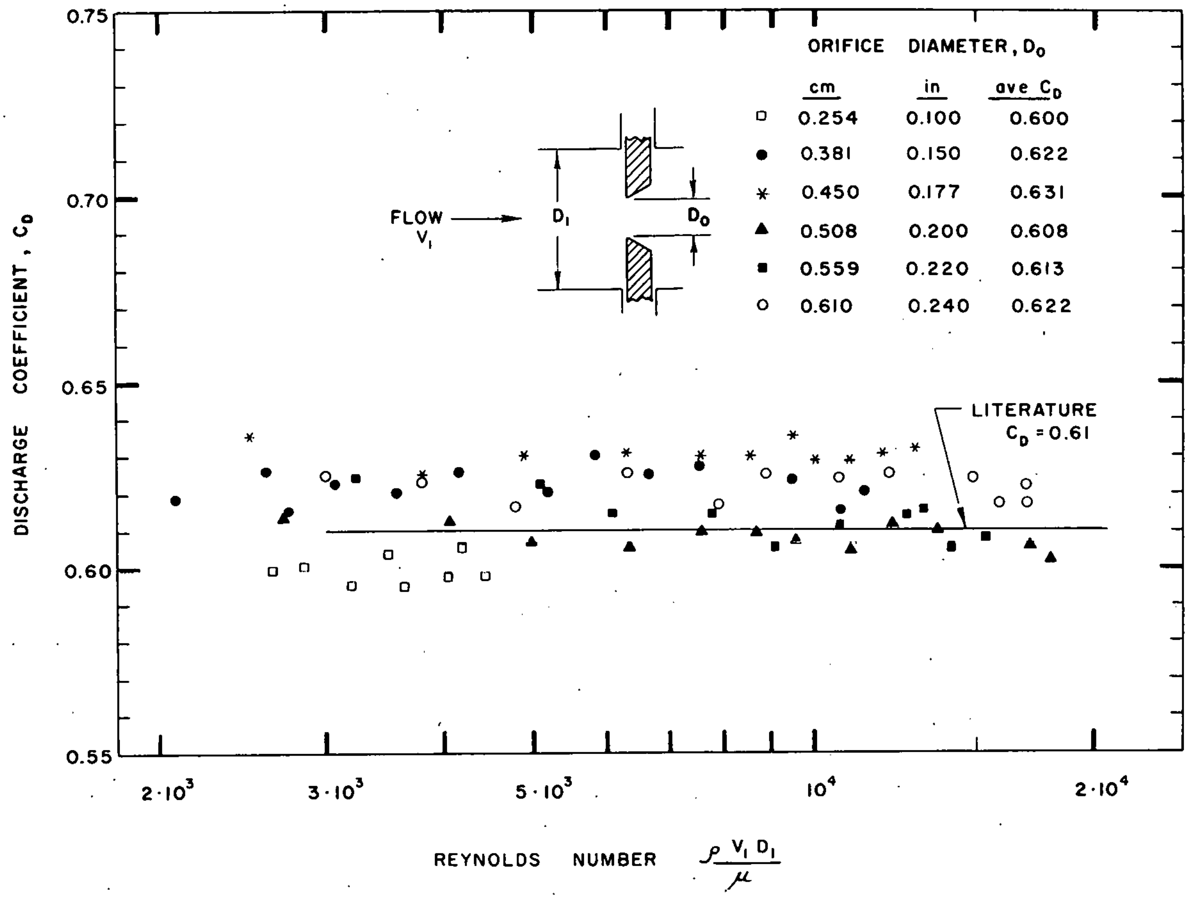

Fig. I.2. Calibration Results for Break Orifices. ANL Neg. No. 900-77-476.

which extends to the break location. The time at which the bottom fluid thermocouple senses saturation temperature should give an approximate time when the liquid slug passes out of the test section and two-phase mixture appears. This happened at about 500 ms in DB-114, as shown in Fig. I.3.

During this early time, the bottom turbine flowmeter was registering an almost steady flow at 5.2 m/s. The velocity increased when the low-density, two-phase mixture reached the turbine meter. This occurred at 450 ms, which is in good agreement with the above finding. Taking a downflow velocity of 5.2 m/s and the steady-state bulk temperature distribution, we calculated the temperature at the lower end of the channel using a quasi-steady approach as shown in Fig. I.3. The calculation predicts an earlier rise in fluid temperature, which is due to the assumption of instantaneous flow reversal and steady flow in the calculation. The rate of temperature rise was well predicted by this simple analysis.

The above-mentioned steady flow, which is indicative of the liquid slug flow, is characteristic of those tests that had a subcooled exiting fluid in steady-state operation. Since the fluid discharge at the break orifice was initially all liquid, the incompressible formula (Eq. 1) applies. The calculated volumetric flow rate based on the measured differential pressure and the appropriate discharge coefficient can be compared with the bottom turbine flowmeter measurement during the liquid-slug-flow period. Figure I.4 shows that the agreement is well within 10% for four different break orifices.

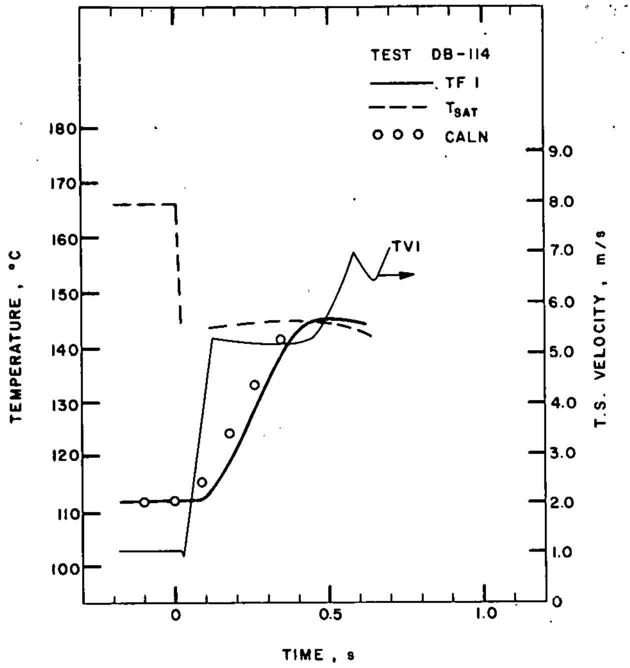

Fig. I.3

Fluid Temperature and Flow Measurement Early in Transient

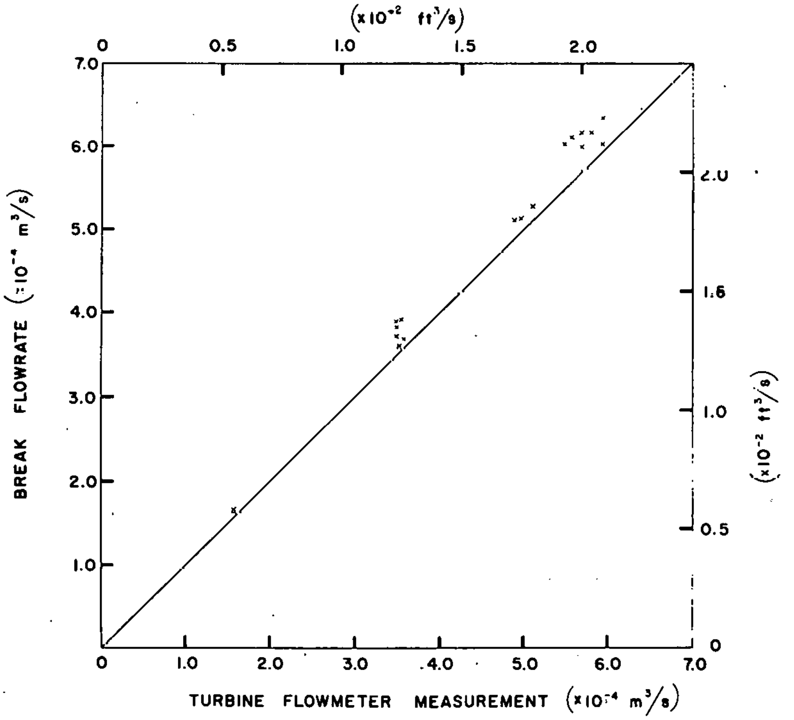

Fig. I.4. Comparison between Discharge-break Flow Rate and Turbine-flowmeter Measurement. ANL Neg. No. 900-77-475.

3. Transient CHF Results

Six blowdown tests with a break-orifice diameter of 0.508 cm have been performed with the initial conditions given in Table I.1. The power level was fixed at 5 kW in each test and was maintained during the transient until power trip. Other parameters are listed in Table I.2. Using Ahmad's scaling approach,[2] we can obtain the equivalent water conditions during the steady-state operation as listed in Table I.3. A critical-heat-flux ratio was calculated for each test. Since the heat flux in the heated section was not uniform, an average value was used in calculating the ratio. (More appropriately. this ratio should be termed the critical-power ratio in the present case; see Table I.1.)

TABLE I.1. Steady-state Test Conditions in Test Section II

Test No.	Break-orifice Diameter, cm	Pressure, MPa	Fluid Temperature, °C		Inlet Velocity, m/s	Mass Flow Rate, kg/m²·s	Total Power, kW	CPR[a] at Exit
			Inlet	Outlet				
DB-113	0.508	2.23	114	149	1.04	1275	4.95	1.82
DB-114	0.508	2.76	113	149	1.01	1252	4.98	1.90
DB-115	0.508	2.69	116	145	1.22	1504	4.94	2.11
DB-117	0.508	1.28	112	122	1.07	1311	4.99	1.88
DB-118	0.508	1.21	114	119	0.98	1204	5.00	1.81
DB-119	0.508	1.69	114	137	0.95	1166	5.00	1.67

[a] CPR = Critical-power ratio, defined here as the ratio of the total power that causes CHF at the exit to the test-section power.

TABLE I.2. Other Parameters during Blowdown[a]

Test No.	Volume above Heated Zone, cm³	Temperature Tripped Setting, °C	Time at Power Trip, s	Location of Overheating Thermocouple, cm
DB-113	2620	221	8.7	48
DB-114	2620	221	5.1	168
DB-115	2620	221	7.9	48
DB-117	2620	221	19.9	48
DB-118	2620	221	20.0	48
DB-119	2620	221	14.9	48

[a] Volume above heated zone = 2620 cm³; temperature-trip setting = 221°C.

TABLE I.3. Equivalent Water Conditions during Steady-state Conditions

Round tubular channel
Diameter = 1.18 cm (0.463 in.)
Length = 2.74 m (9.0 ft)

Test No.	Water Pressure, MPa	Inlet Subcooling, kJ/kg	Inlet Temperature, °C	Mass Velocity, kg/m²·s	Total Power, kW	Average Linear Power,[a] kW/ft
DB-113	12.6	435	248	1640	66.7	7.41
DB-114	15.2	589	238	1600	65.5	7.28
DB-115	14.9	556	243	1930	65.6	7.29
DB-117	7.7	117	271	1680	69.5	7.73
DB-118	7.4	54	279	1550	69.8	7.75
DB-119	9.9	242	266	1490	68.5	7.61

[a] Conversion factor: 1 kW/ft = 3.281 kW/m.

Figures I.5-I.10 show the steady-state wall- and bulk-temperature profiles. Also shown are the regions of the heated section that experienced thermal excursion of the wall within the first second. The computer plots of the transient data are shown in Figs. I.11-I.46.

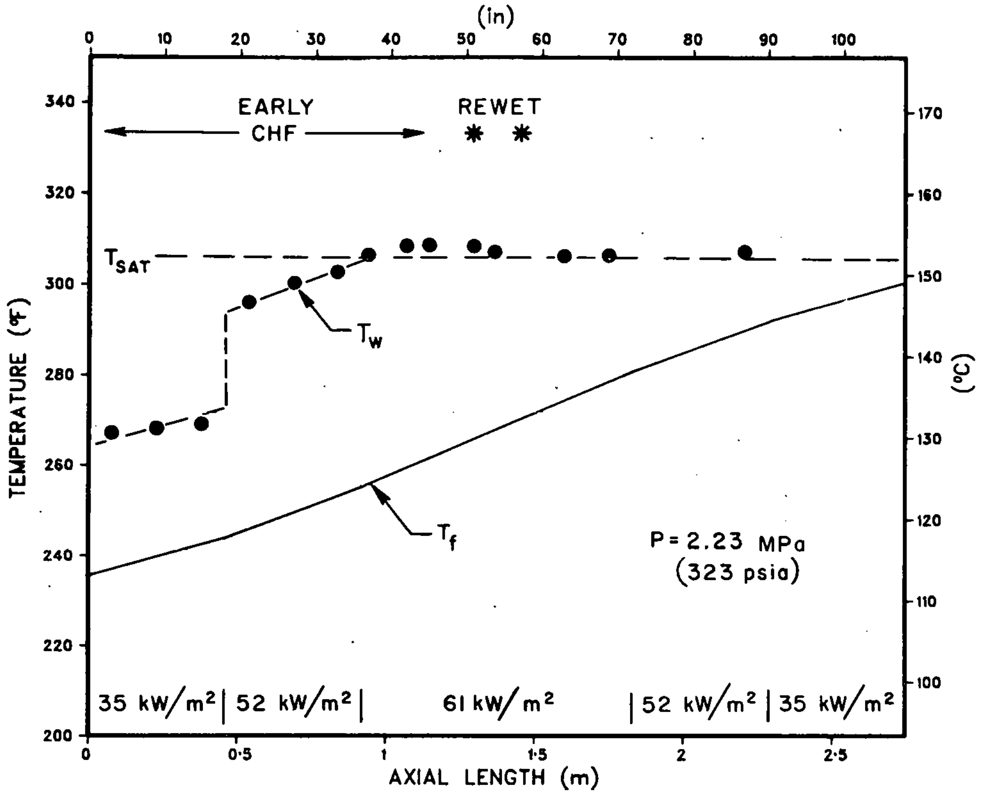

Fig. I.5. Steady-state Wall-temperature Profile in DB-113

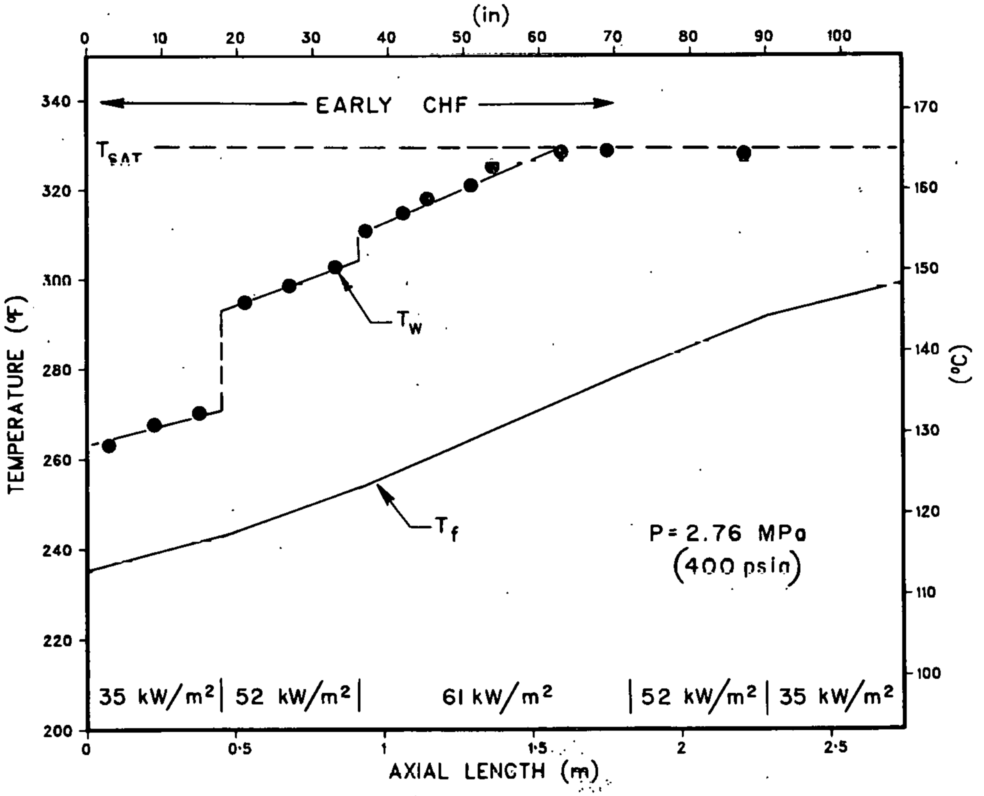

Fig. I.6. Steady-state Wall-temperature Profile in DB-114

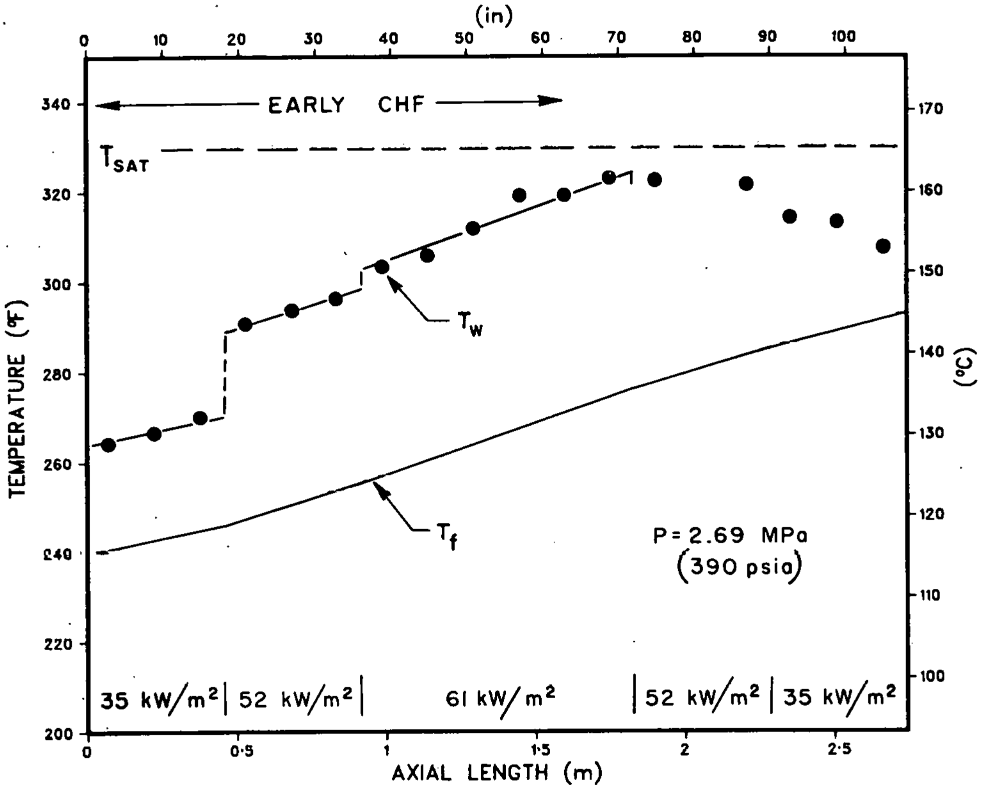

Fig. I.7. Steady-state Wall-temperature Profile in DB-115

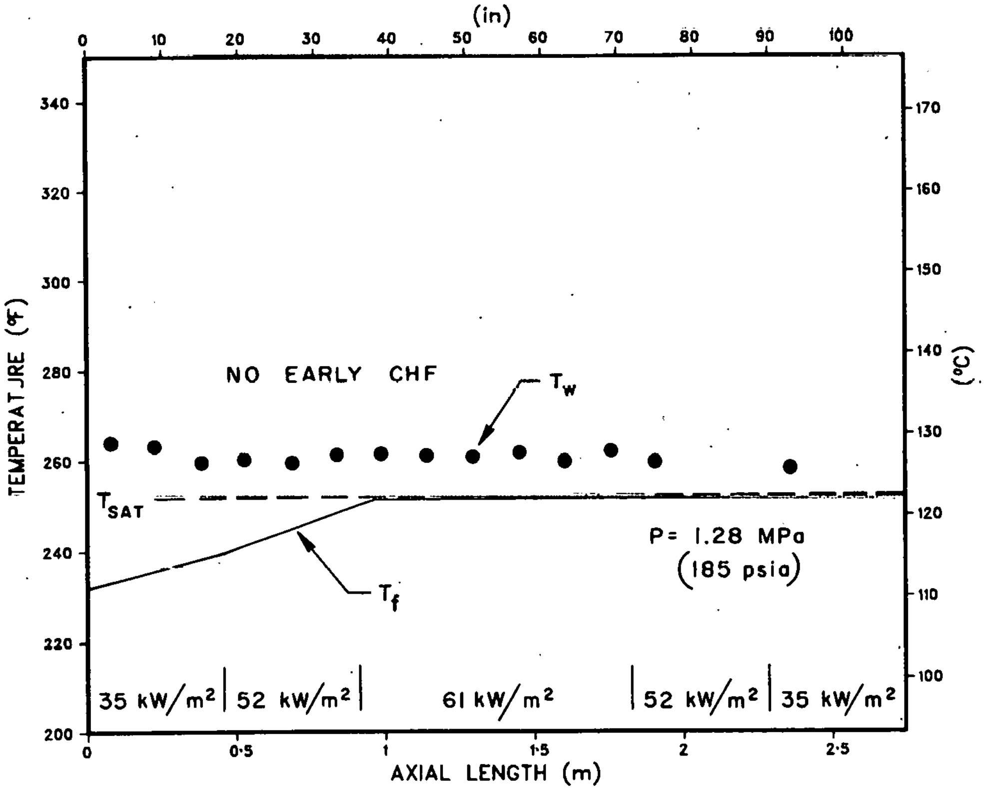

Fig. I.8. Steady-state Wall-temperature Profile in DB-117

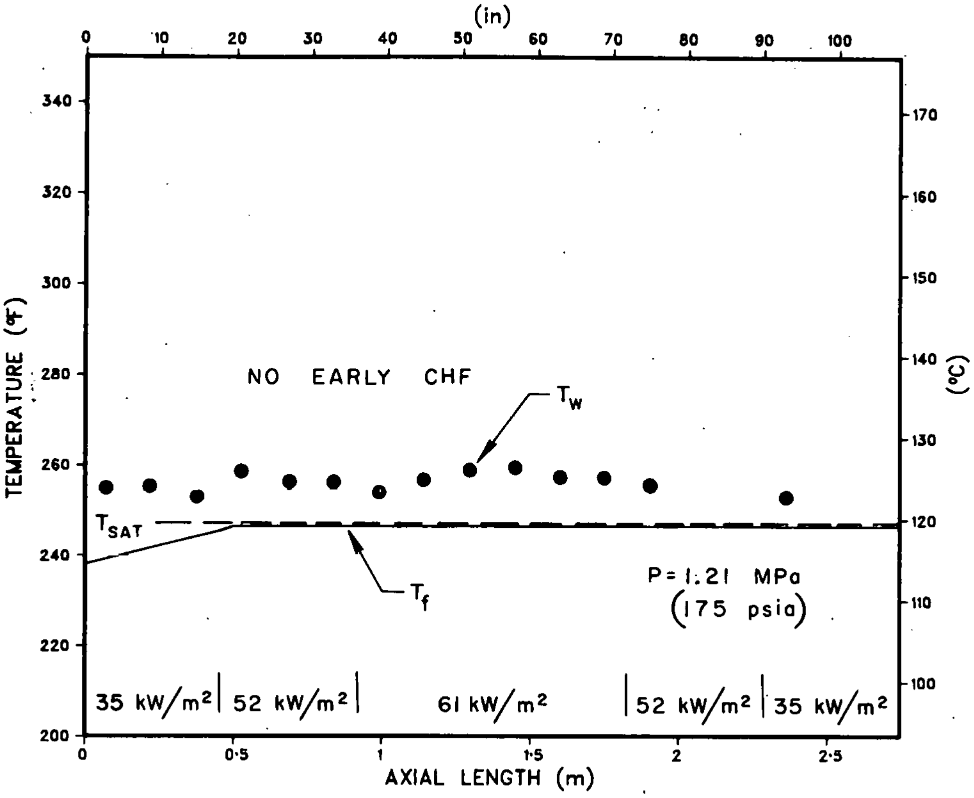

Fig. I.9. Steady-state Wall-temperature Profile in DB-118

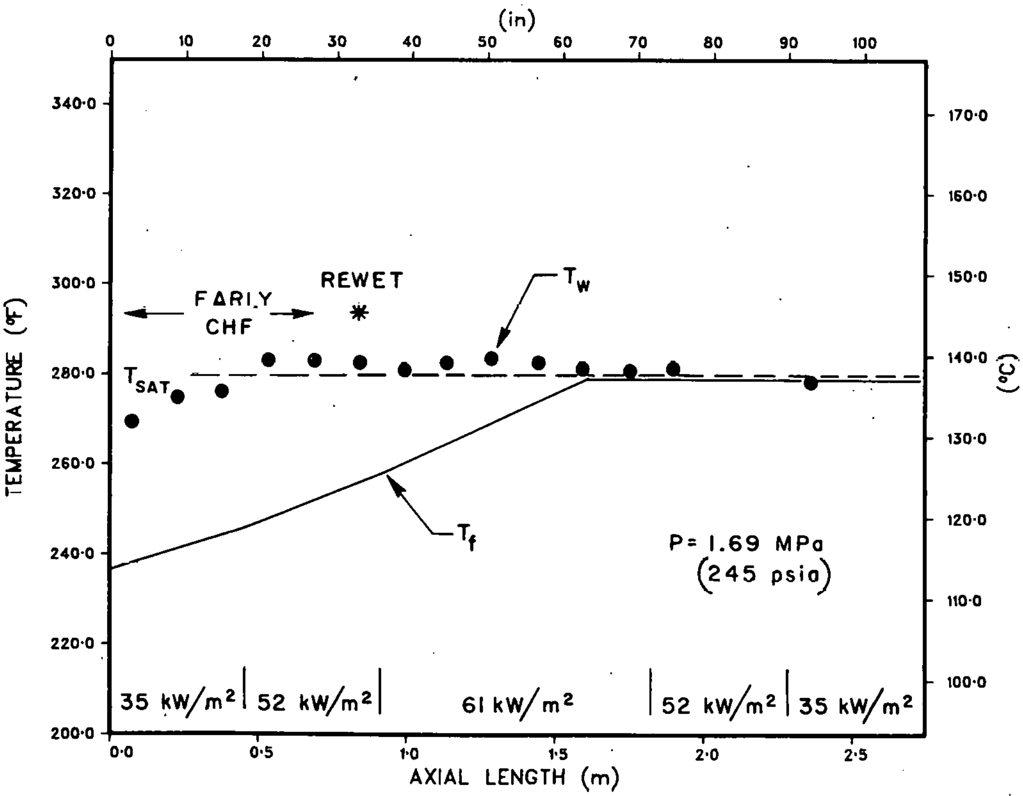

Fig. I.10. Steady-state Wall-temperature Profile in DB-119

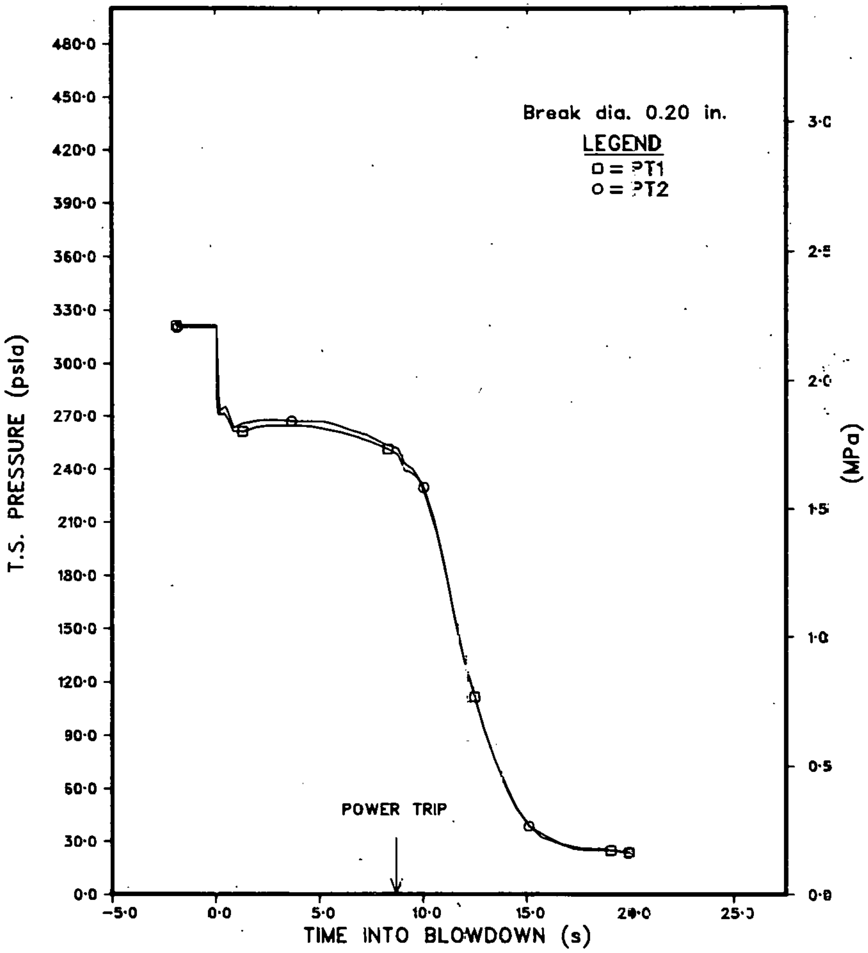

Fig. I.11. System Pressure during Test DB-113

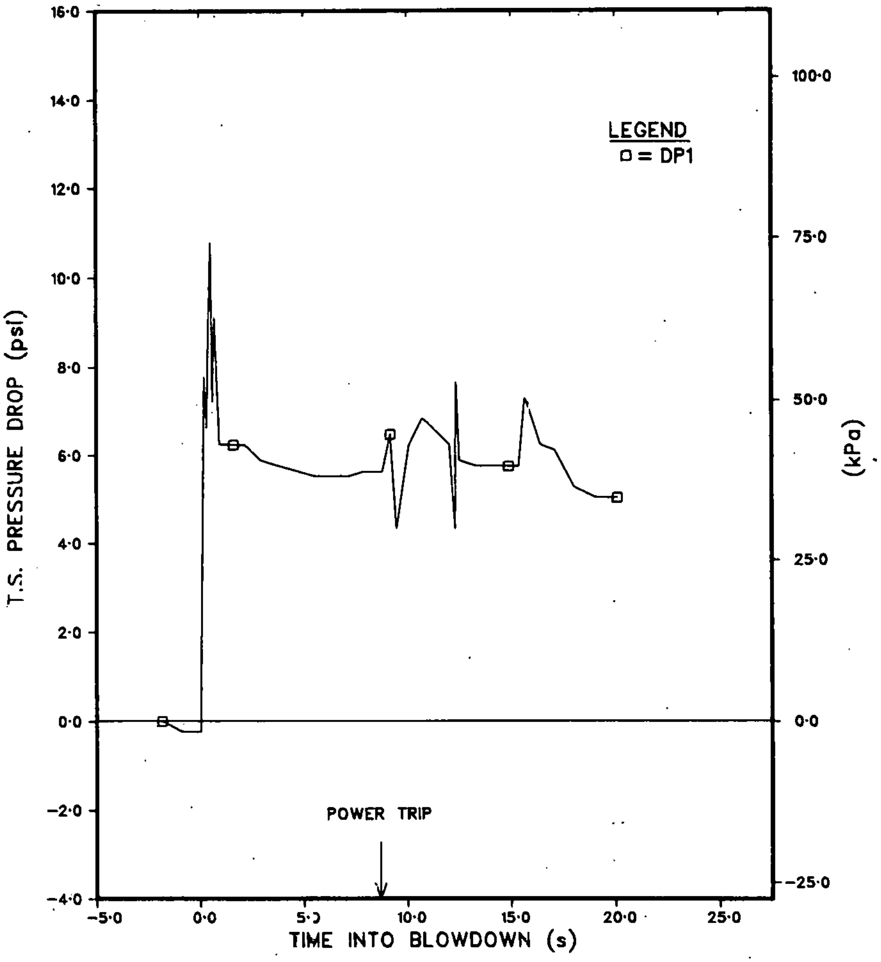

Fig. I.12. Differential Pressure across Test Section during Test DB-113

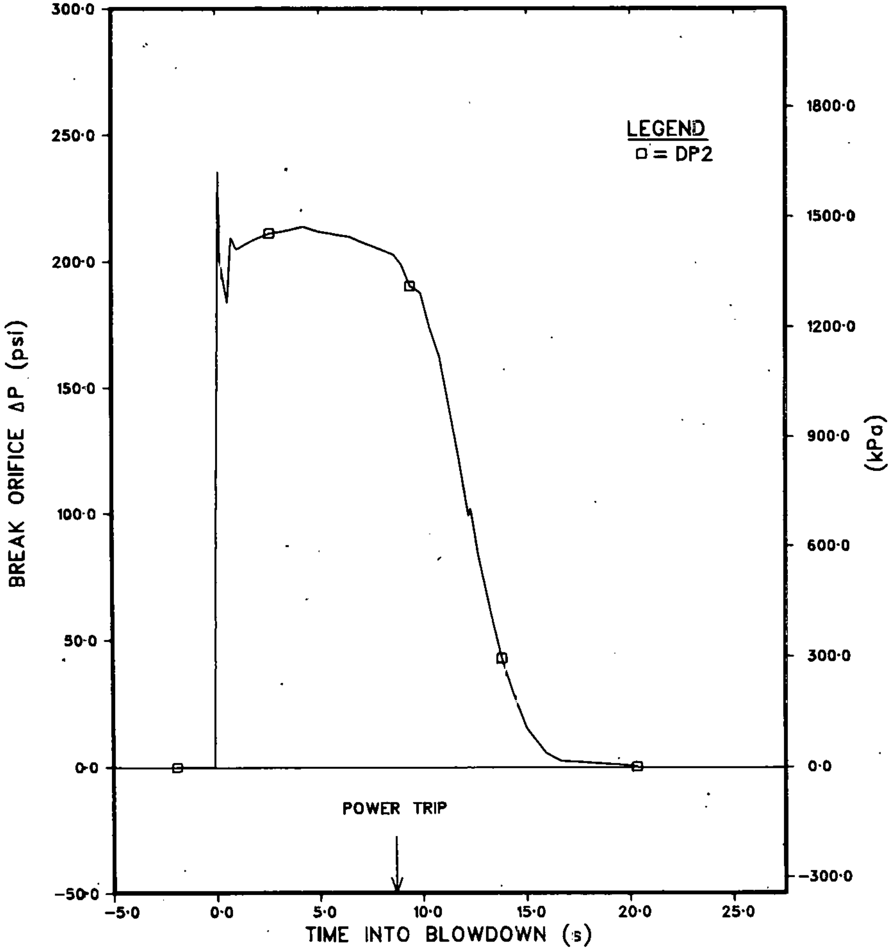

Fig. I.13. Differential Pressure across Break Orifice during Test DB–113

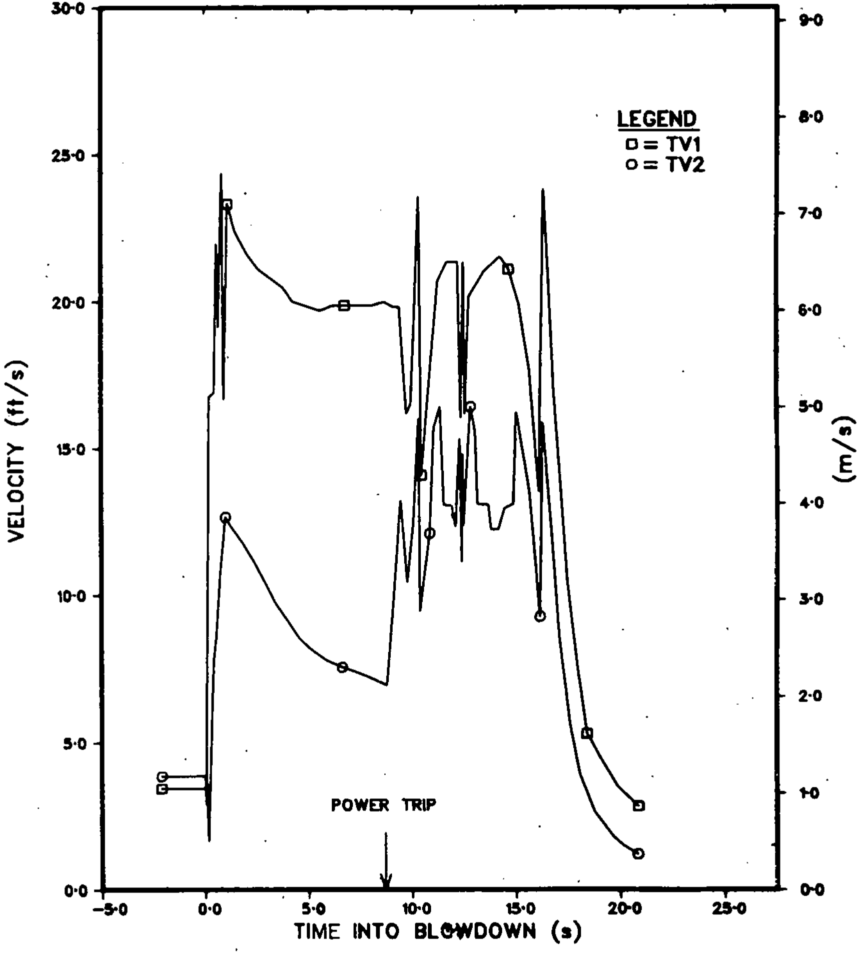

Fig. I.14. Turbine–flowmeter Measurement during Test DB–113

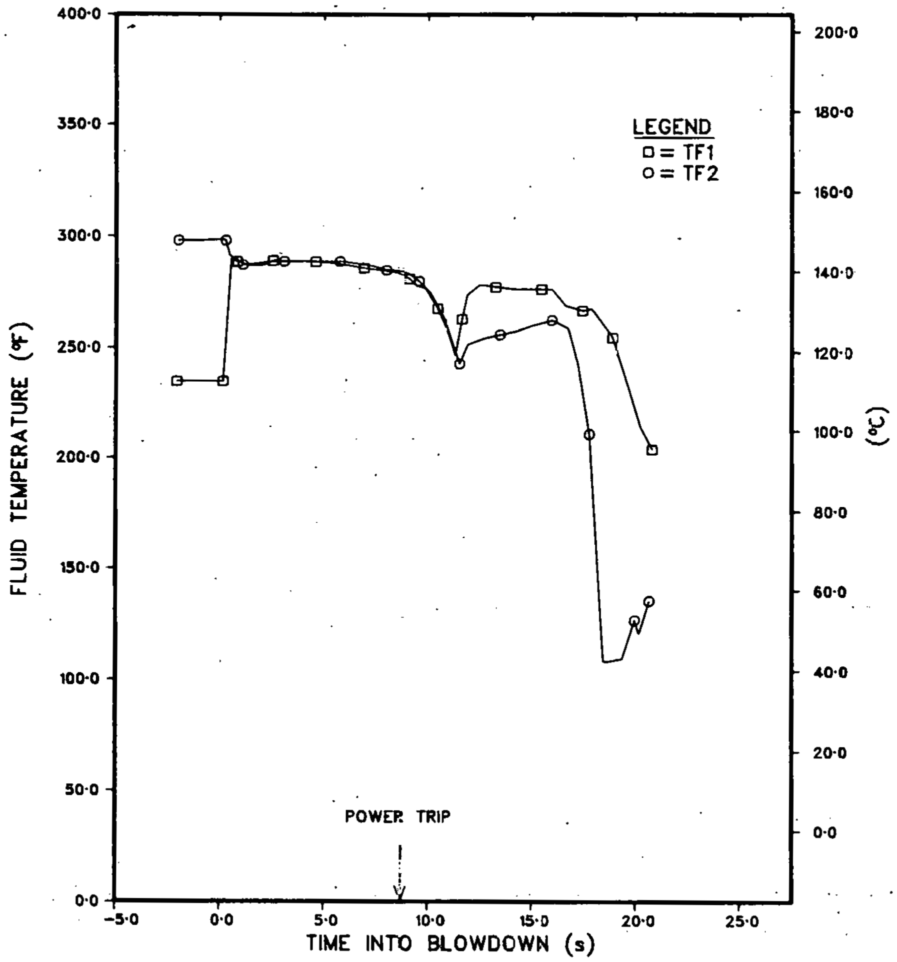

Fig. I.15. Fluid Temperature during Test DB-113

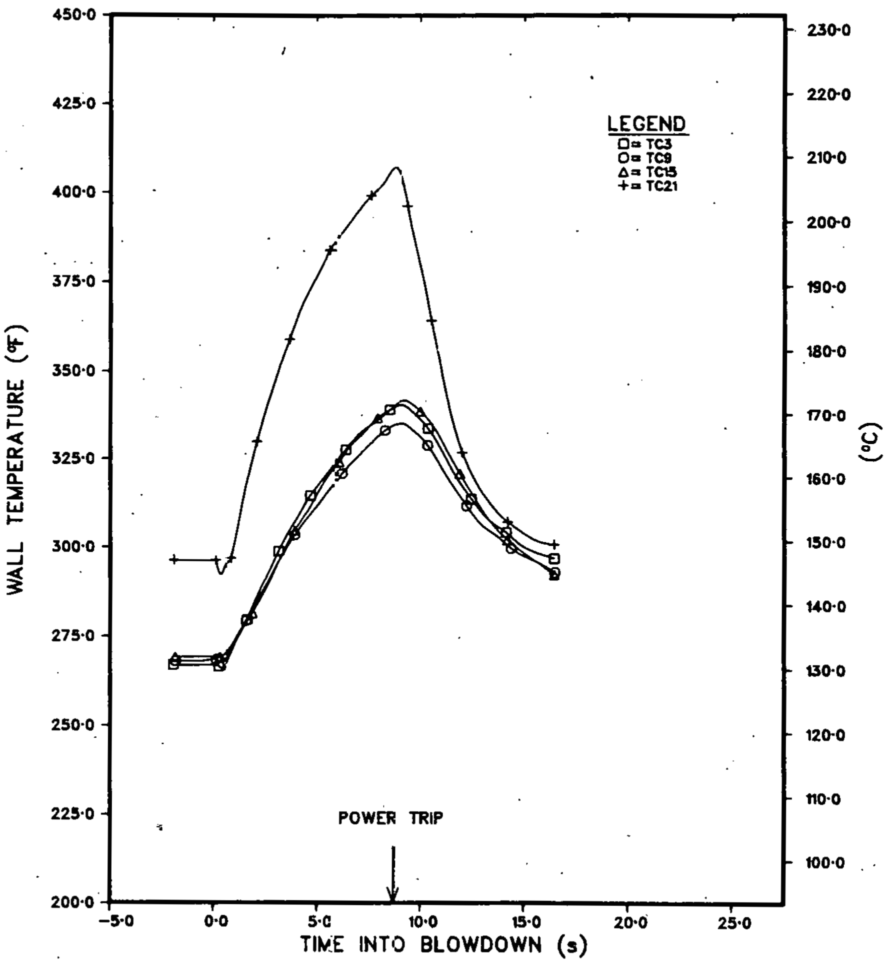

Fig. I.16. Wall-thermocouple Measurement during Test DB-113

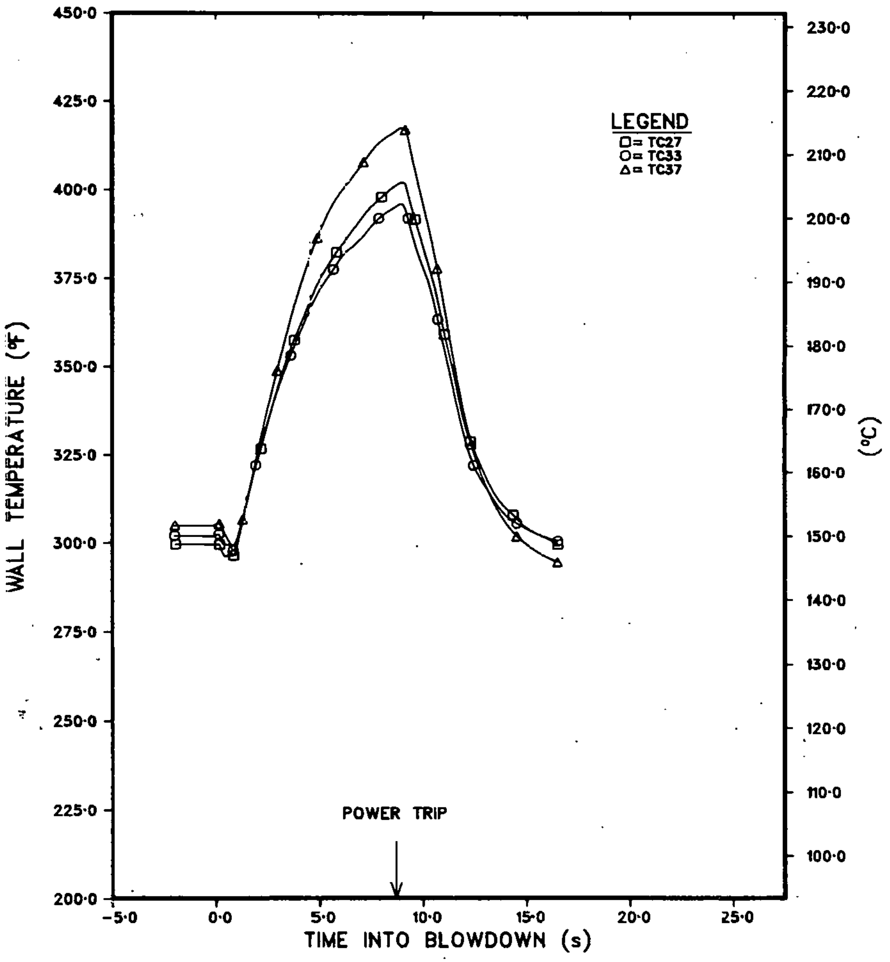

Fig. I.16 (Contd.)

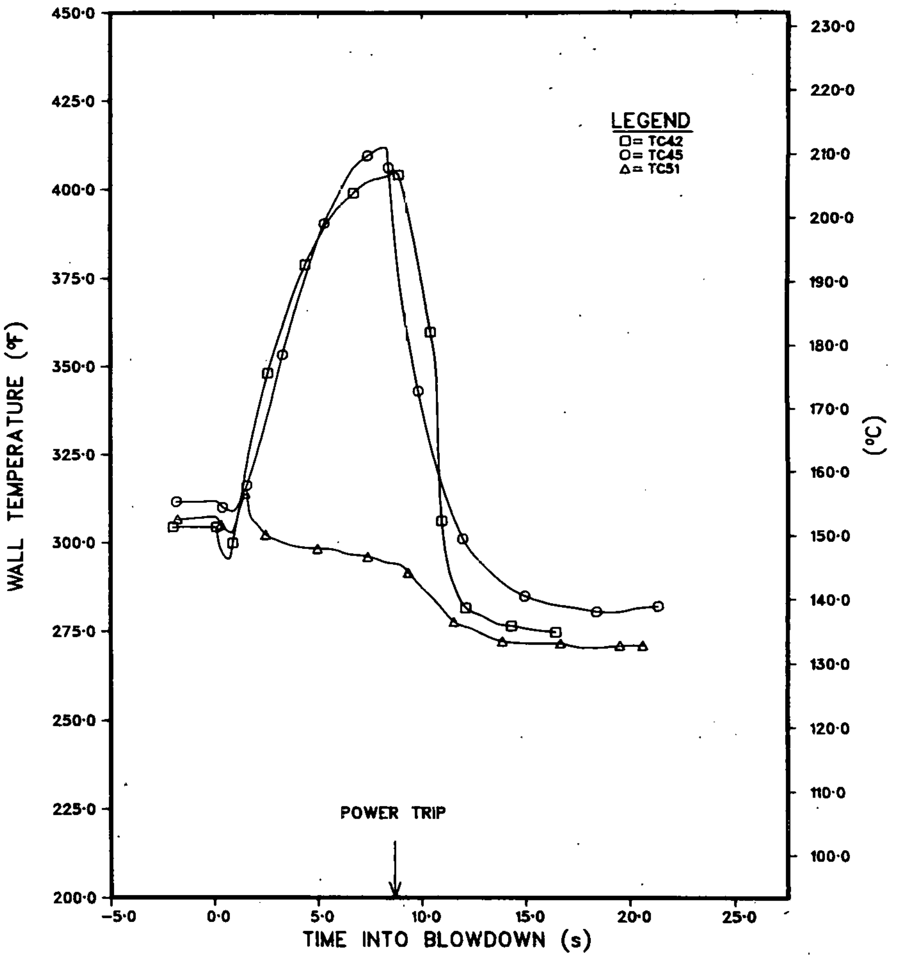

Fig. I.16 (Contd.)

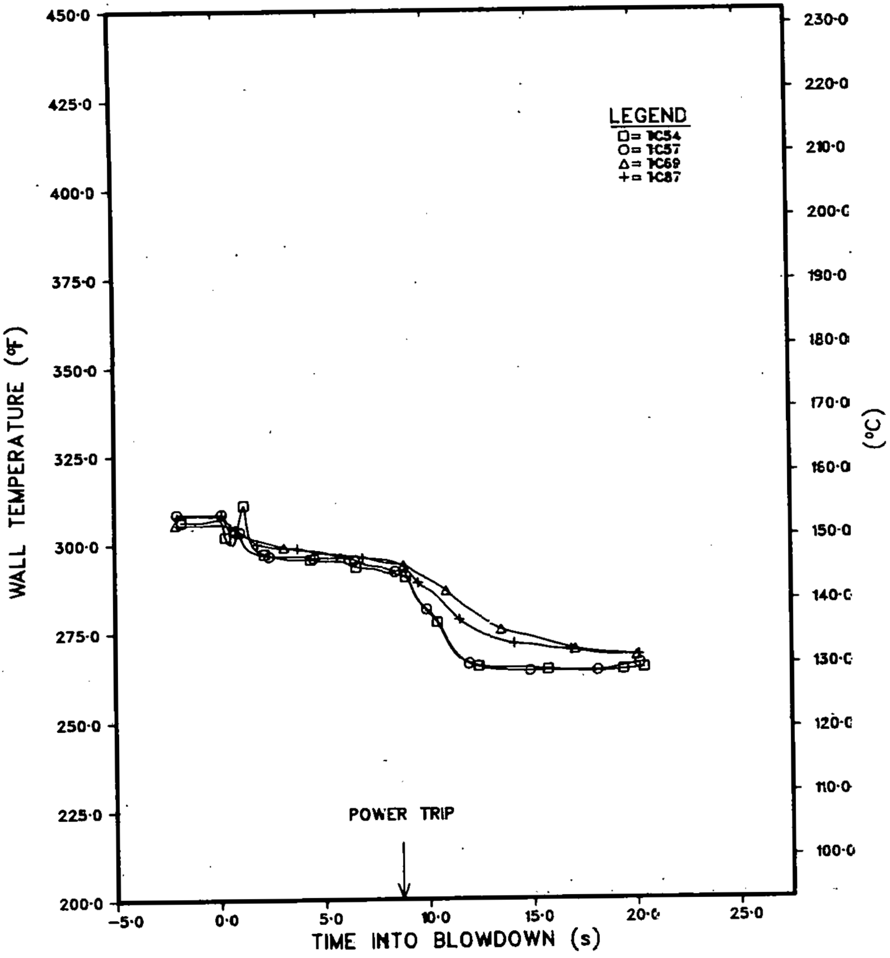

Fig. I.16 (Contd.)

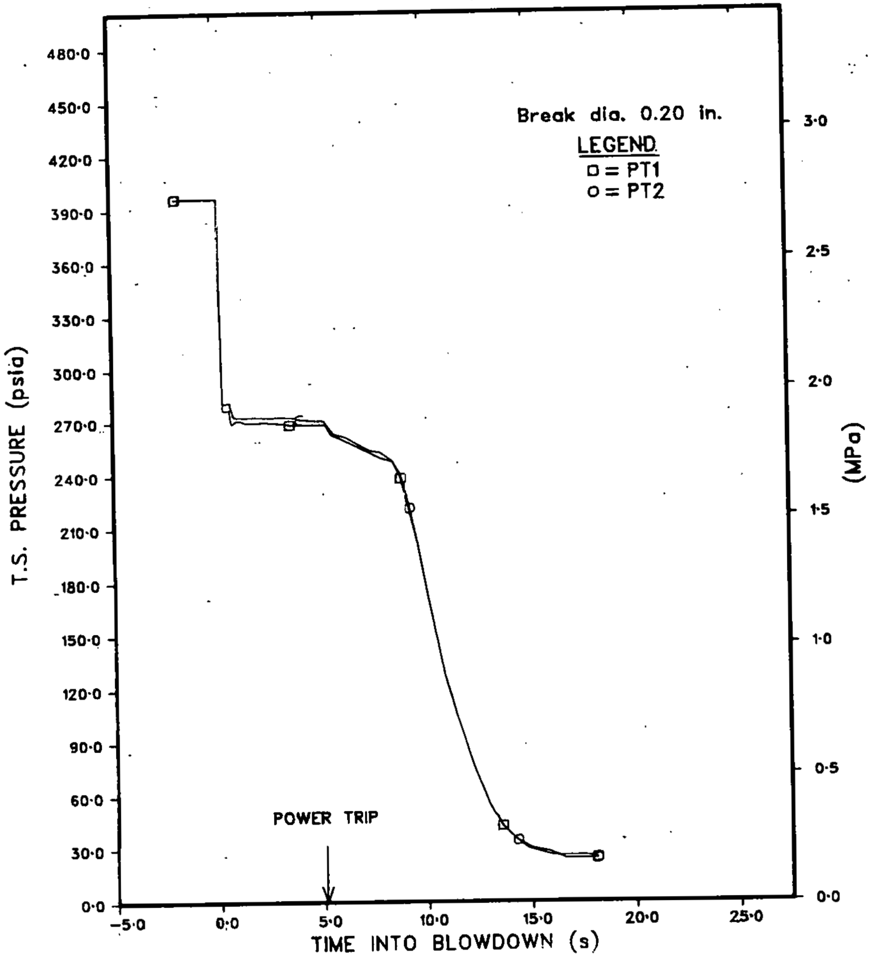

Fig. I.17. System Pressure during Test DB-114

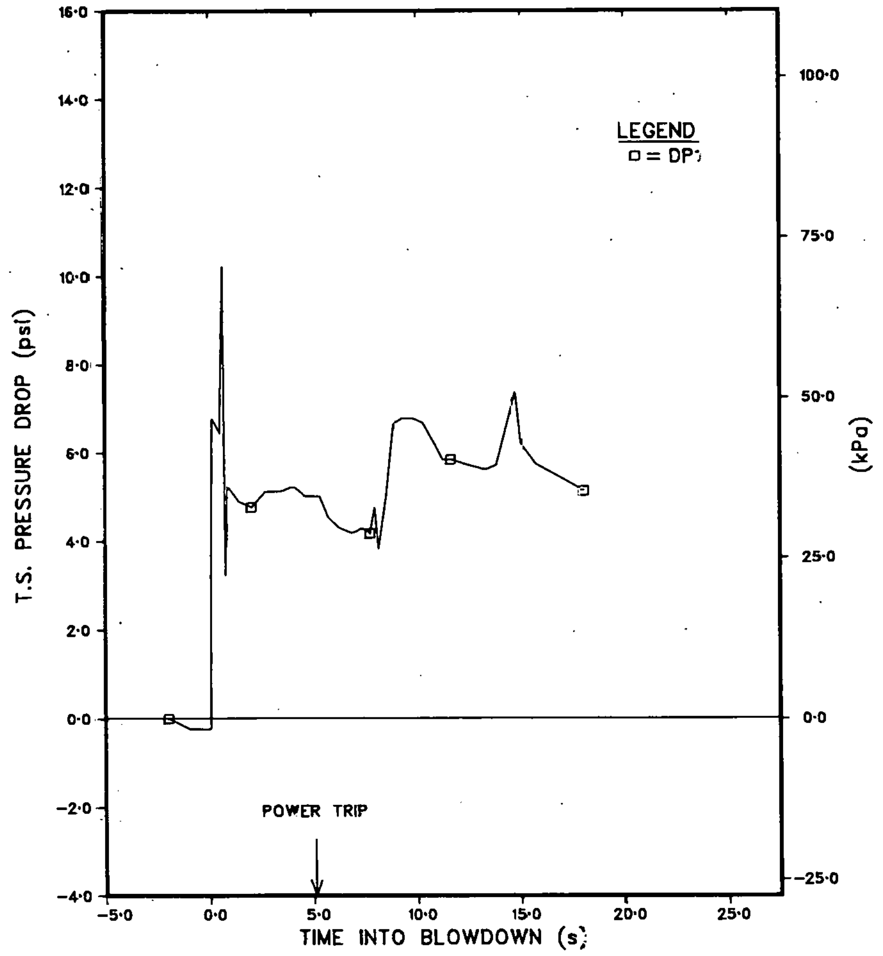

Fig. I.18. Differential Pressure across Test Section during Test DB–114

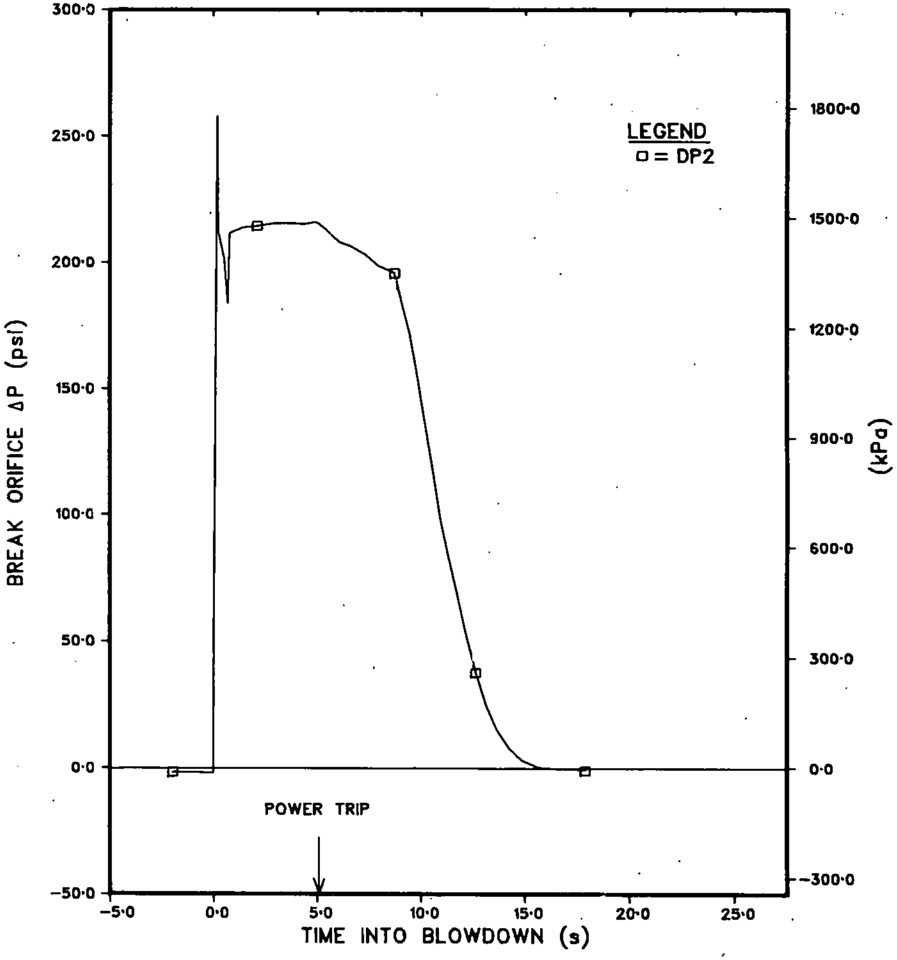

Fig. I.19. Differential Pressure across Break Orifice during Test DB–114

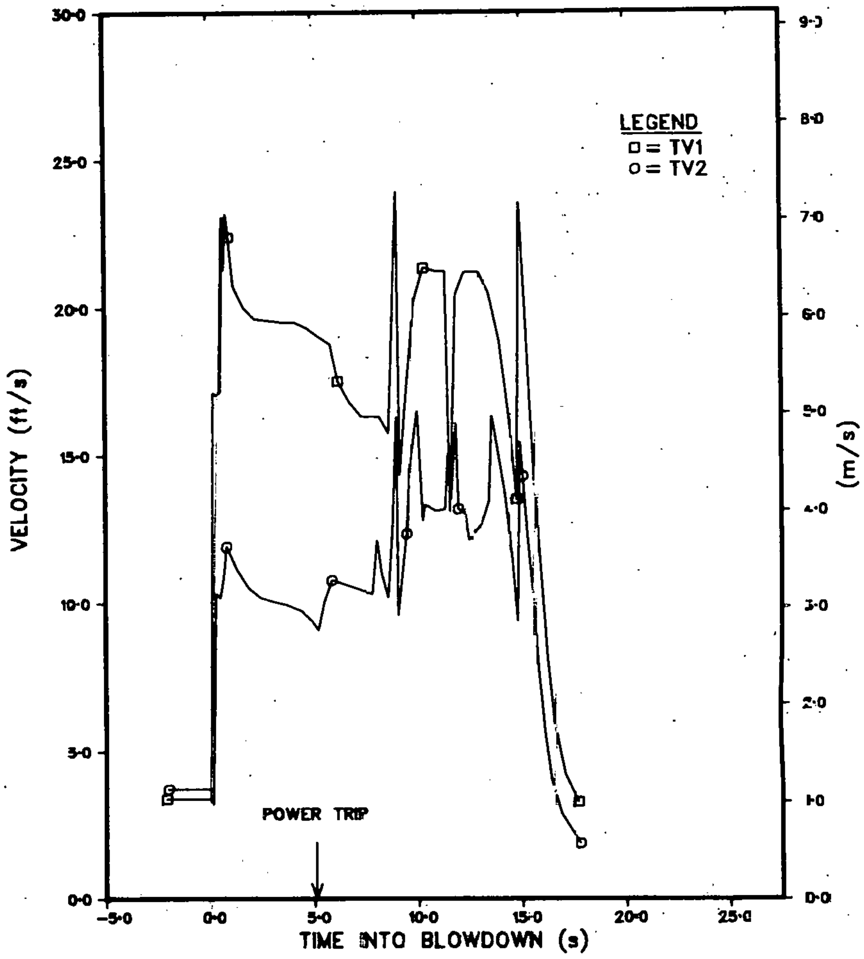

Fig. I.20. Turbine-flowmeter Measurement during Test DB-114

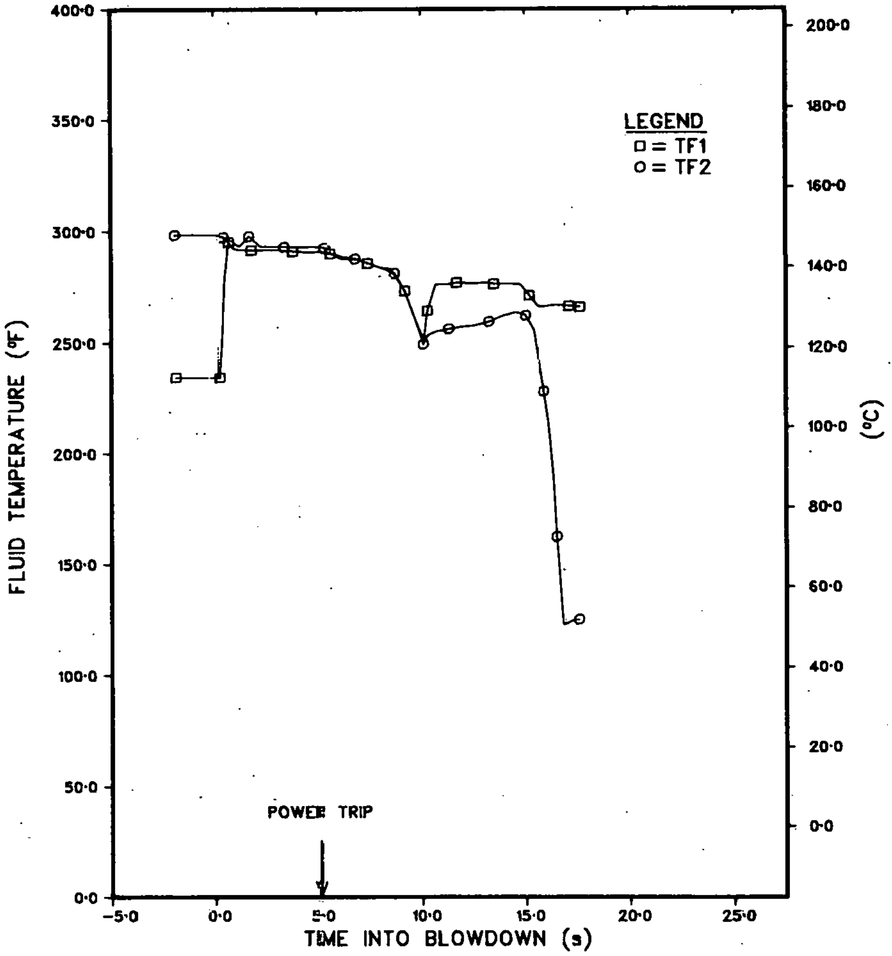

Fig. I.21. Fluid Temperature during Test DB-114

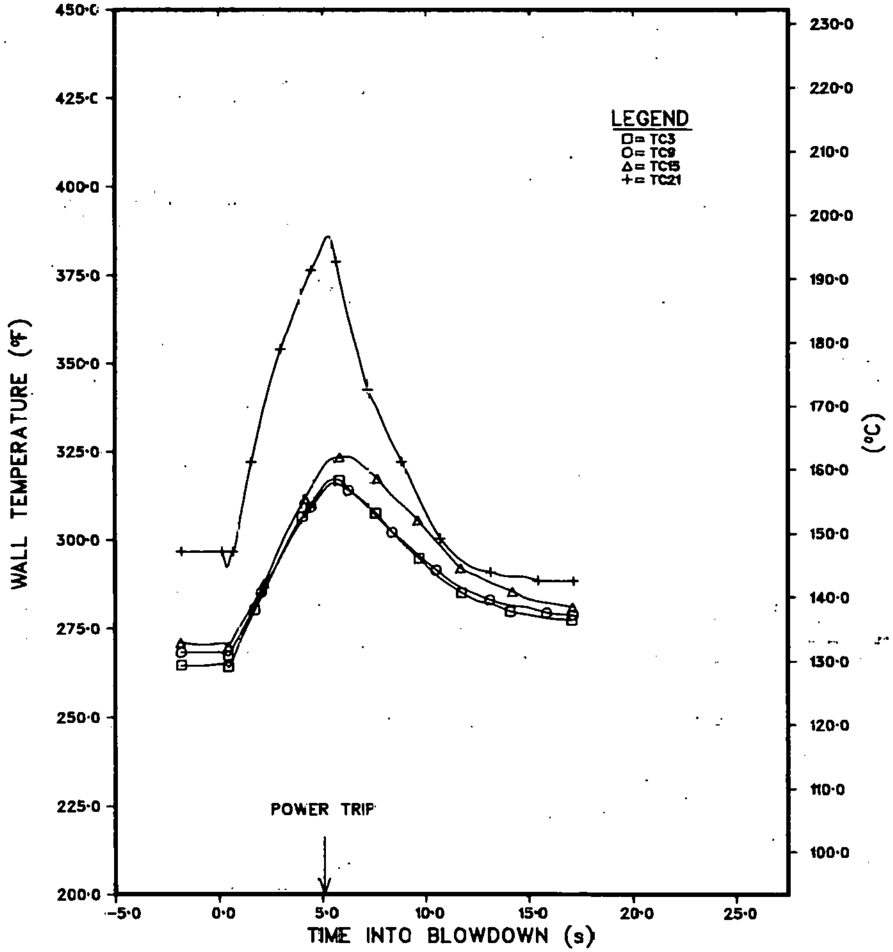

Fig. I.22. Wall-thermocouple Measurement during Test DB-114.

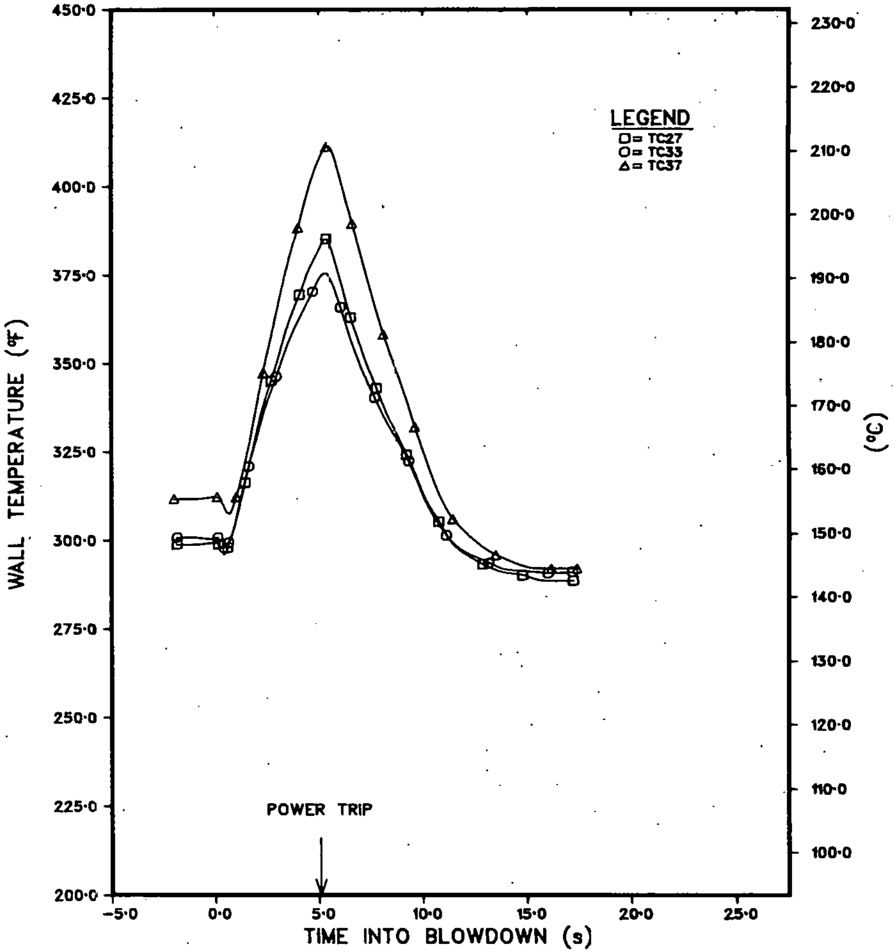

Fig. I.22 (Contd.)

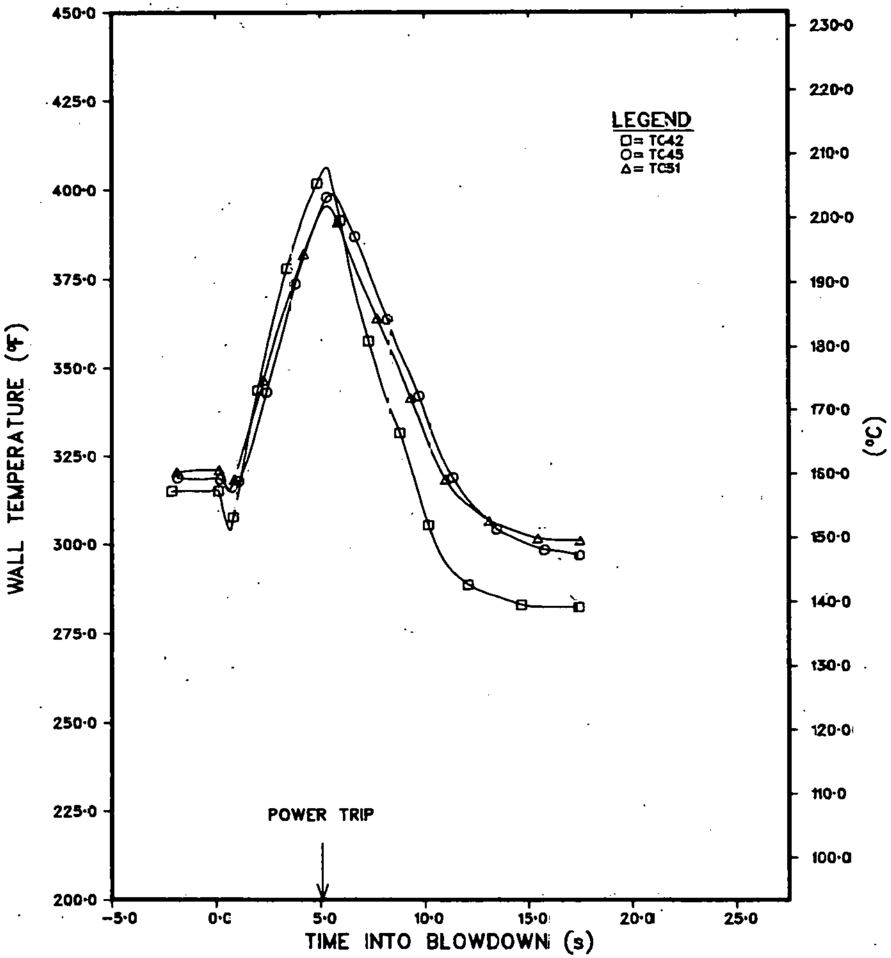

Fig. I.22 (Contd.)

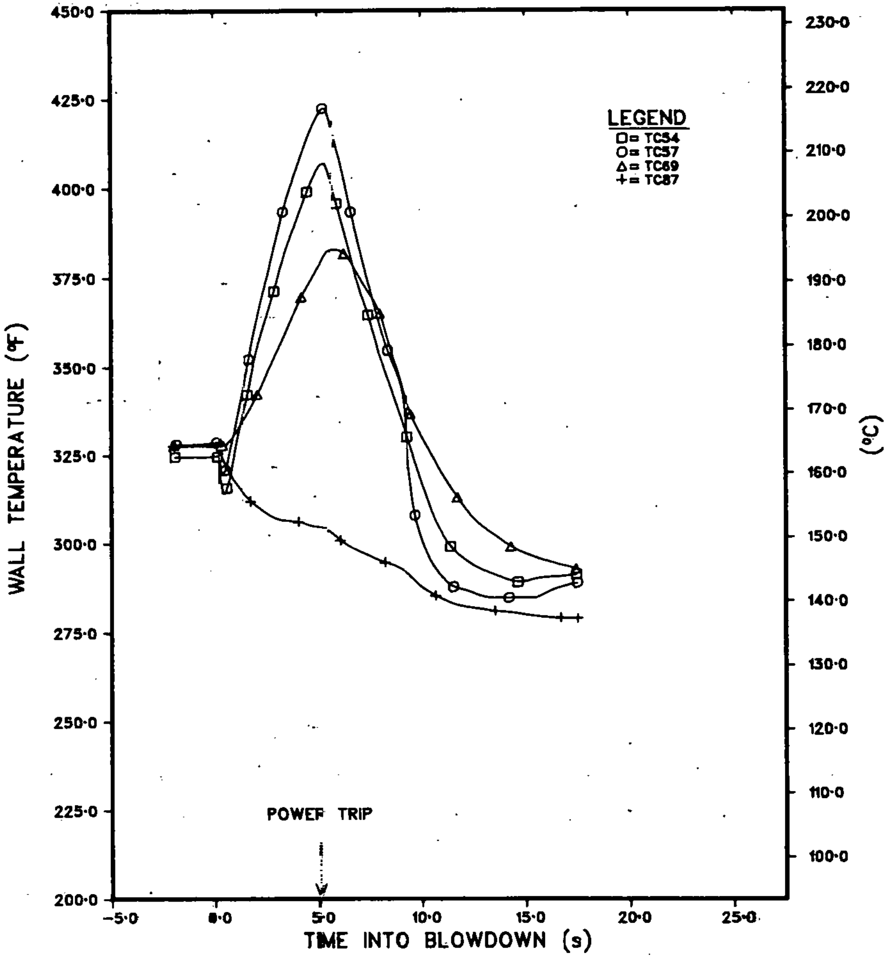

Fig. I.22 (Contd.)

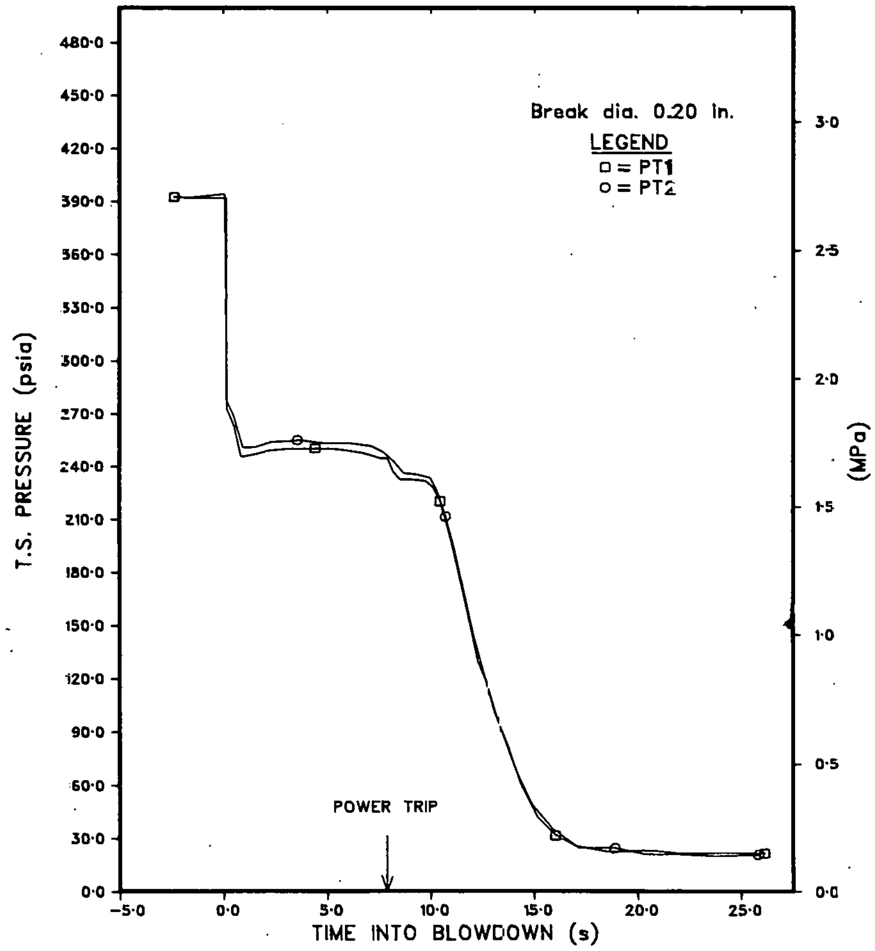

Fig. I.23. System Pressure during Test DB-115

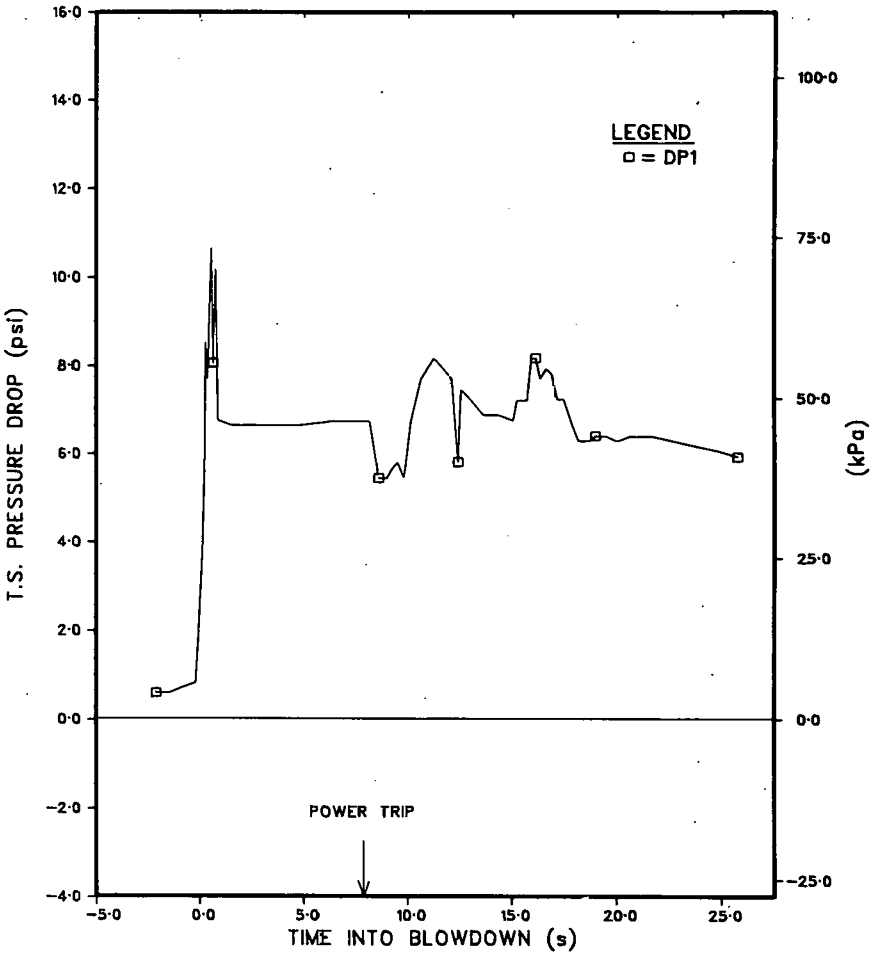

Fig. I.24. Differential Pressure across Test Section during Test DB-115

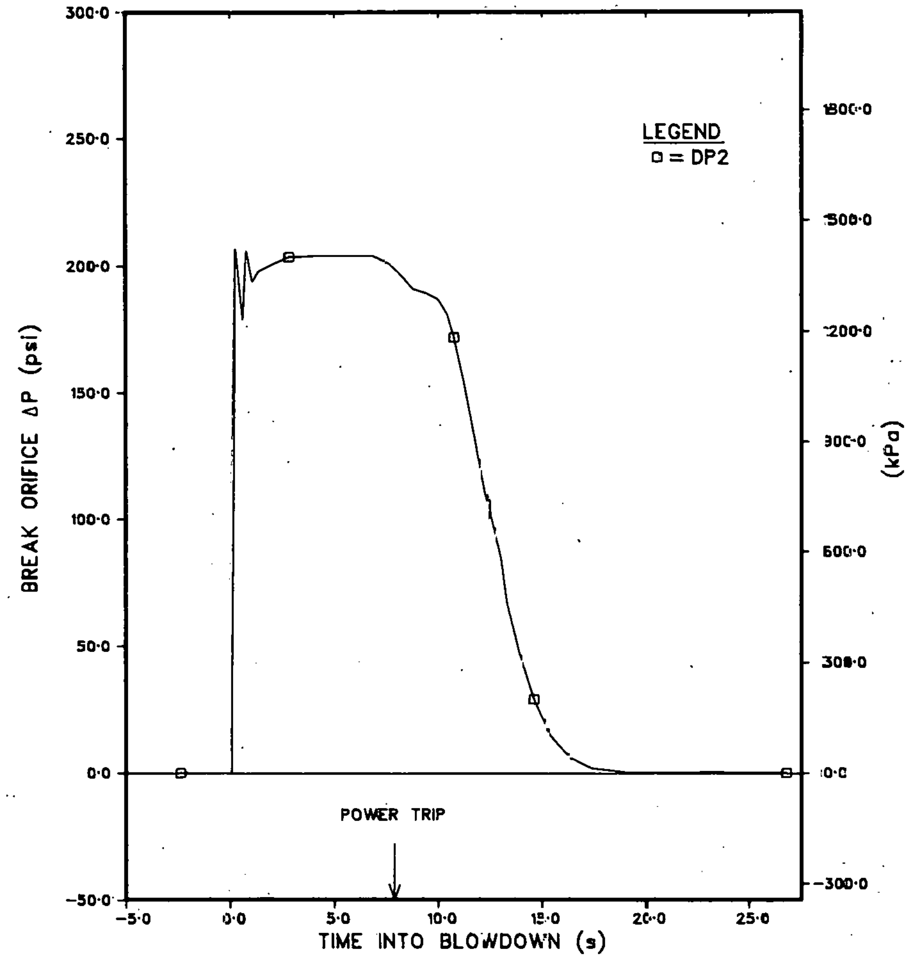

Fig. I.25. Differential Pressure across Break Orifice during Test DB-115

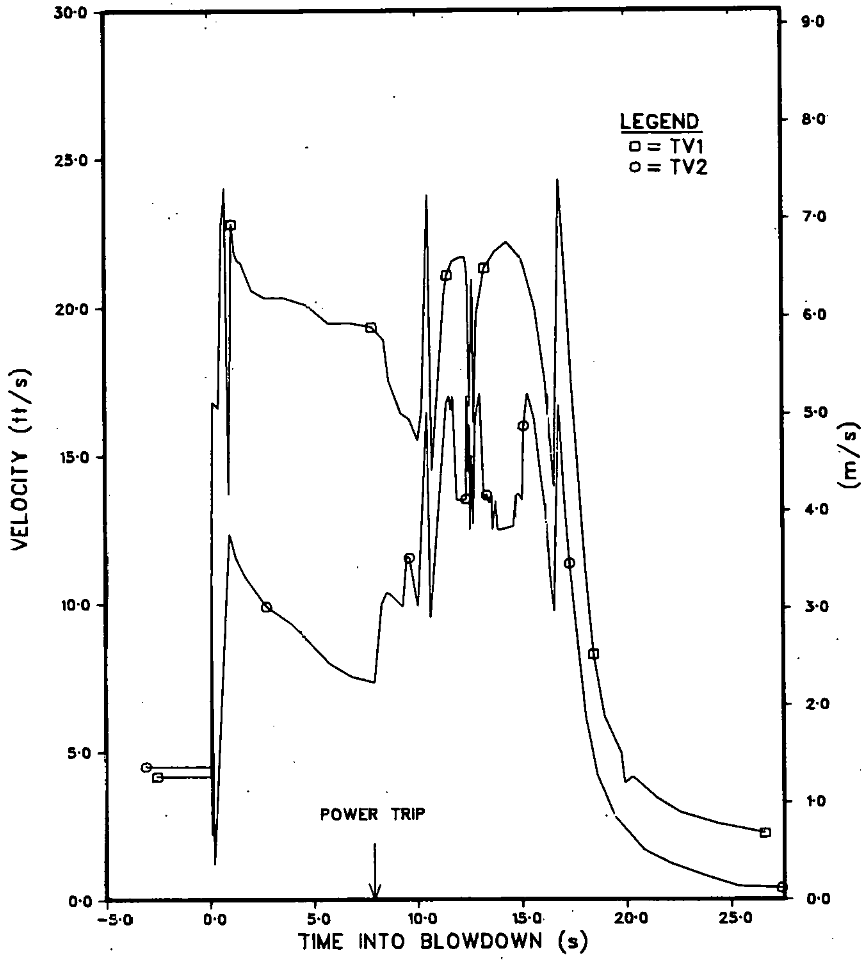

Fig. I.26. Turbine-flowmeter Measurement during Test DB-115

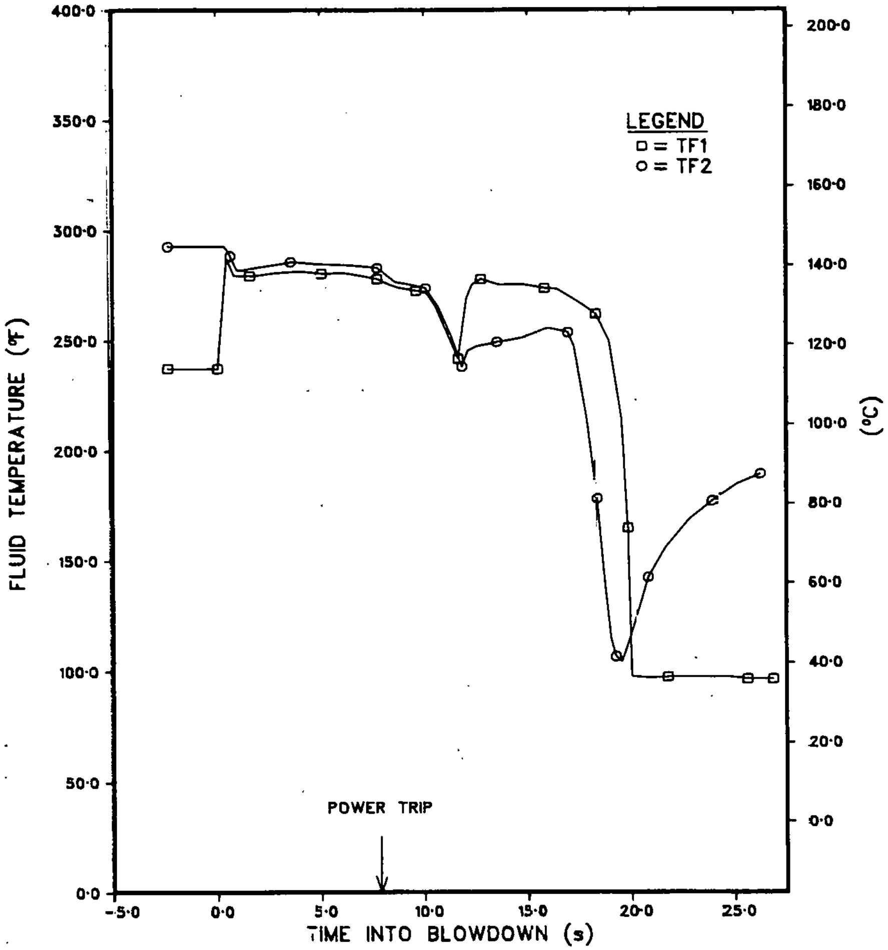

Fig. I.27. Fluid Temperature during Test DB-115

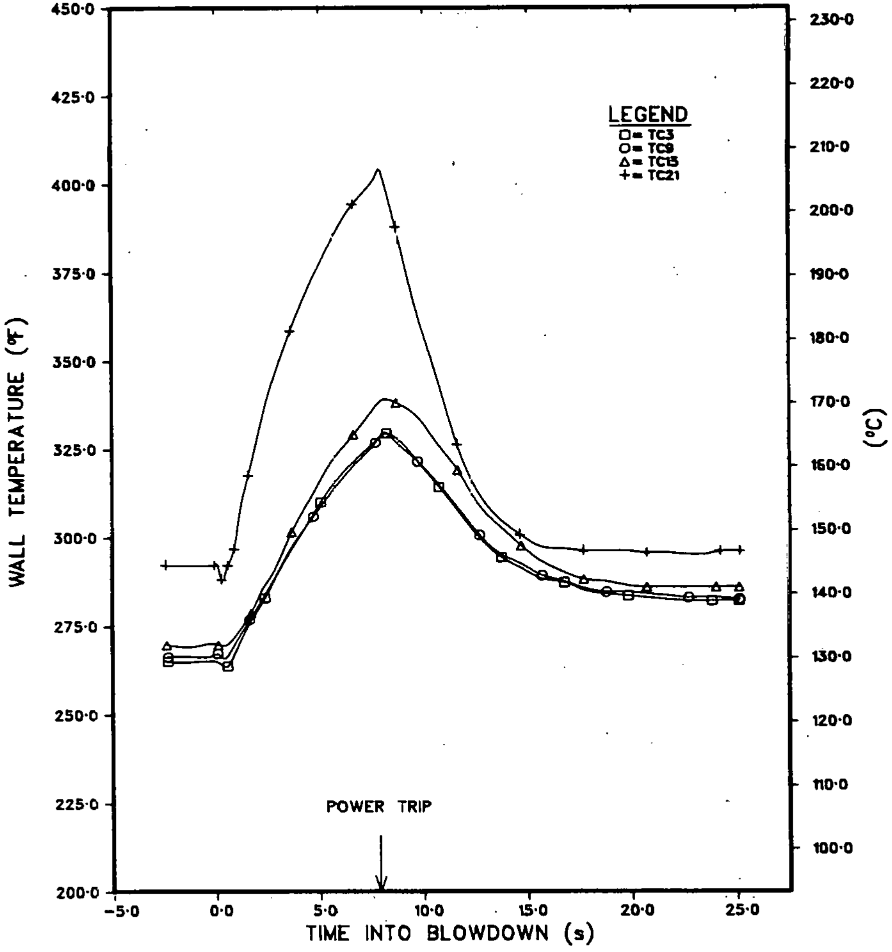

Fig. I.28. Wall-thermocouple Measurement during Test DB-115.

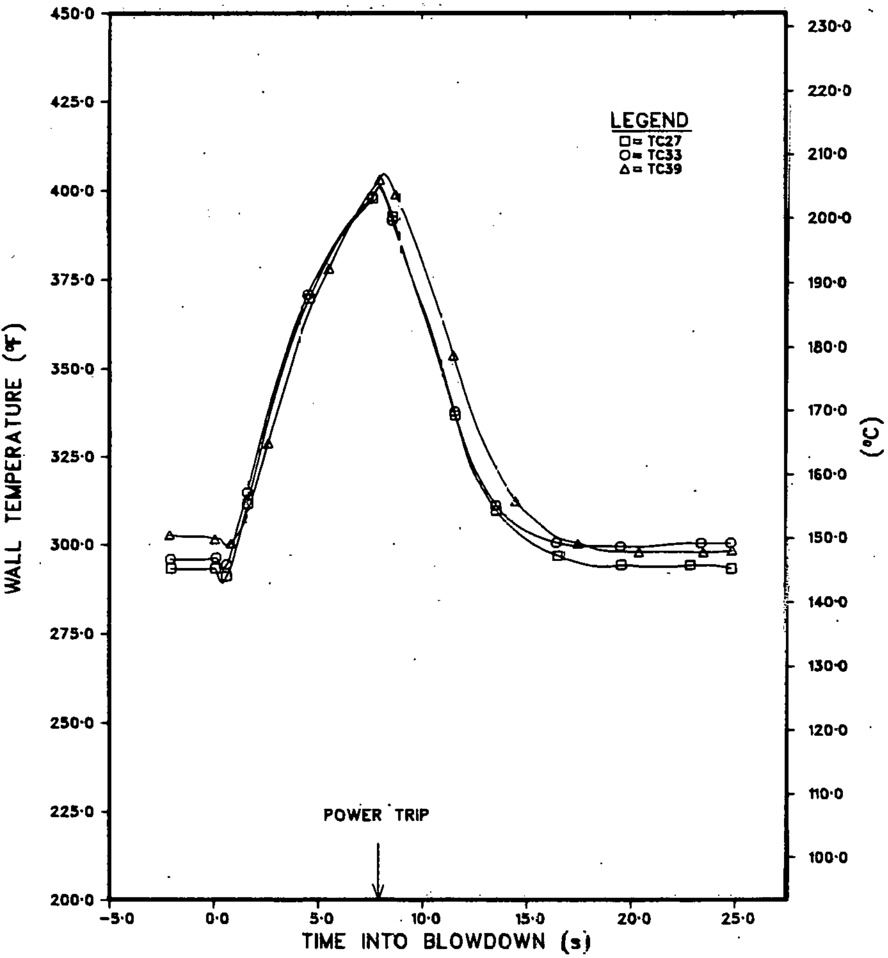

Fig. I.28 (Contd.)

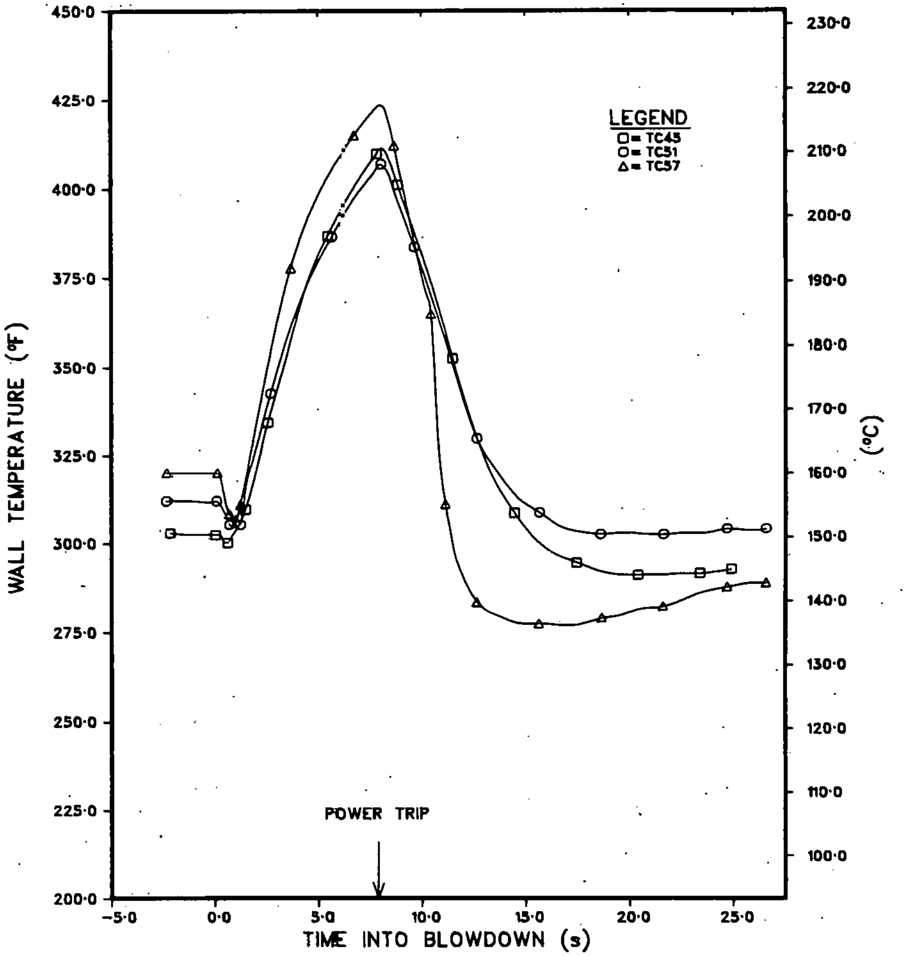

Fig. I.28 (Contd.)

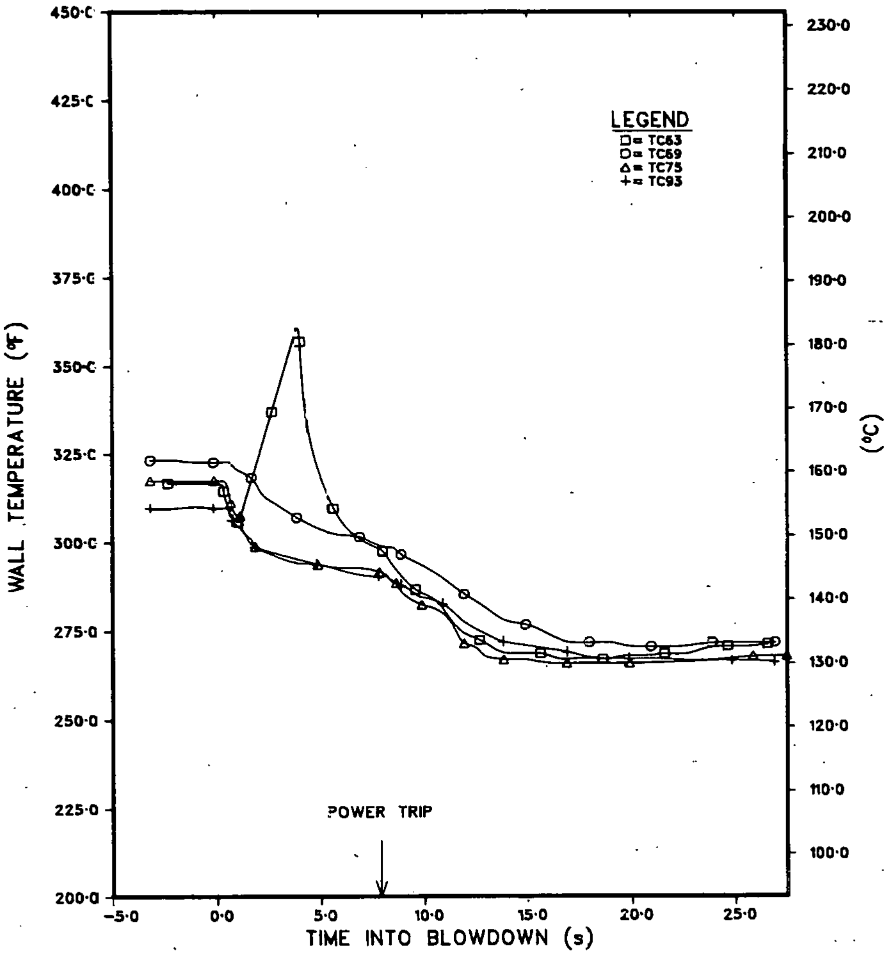

Fig. I.28 (Contd.)

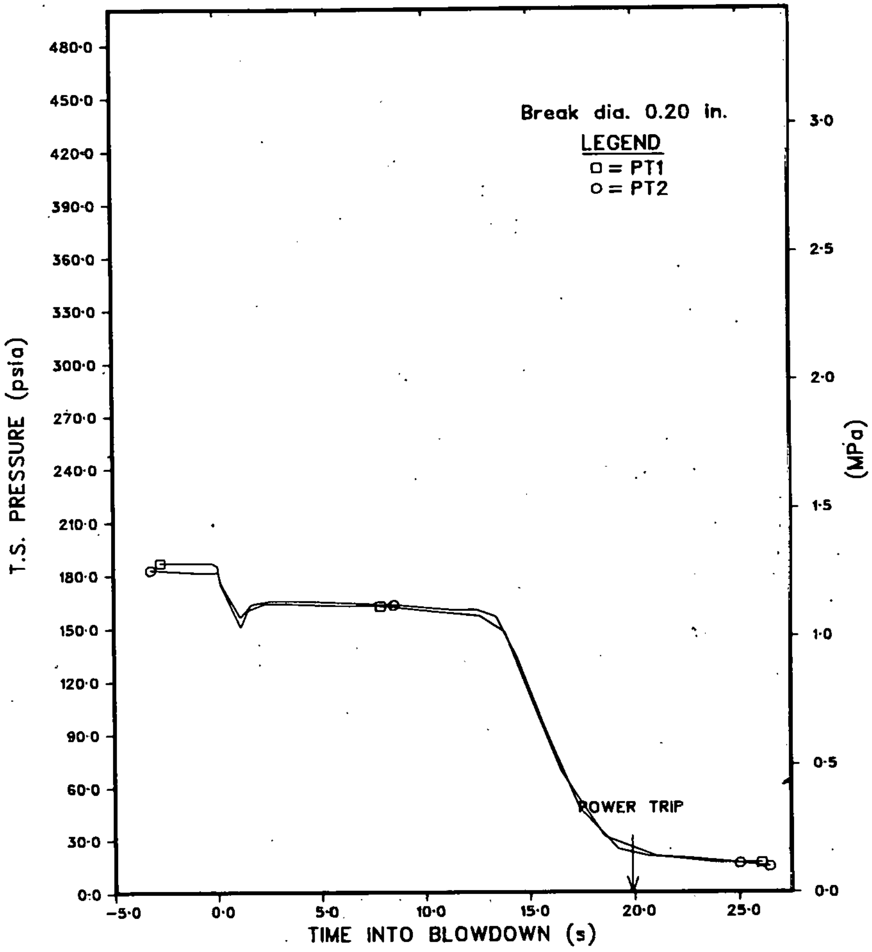

Fig. I.29. System Pressure during Test DB-117

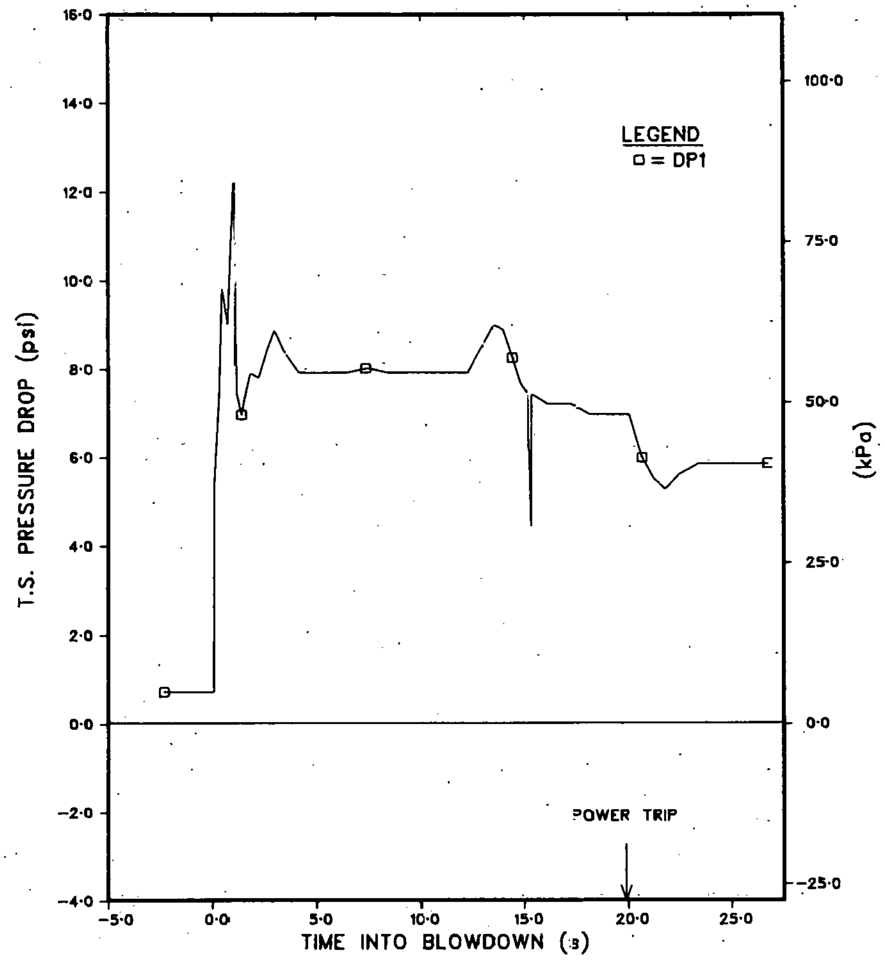

Fig. I.30. Differential Pressure across Test Section during Test DB–117

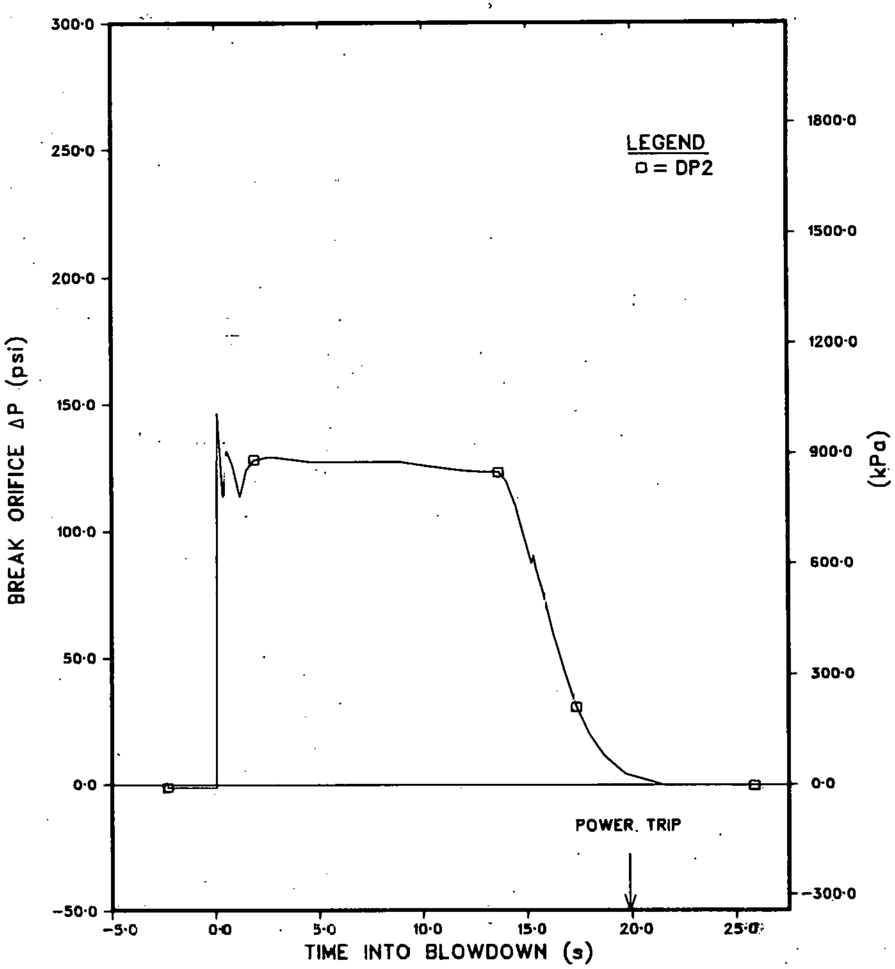

Fig. I.31. Differential Pressure across Break Orifice during Test DB–117

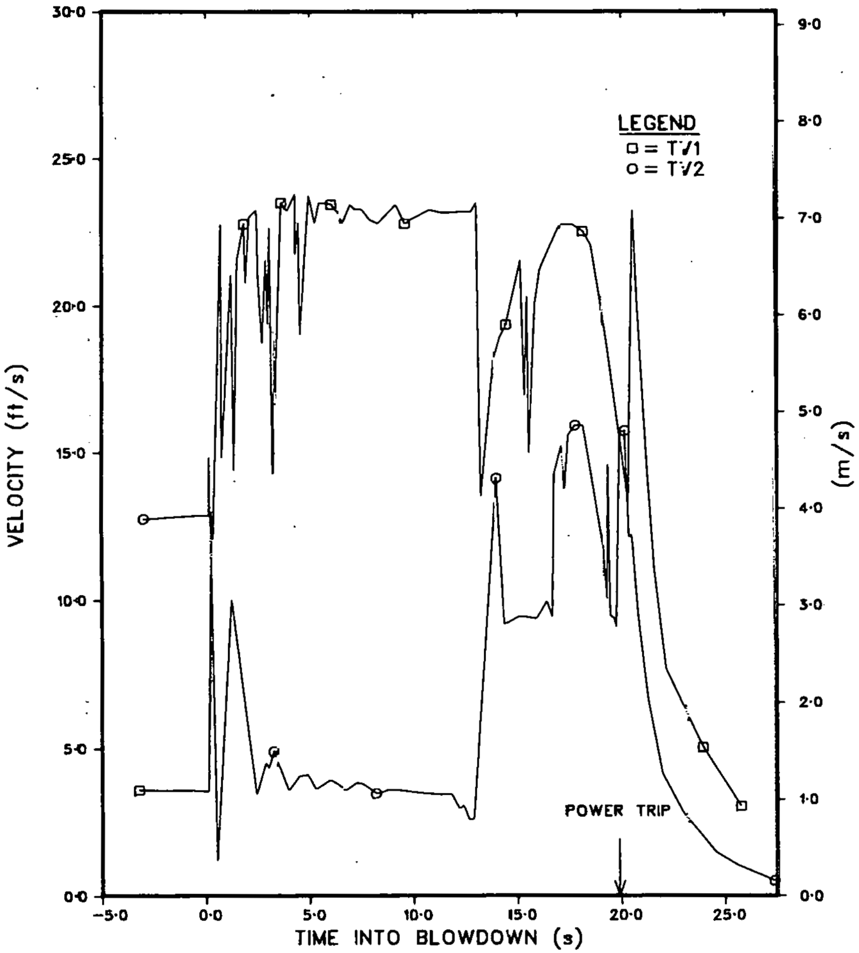

Fig. I.32. Turbine-flowmeter Measurement during Test DB-117

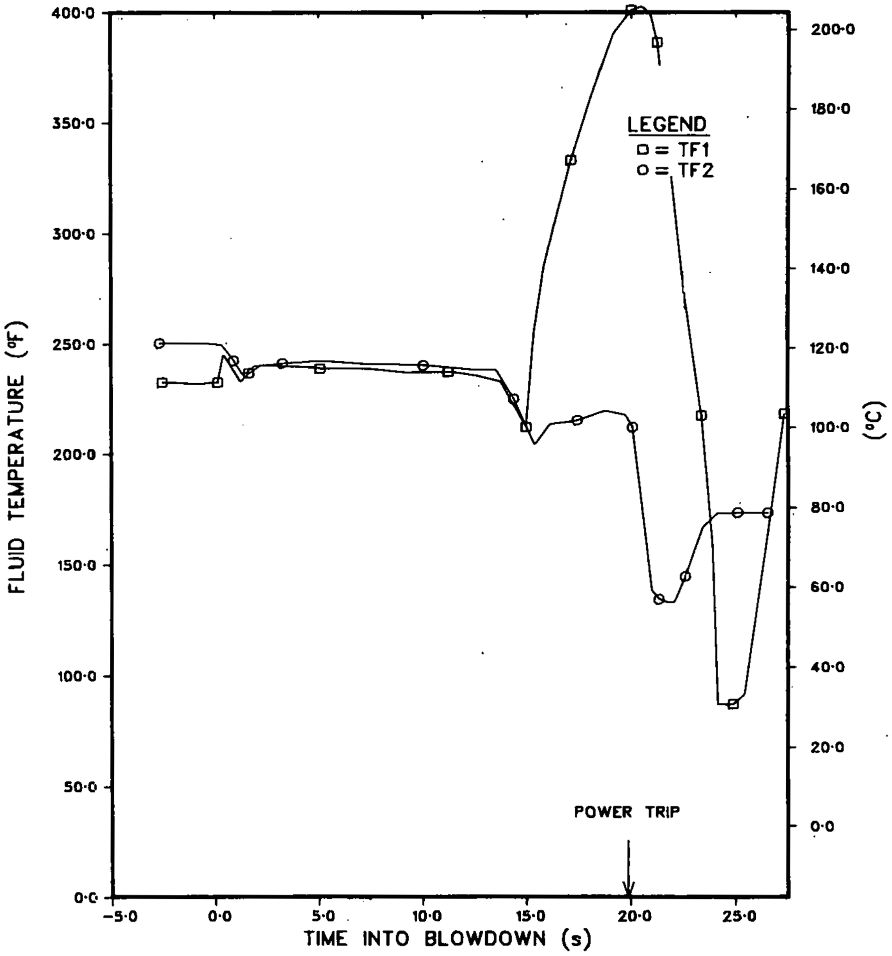

Fig. I.33. Fluid Temperature during Test DB-117

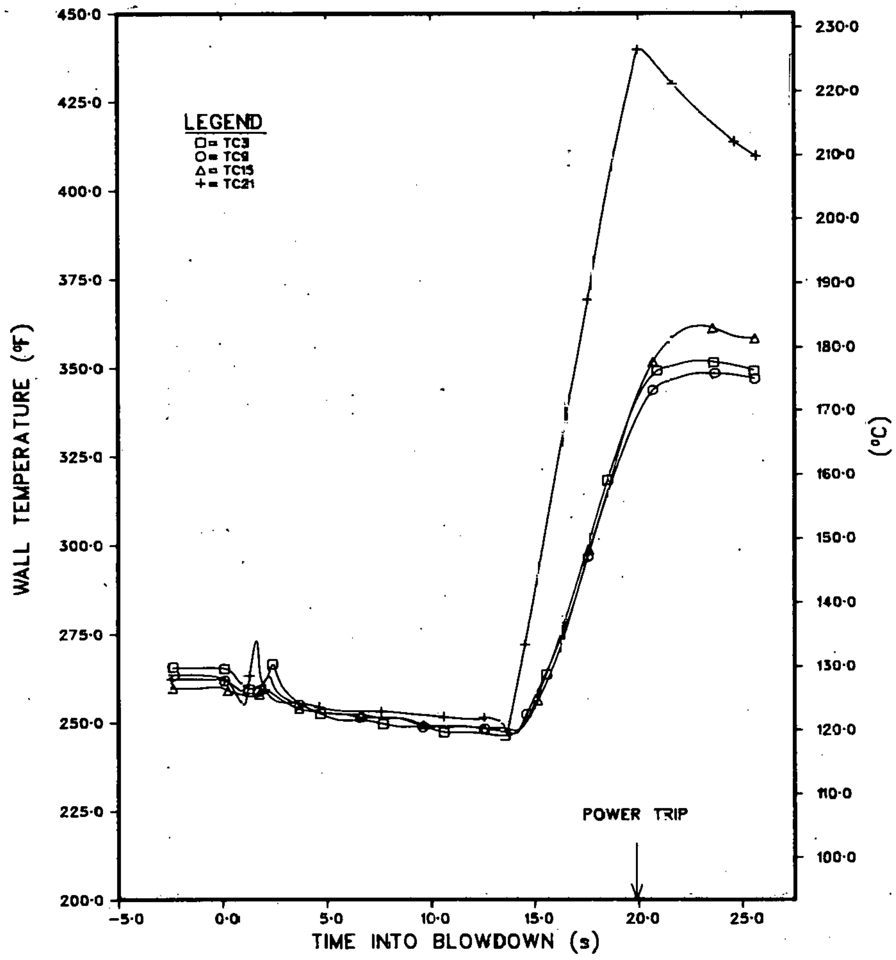

Fig. I.34. Wall-thermocouple Measurement during Test DB-117

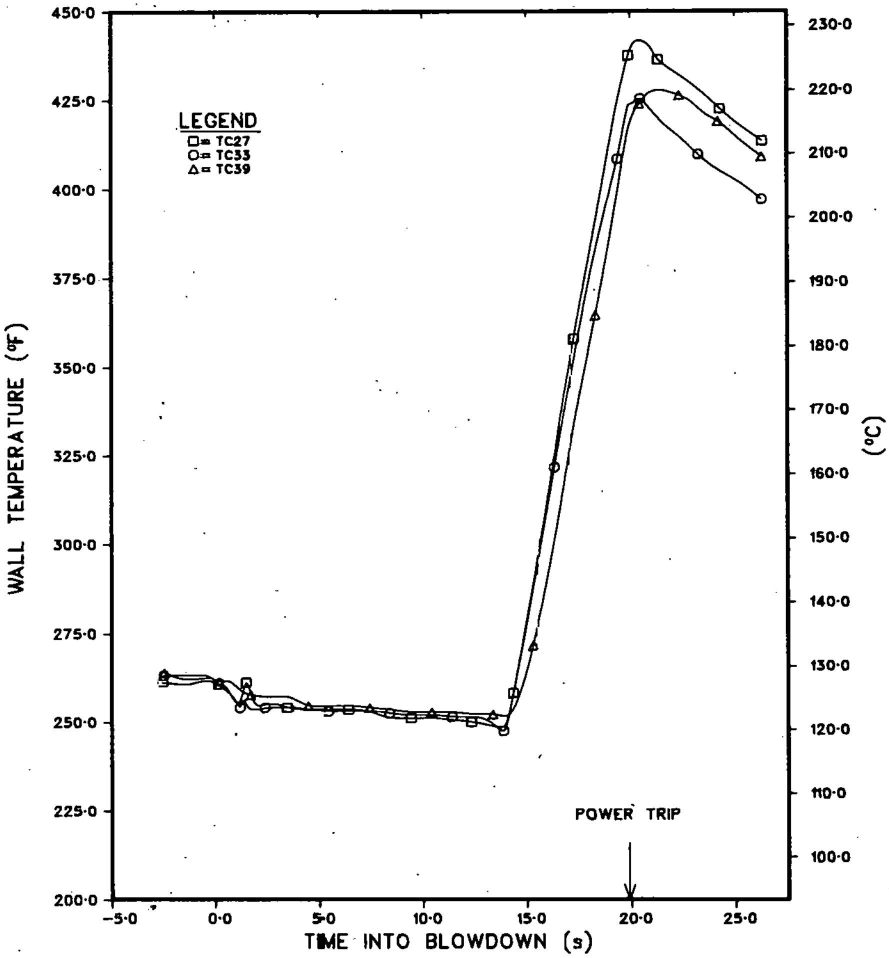

Fig. I.34 (Contd.)

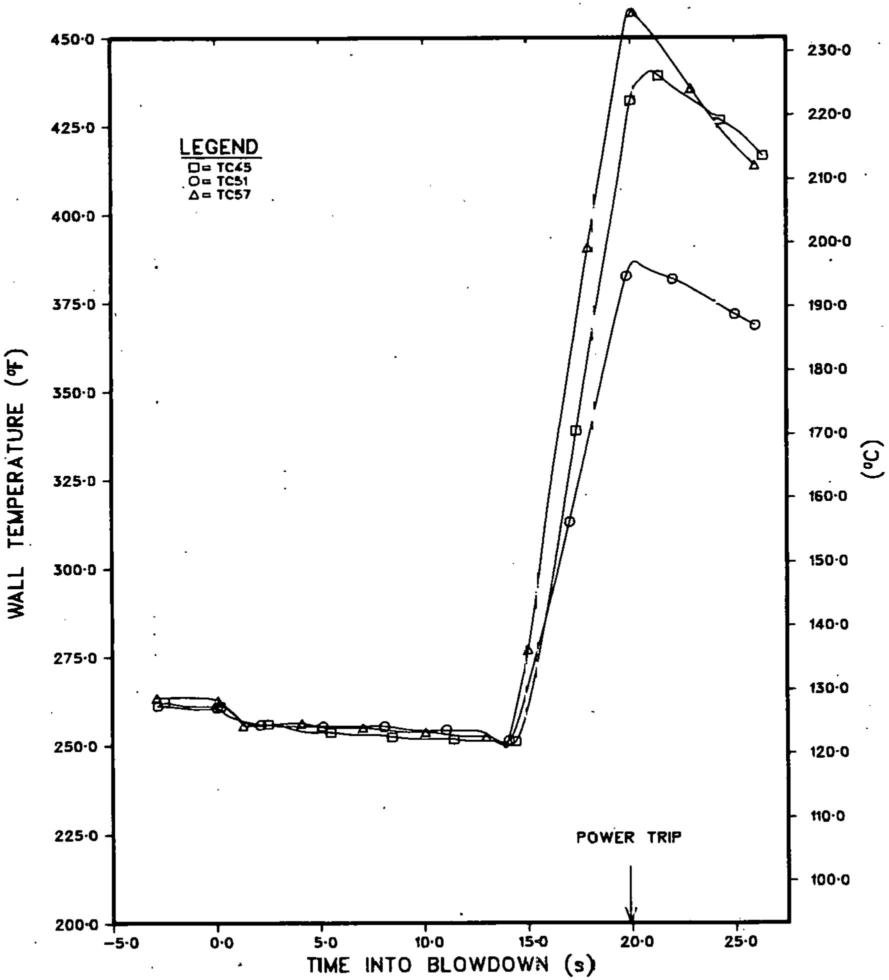

Fig. I.34 (Contd.)

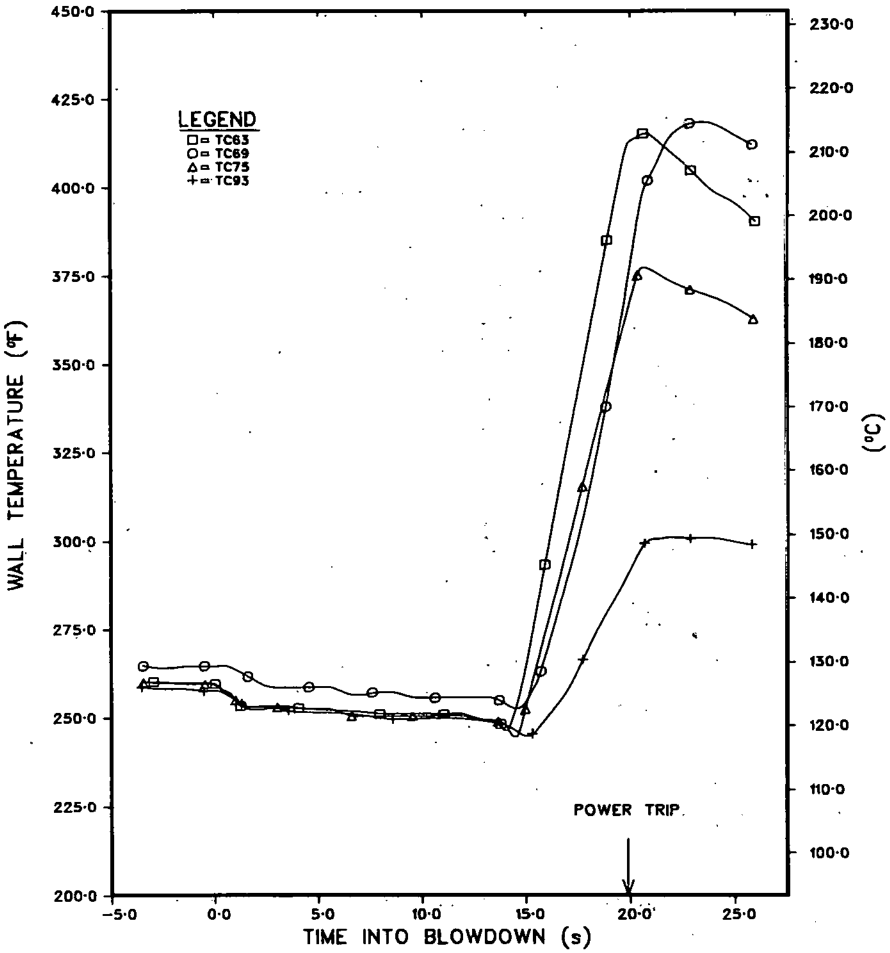

Fig. I.34 (Contd.)

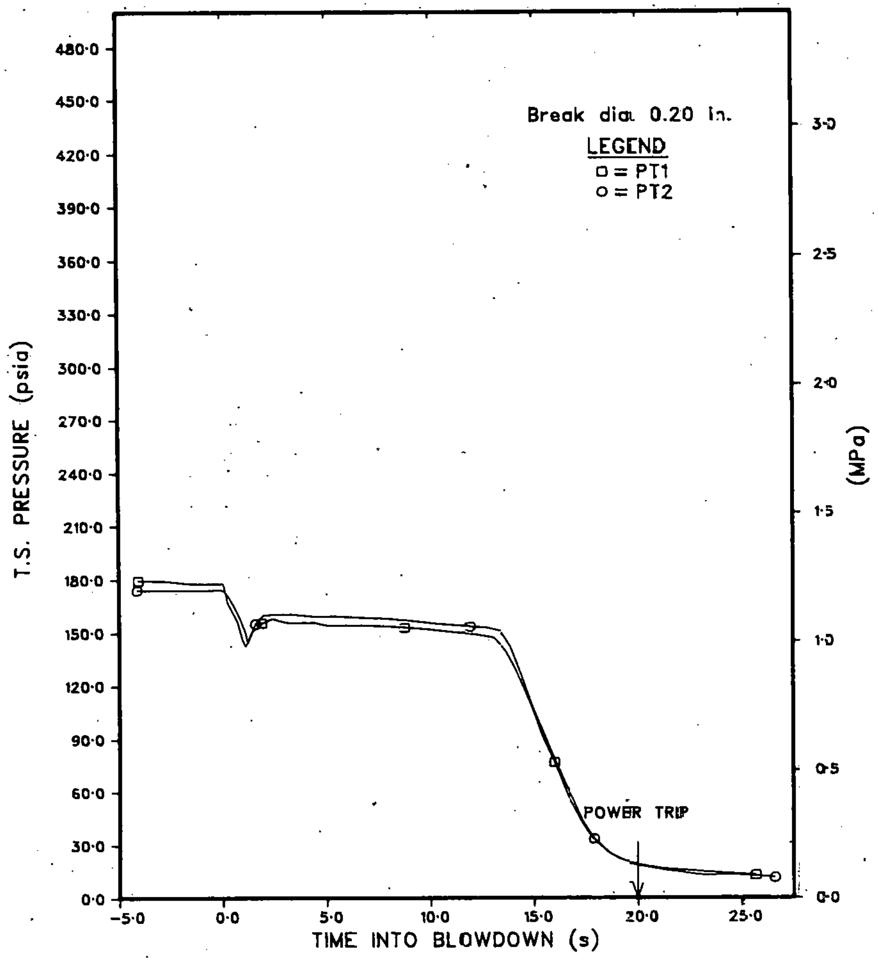

Fig. I.35. System Pressure during Test DB–118

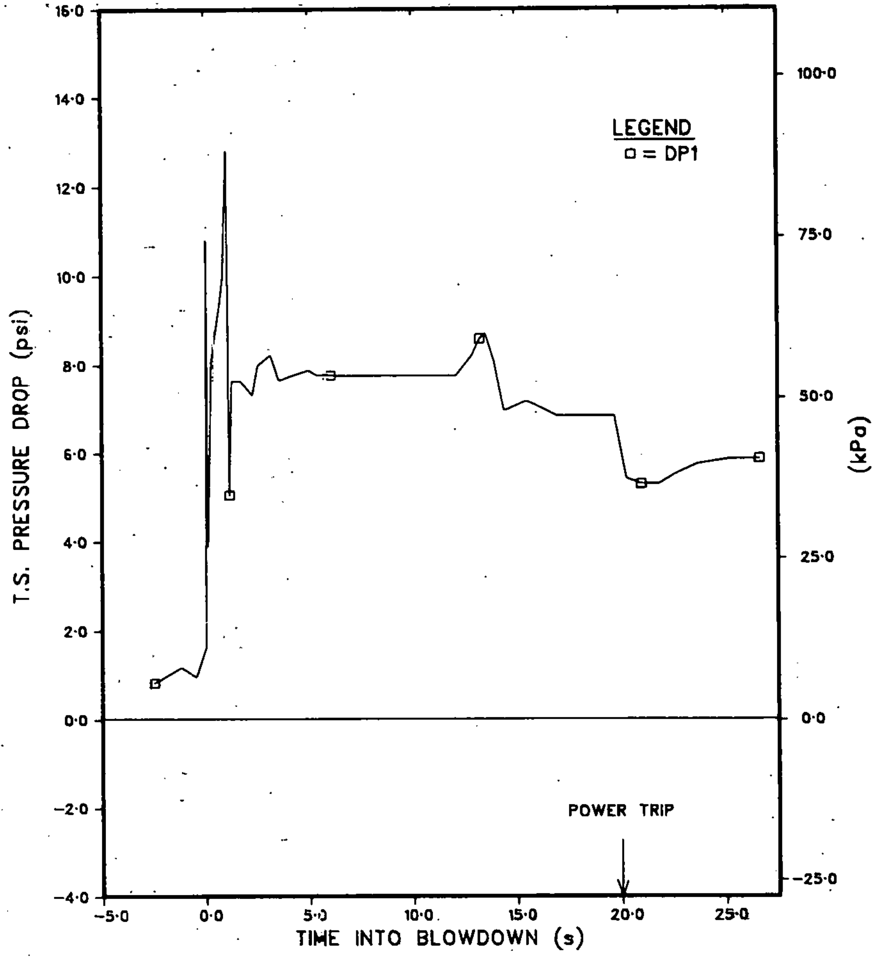

Fig. I.36. Differential Pressure across Test Section during Test DB–118

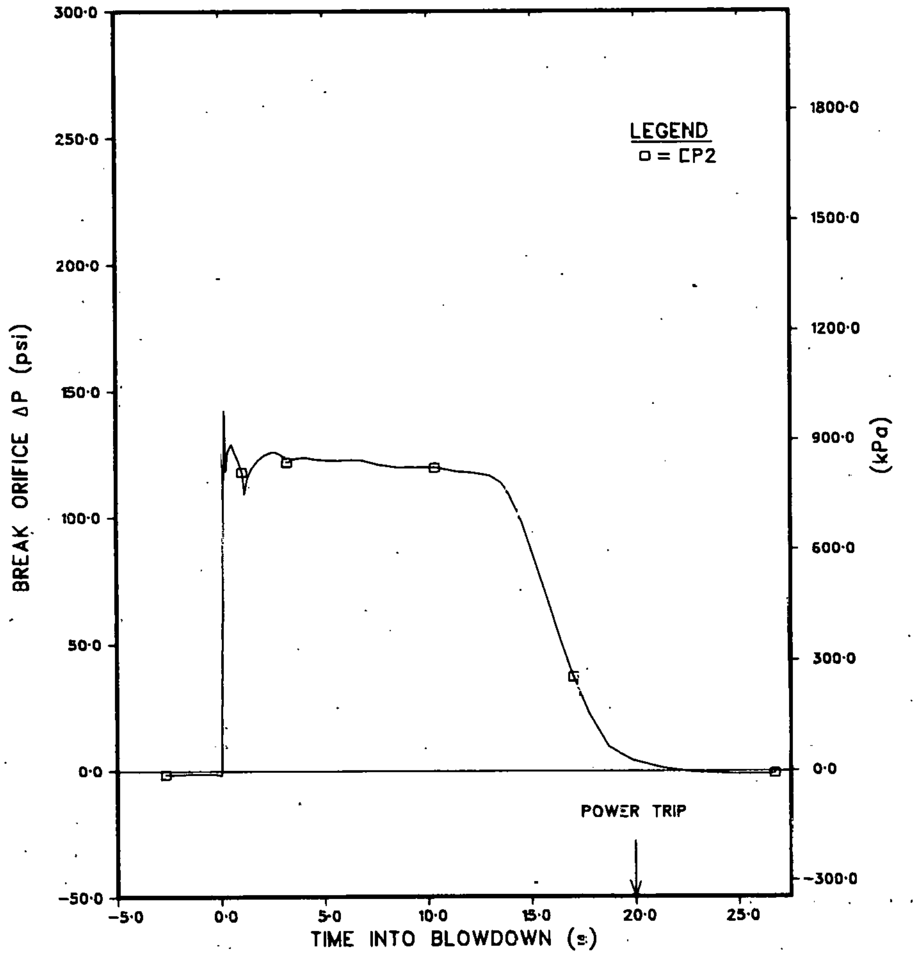

Fig. I.37. Differential Pressure across Break Orifice during Test DB–118

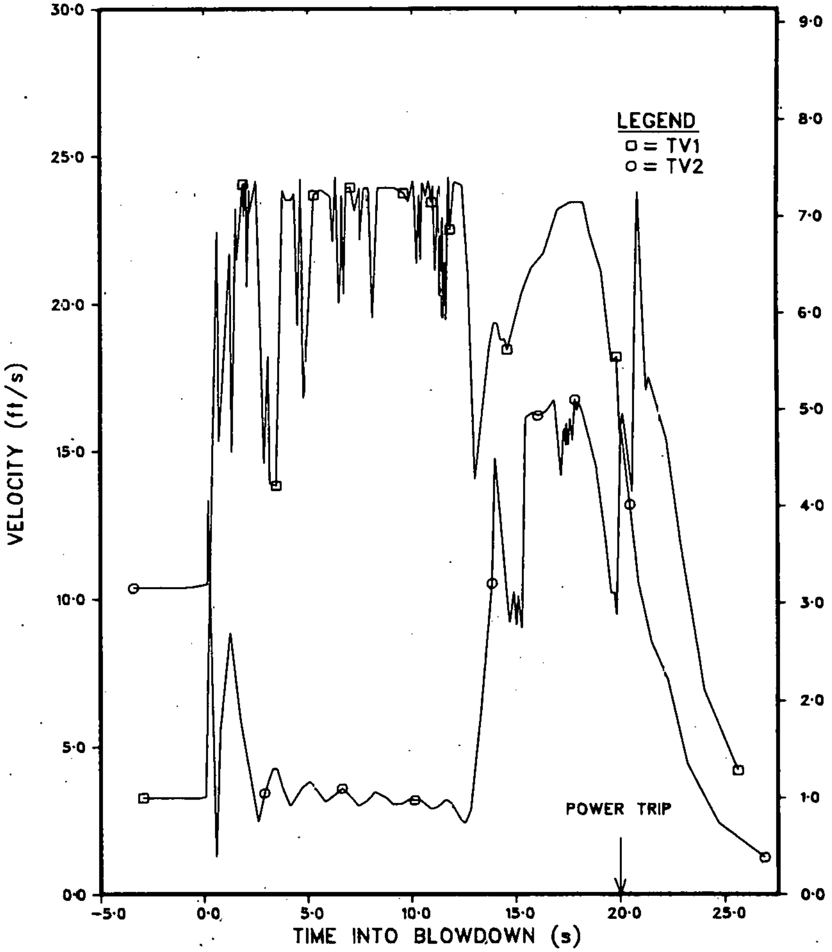

Fig. I.38. Turbine–flowmeter Measurement during Test DB–118

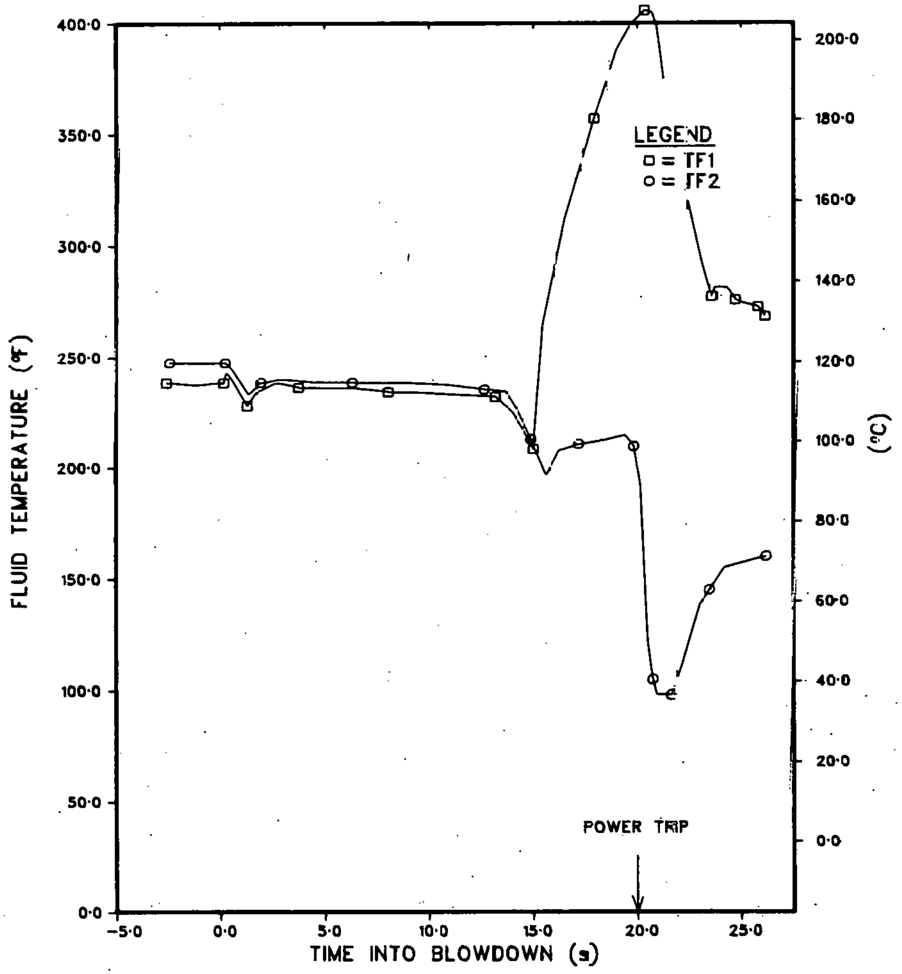

Fig. I.39. Fluid Temperature during Test DB-118

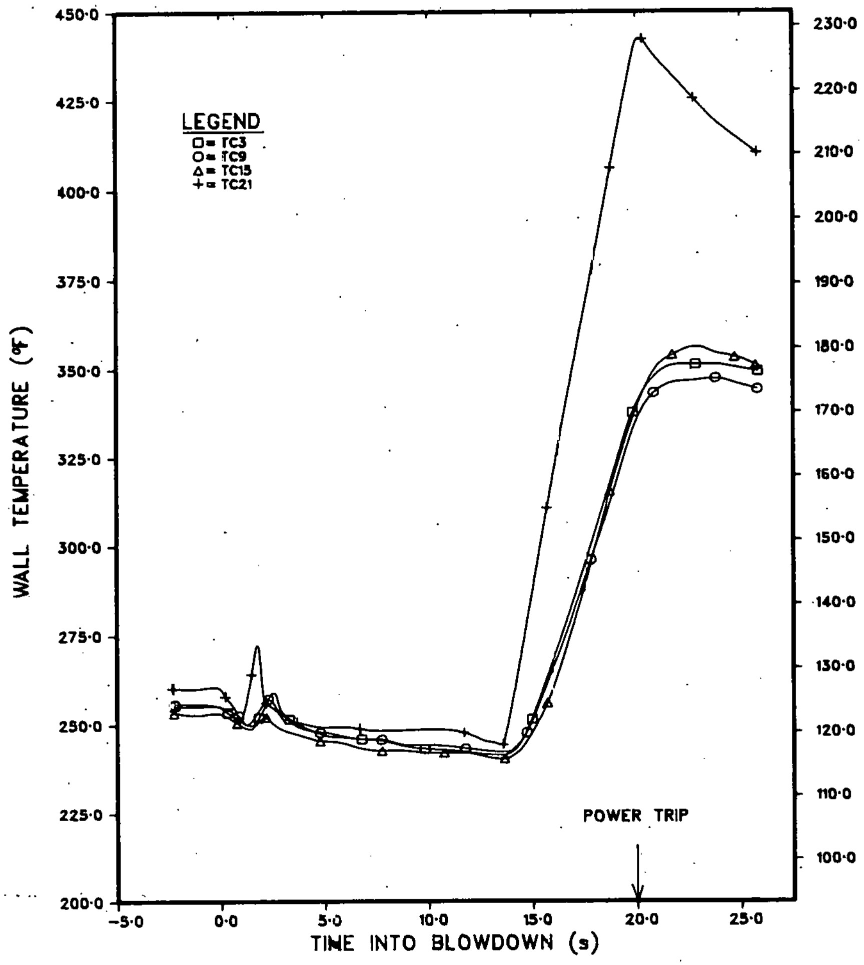

Fig. I.40. Wall-thermocouple Measurement during Test DB-118

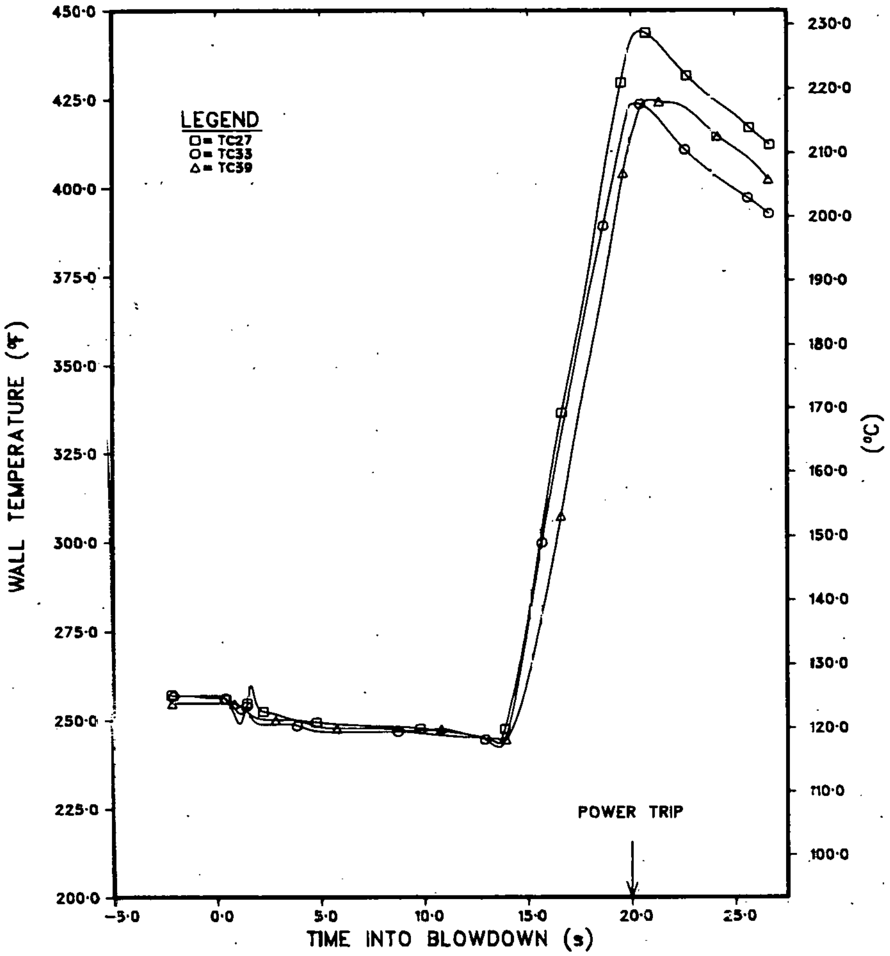

Fig. I.40 (Contd.)

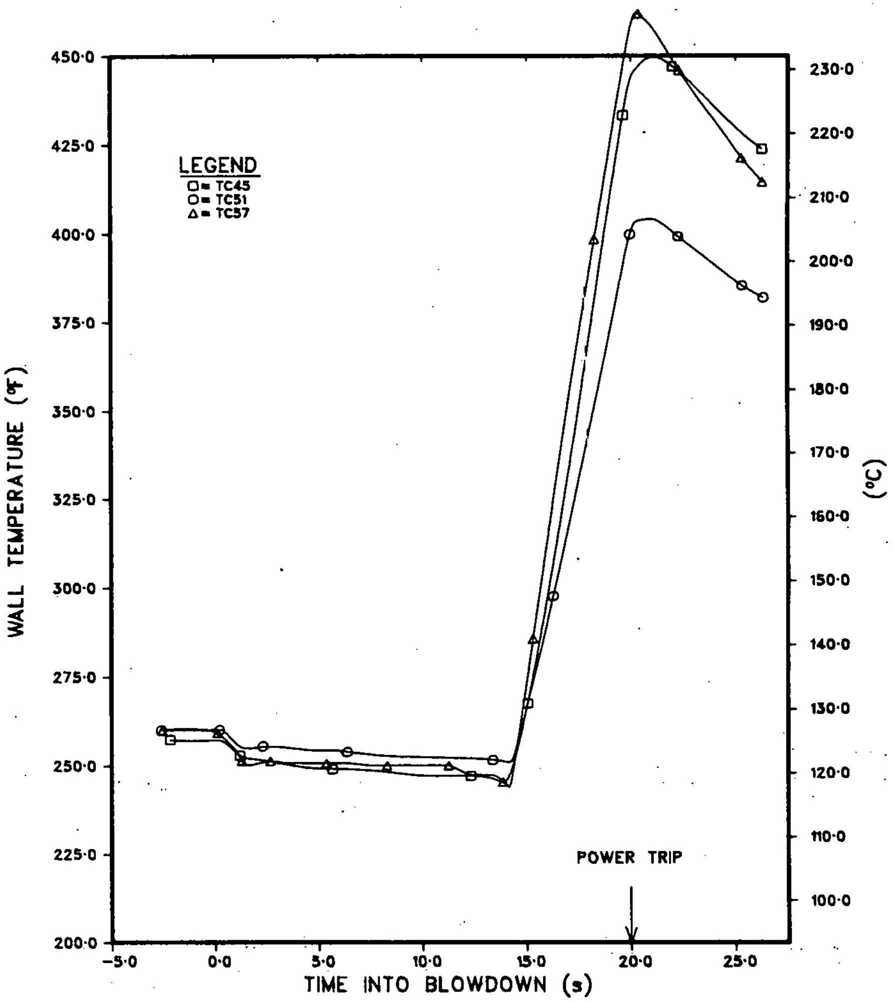

Fig. I.40 (Contd.)

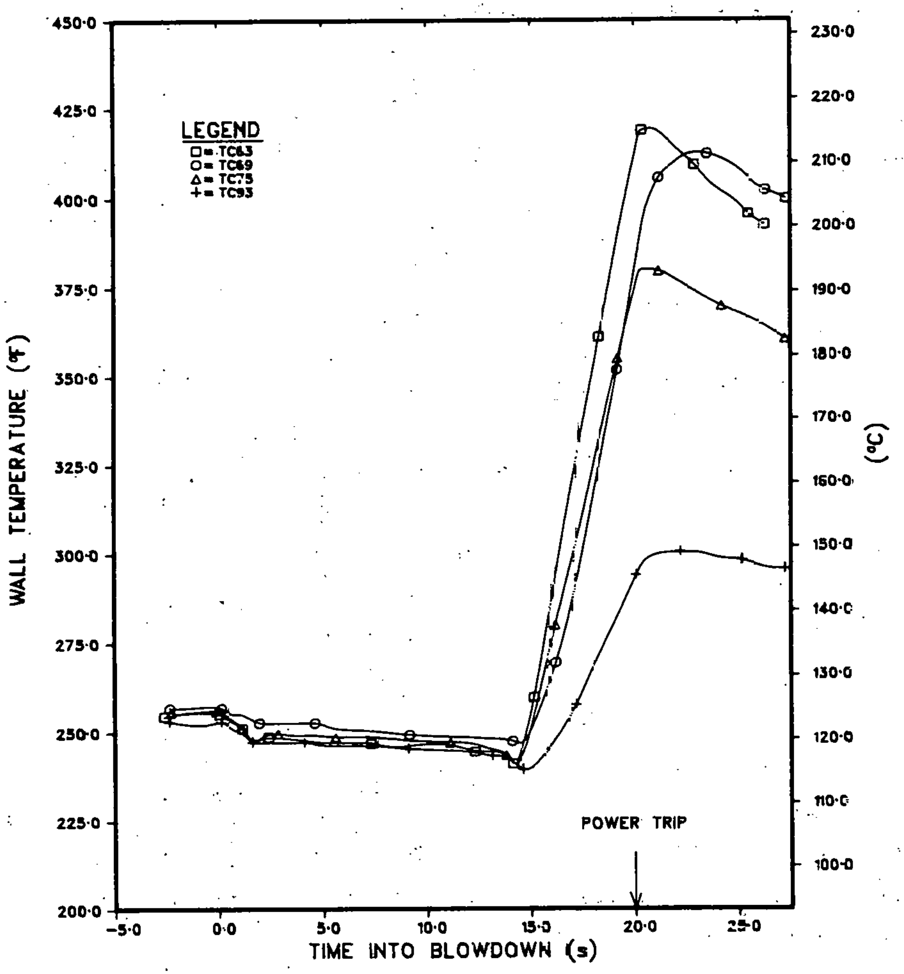

Fig. I.40 (Contd.)

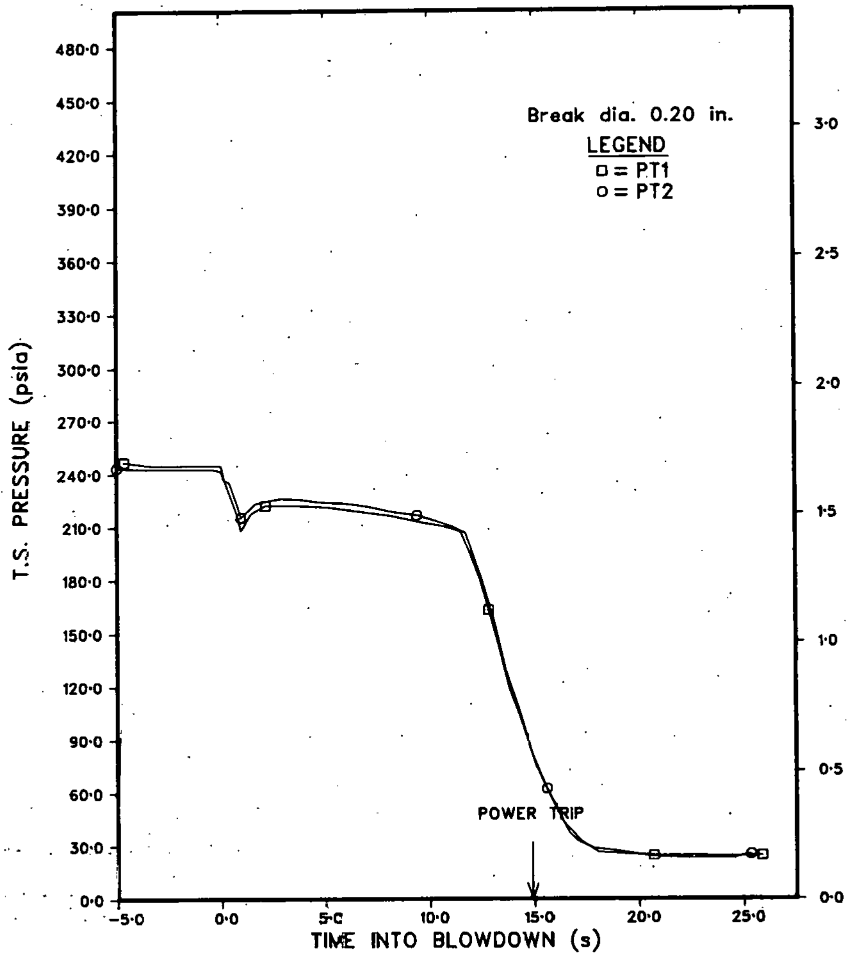

Fig. I.41. System Pressure during Test DB-119

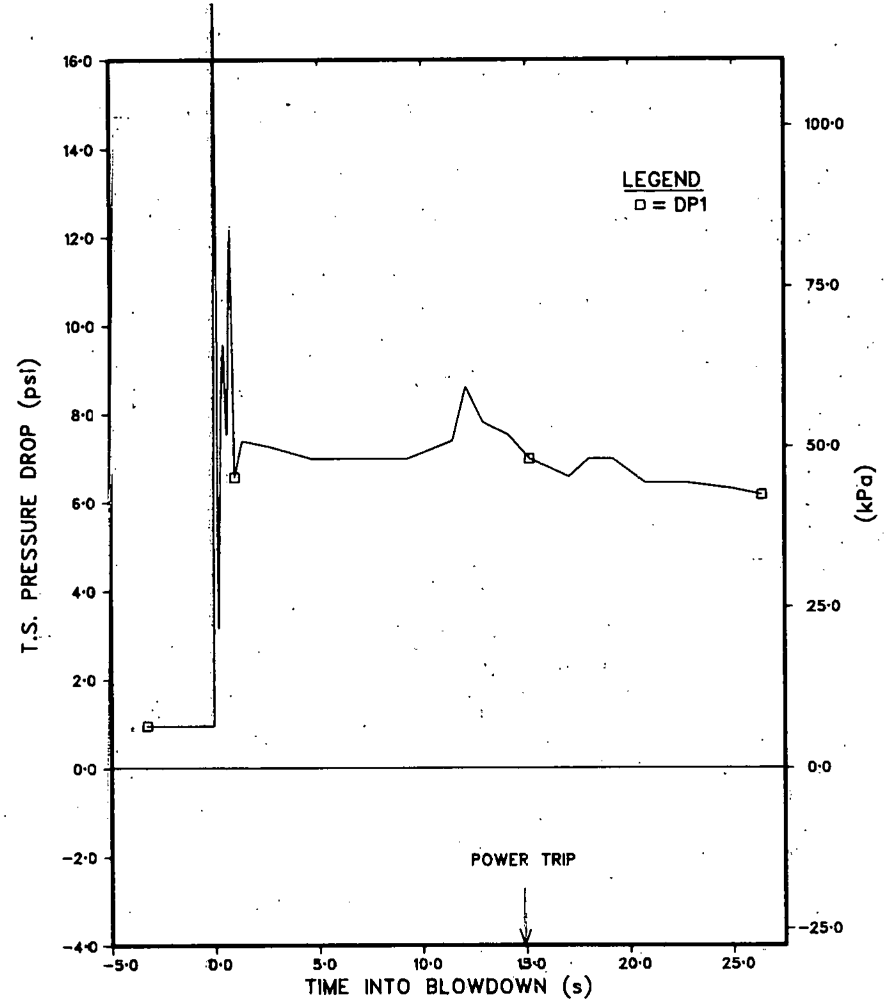

Fig. I.42. Differential Pressure across Test Section during Test DB–119

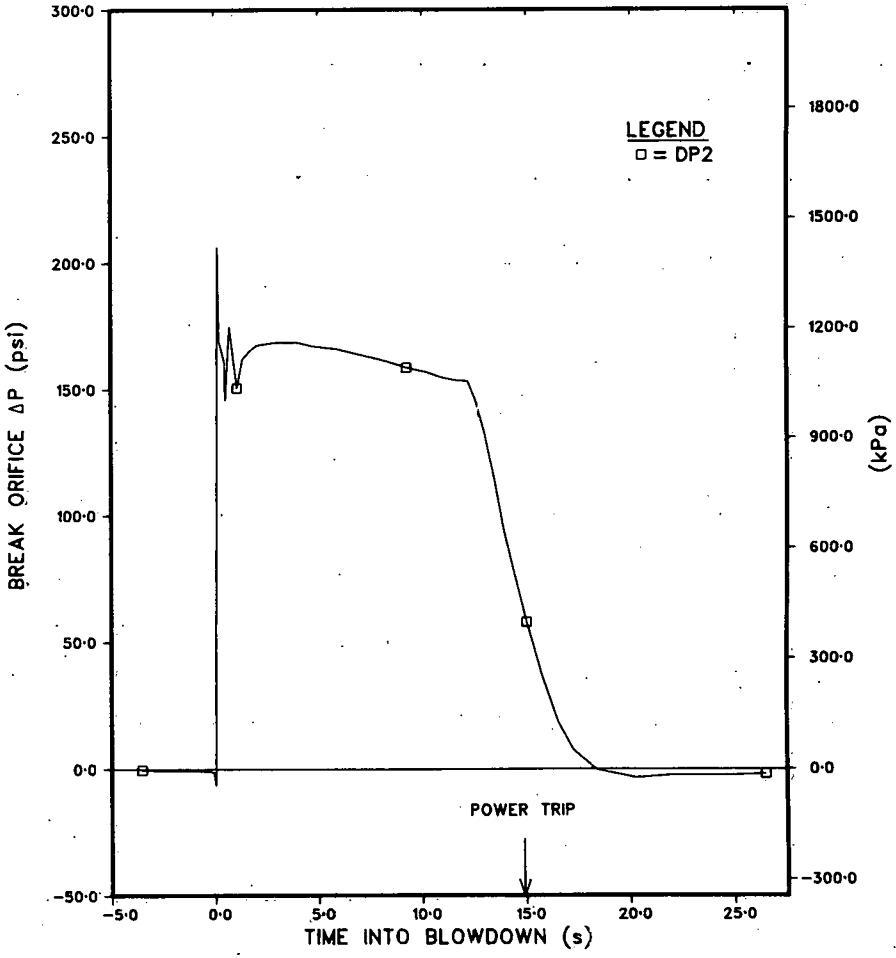

Fig. I.43. Differential Pressure across Break Orifice during Test DB–119

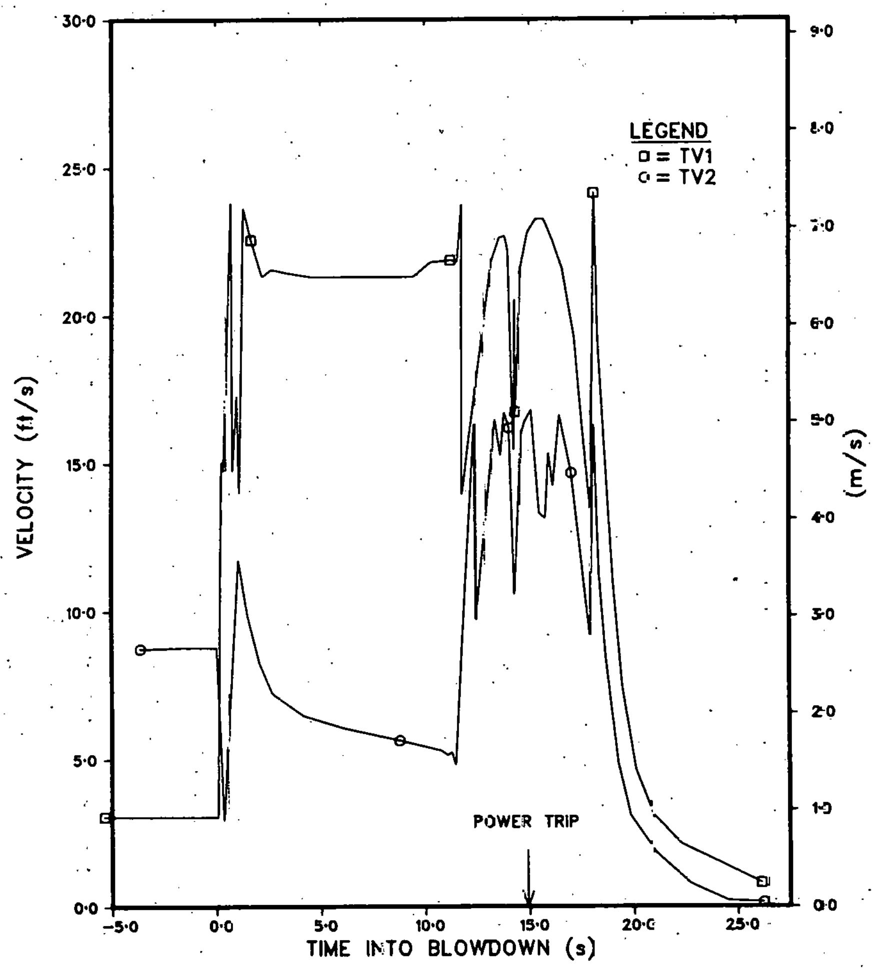

Fig. I.44. Turbine-flowmeter Measurement during Test DB-119

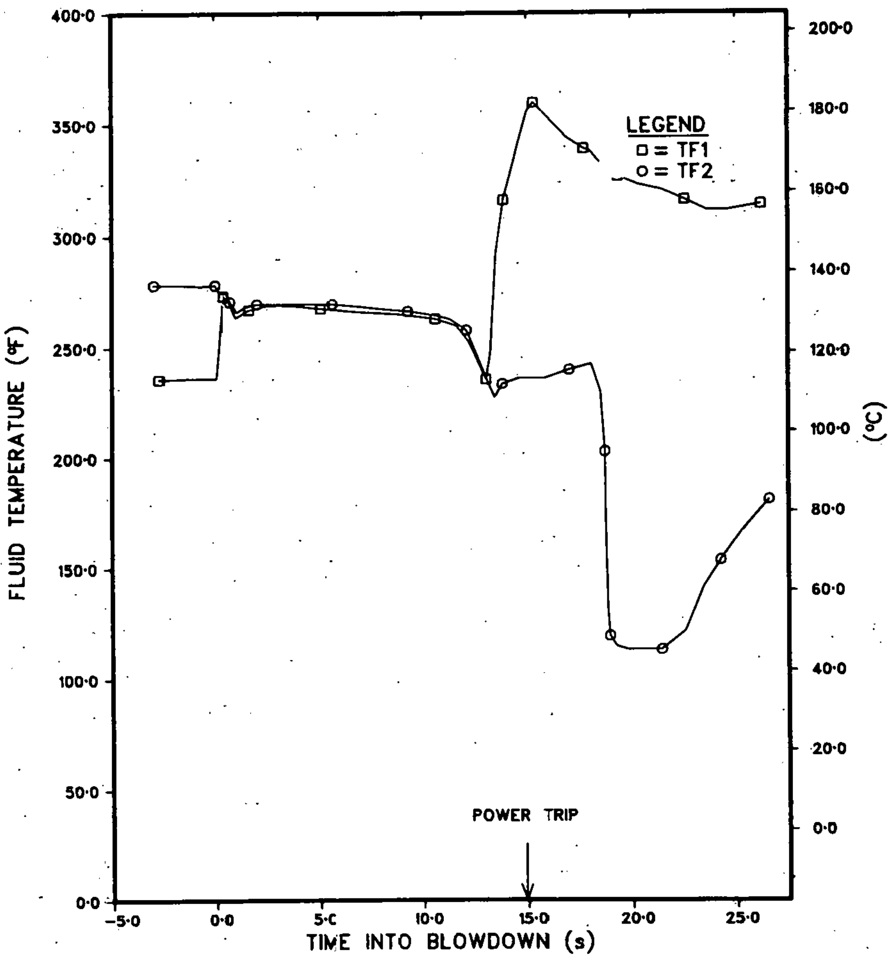

Fig. I.45. Fluid Temperature during Test DB-119

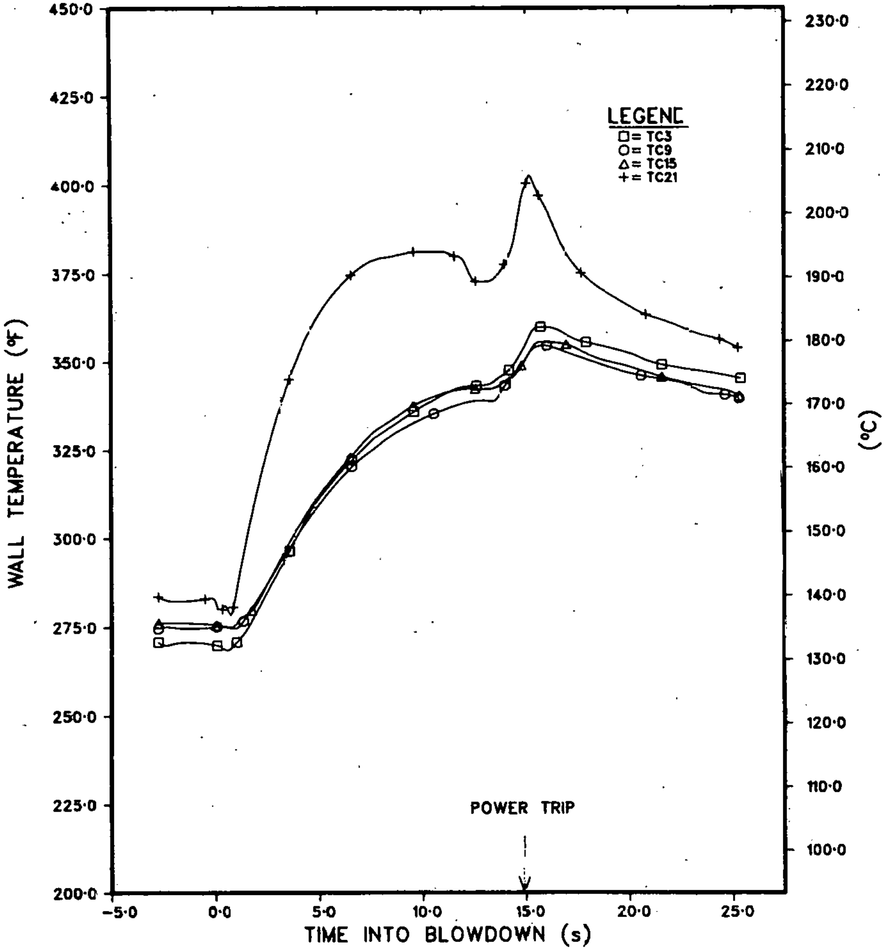

Fig. I.46. Wall-thermocouple Measurement during Test DB-119

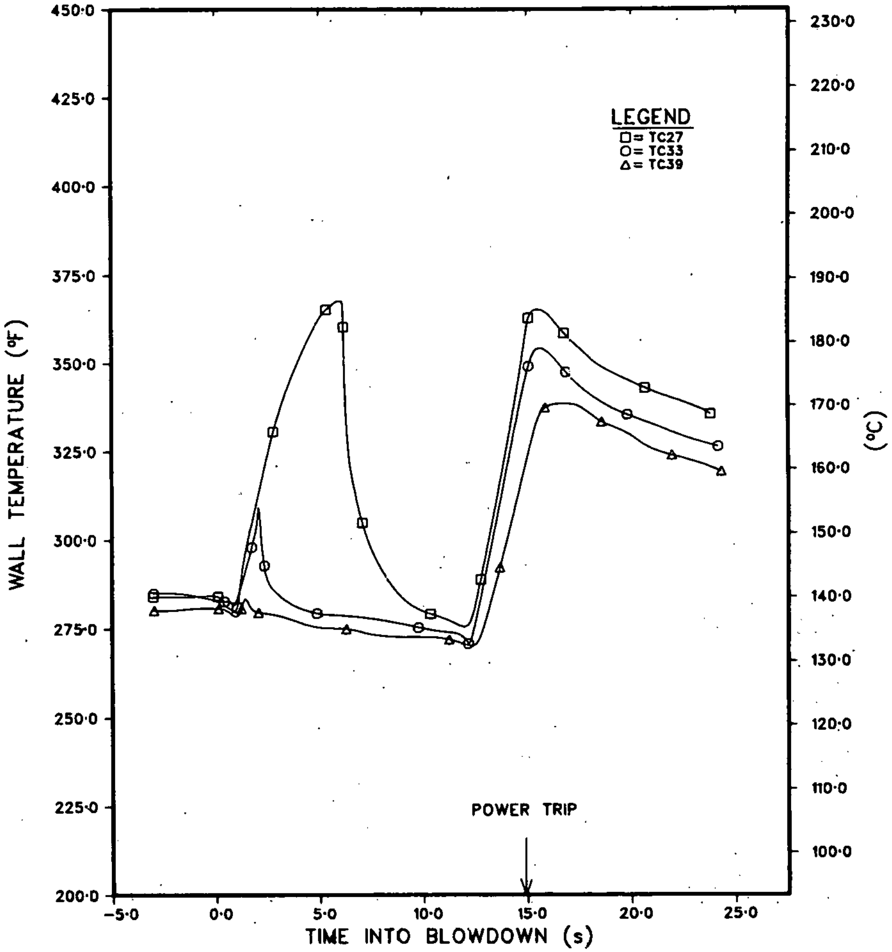

Fig. I.46 (Contd.)

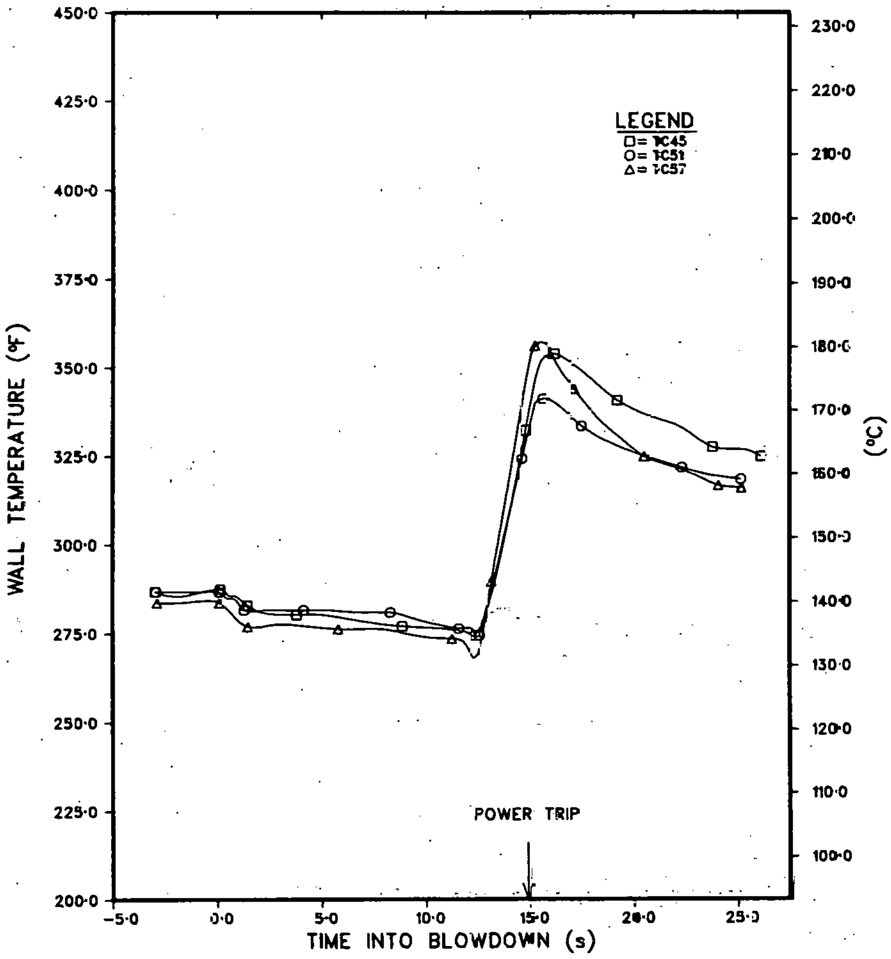

Fig. I.46 (Contd.)

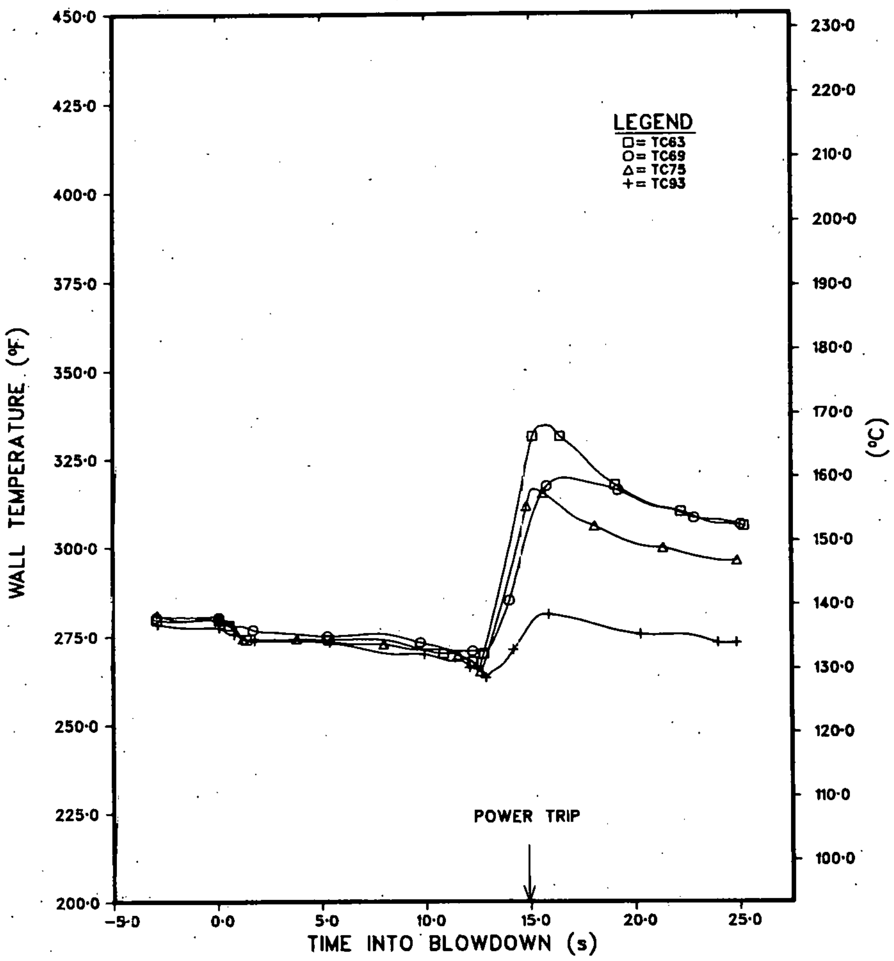

Fig. I.46 (Contd.)

Tests DB-113 and -114 had the same inlet temperature, mass velocity, and test-section power, but the initial steady-state pressures were different; DB-113 was conducted at 2.23 MPa, and DB-114 at 2.76 MPa. As a result, the wall-temperature profiles indicate a longer subcooled boiling region in DB-113. The bulk temperature, however, shows no difference between the two tests. The critical power ratio calculated differs by only 4%, a value within the error band of the correlation.[3]

During the transient, the behavior of the heater wall was the most important piece of information. In DB-113, the lower 114 cm experienced early sustained thermal excursion, as compared to 175 cm in DB-114. The increased cooling capability of the wall in the low-pressure test is again demonstrated, an observation reported in Ref. 4. A qualitative explanation in terms of deactivation and reactivation of the nucleation sites at the wall was suggested in Ref. 4.

Test DB-115 was conducted at a slightly lower pressure than DB-114, but with a higher mass velocity such that no wall temperature had reached the saturation value. Figure I.7 shows that the heater wall was cooled by single-phase forced convection only in steady-state operation. During the transient, a significant portion of the channel experienced early CHF. Note that the hottest zone had efficient cooling. Upon the initial rapid subcooled decompression, the nucleation sites in the hottest zone were believed to be reactivated first. Nucleate boiling was enhanced, and cooling resulted. A slightly shorter region in early CHF was measured when compared with DB-114.

Test DB-117 was conducted from a much lower initial pressure, 1.28 MPa, while keeping other steady-state parameters similar to DB-113 and -114. A positive exit quality was obtained. The wall-temperature profile in Fig. I.8 indicates that subcooled boiling followed by saturated nucleate boiling occurred over the entire length of the heated section.

During blowdown, the entire heated section remained in a coolable configuration for 14 s, at which time the complete loss of coolant caused the delayed CHF. However, a few temperature excursions appeared early in the transient at the lower end, but they were quickly rewet. Another low-pressure test, DB-118, was conducted, and similar wall-temperature behavior was observed. The critical-power ratio for these two tests with positive exit quality is about 1.85, only a slight difference from the higher-pressure tests.

Test DB-119 was then conducted from an intermediate pressure of 1.69 MPa. The wall-temperature profile in Fig. I.10 indicates that the first 0.5 m was in single-phase forced convection, the next 1.0 m in subcooled boiling, and the rest of the test section in nucleate boiling. During the transient, the first 84 cm went into early CHF, with the 84 cm location (TC33) experiencing rapid rewet. Delayed CHF occurred in the rest of the heated channel at about 12.5 s. The cooling capability of this test is between the high- and low-pressure tests.

Therefore, varying the reduced pressure between 0.27 and 0.63 produces quite different blowdown cooling capability. These tests seem to suggest that the well-cooled region results in a greater region in steady-state subcooled or nucleate boiling. These existing nucleation sites at the wall promote efficient cooling.

With the same inlet temperature, mass velocity, and heat input, a lower operating pressure does not necessarily lead to a smaller margin to CHF, or smaller critical-power ratio in this case. This ratio, as shown in Table I.1, bears this out, at least for the present mass velocity under this study. Figure I.47 shows the result of the effect of mass velocity on steady-state CHF in a water system over a wide range of pressure. The case of uniform heat flux was examined with geometric dimensions and inlet temperature typical of a pressurized water reactor. Two CHF correlations were used. The Bowring correlation[3] has the same accuracy as the Macbeth-Thompson round-tube correlation[5] (the rms error is 7% for the 3800 data points), but is much simpler to use. The correlation covers the pressure range from 0.7 to 17 MPa (100-2500 psia). The W-3 correlation has been widely used for design calculations of pressurized water reactors. However, the ranges of parameters of the data used in developing this correlation are more restricted, particularly the quality; x_{CHF} must lie between -0.15 and +0.15. Figure I.47 illustrates the influence of pressure on the steady-state CHF. The two correlations, though of widely different form, exhibit good agreement. It is a subtle fact that CHF can increase or decrease with increasing pressure, depending on the mass velocity G. However, the influence of system pressure is deemed small over the mass-velocity range from 1350 to 2710 $kg/m^2 \cdot s$ ($1.0-2.0 \times 10^6$ $lb_m/h \cdot ft^2$).

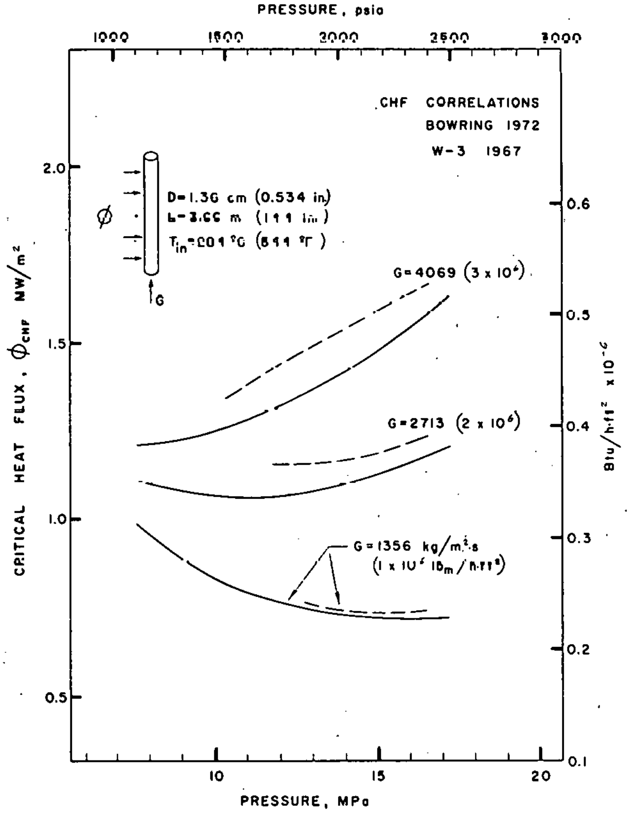

Fig. I.47

Influence of System Pressure on Critical Heat Flux. ANL Neg. No. 900-77-516.

B. LOCA Heat-transfer Analysis (P. A. Lottes and R. E. Henry, RAS)

A general transient conduction code for a heater rod was written for a Hewlett-Packard 9810-A desk calculator. The code can handle up to 60 radial nodes, but is limited to one material with fixed physical properties. The results therefore are useful in showing estimates of heater response during various boundary-condition changes, but the results may not accurately describe heater performance where the change in physical properties with temperature is appreciable.

The internal power generation and the rates of heat transfer during post-CHF blowdown determine the temperature rise rate of the heat rods in the semiscale tests. The transient conduction code was used to study the effect of varying the two-phase-flow heat-transfer coefficient immediately after CHF on the rate of rise of the heater temperature.

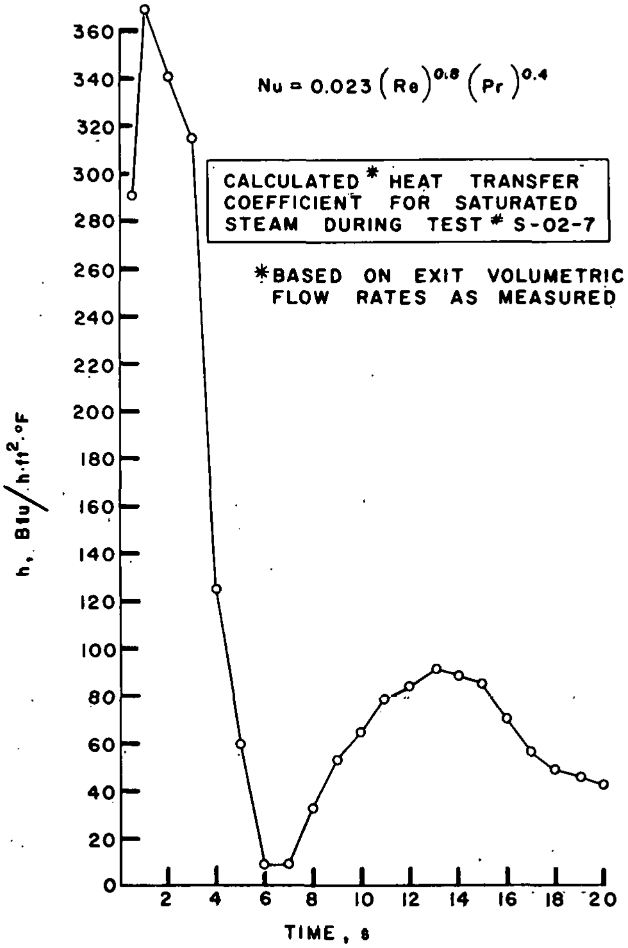

Fig. I.48. Saturated-steam Heat-transfer Coefficient Based on Measured Pressure and Core-inlet Velocity. Conversion factor: 1 Btu/h·ft^2·°F = 5.1×10^{-4} W/cm^2·C. ANL Neg. No. 900-77-498.

Test data from semiscale Test S-02-7 were used as input, i.e., the time variation of heater power, system pressure, and volumetric flow rate as measured at the inlet flowmeter were used to calculate local heat-transfer coefficients as a function of time. It was assumed that the core-inlet turbine meter indicated the steam velocity (homogeneous flow). Based on these velocities, values of the steam heat-transfer coefficient were calculated (Fig. I.48) and used as input for the heater temperature response.

The calculation of heater response was based on an initial linear surface-temperature decrease for 0.5 s to the local saturation value, at which time CHF is assumed to take place. Also included in the analysis is a time constant of 0.18 s (calculated value) for the heater thermocouple. The thermocouple was assumed to be located at a radial distance of 0.419 cm (0.165 in.) from the heater centerline.

Results of the calculations are shown in Figs. I.49 and I.50. The best agreement between analysis and the experiment was reached for values of heat-transfer coefficient equal to 0.5 times the values for steam. It is recognized that the steam velocity at the 29-in. (74-cm) level may be somewhat less than the steam velocity at the bottom of the bundle, and that a wall-temperature correction or adjustment on the heat-transfer coefficient to account for variable properties would be more appropriate. Note also that, for this approximation, the nonequilibrium effects were neglected and the steam temperature was assumed to be held at the saturation temperature by the presence of entrained saturated water. This simple analysis is in excellent agreement with the measured thermocouple behavior.

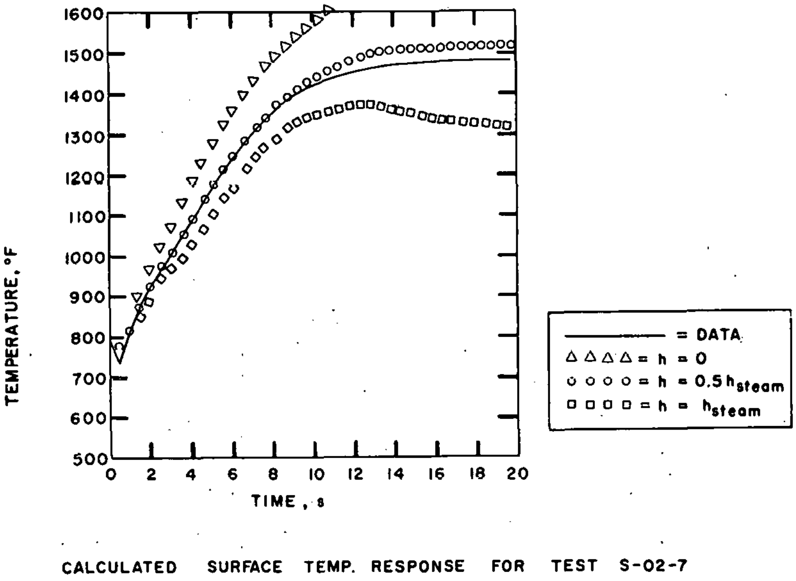

Fig. I.49. Calculated and Measured Heater-thermocouple Response for TH-D5-29 after CHF. Conversion factor: t (°C) = [t (°F) - 32]/1.8. ANL Neg. No. 900-77-499 Rev. 1.

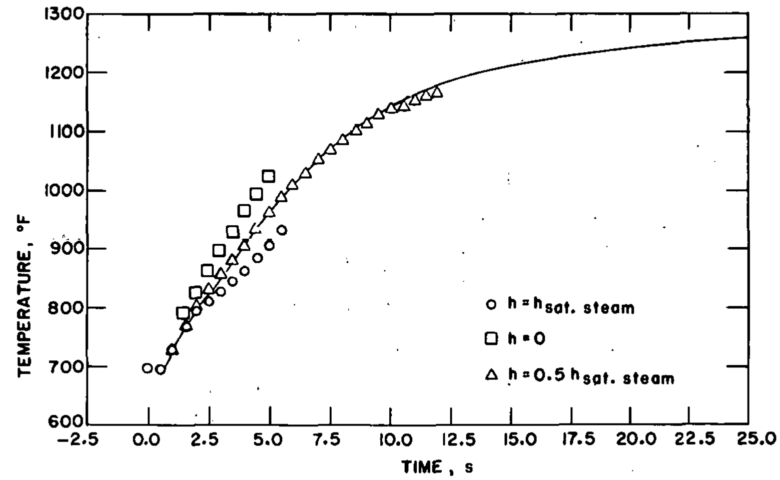

Fig. I.50. Calculated and Measured Heater-thermocouple Response for TH-F6-08E after CHF. Conversion factor: t (°C) = [t (°F) - 32]/1.8. ANL Neg. No. 900-77-496 Rev. 1.

Parametric calculations using the code were also performed for the quenching of heater rods to determine the effect of transition-boiling heat transfer on energy-release time for the heater rods. For this calculation, we assumed that a typical heater rod from the semiscale test would experience a linear decrease in surface temperature during the quenching period. The quench period was varied from 0.0068 s (value of single time step used in the code) to 2.0 s.

A surface-quench-time duration of 0.5 s will produce a time response of thermocouple TH-D5-29 identical to that measured in Test S-03-2. The integrated heat release as a function of time is shown in Fig. I.51, and the energy transferred is shown as a percentage of the total stored energy at the time the quenching begins. Note that over a range of quench times of 0-1.0 s, the rate of energy release is fairly insensitive to quench time, since the heater rod is conduction-limited during the transient. Reactor fuel-rod energy release rates during quenching will be more independent of surface quench time, since the thermal conductivity of fuel is much smaller than the thermal conductivity of heater material (boron nitride), and a low thermal conductivity gap may exist between the fuel and the cladding.

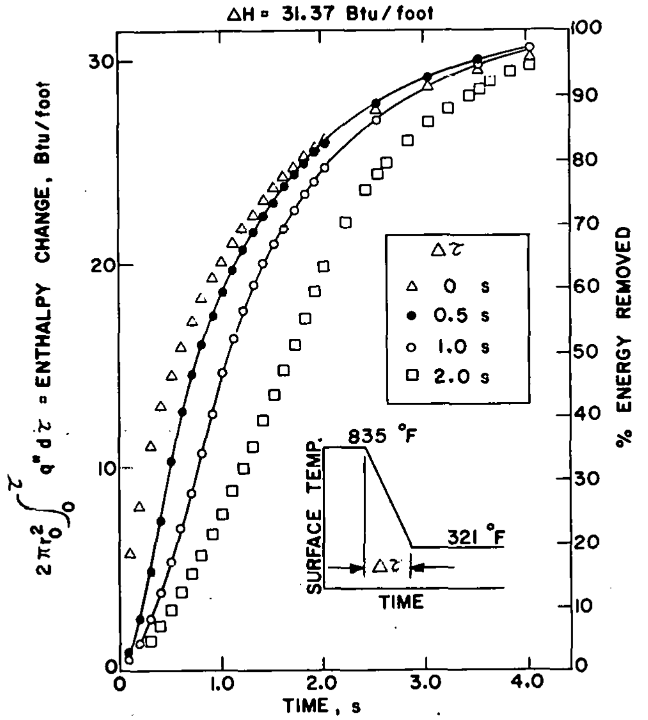

Fig. I.51

Integrated Energy Release during Rewet as a Function of Surface Quenching Time. Conversion factor: 1 Btu/ft = 3460 J/m. ANL Neg. No. 900-77-497 Rev. 1.

C. Reflood Tests (Y. S. Cha, R. E. Henry, and P. A. Lottes, RAS)

A series of tests, with initial test-section temperature ranging from 149 to 774°C (300-1425°F), was performed. The following conditions were maintained for these tests:

Supply-tank water temperature = 65°C (150°F)

Supply-tank pressure = 0.377 MPa (40 psig)

Initial temperature of lower plenum = 65°C (150°F)

Initial temperature of upper plenum = 121°C (250°F)

The combination of the supply-tank pressure and the throttle-valve opening position provided an average velocity in the test section [13-mm (0.5-in.) ID] of about 40 mm/s (1.6 in./s). During the heat-up period before each test, a small amount of argon was purged into the test section from the lower plenum to prevent oxidation of the surface at elevated temperatures. The argon supply was shut off immediately before each test. This resulted in a slightly nonuniform distribution of temperature along the test section. Table I.4 lists the conditions under which these tests were conducted. Most tests were conducted by heating up the test section to a desired temperature and then maintaining this temperature for a short time before opening the throttle valve. Power was turned off at the end of each test, except for Runs No. 6 and 9 in which the power was turned off immediately before the test.

TABLE I.4. Description of Test Conditions

Run No.	Power Input, W	T_{18} (Initial) °C	T_{18} (Initial) °F
1	182	149	300
2	282	188	370
3	486	227	440
4	525	296	565
5	903	399	750
6	0	557	1,035
7	1,432	582	1,080
8	2,065	724	1,335
9	0	771	1,425

Typical temperature-versus-time curves are shown in Fig. I.52, in which T_{10} represents the temperature measured by thermocouple 10, which is

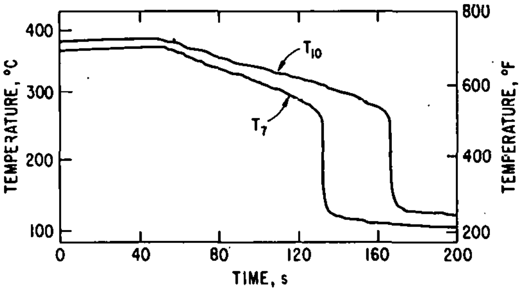

Fig. I.52

Typical Temperature–vs–Time Curve during Reflood of a Vertical Stainless Steel Pipe (Run No. 5)

1.52 m (5 ft) above the bottom electrode, and T_7 represents the temperature measured by thermocouple 7, which is 1.07 m (3.5 ft) above the bottom electrode. Quenching is indicated by the almost vertical drop in temperature shown in Fig. I.52.

Figure I.53 shows the plot of quenching temperature versus axial distance along the test section. In general, the quenching temperatue increases with increasing initial temperature of the test section. The actual quenching temperature may be slightly higher than that shown in Fig. I.53 since all the thermocouples were welded on the outside (instead of on the inside) wall of the test section. Figure I.54 shows the variation of quenching time for thermocouple 18 with initial temperature of the test section. Quenching time increases with initial temperature of the test section and power input to the test section during the test.

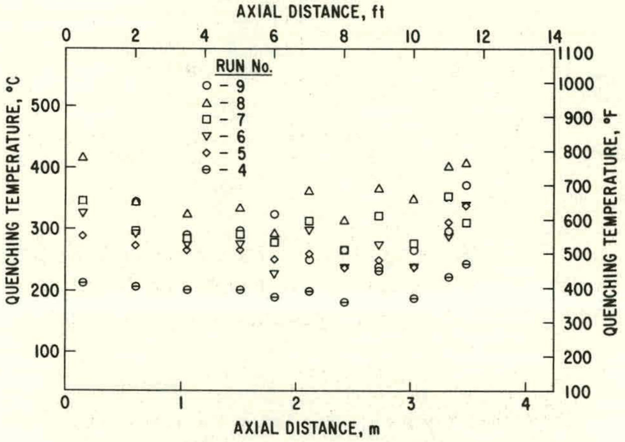

Fig. I.53. Quenching Temperature vs Axial Distance along Test Section

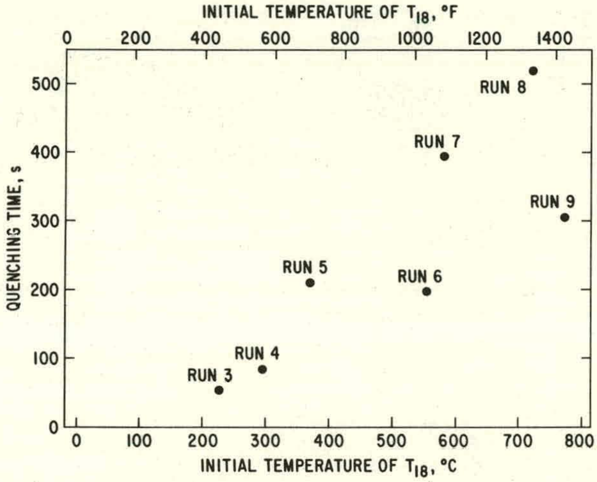

Fig. I.54. Quenching Time vs Initial Temperature of Test Section for Thermocouple 18

Figure I.55 shows the variation of the amplitude of the output from the differential pressure transducer across the orifice plate located upstream of the test section. Flow oscillations occurred throughout the entire test. The amplitude of oscillation decreases with time. Also shown in Fig. I.55 are the same test at two different intervals with increased chart speed. The oscillations appear to be random. If the data were fed into an analog spectrum analyzer, which gives the rms value of the signal versus frequency plot, the results are as shown in Fig. I.56. The peak amplitude occurred between 1.5 and 3.5 Hz.

Figures I.57 and I.58 show the results of another test. The spectrum in Fig. I.58b is typical for all the tests. However, during later stage of the test, a spectrum such as that shown in Fig. I.58c was occasionally observed. (Note the change in scale of the spectrum amplitude in Figs. I.58b and I.58c.)

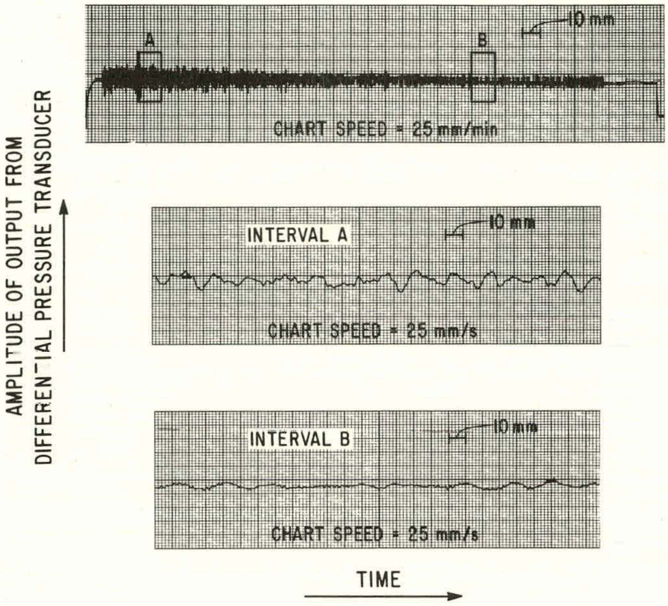

Fig. I.55. Amplitude of Output from Differential Pressure Transducer vs Time: Run No. 9

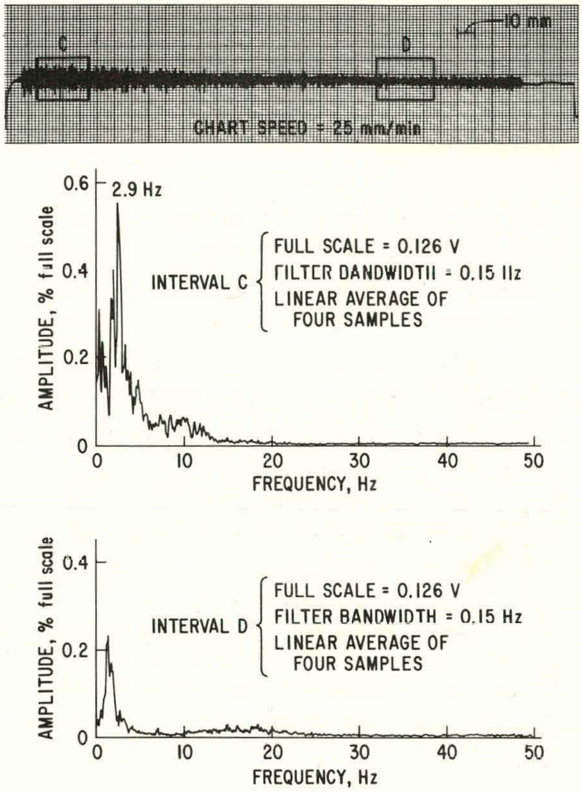

Fig. I.56. Amplitude vs Frequency at Two Different Intervals Obtained by Using an Analog Spectrum Analyzer: Run No. 9

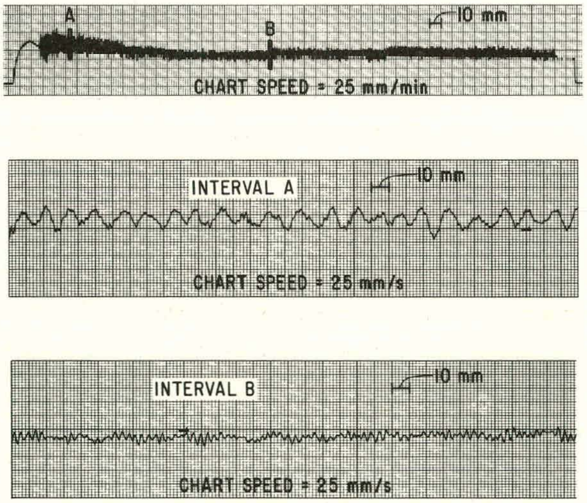

Fig. I.57. Amplitude of Output from Differential Pressure Transducer vs Time: Run No. 7

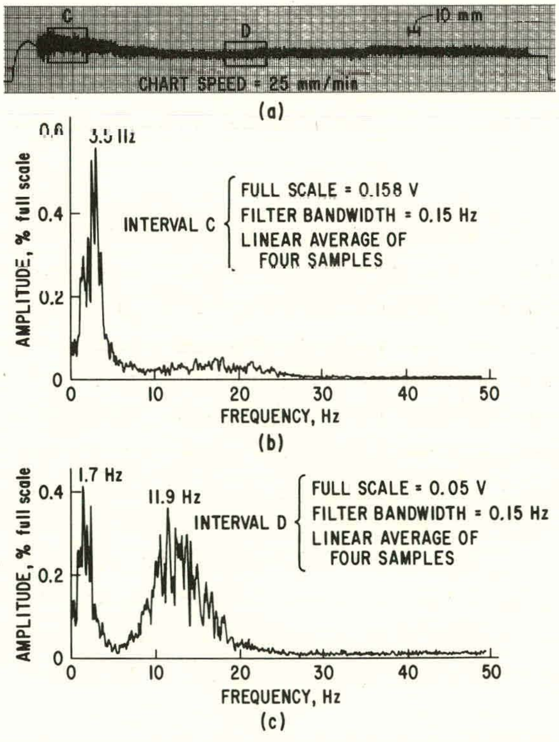

Fig. I.58. Amplitude vs Frequency at Two Different Intervals Obtained by Using an Analog Spectrum Analyzer: Run No. 7

Figure I.59 shows the variation of peak amplitude frequency and peak amplitude during early stages of the test with initial temperature of the test section. The peak amplitude frequency decreased slightly with decreasing temperature. However, it remained in the range 1.5-3.5 Hz. There appeared to be a sharp decrease in peak amplitude when the test-section temperature dropped below ~400°C.

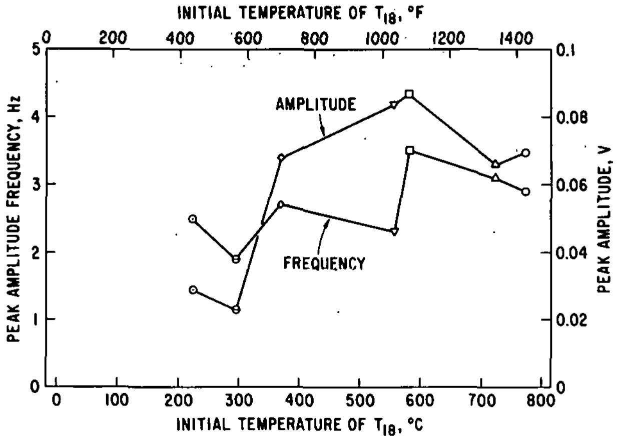

Fig. I.59

Peak Amplitude Frequency and Peak Amplitude vs Initial Temperature of Test Section

References

1. W. L. McCabe and J. C. Smith, Unit Operations of Chemical Engineering, McGraw-Hill, N.Y. 1971.

2. S. Y. Ahmad, Fluid to Fluid Modeling of Critical Heat Flux: A Compensated Distortion Model, Int. J. Heat Mass Transfer 16, 641 (1973).

3. R. W. Bowring, A Simple But Accurate Round Tube, Uniform Heat Flux, Dryout Correlation Over the Pressure Range 0.7-17 MN/m^2, AEEW-R789 (1972).

4. J. C. Leung and R. E. Henry, "Transient Critical Heat Flux," Light-water-Reactor Safety Research Program: Quarterly Progress Report, October-December 1976, ANL-77-10 (Mar 1977).

5. B. Thompson and R. V. MacBeth, "Boiling Water Heat Transfer Burnout in Uniformly Heated Round Tubes: A Compilation of World Data with Accurate Correlations, AEEW-R356 (1964).

6. L. S. Tong, Prediction of Departure from Nucleate Boiling for an Axially Non-Uniform Heat Flux Distribution, J. Nucl. Energy 6, 241 (1967).

II. TRANSIENT FUEL RESPONSE AND FISSION-PRODUCT RELEASE PROGRAM

Responsible Group Leaders:
L. A. Neimark and M. C. Billone, MSD

Coordinated by:
L. R. Kelman, MSD

A physically realistic description of fuel swelling and fission-product release is needed to aid in predicting the behavior of fuel rods and fission products under certain hypothetical Light-Water Reactor (LWR) accident conditions. To satisfy the near-term need, a comprehensive computer-base model, the Steady State and Transient Gas-release and Swelling Subroutine (SST-GRASS) code, is being developed at Argonne National Laboratory (ANL). This model is being incorporated into the Fuel-Rod Analysis Program (FRAP) code being developed by EG&G Idaho, Inc., at the Idaho National Engineering Laboratory (INEL). Also being developed, but at a lower priority, is a model to predict the behavior of volatile fission products in, and release from, LWR fuel under hypothetical accident conditions. The volatile fission-product results will also serve as input to NRC-sponsored programs that are developing a radiological source term for hypothetical accidents.

The analytical effort is supported by a data base and correlations developed from characterization of irradiated LWR fuel and from out-of-reactor transient heating tests of irradiated commercial and experimental LWR fuel under a range of thermal conditions.

Emphasis in the early stages of the program has been on thermal conditions in Pressurized-Water Reactor (PWR) fuel that are applicable to anticipated hypothetical power-cooling-mismatch (PCM) accidents. Recent efforts include conditions typical of other types of hypothetical accidents. The program is also developing information on fission-gas release during steady-state and load-following operations.

During the quarter, we participated in the following pertinent meetings and visits. The Water Reactor Safety Research (WRSR) Fuel Behavior Branch midyear review was held in Silver Spring, Maryland, on January 6. Reviewed at the meeting were highlights of accomplishments since the beginning of the program, current efforts, planned activities in the balance of FY 1977, and budget and schedule. Representatives of EG&G visited us on March 16 to inform us of recent results from the irradiation-effects test series in the Power Burst Facility (PBF) and to discuss the ongoing activities at ANL to cross-check direct-electrical-heating (DEH) test results with PBF test results.

Recent significant analytical and experimental advances and the status of the program at the end of this quarter are summarized below.

1. GRASS-based correlations were developed for fractional fission-gas release from LWR fuel during steady-state irradiations as a function of fuel temperature, temperature gradient, grain size, fission rate, and irradiation time.

2. An analytical approach was developed to provide a description of the release of fission gas as a function of fuel-rod power and burnup.

3. Bounds on, and possible mechanisms of, fission-gas release from LWR fuel during a hypothetical LOCA were obtained from GRASS analyses. The analyses indicate a potential for significant release of fission gases.

4. About 75% of the PCM simulation tests in the initial DEH test plan have been completed.

5. Preliminary correlations between gas release and time-integrated energy input during DEH transients have been made. Improvements in surface-temperature measurements and temperature-profile calculations are being made to permit the development of useful correlations with temperature-related parameters.

6. PBF-tested and sibling irradiated Saxton Load Follower (SLF) fuel was received and characterized as part of the ANL-EG&G cross-check program. Metallographic examination of PBF-tested fuel revealed intergranular separations similar to those observed in DEH-tested Robinson fuel.

A. Modeling of Fuel-Fission-product Behavior (J. Rest, MSD)

1. Modeling of Fission-gas Behavior during Steady-state Conditions

a. Sensitivity Analyses

During this quarter, sensitivity analyses to assess key factors influencing fission-gas release during steady-state conditions were continued. The results of GRASS calculations for fractional fission-gas release from UO_2 grains to the grain edges versus temperature for various values of irradiation time, grain size, fission rate, and temperature gradient are listed in Tables II.1 and II.2. These values for the fractional fission-gas release are upper bounds on the amount of gas that would actually be released from the fuel; due to the incomplete interconnection of grain-edge tunnels within the UO_2, the amount of gas released from the fuel is usually less than that released to the grain edges.

The following observations can be derived from the results of this analysis.

(1) The fractional fission-gas release has a strong dependence on temperature. For example, from Table II.1, the gas released from 10- and 30-μm UO_2 grains, respectively, at the end of 2000 h of irradiation can be classified as shown in Table II.3.

TABLE II.1. GRASS Calculations for Fractional Fission-gas Release for a Fission Rate of
1 x 10^{13} f/cm^3·s and a Temperature Gradient of 200°C/cm

FISSION-GAS RELEASE (%) FROM 10-μm GRAINS FISSION-GAS RELEASE (%) FROM 30-μm GRAINS	TIME (h)												
TEMPERATURE (°C)	60	110	210	510	1010	2010	3010	4010	5010	6010	8010	10010	11960
1200	0.13 0.005	0.14 0.006	0.16 0.008	0.20 0.012	0.24 0.016	0.30 0.021	0.35 0.025	0.38 0.028	0.42 0.031	0.44 0.033	0.49 0.037	0.53 0.041	0.56 0.044
1300	0.22 0.01	0.29 0.02	0.40 0.04	0.61 0.06	0.96 0.10	1.40 0.15	1.73 0.19	1.98 0.22	2.21 0.25	2.41 0.27	2.75 0.32	3.04 0.35	3.29 0.38
1400	0.56 0.04	0.92 0.09	1.66 0.18	3.65 0.50	6.03 0.92	8.99 1.41	11.08 1.74	12.77 2.03	14.21 2.27	15.46 2.47	17.56 2.79	19.28 3.03	20.72 3.25
1500	1.92 0.15	4.26 0.57	7.81 1.35	14.28 2.80	20.83 4.60	29.08 5.82	34.70 6.89	39.01 7.70	42.50 8.36	45.42 8.89	50.14 9.71	53.76 10.34	56.56 10.90
1600	6.48 0.82	12.11 2.20	19.37 4.36	29.74 7.67	36.96 10.16	46.78 13.51	53.98 15.95	59.51 17.94	63.84 19.65	67.32 21.18	72.53 23.84	76.16 26.14	78.74 28.15
1700	14.27 2.35	21.36 4.85	27.75 7.49	41.77 13.32	56.18 19.82	70.93 28.04	78.29 33.78	82.52 38.32	85.19 42.11	87.02 45.40	89.33 50.91	90.75 55.40	91.69 59.08
1800	17.80 4.23	27.15 7.96	42.18 14.26	64.38 25.58	78.69 36.69	87.90 50.22	91.16 59.11	92.83 65.60	93.86 70.56	94.57 74.48	95.49 80.11	96.09 83.92	96.51 86.57
1900	26.73 6.95	44.96 14.98	64.10 25.65	83.33 43.35	91.19 59.62	95.33 76.36	96.77 84.69	97.52 89.36	97.99 92.19	98.31 94.02	98.72 96.14	98.97 97.29	99.14 97.92
2000	42.80 13.30	61.40 26.15	80.90 41.25	92.61 64.67	96.59 81.60	98.43 92.85	98.98 96.30	99.24 97.73	99.39 98.44	99.49 98.83	99.70 99.20	99.90 99.35	100 99.43
2400	86.64 75.31	95.54 91.98	98.05 97.26	100 99.29	100 100	100 100	100 100	100 100	100 100	100 100	100 100	100 100	100 100

TABLE II.2. GRASS Calculations for Fractional Fission-gas Release from 10-μm Grains for a Fission Rate of 1.3 x 10^{12} f/cm^3·s

FISSION-GAS RELEASE (%) WITH A 200° C/cm TEMP. GRADIENT FISSION-GAS RELEASE (%) WITH A 1000° C/cm TEMP. GRADIENT	TIME (h)									
TEMPERATURE (°C)	110	210	310	510	1010	2010	3010	4010	5010	5910
1200	0.29 0.30	0.32 0 36	0.34 0.42	0.39 0.54	0.46 0.80	0.55 1.11	0.64 1.39	0.73 1.66	0.82 1.91	0.89 2.13
1300	0.65 0.88	0.86 1.44	1.09 1.97	1.41 2.89	1.98 4.51	3.08 6.20	4.02 7.76	4.83 9.07	5.55 10.22	6.14 11.15
1400	1.59 2.76	2.54 4.62	3.39 6.07	5.12 8.31	9.19 12.21	13.49 17.49	17.09 21.27	20.02 24.39	22.52 27.06	24.51 29.19
1500	3.78 6.92	8.31 10.97	11.89 13.93	16.56 18.91	24.56 26.48	34.58 36.04	41.54 42.63	46.88 47.71	51.24 51.85	54.57 55.00
1600	10.21 14.73	20.03 22.18	25.78 28.09	33.62 34.93	44.26 43.26	53.28 51.39	59.33 57.96	64.39 63.47	68.57 67.97	71.70 71.32
1700	23.34 26.35	32.46 33.31	35.41 35.46	39.31 39.24	51.21 51.95	68.86 70.35	77.96 79.85	83.12 85.21	86.36 88.54	88.36 90.58
1800	24.39 23.14	28.78 28.64	36.94 38.82	53.58 56.29	74.21 77.78	87.03 90.74	91.46 94.90	93.68 96.80	95.02 97.82	95.83 98.38
1900	24.70 27.52	44.80 51.98	61.07 69.20	76.82 85.02	89.44 95.26	95.58 98.60	97.55 99.33	98.27 99.60	98.72 99.72	98.98 99.77
2000	39.86 53.09	68.75 32.77	80.37 92.16	89.79 97.39	96.37 99.32	98.85 99.73	99.38 99.82	99.57 99.87	99.66 99.89	99.72 99.91
2400	97.63 100	99.73 100	99.92 100	99.96 100	99.98 100	100 100	100 100	100 100	100 100	100 100

TABLE II.3. Dependence of Fractional Gas Release on Temperature and Grain Size. Time = 2000 h; fission rate = 1.0 x 10^{13} f/cm^3·s; temperature gradient = 200°C/cm.

Temperature Region, °C	% Gas Release	
	Grain Size = 10 μm	
1200-1400	0.30-9.0	0.02-1.4
1400-1700	9.0-71.0	1.4-28
>1700	71.0-100	28-100

The fractional fission-gas release as a function of temperature for various values of the fuel burnup calculated from Table II.1 is shown in Fig. II.1.

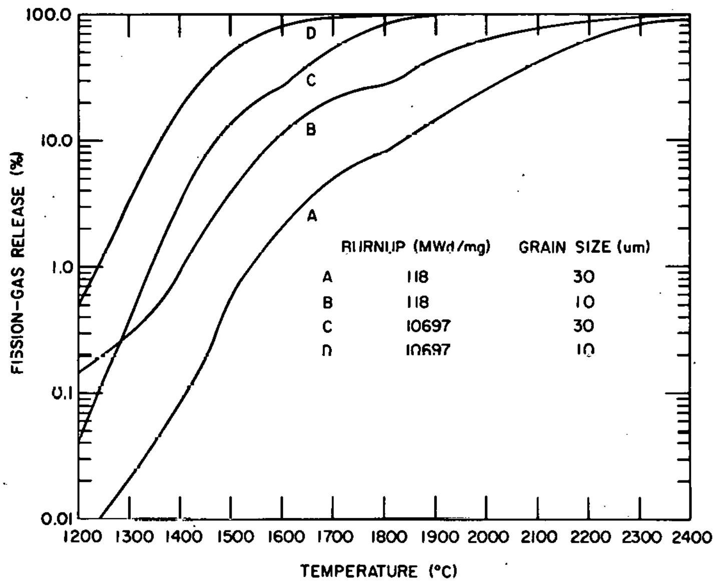

Fig. II.1. GRASS-calculated Fractional Fission-gas Release as a Function of Fuel Temperature and Burnup from 10-μm Grains with 200°C/cm Radial Temperature Gradient. ANL Neg. No 306-77-132 Rev. 1.

(2) The fractional fission-gas release is time-dependent. The rate of gas release depends on the irradiation time as well as on the temperature. In all cases, the fractional gas release increases with the time until saturation has been reached.

(3) The fractional fission-gas release has a strong dependence on the UO_2 grain size. The rate of fission-gas release increases as the UO_2 grain size decreases. For example, the fractional fission-gas release from 10- and 30-μm grains as a function of temperature for two values of the fuel burnup is shown in Fig. II.2.

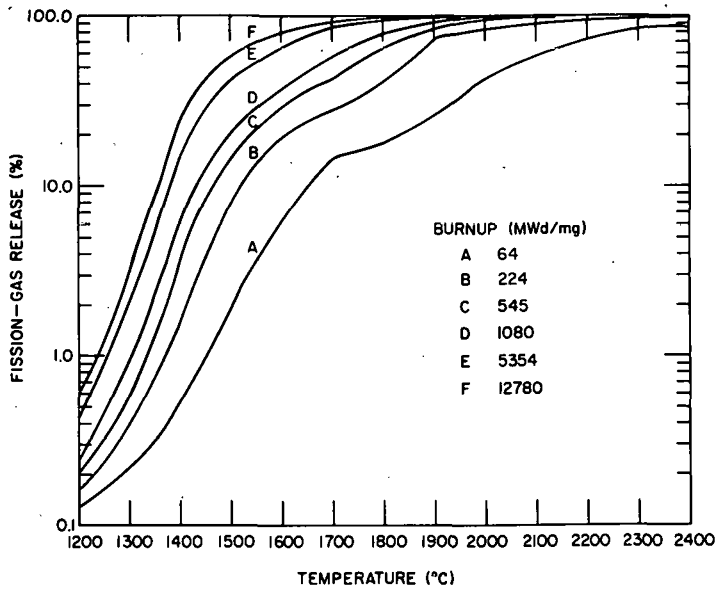

Fig. II.2

GRASS-calculated Fission-gas Release as a Function of Fuel Temperature and Burnup from 10- and 30-μm Grains with 200°C/cm Radial Temperature Gradient. ANL Neg. No. 306-77-131.

(4) The fractional fission-gas release has a moderate dependence on the temperature gradient. The rate of fission-gas release increases as the temperature gradient increases. For example, from Table II.2, the gas released from 10-μm grains at the end of 2000 h of irradiation with a 200 and a 1000°C/cm temperature gradient, respectively, can be classified as shown in Table II.4.

TABLE II.4. Dependence of Fractional Gas Release on Temperature Gradient. Time = 2000 h; fission rate = 1.3 x 10^{12} f/cm^3·s; grain size = 10 μm.

Temperature Region, °C	% Gas Release	
	Temperature Gradient = 200°C/cm	Temperature Gradient = 1000°C/cm
1200-1400	0.55-13.5	1-17.5
1400-1700	13.5-69	17.5-70
>1700	69-100	70-100

(5) The fractional fission-gas release has a weak dependence on the fission rate. The percent of fission-gas release increases as the fission rate decreases. For example, from Tables II.1 and II.2, the gas released from 10-μm grains at the end of 5000 h of irradiation with a fission rate of 1.3 x 10^{12} and 1 x 10^{13} f/cm^3·s, respectively, can be classified as shown in Table II.5. In

TABLE II.5. Dependence of Fractional Gas Release on Fission Rate. Time = 5000 h; temperature gradient = 200°C/cm; grain size = 10 μm.

Temperature Region, °C	% Gas Release	
	Fission Rate = 1.3 x 10^{12} f/cm^3·s	Fission Rate = 1.0 x 10^{13} f/cm^3·s
1200-1400	0.82-22	0.42-14
1400-1700	22-86	14-85
>1700	86-100	85-100

general, the differences in fractional gas release from fuels having different fission rates become greater for fuels having lower temperatures and longer irradiation times.

(6) The fractional fission-gas release has a strong dependence on the degree of interconnection of grain-edge tunnels. Due to the incomplete interconnection of the grain-edge tunnels, the amount of gas actually released from the fuel will be less than the amount released to the grain edges. For example, if the degree of grain-edge tunnel interconnection is 50%, the maximum releases in Tables II.1 and II.2 will be 50% instead of 100%. In general, the degree of interconnection depends on the fuel microstructure (e.g., grain size, UO_2 density, fabricated pore-size distribution) and, hence, is a function of the irradiation time.

In a recent SST-GRASS analysis (see ANL-77-10, p. 69) of the burnup dependence of fission-gas release from LWR fuel rods irradiated at a constant power level, the fractional gas release as a function of burnup was found to reach a maximum and subsequently decrease. This burnup dependence of the fractional fission-gas release was primarily ascribed as a thermally induced effect; the SST-calculated fuel temperatures decreased as a function of time due to gap closure. These SST-GRASS results can be approximated using Table II.1 or II.2. For example, using Table II.1, one can obtain a fractional fission-gas release distribution as shown in Table II.6.

TABLE II.6. Dependence of Gas Release on Temperatures That Decrease Slowly with Time. Fission rate = 1×10^{13} f/cm^3·s; temperature gradient = 200°C/cm; grain size = 10 μm.

Temperature, °C	Time, h	Gas Release, %
1800	60	18
1700	1010	56
1600	3010	54
1500	5010	42

Note that, for this case, the fuel temperatures decrease substantially over a major part of the irradiation. A maximum in the percent gas release occurs after about 1000 h of irradiation. However, the maximum in the percent gas release can be avoided if the fuel temperatures fall off early in life and then stabilize. For example, using Table II.1, one can obtain a fractional fission-gas release distribution as shown in Table II.7.

TABLE II.7. Dependence of Gas Release on Temperatures That Stabilize Early in Life. Fission rate = 1×10^{13} f/cm^3·s; temperature gradient = 200°C/cm; grain size = 10 μm.

Temperature, °C	Time, h	Gas Release, %
1800	60	18
1600	210	19
1500	1010	21
1500	3010	35
1500	5010	42
.	.	.
.	.	.
.	.	.

Thus, if the fractional fission-gas release is to always increase as a function of burnup for a constant power irradiation, the fuel temperatures must stabilize early in life; i.e., the fuel-cladding gap must close early in life. For the SST-GRASS analyses reported last quarter, the fuel-cladding gap closed very late in life and hence caused the fuel temperatures to decrease for a major part of the irradiation. This in turn resulted in the fractional fission-gas release having a maximum as a function of burnup. These results are not surprising in that SST is based on an outdated version of the LIFE LMFBR fuel-element performance code and does not include any LWR-based modifications of the mechanical analyses. LIFE-LWR (see ANL-76-121, pp. 50-61) was generated on the basis of the latest version of LIFE (LIFE-III) and includes mechanical as well as thermal LWR properties and models. (GRASS is not presently coupled to LIFE-LWR.)

The conclusions of the SST-GRASS Code Analysis indicated that the experimentally observed rapid increase in fission-gas release rate at high burnup (~3 at. %) could be explained qualitatively by the venting of gas residing along grain edges and boundaries through stress-induced separations of grain boundaries that have been weakened by fission-gas concentration. The results of the analysis showed little evidence for enhanced release due to the development of channels on the grain faces after a saturation density of grain-boundary fission gas has been attained. However, the calculation of grain-boundary channel formation depends on an accurate calculation of grain size as well as fuel temperatures. For example, Table II.8 shows when grain-boundary channel formation occurred for the cases listed in Table II.1. (Gas release due to channel formation was not included in the results of Table II.1.)

TABLE II.8. Grain-boundary Channel Formation for Table II.1

Temperature, °C	Channel Formation, 10-μm Grains	Time Occurred, h	Channel Formation, 30-μm Grains	Time Occurred, h
1200	Yes	9710	Yes	8560
1300	Yes	4711	Yes	3511
1400	Yes	1862	Yes	1062
1500	Yes	1463	Yes	513
1600	No	-	Yes	564
1700	No	-	Yes	615
1800	No	-	Yes	766
1900	No	-	Yes	1667
2000	No	-	No	-
2100	No	-	No	-

Thus, in general, any description of the release of fission gas at high burnup should include the possibility for enhanced release due to grain-boundary channel formation. In addition, the degree of interconnection of grain-edge tunnels is also a function of burnup and could contribute to an increase in the fission-gas release rate at high burnup. The analytical (GRASS) approach to modeling the release of fission gas at high burnup will include models for grain-boundary separation due to induced stresses on grain boundaries weakened by fission-gas concentration. These models will be included with the GRASS models for both grain-boundary channel formation and grain-edge tunnel interlinkage in a general correlation for the prediction of fission-gas release at high burnup.

b. Formulation of Models to Describe Grain-boundary Separation

The conclusions of the SST-GRASS code analysis reported last quarter and discussed above indicated that the experimentally observed rapid increase in fission-gas release rate at high burnup (~3 at. %) could be explained qualitatively by the venting of gas residing along grain edges and boundaries through stress-induced separations at grain boundaries that have been weakened by fission-gas concentration. The accumulation of fission gas on grain boundaries would degrade the strength of these boundaries as a function of burnup. If the intergranular fracture stress falls to the level of the induced stresses, then intergranular cracks occur that provide additional pathways for gas release. During this quarter, an approach was formulated for describing this phenomenon.

In irradiated LWR fuel, a grain-boundary fission-gas bubble can be interpreted as a microcrack having a length equal to the diameter of the bubble. The required applied stress for grain-boundary fracture will depend on the number and size of the grain-boundary fission-gas bubbles, and on the spacings between the bubbles. Because the GRASS analysis of grain-boundary fracture is going to be used to predict gross effects that lead to observable releases of fission gas, a phenomenological approach seems the most reasonable where the key parameters influencing cracking (calculated as a function of burnup) are correlated with experimental observations.

In addition to the number and size of the grain-boundary fission-gas bubbles and the spacings between the bubbles, other parameters may be important. The bubbles present on a grain boundary reduce the boundary effective surface area by an amount equal to the sum of all the bubble surface projections. As the effective grain-boundary surface area is reduced, the applied stress on the boundary increases, and hence facilitates grain-boundary fracture. In addition, the grain-boundary surface energy decreases with burnup due to solute-atom segregation and to adsorbed layers of impurities on the bubble surface. Precipitates have been associated with fission-gas bubbles, and therefore the bubble surface is probably contaminated by an adsorbed layer of fission products. The decrease in surface energy is important, since, for a given number of gas atoms in a single bubble, a reduction in the surface energy by a factor of two results in a bubble occupying approximately four times the previous equilibrium volume.

Given the above considerations, an analytical approach to modeling grain-boundary separation is as follows:

(1) Accurately describe the mechanical and thermal behavior of LWR fuel rods as a function of irradiation history (e.g., SST, LIFE-LWR, FRAP-S).

(2) Calculate the decrease in the grain-boundary surface energy.

(3) Calculate the evolution of the grain-boundary fission-gas bubble-size distribution as a function of the fuel microstructure, temperature, and stresses (GRASS).

(4) Calculate the reduction in the effective grain-boundary surface area based on the bubble-size distribution of fission-gas at the grain boundary.

(5) Calculate the mean bubble-bubble spacings. This calculation would require an assumption on how the various bubbles are distributed physically on the boundary (e.g., Poisson statistics).

(6) Develop a correlation between items 1-5 above, the local stresses in the fuel (calculated in item 1), and the extent of grain-boundary separation. This correlation would require experimental support, i.e., examinations of fuel exhibiting grain-boundary separation to provide information on the grain-boundary bubble distributions, etc. For example, results of direct investigations of some of the fuel that had high releases of fission gas would be valuable.

Once a description of the stress-induced separation of grain boundaries weakened by fission-product concentration is available, the GRASS calculation of fission-gas release can be straightforwardly extended to include a capability for a rapid increase in the release rate (burst) of gas as a result of extensive grain-boundary separation occurring during design transients (i.e., power changes). This rapid increase in the release of fission gas would most likely take place at relatively high burnup after sufficient diffusion of fission products to, and bubble growth on, the grain boundaries has occurred.

2. Modeling of Fission-gas Behavior during Transient Conditions

During this quarter, GRASS calculations of gas release during a hypothetical loss-of-coolant accident (LOCA) were performed. The results of these analyses will be used to aid in the formulation of decisions on the need for, and the requirements of, modifications to the present ANL LWR DEH apparatus in order to simulate LOCA-type transients. Additional analyses to assess characteristic temperature profiles of, and gas release from, LWR fuel undergoing a LOCA will be forthcoming as soon as EG&G is successful in linking GRASS with FRAP-T.

GRASS-Mod 3 was used to calculate the response of fission gases in an LWR fuel rod during a hypothetical LOCA. The ability to predict and, if necessary, limit the amount of gas released from a fuel rod in the event of a LOCA in a commercial LWR is important, not only in predicting radiological releases, but also in limiting cladding deformation; the gas released to the fuel-cladding gap and fuel-rod plenum increases the internal loading on the cladding. For the same reasons, the amount of gas released during steady-state irradiations can also influence the outcome of a LOCA.

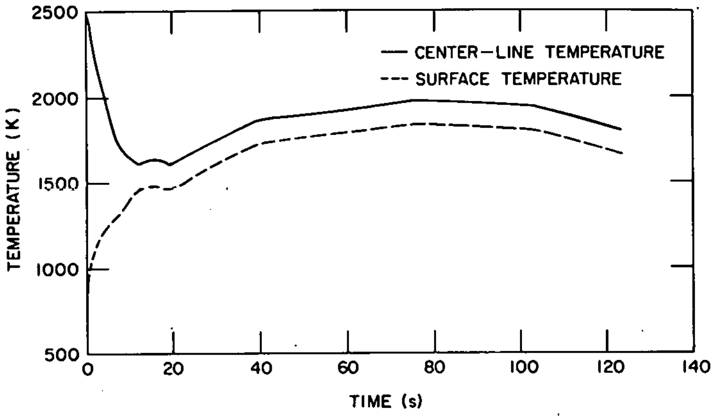

Fig. II.3. Fuel-surface and Centerline Temperature Histories during LOCA for Hottest 0.25 m of a ~4-m (12-ft) Fuel Rod. ANL Neg. No. 306-77-130.

The fuel temperature and power profiles used in the LOCA analysis were obtained from calculations performed with the FRAP-T and the RELAP codes at EG&G. The fuel-surface and centerline transient temperature histories for the hottest 0.25 m of a 4-m LWR fuel rod are shown in Fig. II.3. The steady-state fuel-rod conditions are atypical of fuel rods irradiated in commercial reactors; the operating temperatures and power levels are quite high. However, because of the high fuel temperatures, the present study highlights the importance of the distributions of retained fission gas in influencing fission-gas release during a LOCA.

GRASS-Mod 3 was used to calculate the steady-state fission-gas-bubble-size distributions for this section of the fuel rod at the pretransient power level (54 kW/m) and fuel temperatures to a burnup of 16,000 MWd/Mg. Assuming the as-fabricated fuel density (93.25% TD) and a radial distribution of grain sizes of 5-35 μm, the code predicted that ~30% of the generated fission gas in this section of the fuel had been released before the initiation of the LOCA.

Fission gas, generated primarily within the UO_2 grains, migrates to the grain-boundary surfaces and then to the grain edges at rates that depend on factors such as fuel temperatures and microstructure. Figure II.4 shows the GRASS-calculated pretransient radial distribution of retained gas for the above fuel section for intra- and intergranular gas, and for gas in closed porosity along the grain edges. More than 99% of the retained gas located within the inner 30% of this fuel section is in closed porosity along the grain edges; the relative absence of intra- and intergranular gas is due to the high irradiation temperatures. In contrast, more than 99% of the retained gas located within the outer 30% of the fuel is intragranular. Between these regions, the fuel is characterized mainly by intragranular gas, or gas in closed porosity; very little gas (<<1%) is intergranular. Intergranular gas has a high potential to vent to the porosity along the grain edges in the case of grain-boundary channel formation. The gas in the closed porosity has a high potential for release by either grain-boundary separation or the evolving of the closed porosity to an open porosity due to changes in the fuel microstructure.

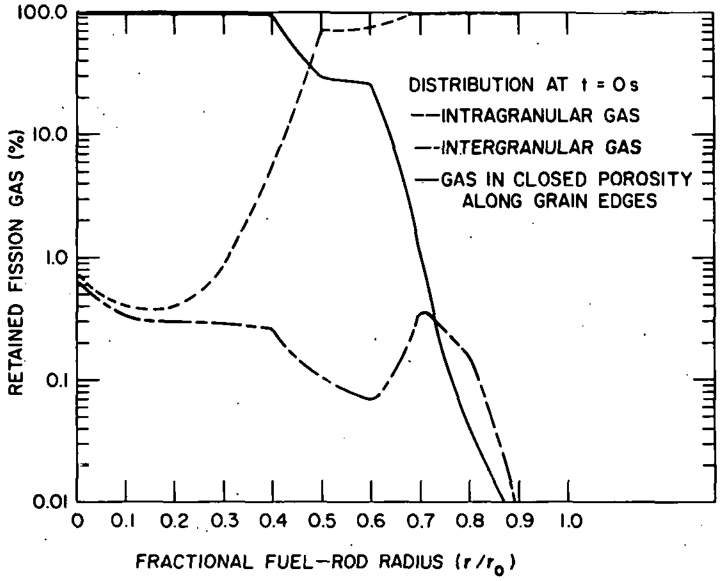

Fig. II.4

GRASS-calculated Pretransient Radial Distributions of Retained Gas. ANL Neg. No. 306-77-129.

During the first phase of the LOCA, as shown in Fig. II.3, the fuel-surface temperatures increased while the centerline temperatures decreased. After ~12 s into the transient, the fuel temperatures tended to stabilize. At ~20 s, the refill phase of the LOCA began and fuel temperatures rose due to fission-product decay heat. (A linear rise in the fuel temperatures was assumed.) After ~123 s, the core was essentially full of water (end of reflood phase) and the fuel temperatures decreased quite rapidly. Figure II.5 shows the radial distribution of retained gas calculated to exist in the fuel at the end of the reflood phase of the LOCA. Gas release due to grain-boundary separation, or venting of intergranular gas to the grain edges due to grain-boundary channel formation has not been included in these results. Comparison of Figs. II.4 and II.5 shows that the major effect of the transient on the distribution of retained fission gas was to increase the gas retained on grain boundaries in the outer 50% of the fuel. For example, the intergranular

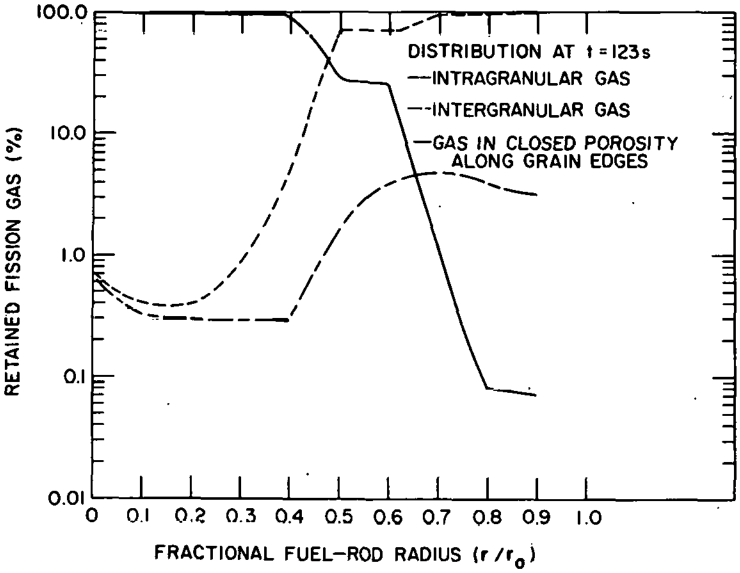

Fig. II.5

GRASS-calculated Radial Distributions of Retained Gas after Reflood. ANL Neg. No. 306-77-128.

gas population at a fractional radius, r/r_0, equal to 0.6 has increased by a factor of ~43 from the pretransient quantities, and is ~4% of the total retained gas in this region. Furthermore, the increase in the intergranular fission gas took place primarily during the refill and reflood phases of the LOCA, when the fuel temperatures were elevated due to fission-product decay heat, and was a consequence of time at temperature.

Gas released from the fuel during the LOCA was calculated for a variety of fuel microstructures: the pretransient microstructure, the pretransient microstructure with the addition of channel formation on grain boundaries due to saturation by fission gas, and a series of microstructures characterized by channel formation as well as by varying degrees of grain-boundary separation. The time evolution of channel formation on grain boundaries was calculated with GRASS-Mod 3; grain-boundary separation was put in by hand, as there is currently no available model describing this phenomenon. Grain-boundary separation was assumed to occur only along boundaries where GRASS-Mod 3 predicted channel formation. When channel formation occurred, the gas on the boundary was vented to the porosity residing along the grain edges; if the porosity was calculated to be open, the gas was released to the exterior of the fuel; if the porosity was closed, the gas was trapped along the grain edges and contributed to fuel swelling. When grain-boundary separation occurred, the gas located in the closed porosity along the grain edges was vented directly to the exterior of the fuel.

Because of the relatively low temperatures and the short time of the LOCA, not much gas is expected to be released by diffusional processes. However, from Fig. II.5, there is a potential for sizable releases due to grain-boundary channel formation and intergranular fracture. The time evolution of the predicted channel formation on the grain boundaries for the fuel section under consideration is shown in Fig. II.6. The values of the fractional radii, r/r_0, indicate the regions in the fuel where channel formation has occurred. From Fig. II.6, at the end of the LOCA, channel formation has occurred on grain boundaries located within the outer 50% of the fuel. Thus, Figs. II.5 and II.6 indicate that grain-boundary channel formation can provide an enhancement of the fission-gas release during the LOCA.

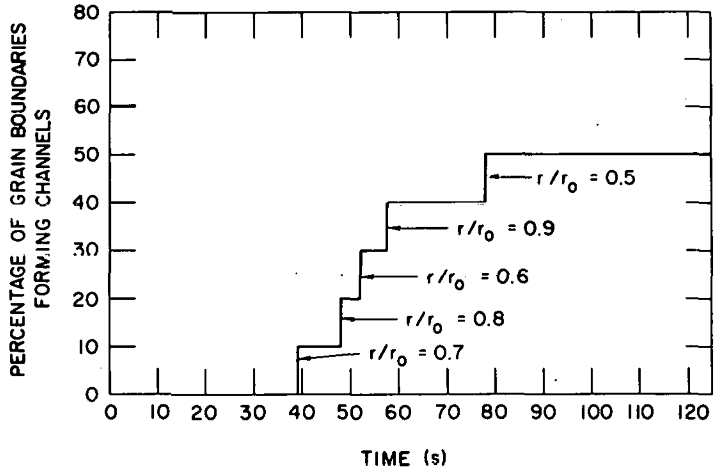

Fig. II.6

GRASS-calculated Evolution of Grain-boundary Channel Formation during LOCA. The values of the fractional radii, r/r_0, indicate the regions in the fuel where channel formation has occurred. ANL Neg. No. 306-77-125.

Figure II.7 shows the calculated fission-gas release as a function of the transient time for a variety of fuel microstructures. Curve A is the predicted gas release for the pretransient microstructure in which most of the release occurred by diffusional processes. As expected, very little gas (~0.04%) was released. Curve B is the predicted gas release allowing for an enhanced release due to grain-boundary channel formation. Enhanced gas release began to occur at ~39 s, when grain-boundary channel formation was initiated, and ~1.5% of the generated fission gas was released by the end of the LOCA.

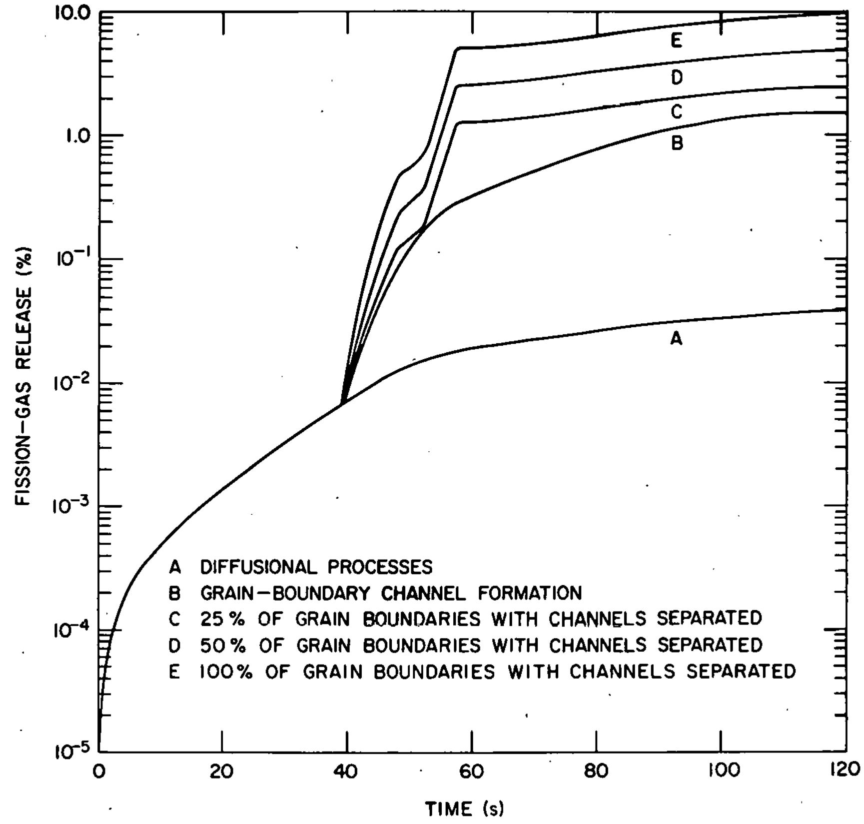

Fig. II.7. GRASS-calculated Fission-gas Release during LOCA for a Variety of Fuel Microstructures. ANL Neg. No. 306-77-127.

Extensive grain-boundary separation in the form of intergranular swelling and directional patterns of grain-boundary fissures has been observed at ANL in irradiated LWR fuel that has undergone PCM-type direct-electrical-heating (DEH) transients at heating rates of 25-400°C/s. The fuel used in these DEH tests was irradiated in the H. B. Robinson reactor to a burnup of ~30,000 MWd/mg. This DEH apparatus does not have the capability to simulate conditions that might be typical of those found in commercial LWR fuel undergoing a LOCA. DEH tests to date have been on bare fuel pellets (no radial constraint) that were irradiated at a relatively low power level so that most of the generated fission gas was retained (<<1% release).

The results of the tests indicate that gas release, intergranular swelling, and fissuring are functions of the stress state (e.g., degree of radial constraint) and the extent of grain-boundary weakening by fission-gas concentration during transient heating. GRASS-code calculations of the pre- and posttest bubble-size distributions are in qualitative agreement with experimental observations. The observed channel formation on grain boundaries of the transient-tested fuel was predicted; no channel formation was observed, and none was predicted for the steady-state irradiation. For the 25°C/s tests, the measured transient gas release was proportional to the areal fraction of grain boundaries that participated in either intergranular swelling or fissuring. The results of GRASS-code analyses support the hypothesis that these phenomina provide an interlinked network of escape paths for fission gas that diffuses to grain boundaries.

The rate of increase in fuel temperatures due to fission-product decay heat for the LOCA depicted in Fig. II.3 is similar to heating rates generated during PCM-type DEH tests. However, the temperature profiles for the LOCA differ markedly from the PCM-type temperature profiles in that much smaller temperature gradients are established across the fuel during a LOCA than during a PCM. Thus, whether extensive grain-boundary separation can occur during a LOCA is presently unclear.

In addition, the DEH tests performed thus far have been on radially unconstrained UO_2 pellets. Conceivably, the degree of radial restraint on the pellet will affect the local stresses generated within the fuel and will thus affect the degree of grain-boundary separation. However, grain-boundary separation has also been observed in Saxton-Load-Follower fuel that underwent a PCM transient in the PBF facilities (see Sec. B below); presumably, there was some radial constraint on the fuel during these tests. During a LOCA, the fuel may or may not be radially constrained; a lack of radial constraint on the fuel can occur due to factors such as ballooning of cladding. In what follows, the affect of possible grain-boundary separation on the gas release from fuel during a LOCA will be considered.

Intergranular separation is most likely due to stresses on boundaries weakened by fission-gas concentration. Thus, there should be a correlation between grain surfaces on which channels form due to saturation concentrations of fission gas and intergranular separation. When intergranular separation occurs, the gas located in closed porosity along the grain edges vents to the exterior of the fuel. Curves C, D, and E of Fig. II.7 show the predicted gas release assuming that 25, 50, and 100%, respectively, of the grain boundaries calculated to have channel formation also participated in intergranular separation. Under these conditions, the predicted gas release during the LOCA is between 2.5% (for 25% separation) and 10% for 100% separation) of the generated fission gas. Thus, the conclusion of the present analyses is that there is a potential for significant releases of fission gas during a LOCA under conditions amenable to the formation of grain-boundary channel and the occurrence of intergranular separation.

The conclusions of the analysis can be summarized as follows:

a. Gas release by diffusional processes during a LOCA will be negligible.

b. Gas release during a LOCA will be low if the steady-state concentrations of fission gas on grain boundaries and in closed porosity along grain edges located in the outer radial regions of the fuel are low. (A predominantly intragranular distribution of retained fission gas can be brought about by low fuel temperatures and/or low burnups.) This conclusion assumes that the microstructure in the inner radial regions of the fuel will not be altered by the LOCA.

c. Gas release during a LOCA will be low if no extensive intergranular separation occurs. Some gas release (~1.5% in the present analysis) can be expected if grain-boundary channel formation occurs. The formation of grain-boundary channels will depend on the pretransient gas concentrations as well as on the transient temperature history.

d. The potential for gas release during a LOCA is greatest during the refill and reflood phases when fuel temperatures rise, or are elevated, due to fission-product decay heat.

In the near future, FRAP-GRASS analyses of the response of fission gas in fuel rods irradiated under conditions more typical of those found in a commercial reactor during a hypothetical LOCA will be made. The results of these analyses will be used in conjunction with the results of an initial series of LOCA-type DEH tests, to be performed in an ANL LMFBR DEH facility, to assess the need for, and the requirements of, modifications to the present LWR DEH apparatus in order to simulate LOCA-type transients.

B. Experimental Program (S. M. Gehl and L. R. Kelman, MSD)

1. Transient-heating Tests (S. M. Gehl, L. R. Kelman, D. R. Pepalis, and R. B. Holdsworth, MSD)

a. Test Conditions

Three transient-heating tests using H. B. Robinson fuel were conducted at a slow heating rate. The conditions for these tests, designated 28-30, are summarized in Table II.9 along with the conditions of Tests 26 and 27, reported in ANL-77-10 (p. 73). Tests 26-30 comprised a group of experiments based on the test plan for PCM accident simulations (ANL-76-15, p. 45), which was revised last quarter (ANL-77-10, p. 72). These tests were intended as a series of experiments run at nominal 25°C/s centerline heating rates for various times short of melting. The development of techniques for measuring surface temperature using thermocouples was an additional objective of the tests.

TABLE II.9. Conditions of Interrupted DEH Transient-heating Tests of Robinson Fuel

Test Number	Fuel Weight, g	Fuel Burnup,[a] %	Transient-heating Time, s	Total Energy Input, 10^4 J
26	11.0	3.09	53.6	4.32
27	10.2	3.09	53.7	3.24
28	11.2	3.09	50.2	2.55
29	10.1	3.09	59.0	2.50
30	10.1	3.03	70.0	1.46

[a] Fuel burnup estimated from gamma-scan intensity normalized to ^{148}Nd mass spectrometric burnup analyses (see ANL-76-15, p. 50).

Because of problems with the control circuitry of the DEH power supply, the transient power histories of the tests departed considerably from the ramp that produces the 25°C/s heating rate. In particular, Tests 29 and 30 were operated at nearly constant power inputs of 420 and 210 W, respectively, during the portion of the experiments intended to be a programmed power ramp of 4 W/s. The actual heating rates in Tests 29 and 30 varied from 3 to 5°C/s. The effect of transient power history on gas release is discussed in Sec. b below.

A thermocouple was in contact with the fuel-pellet surface in each of Tests 26-30. A Pt-Pt 10% Rh (Type S) thermocouple was used in Test 26 and Chromel-Alumel (Type K) thermocouples in Tests 27-30. The thermocouple beads were pressed against the specimen surfaces by spring tension in the thermocouple wires and were covered over with a layer of UO_2 slip. The response of the thermocouples was good below ~850°C and for small thermal ramps. At higher temperatures, the thermocouples read consistently below the true surface temperature, as measured by optical pyrometry. The latter effect is probably due to heat conduction away from the bead along the wires.

b. Fission-gas Release during Transient Heating

Table II.10 summarizes the results of the analyses of the gases released from the fuel during Tests 26-30. Data for the other tests run at nominal 25°C/s ramps are also included. The previously reported gas-release data for these tests contained several calculational errors, which were corrected in the preparation of Table II.10. The gas-release data from Test 28 are obviously incorrect, perhaps because of contamination of the gas sample.

TABLE II.10. Fission Gas Collected during DEH Tests Conducted at Nominal 25°C/s Heating Rates

Test Number	Gas Collected, cm^3 (STP)/g		Percent Released[a]		Percent Released from Solid Fuel[b]	
	Xe	Kr	Xe	Kr	Xe	Kr
21	0.320	0.030	50.0	60	44	55
22	0.0848	0.012	13.1	25		
23	0.0056	0.001	0.84	2.0		
24	0.0820	0.016	12.0	30		
26	0.427	0.032	63.1	61	59	57
27	0.225	0.033	33.3	63		
28	1.50[c]	0.003[c]				
29	0.0136	0.002	2.01	3.2		
30	1.7×10^{-4}	2×10^{-5}	0.03	0.04		

[a] Corrected for burnup and normalized to retained gas content of 0.685 cm^3/g for xenon, 0.053 cm^3/g for krypton at the peak burnup positions.

[b] Assuming 100% release from liquid fuel.

[c] Xenon release and Xe/Kr ratio are highly improbable; sample may have been contaminated.

Inspection of the power traces for Tests 21-24 indicated the occurrence of variations from the programmed power input, similar to those observed for Tests 26-30. The resulting differences in the transient temperature histories for the nominal 25°C/s tests mean that attempts correlating gas release and test conditions must include the time-integrated power or temperature histories. An initial attempt at such a correlation is shown in Fig. II.8, in which the burnup-corrected xenon release is plotted against the total energy input to the sample during transient heating. This figure indicates that no gas was released for energy inputs below ~1.5 x 10^4 J, and that there is a roughly linear relationship between gas release and energy for higher energy inputs. The low xenon release fractions for Tests 29 and 30, in which the power increased at low rates, suggest that the apparent scatter in Fig. II.8 is partly an indication that other test parameters, in addition to total energy input, have a part in determining gas release. The analysis of the temperature histories for these experiments is continuing in order to develop additional relationships between gas release and test conditions.

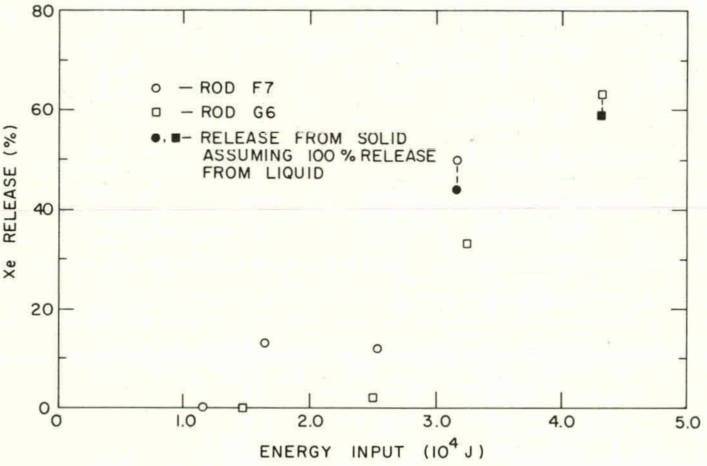

Fig. II.8. Fractional Xenon Release vs Energy Input for DEH Tests at Nominal 25°C/s (4W/s)

Areal melt fractions of 0.11 and 0.10 were observed in Tests 21 and 26, respectively. The melt zones produced during these tests, shown in ANL-76-87, Fig. II.7, for Test 21 and Fig. II.9 of this report for Test 26 contain gas bubbles in the size range 0.02-0.5 μm. Since the solubility of fission gas in liquid UO_2 at temperatures close to the melting point is low, the bubbles observed in the melt zone probably formed as gas precipitation occurred concurrently with fuel

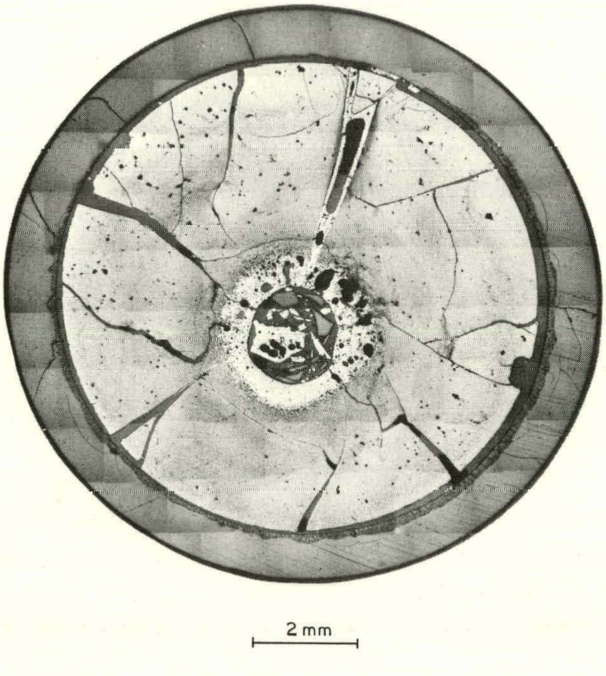

Fig. II 9

Transverse Section through Robinson Fuel Pellet Transient-tested to Central Melting in Test 26. Neg. No. MSD-189963.

melting. Most of the gas in these bubbles is likely to have been vented to the outside, either by percolation of the bubbles through the liquid or through cracks that formed during cooldown following solidification. The last two columns in Table II.10 indicate the gas-release fractions from unmelted fuel (for tests in which melting occurred) under the limiting assumption that 100% of the gas was released from the melted fuel. These values are only slightly smaller than the corresponding overall release fractions. The actual release fractions from the melted material lie between the overall release fractions and the limiting value of 100%. Similarly, the release from unmelted fuel is intermediate to the overall release and the values calculated for 100% release from the liquid.

2. Temperature Measurement and Calculation (S. M. Gehl, J. Rest, and D. R. Pepalis, MSD; J. J. Eichholz, EL)

Accurate determinations of the radial temperature profiles are necessary for the description of fission-gas release in terms of temperature-dependent processes such as differential thermal expansion, diffusion, and creep. The computer code used for temperature-profile calculations, DEHTTD (see ANL-75-28, p. 27), contains literature values for the thermal and electrical conductivities of UO_2 and requires as input the time histories of pellet voltage, current, power, and surface temperature. Since thermal and electrical conductivity data for high-burnup UO_2, which is chemically and structurally different from unirradiated material, are not available, conductivities of unirradiated UO_2 are used in the code. Centerline temperature calculations using this data can be in error by as much as 600°C for DEH transients on high-burnup fuel. The results of recent attempts at improving the temperature-profile calculations by determining the physical properties of Robinson fuel are presented in this section. Inaccurate surface-temperature measurement is a secondary cause of errors in temperature-profile calculations. Progress in improving the accuracy of surface temperature measurement is included in this section.

a. Surface-temperature Measurement

As indicated in Sec. B.1.a above, thermocouples have proved useful at temperatures below ~850°C and at low heating rates. The limitations of thermocouple measurements are intrinsic to the DEH technique, which produces radial temperature gradients in the fuel that are largest at the specimen surface. To avoid interference with the fuel column, the thermocouple itself is in a temperature gradient, with the thermocouple wires always at a lower temperature than the bead. Thus, heat conduction along the wires away from the bead results in the thermocouple bead being at a lower temperature than the specimen surface. Modifications of the DEH equipment to remedy this problem have been considered, but are likely to cause additional problems. For example, the use of smaller-diameter thermocouple wire would improve the time response of the thermocouple and reduce heat-conduction losses. However, to be effective, the wires would have to be so small (i.e., <~0.05 mm in diameter) as to make remote handling difficult.

As an alternative, infrared pyrometry is being used for surface-temperature measurement. The pyrometer in current use (Ircon Model 230C99) views the specimen through the hot-cell window and is sensitive to radiation in the 0.7-0.9-μm-wavelength band. The design of the instrument and the attenuation of infrared radiation by the cell window limit this instrument to temperatures above 1300°C. A second pyrometer (E^2 Thermodot Model 7 Auto) was procured to cover temperatures between 500 and 1500°C. This instrument, which senses radiation in the 1.7-2.7-μm-wavelength band, will be placed inside the hot cell and is designed to provide some radiation shielding of the electronic components. Additional shielding will be used to allow the instrument to operate in the high radiation field near the DEH specimen chamber.

Calibration of both pyrometers against a National Bureau of Standards-calibrated tungsten-filament lamp indicated that the apparent emissivities of tungsten differed for the two instruments. At 1200°C, the Ircon and Thermodot pyrometers indicated emissivities of 0.53 and 0.17, respectively. The former value is equal to the spectral emissivity of tungsten at 0.7 μm and 1200°C; the latter value is close to the total emissivity (i.e., the emissivity measured over the total wavelength spectrum) at the same temperature.[1] Similar literature values for the emissivity of UO_2 are not available. However, the experience of ANL workers has indicated that a value of 0.8 is appropriate for the Ircon instrument. Preliminary comparison of the response of the Ircon and Thermodot pyrometers on an electrically heated UO_2 surface indicated that the emissivity of UO_2 in the spectral range of the latter is between 0.6 and 0.7. Work is continuing to determine the required emissivity more accurately.

b. Radial Temperature-profile Calculation

The temperature profiles calculated by the DEHTTD code are sensitive to the value for the electrical conductivity of UO_2 used to obtain the radial distribution of power generation. Because we can easily measure the effective electrical conductivity of DEH pellet stacks, which consist of an irradiated pellet sandwiched between two unirradiated pellets, the initial attempt at improving the calculations will consist of including empirically determined electrical conductivities in the code. This section discusses the results of electrical-conductivity measurements and compares these values with those presently used in the DEHTTD code.

The resistance of pellet stacks is monitored as they are heated from room temperature to ~300°C by an external line heater (see ANL-75-72, p. 35) before the start of DEH. The measured conductivity values were fitted to an equation of the form

$$\sigma = \frac{A}{T}\exp\left(\frac{B}{T}\right),$$

where σ is conductivity in $(\mathrm{ohm\cdot cm})^{-1}$, T is temperature in K, and A and B are constants. The conductivities for the pellet stacks in the last 10 tests were divided into two groups as shown in Table II.11. The entries for A, B, and r^2 (square of the correlation coefficient) were determined by a linear-regression analysis of the variable $\ell n(T)$ on 1/T. The conductivities of the stacks in Group I were greater than the Group II conductivities by a factor of ~3 for temperatures between 350 and 600K. The stack conductivity in Test 24 was intermediate to the values observed for the two groups. At 600 K, the measured conductivities were approximately two orders of magnitude greater than the value currently used in the DEHTTD code.

TABLE II.11. Summary of Pellet-stack Electrical-conductivity Parameters

Group	Tests	A	B	r^2
I	21-23, 25-27	8527	3954	0.990
-	24	13520	4326	0.994
II	28-30	4822	4133	0.991

To improve the accuracy of the DEHTTD calculations, we must incorporate the empirically determined electrical conductivities into the code. A study is currently underway to determine the optimum method for using the empirical values in the DEHTTD code.

3. ANL-EG&G Cross-check Program (S. M. Gehl, L. R. Kelman, R. B. Holdsworth, and C. H. Gebo, and D. R. Pepalis, MSD)

Eight sections of fuel from rods 007 and 008 of the PBF IE-1 experiment and two irradiated Saxton Load Follower (SLF) rods were shipped from EG&G and received at ANL. Plenum-gas analysis of sibling rod 843 and preliminary metallographic examination of the sibling and PBF-tested fuel have been completed. The metallographic examination revealed the presence of intergranular separations similar to those observed for DEH-tested Robinson fuel. Preparations for DEH tests of the sibling irradiated material are underway.

a. Fuel Characterization

The results of plenum gas analysis for sibling rod 843 are presented in Table II.12. (The plenum gas from rod 844 was inadvertently lost during puncturing.) The gas analysis of rod 843 is similar to that of rod 837 reported by EG&G,[2] although the backfilled void volume is higher for rod 843 (8.86 versus 7.59 cm^3). This difference is probably due to the slightly longer fuel column of rod 837 revealed by neutron radiography.[3] Estimates based on the retained fission-gas determination in Robinson fuel (see ANL-76-121, pp. 75-77) and the relative burnups of the Robinson and SLF fuels indicate that the amounts of fission gas shown in Table II.12 represents ~12% of the total formed during irradiation. A more precise determination of the release of gas from SLF fuel before PBF and DEH testing will be obtained by dissolving whole pellets in HNO_3 and collecting the evolved fission gas.

TABLE II.12. Gas Analysis of Rod 843

Volume of plenum Gas = 141.22 ± 0.77 cm^3
Backfilled void volume = 8.86 ± 0.06 cm^3

Chemical Analysis

Element	Mole %	Element	Mole %
H_2	<0.05	Ar	0.2
He	84.5	CO_2	<0.02
H_2O	0.05	Kr	2.05
N_2	0.06	Xe	13.2
O_2	<0.02		

Isotopic Analysis

Isotope	Mole %	Isotope	Mole %
^{82}Kr	0.035 ± 0.005	^{128}Xe	0.011 ± 0.002
^{83}Kr	13.7 ± 0.1	^{130}Xe	0.03 ± 0.01
^{84}Kr	28.2 ± 0.1	^{131}Xe	11.1 ± 0.1
^{85}Kr	5.0 ± 0.1	^{132}Xe	18.7 ± 0.2
^{86}Kr	53.0 ± 0.2	^{134}Xe	31.6 ± 0.2
		^{136}Xe	38.6 ± 0.2

The existing apparatus for performing whole-pellet dissolutions deteriorated as a result of an ~6-month residence in a high radiation field. This equipment has been redesigned and built, and will be installed in a small, low-gamma-background, analytical hot cell. The need for rebuilding the pellet-dissolution apparatus is causing a delay in completing this part of the cross-check program.

A composite micrograph of a section through rod 844 at ~0.72 m (28 in.) above the rod bottom is shown in Fig. II.10. The overall radial and circumferential cracking pattern and the distribution of large pores (20-120-μm diameter) are similar to those observed for the Robinson fuel.

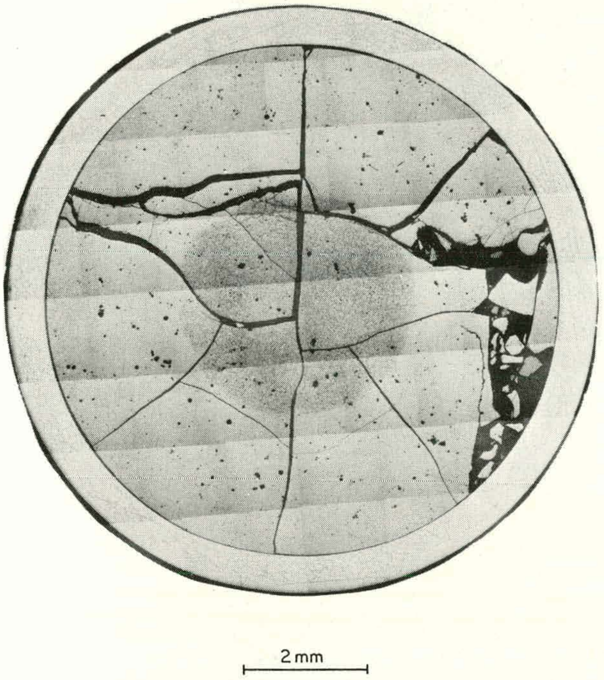

Fig. II.10. Transverse Section through SLF Rod 844 at ~0.72 m (28 in.) above Rod Bottom. Neg. No. MSD-189961.

There is no evidence to suggest that the fuel is bonded to the cladding or that cladding collapse has occurred. A zone of larger grain-size material extends from the centerline to a fractional radius $r/r_0 \simeq 0.43$. The mean grain intercept in this zone is ~10 μm. The microstructure near the highest power region of the rod, i.e., at ~0.38 m (15 in.) above the rod bottom, is similar to that shown in Fig. II.10, except that the large-grained region extends to $r/r_0 \simeq 0.57$.

The unetched microstructures of rods 007 and 008 from Test IE-1 show varying types and amounts of intergranular separation. In the film-boiling zone of rod 007 (see Figs. II.11-II.13), the intergranular separation was so severe that much of the unmelted fuel was reduced to a powdery mass of individual grains. This structure was responsible for a pullout problem experienced during specimen preparation. Transverse sections at axial positions just below and above the film-boiling boundary of rod 008 are shown in Figs. II.14 and II.15, respectively. Intergranular separation in the film-boiling region is less extensive in rod 008 than in rod 007. The intergranular separation in the film-boiling region of rod 008

Fig. II.11

Transverse Section at a Level Just above Film-boiling Boundary in Rod 007 from Test PBF IE-1. Neg. No. MSD-189835.

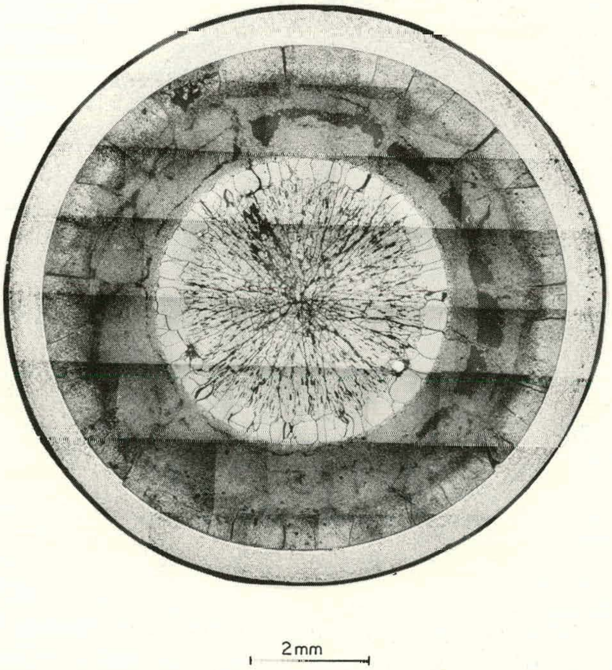

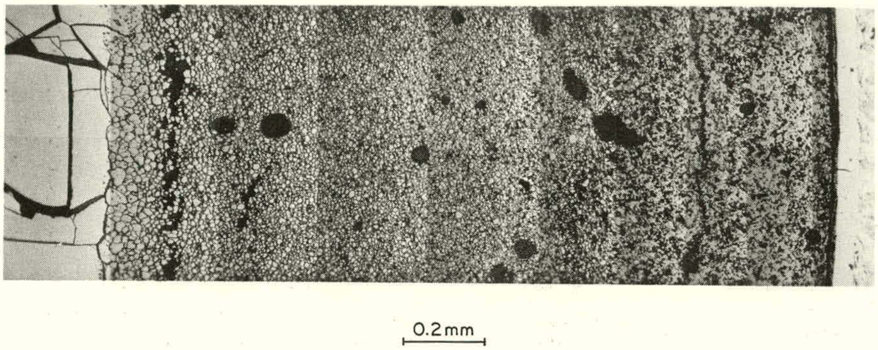

Fig. II.12. Detailed View of Grain-boundary Separation in Unmelted Region of Section Shown in Fig. II.11. Neg. No. MSD-189848.

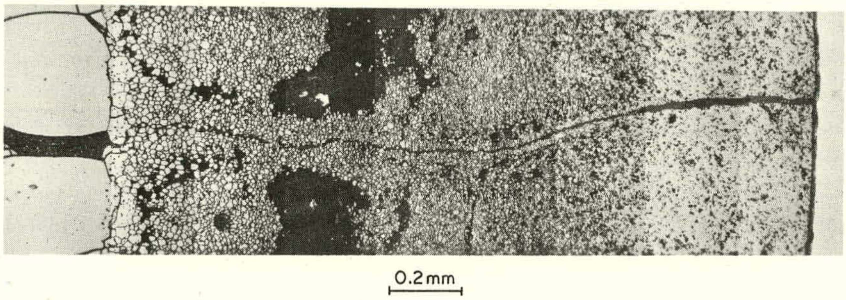

Fig. II.13. Grain-boundary Separation in Vicinity of Radial Crack in Section Shown in Fig. II.11. Neg. No. MSD-189852.

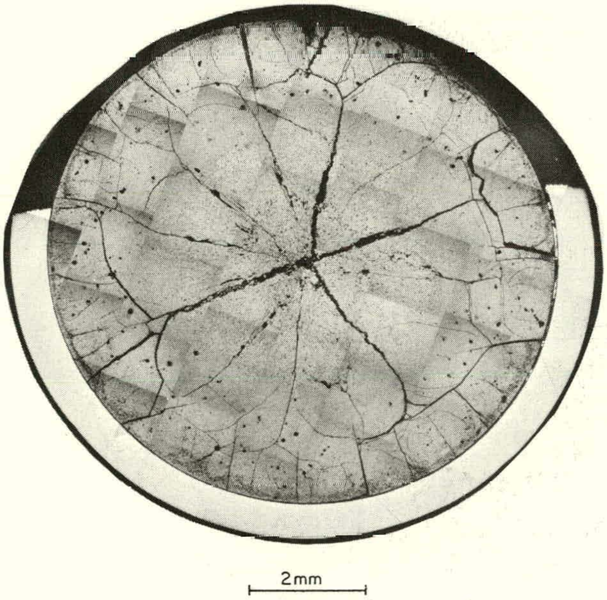

Fig. II.14. Transverse Section at a Level Just below Film-boiling Region in Rod 008 of Test PBF IE-1. Neg. No. MSD-189834.

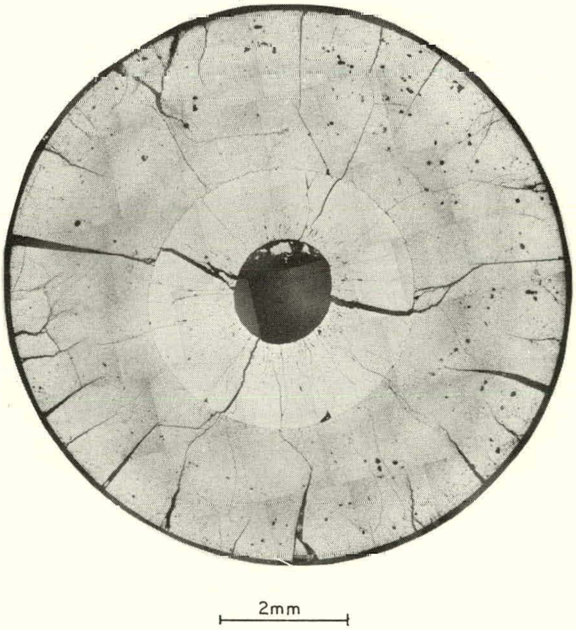

Fig. II.15. Transverse Section at a Level Just above Film-boiling Region in Rod 008 of Test PBF IE-1. Neg. No. MSD-189837.

was less extensive. Intergranular separations were most pronounced in the vicinity of large preexisting cracks, where the separations occurred preferentially along grain boundaries that were roughly parallel to the cracks. For examples, see Figs. II.16 and II.17. This structure is similar, but not identical, to the directionally oriented separations observed in DEH-tested commercial PWR (Robinson) fuel. Intergranular separation also occurred away from the large cracks in rod 008, as shown in Fig. II.18. The latter separations appeared to be randomly oriented. As the central melt zone was approached, the intergranular separations became less angular and more rounded and more closely resembled the intergranular porosity that formed in the hottest unmelted material during DEH tests of the Robinson fuel.

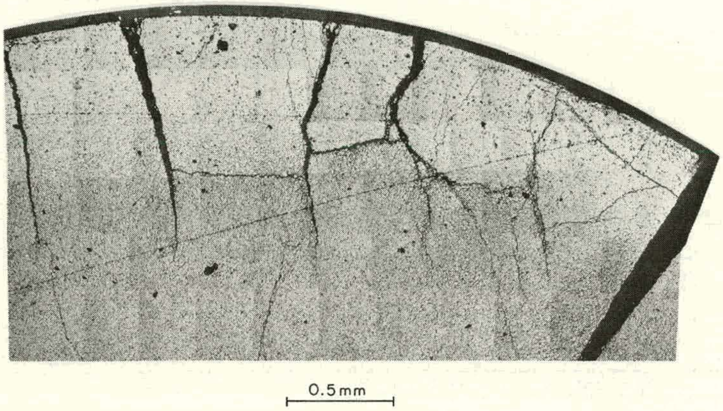

Fig. II.16. Grain-boundary Separation in Vicinity of Cracks near Edge of Section Shown in Fig. II.15. Neg. No. MSD-189836.

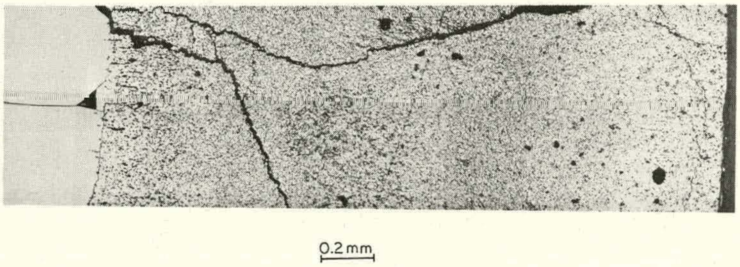

Fig. II.17. Grain-boundary Separation in Vicinity of Large Radial Cracks in Section Shown in Fig. II.15. Neg. No. MSD-189840.

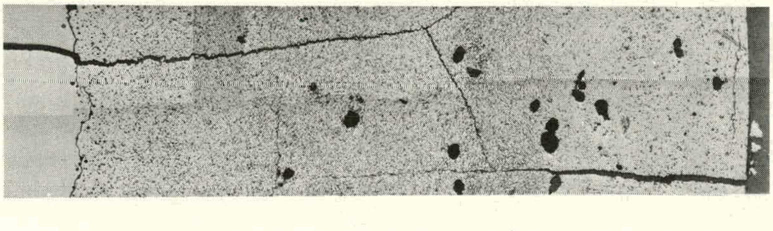

Fig. II.18. General View of Grain-boundary Separation in Section Shown in Fig. II.15. The long crack at the bottom of the figure is a shutdown crack. Neg. No. MSD-189844.

The melt zones of the PBF-tested fuel were virtually pore-free, in contrast to the extensive gas porosity observed in the melt zones of the Robinson fuel after DEH tests.

b. DEH Testing

The metallographic examination of the irradiated SLF fuel indicated that there was sufficient clearance between the fuel and cladding to permit useful DEH specimens to be recovered from short lengths of the fuel rod by the techniques already developed for the Robinson fuel. The fuel extraction apparatus has been modified to accept the smaller diameter of the SLF fuel, and smaller-diameter spacer pellets are being fabricated. DEH testing of the SLF fuel is scheduled for May.

References

1. CRC Handbook of Chemistry and Physics, 56th edition, CRC Press, Cleveland, OH, p. E230 (1975).

2. G. W. Gibson et al., Characteristics of UO_2-Zircaloy Fuel Rod Materials From the Saxton Reactor for Use in Power Burst Facility, ANCR-NUREG-1321, p. 73 (Sept 1976).

3. Ibid., pp. 40-41.

III. MECHANICAL PROPERTIES OF ZIRCALOY CONTAINING OXYGEN

H. M. Chung, A. M. Garde, and T. F. Kassner, MSD

A. Summary

Uniaxial and biaxial mechanical-property data on Zircaloy-4 are being obtained over a wide range of temperatures and strain rates to establish a more quantitative cladding-embrittlement criterion applicable to postulated loss-of-coolant-accident (LOCA) situations in light-water reactors (LWR's). The mechanical-property information will be incorporated into fuel-element modeling codes that will provide a quantitative basis for evaluating cladding deformation over a wide range of LOCA and power-coolant-mismatch (PCM) conditions.

The tensile properties of Zircaloy have been investigated for the following experimental conditions: temperature, 25-1400°C; strain rate, 10^{-6}-10^{-1} s^{-1}; grain size, 5-55 μm; texture, longitudinal, transverse, and diagonal; and oxygen concentration, 0.11-4.4 wt % in homogeneous and composite $ZrO_2/\alpha/\beta$ specimens. Completed results for the work-hardening behavior of as-received Zircaloy-4 and alloys with oxygen have been obtained as functions of strain rate and temperature. The work-hardening exponent for homogeneous Zircaloy-4/oxygen alloys has a minimum value at intermediate oxygen concentrations (0.25-0.4 wt %) at temperatures between 1000 and 1200°C, and the oxygen concentration at which the minimum occurs increases as the temperature increases. At higher temperatures, the work-hardening rate decreases as the oxygen content increases, although the minimum is not observed, because the alloy composition approaches the β-phase boundary.

The tensile properties of composite Zircaloy-4 oxygen specimens show significant differences for temperatures below and above ~1000°C. Below this temperature, the oxide and α layers exhibit cracking, whereas at higher temperatures, dissolution of the oxide layer occurs and cracking of the α layer is minimal. As a result, the yield stress and ultimate tensile strength are not highly dependent on the oxygen content at the lower temperatures. (Strengthening due to oxygen diffusion into the material compensates for the reduced section thickness that results from cracking of the oxide.) However, the strength properties increase and the ductility decreases as the oxygen content increases at higher temperatures. Oxygen also decreases the work-hardening rate of the major deformation stage.

Additional information has been obtained on the diametral expansion and rupture characteristics of axially constrained Zircaloy-4 cladding in a steam environment. To determine whether specimen length had any effect on the deformation characteristics, we performed several tube-burst experiments on 300-mm-long tubes in vacuum and steam at heating rates of 5, 45, and 115°C/s. The results indicated no effect of specimen length on the tube-burst properties.

The effect of circumferential temperature variations on cladding-deformation behavior was investigated at the three heating rates. A radial-strain-localization parameter was defined and evaluated from the measurements of the cladding thickness at several positions along the circumference of the tube in the region of maximum circumferential strain. The parameter was used to correlate quantitatively the circumferential strain at failure with the maximum circumferential temperature variation around the tube. The maximum circumferential strain at burst temperatures in the vicinity of the 800°C strain peak decreased considerably as a result of temperature nonuniformity in the cladding. The present results will provide the basis for interpreting the deformation behavior of Zircaloy fuel cladding in nuclear-heated fuel rods.

Initial experiments have been conducted to establish the degree of embrittlement of Zircaloy cladding under "normal handling conditions" after cooling from oxidation temperatures between 1000 and 1500°C at a controlled rate. The capability of the cladding to remain intact after twisting and bending without excessive force was correlated with several criteria based upon oxidation parameters that were calculated from the amount of oxidation after different times at the various temperatures. Failure maps were developed relative to the various parameters and the oxidation temperatures. The criterion based on fractional saturation of the β phase for oxidation temperatures below ~1200°C provided the best correlation for failure of the cladding during normal handling at room temperature.

B. Mechanical Properties of As-received Zircaloy

1. Flow Stress and Ductility of Zircaloy-4 in Temperature Interval 25-700°C

The temperature dependence of the ultimate tensile strength (UTS) of Zircaloy-4 at three strain rates is plotted in Fig. III.1. The UTS decreases as the temperature increases as a result of the larger extent of dynamic recovery at higher temperatures. In Fig. III.1, a tendency toward a plateau in the temperature interval 300-500°C appears to exist. This is a manifestation of dynamic strain aging. Yield points were observed on the load-elongation curves at 200 and 400°C.

The uniform and total strains of Zircaloy-4 over the temperature interval 25-700°C at three strain rates are plotted in Fig. III.2. The uniform strain shows a peak near 200°C ($\dot{\epsilon} = 3.3 \times 10^{-3}\ s^{-1}$) due to the high work-hardening rate at this temperature associated with dynamic strain aging. The minimum in the total strain in the temperature interval 400-550°C is associated with a minimum in the strain-rate sensitivity within this temperature interval; this is another manifestation of dynamic strain aging.

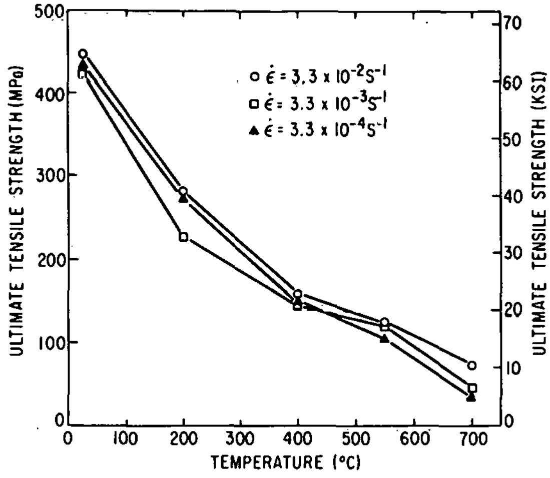

Fig. III.1. Ultimate Tensile Strength of Zircaloy-4 at Three Strain Rates over Temperature Interval 23–700°C. ANL Neg. No. 306-77-67 Rev. 1.

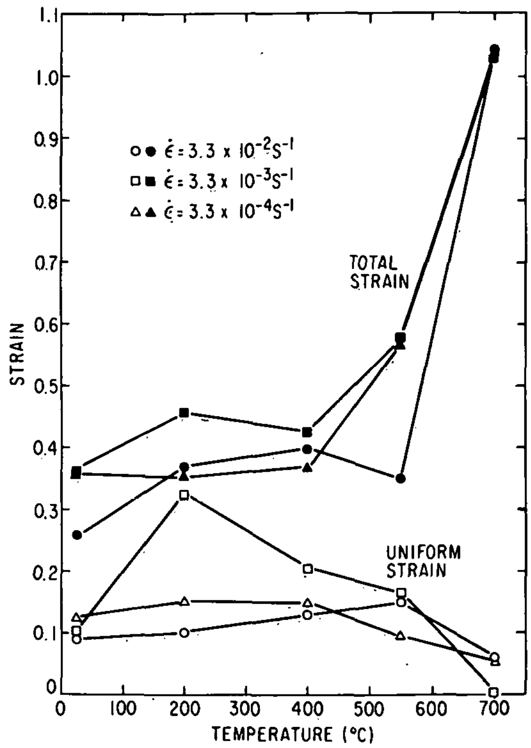

Fig. III.2. Uniform Strain and Total Strain for Zircaloy-4 Specimens as a Function of Deformation Temperature at Three Strain Rates over Temperature Interval 23–700°C. ANL Neg. No. 306-77-54 Rev. 1.

2. Work-hardening Analysis of Zircaloy-4

The Crussard-Jaoul work-hardening analysis, based on the Ludwik equation that relates the flow stress σ to the plastic strain ϵ by the empirical relationship $\sigma = \sigma_0 + k\epsilon^n$, was applied to Zircaloy-4 tensile data. Initial data were presented in previous quarterly reports,[1,2] and completed results are plotted in Figs. III.3-III.5. The temperature dependence of the work-hardening exponent for the stage that covers a major portion of the uniform strain region at three strain rates is plotted in Fig. III.3. In the α-phase region ($\lesssim 805°C$), peak values of the work-hardening exponent are observed at 200 and ~700°C. At these two temperatures, dynamic strain-aging effects are observed. Positive work-hardening exponents are observed below 600°C, where transgranular deformation is important. In the two-phase region (810-980°C), negative work-hardening exponents are observed due to intergranular deformation (grain-boundary sliding). At lower strain rates,[3] the extent of grain-boundary sliding is greater, and therefore the work-hardening exponent assumes larger negative values over a wider temperature interval. In the β-phase field ($> 1000°C$), extensive grain growth during deformation results in positive work-hardening exponents. The variation of k with temperature is similar to that of n (Fig. III.4). Since the product kn is proportional to the slope of the stress-strain curve ($d\sigma/d\epsilon$), the data in Figs. III.3 and III.4 imply a similar variation of the work-hardening rate with temperature. The parameter σ_0 decreases as the temperature increases (Fig. III.5).

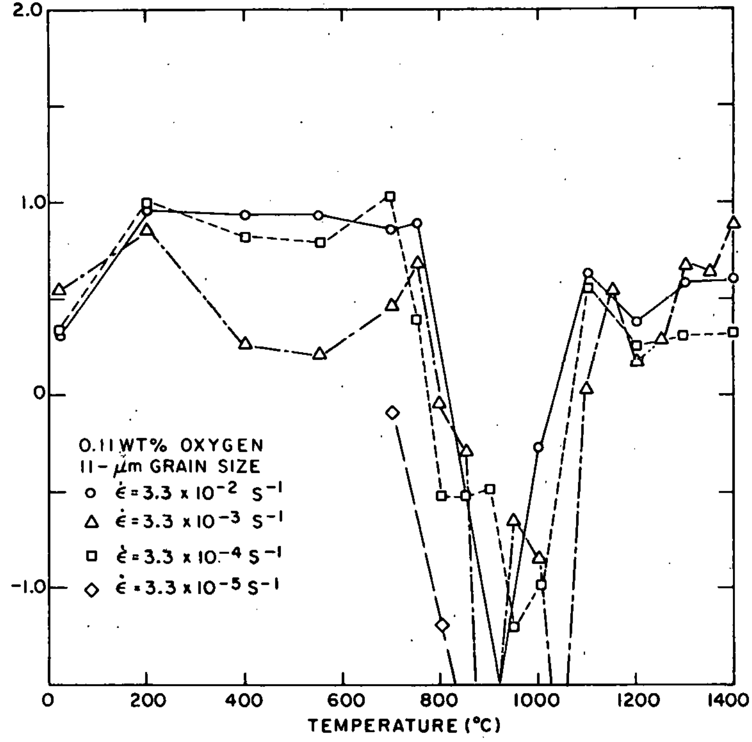

Fig. III.3

Work-hardening Exponent of Zircaloy-4 as a Function of Temperature at Four Strain Rates. ANL Neg. No. 306-77-74 Rev. 1.

Fig. III.4

Temperature Dependence of Parameter k for Zircaloy-4 at Three Strain Rates. ANL Neg. No. 306-77-73 Rev. 1.

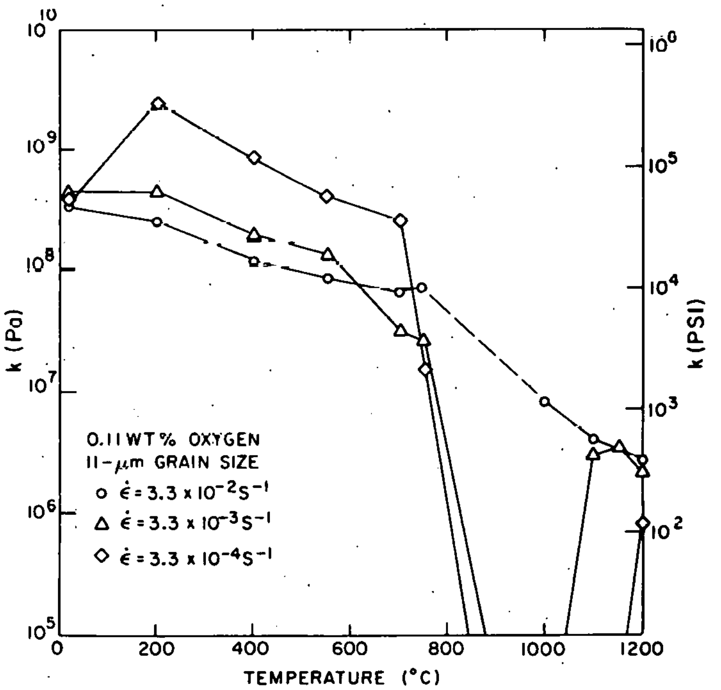

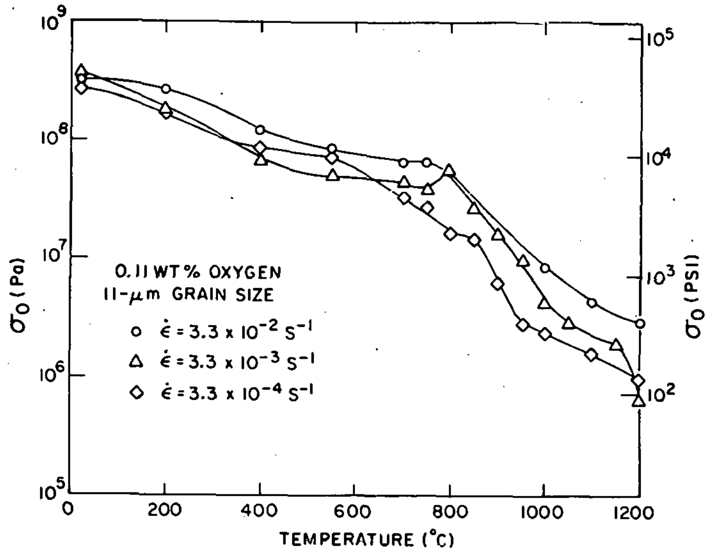

Fig. III.5

Variation of σ_0 with Temperature for Zircaloy-4 at Three Strain Rates. ANL Neg. No. 306-77-112.

3. Effect of Texture on the Work-hardening Rate

Since the Zircaloy sheet had a texture in which most of the grains had basal poles tilted ~30° from the normal (thickness) direction toward the transverse direction, the longitudinal specimens had more grains favorably oriented for prism slip than the transverse specimens. The diagonal orientation is midway between the longitudinal and transverse orientations. Results presented in Refs. 2 and 3 have shown that, although texture has some effect below 800°C, most of the mechanical properties (i.e., uniform strain, total strain, UTS, and strain-rate sensitivity) are independent of texture above 800°C.

The effect of texture on the work-hardening parameters is shown in Fig. III.6. Above 800°C, the work-hardening rate does not seem to be a strong function of the texture.

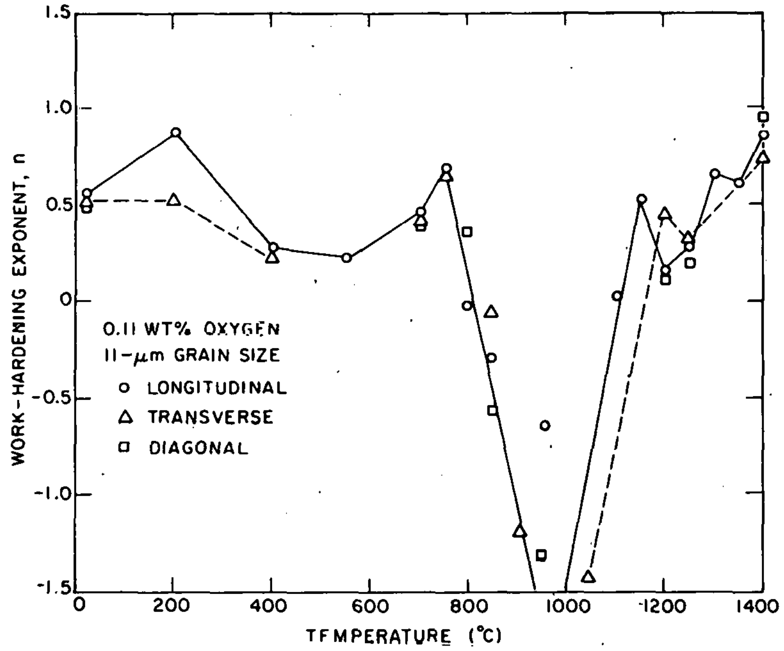

Fig. III.6

Work-hardening Exponent as a Function of Temperature for Zircaloy-4 Specimens with Three Textures. ANL Neg. No. 306-77-78 Rev. 1.

4. Fine-grain Zircaloy-4

Figure III.7 shows the total strain of 5-µm grain-size specimens as a function of deformation temperature at three initial strain rates. Near 400°C, an elongation minimum exists that is associated with dynamic strain-aging effects. The results for the fine-grain Zircaloy-4 in Fig. III.7 are similar to those for the 11-µm grain-size Zircaloy-4 in Fig. III.2.

The work-hardening characteristics of fine-grain Zircaloy at three strain rates are presented in Fig. III.8 and Tables III.1-III.3. Similar to the 11-µm grain-size material, the work-hardening exponent is positive below 600°C and negative over the interval ~700-1000°C.

5. Work-hardening Analysis of Transformed β-phase Zircaloy-4

Figure III.9 presents the results of a work-hardening analysis of transformed β-phase Zircaloy-4 specimens with four types of structures. The work-hardening exponent shows a maximum value between 200 and 400°C, due to dynamic strain aging, and negative values with a minimum between 700 and 900°C, due to intergranular deformation. Figure III.10 shows the influence of strain rate on the temperature dependence of the work-hardening exponent of the basketweave structure of Zircaloy-4.

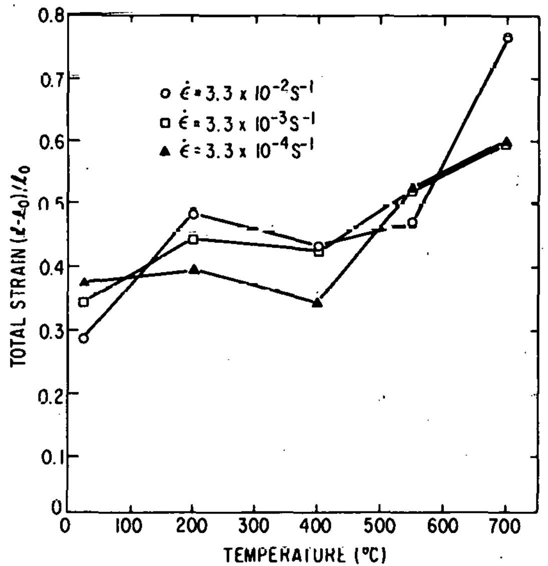

Fig. III.7. Total Strain as a Function of Temperature for 5-µm Grain-size Zircaloy-4 Specimens at Three Strain Rates over Temperature Interval 23-700°C. ANL Neg. No. 306-77-58 Rev. 1.

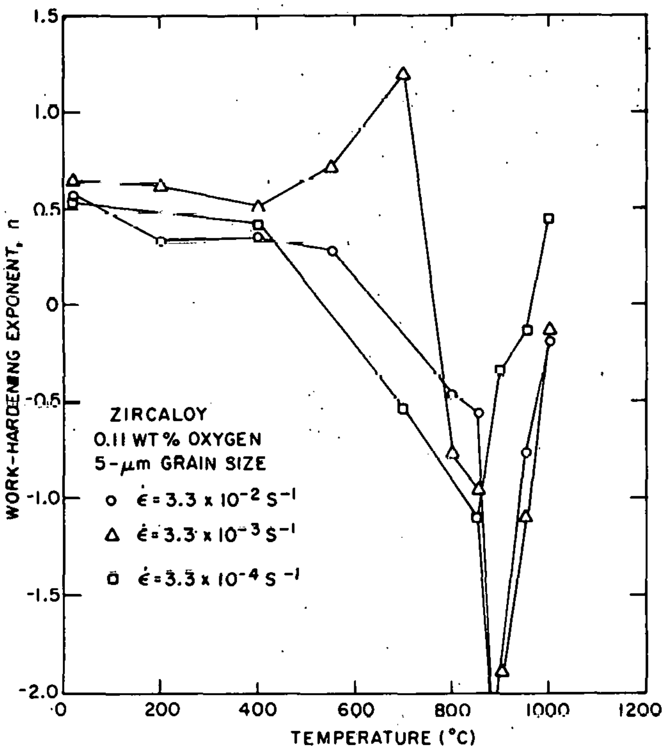

Fig. III.8. Work-hardening Exponent of Fine Grain-size Zircaloy-4 as a Function of Temperature at Three Strain Rates. ANL Neg. No. 306-77-59 Rev. 1.

TABLE III.1. Least-squares Work-hardening Constants for Deformation Stages of 5-μm Grain-size Zircaloy-4, $\dot{\epsilon}$ = 3.3 x 10^{-2} s^{-1}

Temp., °C	Stage Number	Strain Interval	n	k, Pa	Average σ_o, Pa
25	2	0.0004-0.09	0.57	5.2 x 10^8	4.2 x 10^8
200	2	0.0002-0.13	0.34	2.8 x 10^8	1.8 x 10^8
400	2	0.02-0.17	0.36	2.5 x 10^8	1.2 x 10^8
550	2	0.013-0.15	0.28	1.7 x 10^8	8.3 x 10^7
800	2	0.0004-0.0016	-0.46	-2.1 x 10^5	6.5 x 10^7
850	2	0.0004-0.005	-0.57	-9.4 x 10^4	4.5 x 10^7
900	1	0.0004-0.002	0.04	5.9 x 10^7	-1.2 x 10^7
	2	0.0024-0.004	-3.30	-9.8 x 10^{-4}	3.4 x 10^7
950	2	0.0004-0.0012	-0.76	-5.1 x 10^3	2.4 x 10^7
1000	1	0.0004-0.0016	-0.19	-4.4 x 10^4	8.6 x 10^6
1050	1	0.0004-0.0032	1.00	2.5 x 10^8	5.1 x 10^6
	2	0.004-0.011	-1.20	-5.3 x 10^2	6.2 x 10^6
	3	0.012-0.09	0.73	5.7 x 10^6	5.8 x 10^6

TABLE III.2. Least-squares Work-hardening Constants for Deformation Stages of 5-μm Grain-size Zircaloy-4, $\dot{\epsilon}$ = 3.3 x 10^{-3} s^{-1}

Temp., °C	Stage Number	Strain Interval	n	k, Pa	Average σ_o, Pa
25	1	0.0004-0.004	0.41	3.6 x 10^8	3.8 x 10^8
	2	0.005-0.15	0.64	5.6 x 10^8	4.0 x 10^8
200	2	0.025-0.25	0.62	5.0 x 10^8	2.0 x 10^8
400	2	0.015-0.19	0.50	3.0 x 10^8	1.3 x 10^8
550	1	0.0004-0.0032	-0.32	-1.5 x 10^6	1.3 x 10^8
	2	0.0036-0.13	0.72	1.6 x 10^8	1.2 x 10^8
700	2	0.012-0.05	1.20	9.8 x 10^7	5.3 x 10^7
800	2	0.0004-0.002	-0.77	-7.4 x 10^3	3.9 x 10^7
850	2	0.0004-0.0024	-0.96	-2.0 x 10^3	2.6 x 10^7
900	2	0.0004-0.004	0.34	3.2 x 10^7	1.3 x 10^7
950	2	0.005-0.012	-1.90	-3.4 x 10^1	1.8 x 10^7
1000	2	0.0004-0.0024	-0.13	-1.6 x 10^5	4.9 x 10^6
1050	1	0.0004-0.0032	-0.42	-6.9 x 10^3	3.4 x 10^6
	2	0.0036-0.05	0.92	3.3 x 10^6	3.3 x 10^6
1100	1	0.0004-0.012	0.01	5.8 x 10^6	-2.7 x 10^6
	2	0.013-0.07	0.94	4.1 x 10^6	2.8 x 10^6

TABLE III.3. Least-squares Work-hardening Constants for Deformation Stages of 5-μm Grain-size Zircaloy-4, $\dot{\varepsilon} = 3.3 \times 10^{-4}\ s^{-1}$

Temp., °C	Stage Number	Strain Interval	n	k, Pa	Average σ_o, Pa
25	2	0.011-0.13	0.53	5.2×10^{8}	3.4×10^{8}
200	2	0.025-0.15	∼0	1.6×10^{10}	-1.5×10^{10}
400	2	0.013-0.15	0.41	2.7×10^{8}	1.3×10^{8}
700	2	0.0004-0.0028	-0.54	-4.3×10^{4}	4.8×10^{7}
800	1	0.0004-0.006	-0.23	-3.6×10^{5}	2.2×10^{7}
850	1	0.0004-0.002	0.55	1.1×10^{8}	7.5×10^{6}
	2	0.0024-0.013	-1.10	-1.5×10^{3}	1.3×10^{7}
900	1	0.0004-0.0024	0.81	1.4×10^{8}	2.6×10^{6}
	2	0.0028-0.09	-0.16	-2.3×10^{6}	9.9×10^{6}
950	1	0.0004-0.045	-0.11	-1.8×10^{6}	7.6×10^{6}
1000	1	0.0004-0.002	-0.35	-9.8×10^{3}	2.4×10^{6}
	2	0.0024-0.007	0.47	9.6×10^{5}	2.3×10^{6}
1050	1	0.0004-0.004	0.63	1.6×10^{6}	1.8×10^{6}
1100	1	0.0004-0.004	0.56	8.2×10^{6}	1.1×10^{6}
	2	0.005-0.07	-0.03	-4.7×10^{6}	7.0×10^{6}

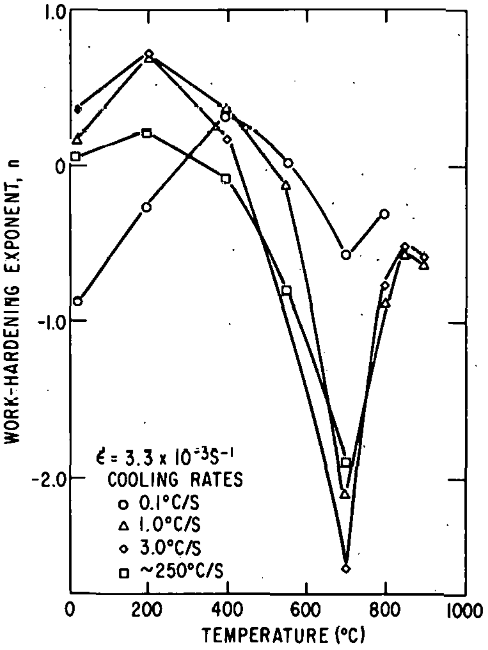

Fig. III.9

Temperature Dependence of Work-hardening Exponent of Various Transformed β-phase Zircaloy-4 Structures. ANL Neg. No. 306-77-50 Rev. 1.

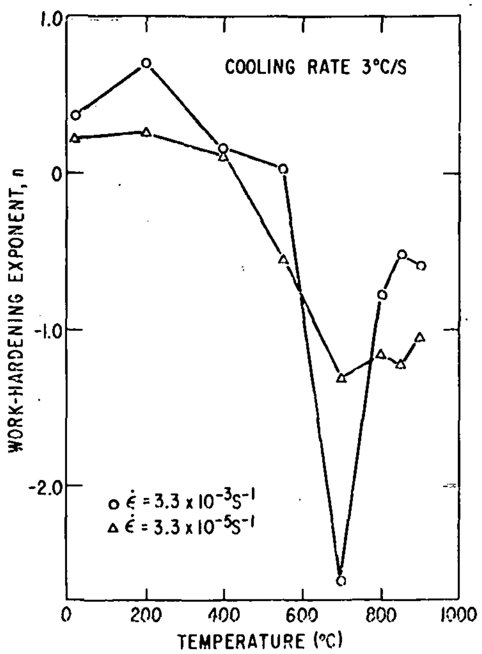

Fig. III.10

Work-hardening Exponent of Basketweave Structure of Zircaloy-4 as a Function of Temperature at Two Strain Rates. ANL Neg. No. 306-77-51 Rev. 1.

6. Relationship between Work-hardening Rate and Dynamic Strain Aging

As reported in Ref. 4, manifestations of dynamic strain aging such as yield points and serrated stress-strain curves are observed in Zircaloy near 700°C.

The work-hardening analysis of Zircaloy specimens deformed at 700°C and at various strain rates is presented in Fig. III.11 and Tables III.4-III.6. The yield-point effect was significant at strain rates $> 10^{-3}$ s^{-1}, where the work-hardening exponent had positive values. At strain rates $< 10^{-3}$ s^{-1}, the work-hardening exponent, in general, had lower values (often negative) and the yield-point behavior was absent. Thus, dynamic-strain-aging behavior is associated with peak values of the work-hardening exponent.

Fig. III.11

Strain-rate Dependence of Work-hardening Exponent of Zircaloy at 700°C. ANL Neg. No. 306-77-66.

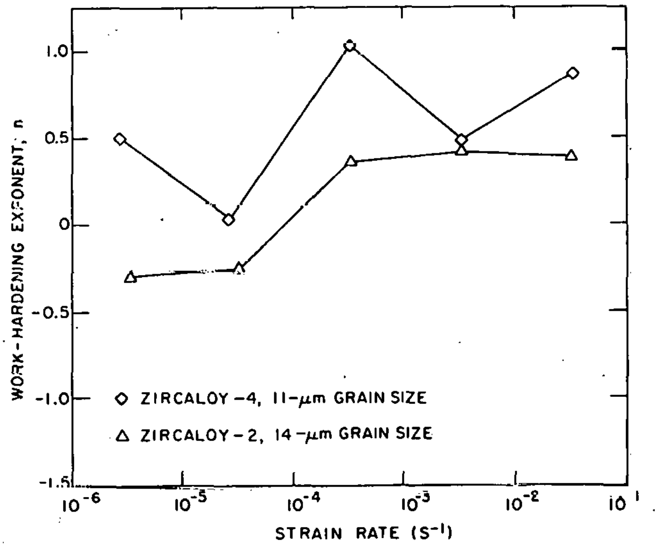

TABLE III.4. Least-squares Work-hardening Constants of Longitudinal Zircaloy-2 Specimens Deformed at 700°C and Various Strain Rates

Strain Rate $\dot{\varepsilon}$, s^{-1}	Stage Number	Strain Interval	n	k, Pa	Average σ_o, Pa
3.3×10^{-2}	2	0.013-0.05	0.38	4.5×10^{7}	6.6×10^{7}
3.3×10^{-3}	2	0.007-0.05	0.41	3.1×10^{7}	4.8×10^{7}
3.3×10^{-4}	2	0.0028-0.035	0.35	3.1×10^{7}	3.5×10^{7}
3.3×10^{-5}	2	0.0004-0.014	-0.25	-1.2×10^{6}	3.2×10^{7}
3.3×10^{-6}	2	0.0004-0.02	-0.30	-3.8×10^{5}	2.1×10^{7}

TABLE III.5. Least-squares Work-hardening Constants for 5-μm Grain-size Zircaloy-4 Specimens Deformed at 700°C and Various Strain Rates

Strain Rate $\dot{\varepsilon}$, s^{-1}	Stage Number	Strain Interval	n	k, Pa	Average σ_o, Pa
3.3×10^{-2}	2	0.03-0.05	0.79	5.2×10^{7}	7.2×10^{7}
3.3×10^{-3}	2	0.012-0.05	1.20	9.8×10^{7}	5.3×10^{7}
3.3×10^{-4}	1	0.0004-0.006	-0.67	-8.6×10^{3}	3.9×10^{7}
	2	0.007-0.025	1.25	8.9×10^{7}	3.8×10^{7}
	3	0.03-0.05	0.58	2.3×10^{7}	3.6×10^{7}

TABLE III.6. Least-squares Work-hardening Constants for 11-μm Grain-size Zircaloy-4 Specimens Deformed at 700°C and Various Strain Rates

Strain Rate $\dot{\varepsilon}$, s^{-1}	Stage Number	Strain Interval	n	k, Pa	Average σ_o, Pa
3.3×10^{-2}	2	0.0004-0.05	0.86	8.1×10^{7}	6.8×10^{7}
3.3×10^{-3}	2	0.006-0.05	0.46	3.2×10^{7}	4.3×10^{7}
3.3×10^{-4}	1	0.0004-0.002	-0.53	-3.2×10^{4}	3.2×10^{7}
	2	0.002-0.013	1.03	2.7×10^{8}	3.1×10^{7}
	3	0.013-0.045	-0.24	-3.6×10^{6}	4.4×10^{7}
2.6×10^{-5}	2	0.0004-0.04	-0.04	-2.2×10^{7}	5.6×10^{7}
3.3×10^{-6}	1	0.0004-0.004	-0.63	-1.7×10^{4}	1.6×10^{7}
	2	0.005-0.07	0.50	1.0×10^{7}	1.4×10^{7}

Figure III.12 represents engineering stress-strain curves of Zircaloy-4 specimens deformed at 750°C after various heat treatments. The stress-strain curve that corresponds to 0.16-h hold time at 750°C prior to deformation (curve A) shows a load drop only at the start of plastic deformation (yield point). Subsequently, no load drops or serrations occur. Curve B represents the stress-strain behavior during final loading of a specimen that was prestrained to 0.02 at 750°C, unloaded, and held for 4 h at 750°C prior to restraining at 750°C. Note that the stress-strain curve is smooth with no load drops and the yield point is absent.

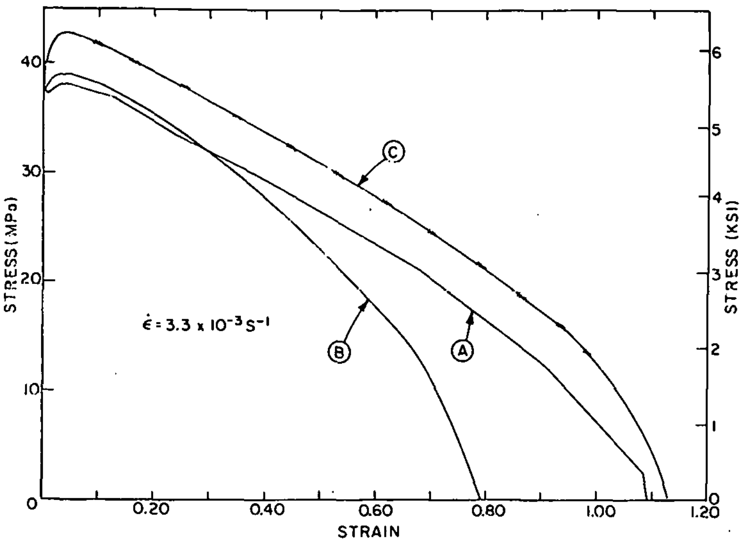

Fig. III.12. Engineering-stress/Engineering-strain Curves for Zircaloy-4 at 750°C after Various Heat Treatments. ANL Neg. No. 306-77-75.

Curve C corresponds to a specimen that was prestrained to 0.02 at 750°C, unloaded, and annealed for 4 h at 800°C, and then deformed at 750°C. Note that curve C shows a higher flow-stress level than the other two specimens and load drops at regular intervals throughout the curve (serrations). This difference in the stress-strain behavior is related to the difference in the work-hardening characteristics presented in Table III.7. All specimens were held for 0.16 h prior to deformation at the prestraining or restraining temperature. Specimens prestrained and heated to 800°C show larger positive n values, which is indicative of dynamic strain aging. The strain-rate sensitivity does not appear to depend on the heat treatment (Fig. III.13). The heat-treatment designation is the same as in Fig. III.12.

7. Correlation between Superplasticity and Work-hardening Rate

Results presented in Refs. 4-6 clearly demonstrate the significance of superplasticity in the tensile deformation of Zircaloy near 850°C.

The influence of strain rate and grain size on the work-hardening characteristics of Zircaloy at 850°C is presented in Fig. III.14 and Tables III.8-III.10. These results, together with the ductility data presented in earlier reports,[4,6] show that superplasticity is associated with a minimum value of the work-hardening exponent that occurs at intermediate strain rates (10^{-4} to 10^{-3} s^{-1}). At higher strain rates ($> 10^{-2}$ s^{-1}), the work-hardening exponent is larger due to transgranular deformation, and superplasticity is less significant. At lower strain rates ($< 10^{-4}$ s^{-1}), although grain-boundary sliding is

TABLE III.7. Least-squares Work-hardening Constants for 11-μm Grain-size Zircaloy-4 Specimens Deformed at 750°C after Various Heat Treatments, $\dot{\varepsilon}$ = 3.3 x 10^{-3} s^{-1}

Stage Number	Strain Interval	n	k, Pa	Average σ_0, Pa	Comment[a]
2	0.008-0.035	0.68	2.8 x 10^7	3.7 x 10^7	A
2	0.0004-0.03	0.05	2.8 x 10^7	2.4 x 10^7	B
2	0.013-0.04	0.08	2.5 x 10^7	2.4 x 10^7	C
2	0.0004-0.04	-0.07	-1.7 x 10^7	6.2 x 10^7	D
2	0.0004-0.045	0.08	3.1 x 10^7	1.9 x 10^7	E
2	0.0004-0.04	0.11	3.0 x 10^7	2.3 x 10^7	F
2	0.0004-0.04	0.19	2.1 x 10^7	3.3 x 10^7	G
2	0.009-0.04	0.46	3.1 x 10^7	4.7 x 10^7	H
2	0.009-0.035	0.49	3.2 x 10^7	6.0 x 10^7	I

[a] A = As-received.
B = 0.02 prestrain at 750°C, unload and immediately reload.
C = 4-h hold time at 750°C prior to deformation.
D = 0.02 prestrain at 750°C, unload, 4-h hold at 750°C.
E = 0.02 prestrain at 750°C, unload, 0.33-h hold at 800°C.
F = 0.02 prestrain at 750°C, unload, 4-h hold at 800°C.
G = 0.02 prestrain at 750°C, unload, 0.16-h hold at 800°C.
H = Equiaxed homogeneous α-phase containing 0.46 wt % oxygen.
I = Equiaxed homogeneous α-phase containing 0.90 wt % oxygen.

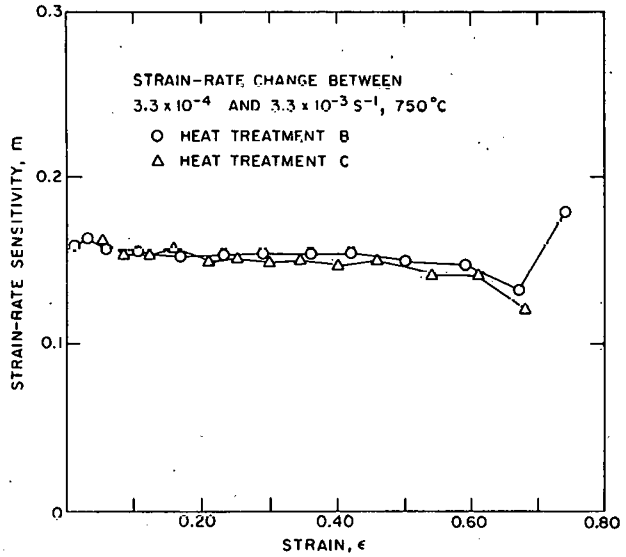

Fig. III.13. Strain Dependence of Strain-rate Sensitivity of Zircaloy-4 at 750°C after Two Heat Treatments. ANL Neg. No. 306-77-76 Rev. 1.

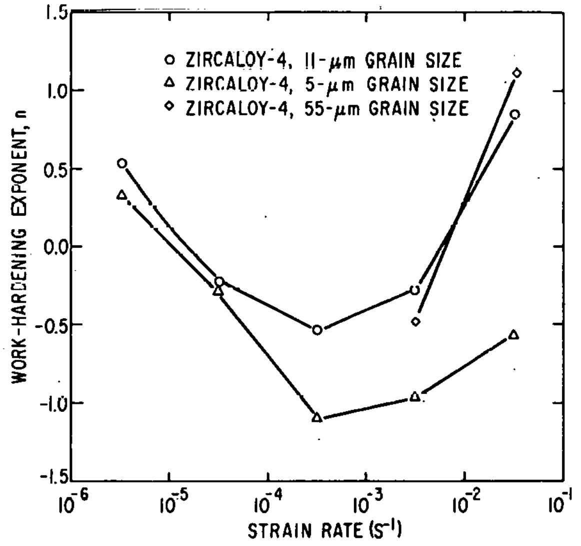

Fig. III.14. Strain-rate Dependence of Work-hardening Exponent of Zircaloy-4 at 850°C. ANL Neg. No. 306-77-79 Rev. 1.

TABLE III.8. Least-squares Work-hardening Constants for 5-μm Grain-size Zircaloy-4 Specimens Deformed at 850°C and Various Strain Rates

Strain Rate $\dot{\varepsilon}$, s^{-1}	**Stage Number**	**Strain Interval**	**n**	**k, Pa**	**Average σ_o, Pa**
3.3×10^{-2}	2	0.0004-0.005	-0.57	-9.4×10^{4}	4.5×10^{7}
3.3×10^{-3}	2	0.0004-0.0024	-0.96	-2.0×10^{3}	2.6×10^{7}
3.3×10^{-4}	1	0.0004-0.002	0.55	1.1×10^{8}	7.5×10^{6}
	2	0.0024-0.013	-1.10	-1.5×10^{3}	1.3×10^{7}
3.3×10^{-5}	1	0.0004-0.006	0.90	1.1×10^{8}	3.3×10^{6}
	2	0.007-0.09	-0.26	-6.1×10^{5}	6.7×10^{6}
3.3×10^{-6}	1	0.0004-0.0032	0.82	1.2×10^{8}	1.0×10^{6}
	2	0.0036-0.13	0.32	2.0×10^{2}	1.4×10^{7}
3.3×10^{-6}	1	0.0004-0.014	0.05	6.9×10^{6}	-2.4×10^{6}
	2	0.015-0.37	0.99	7.8×10^{6}	3.1×10^{6}

TABLE III.9. Least-squares Work-hardening Constants for 11-μm Grain-size Zircaloy-4 Specimens Deformed at 850°C and Various Strain Rates

Strain Rate $\dot{\varepsilon}$, s^{-1}	**Stage Number**	**Strain Interval**	**n**	**k, Pa**	**Average σ_o, Pa**
3.3×10^{-2}	2	0.0004-0.009	0.85	4.7×10^{8}	2.9×10^{7}
	3	0.01-0.035	-0.83	-1.3×10^{5}	4.4×10^{7}
3.3×10^{-3}	1	0.0004-0.0012	0.70	3.5×10^{8}	1.9×10^{7}
	2	0.0016-0.03	-0.27	-1.2×10^{6}	2.9×10^{7}
3.3×10^{-4}	1	0.0004-0.0016	0.55	1.0×10^{8}	8.3×10^{6}
	2	0.002-0.025	-0.52	-1.1×10^{5}	1.5×10^{7}
2.6×10^{-5}	2	0.0004-0.015	-0.23	-5.3×10^{5}	8.4×10^{6}
3.3×10^{-6}	2	0.0004-0.39	0.53	5.8×10^{6}	1.1×10^{6}

TABLE III.10. Least-squares Work-hardening Constants for 55-μm Grain-size Zircaloy-4 Deformed at 850°C and Several Strain Rates

Strain Rate $\dot{\varepsilon}$, s^{-1}	**Stage Number**	**Strain Interval**	**n**	**k, Pa**	**Average σ_o, Pa**
3.3×10^{-2}	1	0.0004-0.0028	-0.88	-5.3×10^{3}	3.8×10^{7}
	2	0.0032-0.035	1.10	1.2×10^{8}	3.8×10^{7}
3.3×10^{-3}	1	0.0004-0.004	0.89	3.0×10^{8}	2.0×10^{7}
	2	0.004-0.025	-0.48	-3.0×10^{5}	2.7×10^{7}

significant, extensive grain growth due to the substantial test times gives rise to hardening, and superplasticity is less significant. An optimum combination of grain-boundary sliding and stable equiaxed-grain structure is obtained at intermediate strain rates, where superplasticity is predominant.

C. Mechanical Properties of Zircaloy-Oxygen Alloys

1. Homogeneous Oxygen Distribution

a. Beta-phase Zircaloy-2

Scoping tests were conducted to investigate the effect of oxygen on the properties of β Zircaloy-2 at 1300 and 1400°C. Figure III.15 shows the oxygen-concentration dependence of uniform and total strain of β Zircaloy at 1300 and 1400°C and a strain rate of 3.3×10^{-3} s^{-1}. Near 0.35% oxygen concentration, the uniform strain shows a minimum and the total strain shows a maximum. The oxygen concentration dependence of the yield stress and UTS is presented in Fig. III.16. The significant grain growth observed at 1300 and 1400°C may be responsible for the complex nature of data presented in Figs. III.15 and III.16. Similar data for a lower strain rate of 3.3×10^{-4} s^{-1} are shown in Fig. III.17. In general, the data indicate that oxygen increases the yield stress and UTS and decreases total and uniform strains.

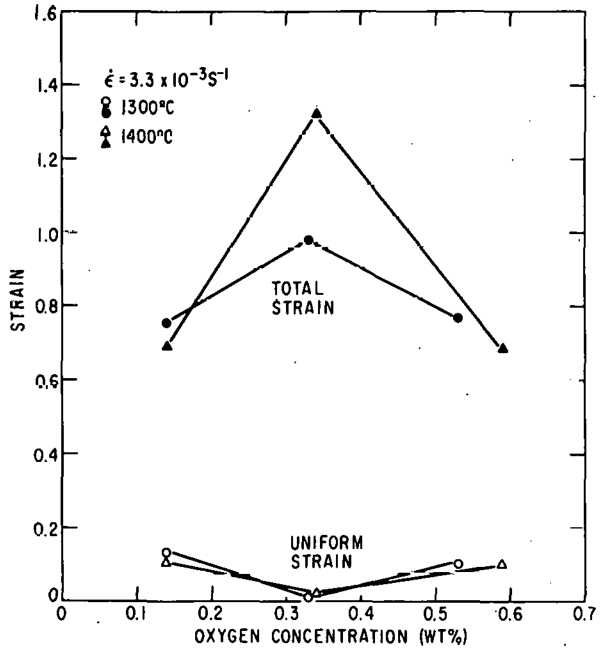

Fig. III.15

Uniform and Total Strain as a Function of Oxygen Concentration for Zircaloy-2 Specimens at 1300 and 1400°C. ANL Neg. No. 306-77-64 Rev. 1.

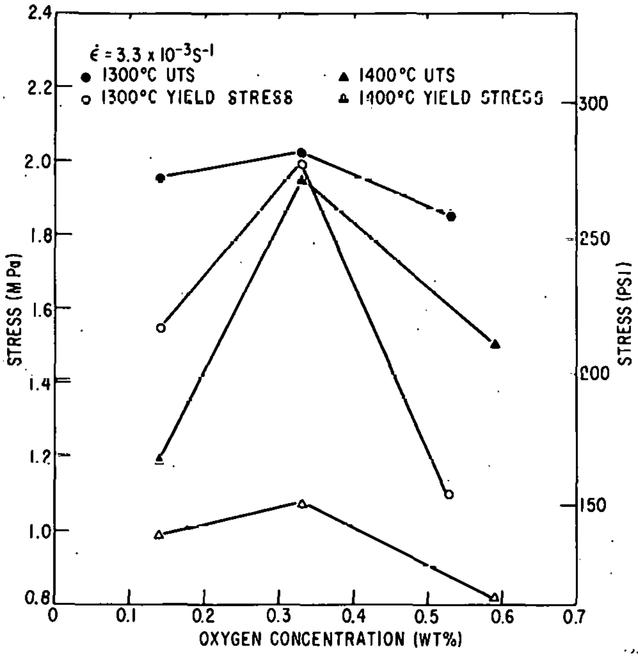

Fig. III 16

Oxygen-concentration Dependence of Yield Stress and UTS of Zircaloy-2 at 1300 and 1400°C. ANL Neg. No. 306-77-63 Rev. 1.

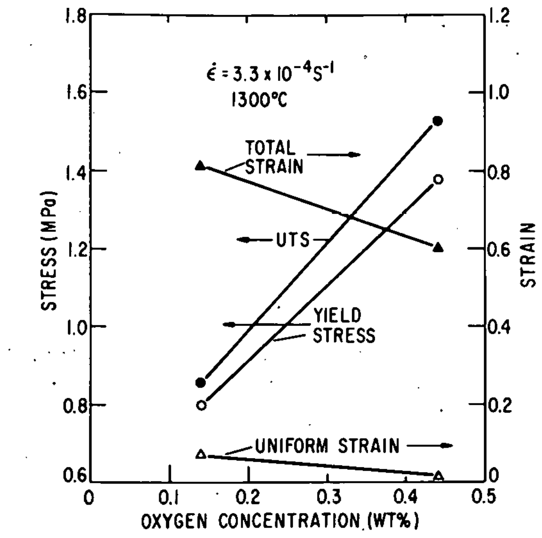

Fig. III.17

Total Strain, Uniform Strain, Yield Stress, and UTS of Zircaloy-2 at 1300°C as a Function of Oxygen Concentration. ANL Neg. No. 306-77-69 Rev. 1.

b. Alpha-phase Zircaloy-4

The effect of oxygen concentration (homogeneous oxygen distribution) in α-phase Zircaloy-4 on the UTS is shown in Fig. III.18. Oxygen increases the UTS of α-Zircaloy-4 monotonically. Similar behavior is also observed in (α + β) Zircaloy-4 at higher temperatures.[3] Figure III.19 exhibits the oxygen concentration dependence of uniform strain of the α-phase Zircaloy-4. An increase in the oxygen concentration produces a decrease in the uniform strain. The trend at higher temperatures is opposite, i.e., the uniform strain of (α + β) Zircaloy-4 increases as the oxygen concentration

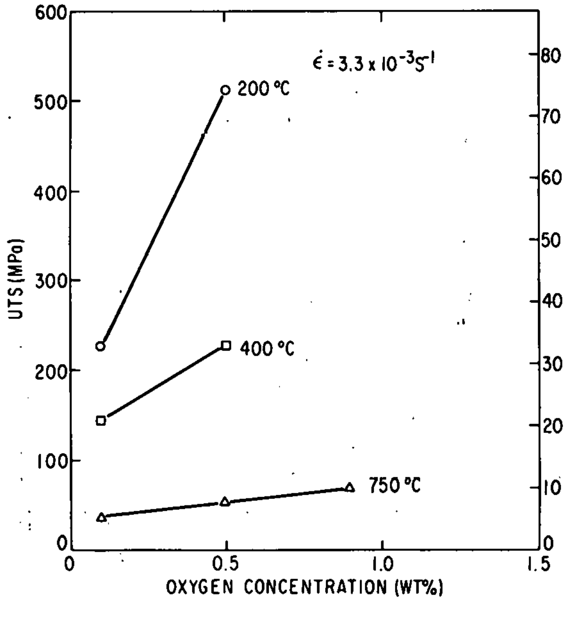

Fig. III.18

Effect of Oxygen on UTS of Zircaloy-4 at Several Temperatures between 200 and 750°C. ANL Neg. No. 306-77-62 Rev. 1.

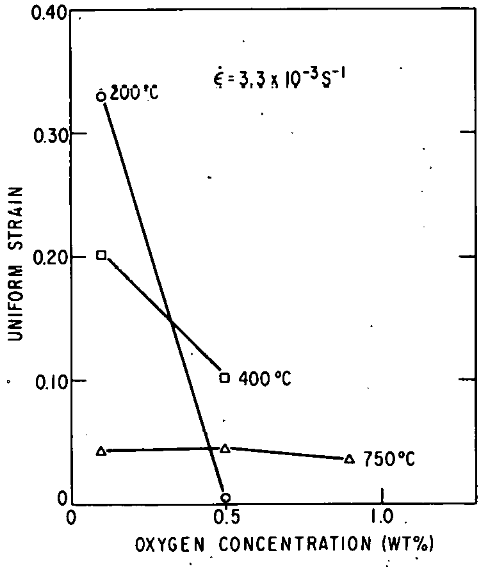

Fig. III.19

Oxygen-concentration Dependence of Uniform Strain of Zircaloy-4 at 200, 400, and 750°C. ANL Neg. No. 306-77-61 Rev. 1.

increases.[3] Figure III.20 shows the influence of oxygen on the total strain of Zircaloy-4. When the oxygen concentration increases, the ductility of α-phase Zircaloy-4 decreases.

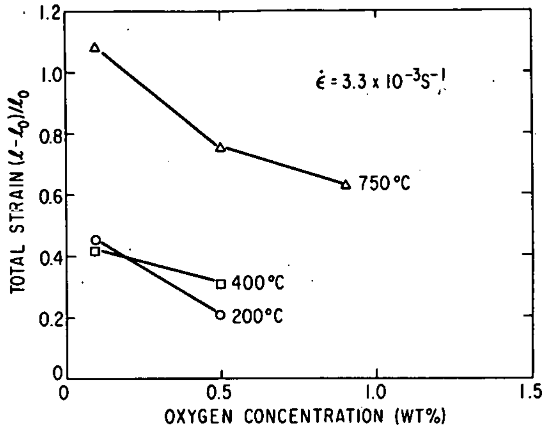

Fig. III.20

Total Strain of Zircaloy-4 as a Function of Oxygen Concentration at 200, 400, and 750°C. ANL Neg. No. 306-77-80 Rev. 1.

c. Beta-phase Zircaloy-4

The effect of oxygen on the work-hardening behavior of Zircaloy-4 is shown in Figs. III.21-III.26. The data in these figures refer to specimens that were cooled through the two-phase region after charging and/or

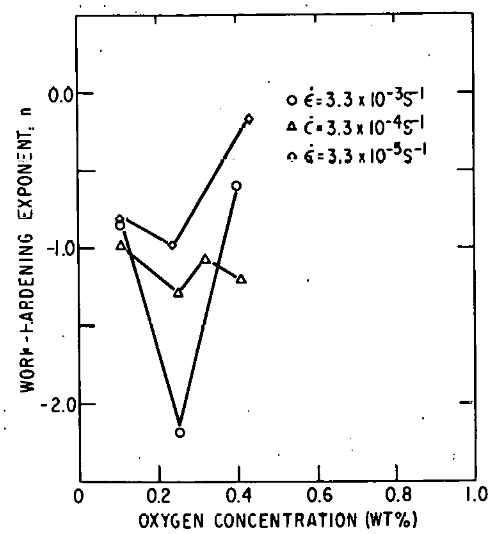

Fig. III.21

Work-hardening Exponent of Zircaloy-4 at 1000°C as a Function of Oxygen Concentration. ANL Neg. No. 306-77-60 Rev. 1.

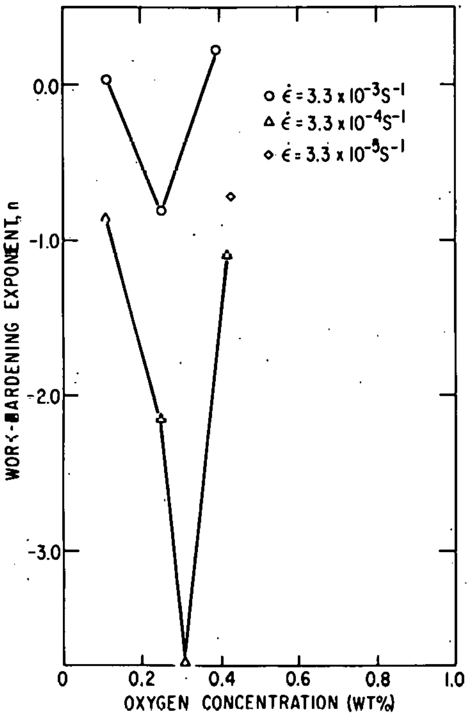

Fig. III.22

Oxygen-concentration Dependence of Work-hardening Exponent of Zircaloy-4 at 1100°C. ANL Neg. No. 306-77-55 Rev. 1.

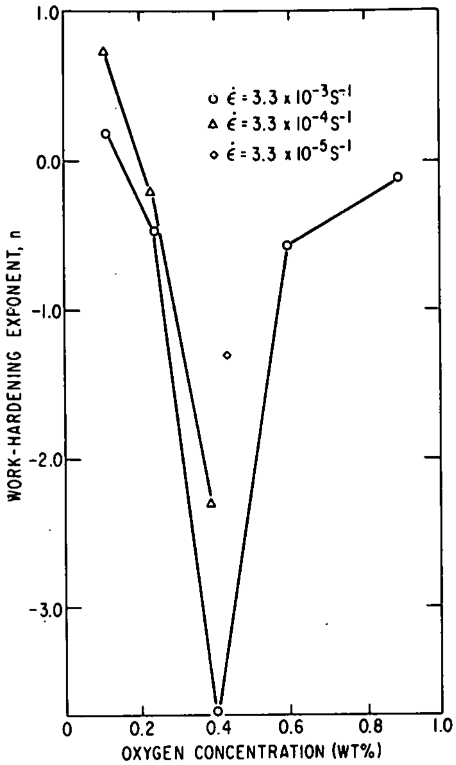

Fig. III.23

Effect of Oxygen Concentration on Work-hardening Exponent of Zircaloy-4 at 1200°C. ANL Neg. No. 306-77-56 Rev. 1.

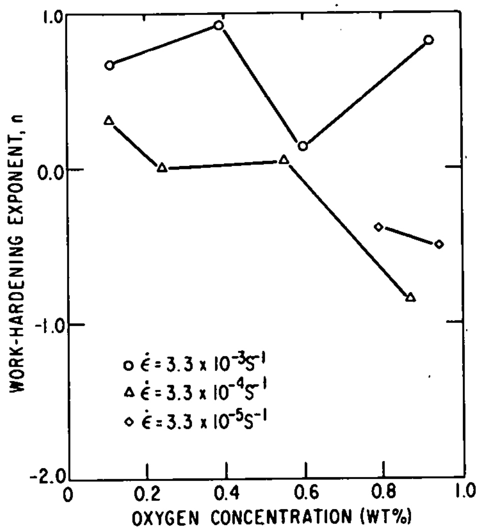

Fig. III.24

Variation of Work-hardening Exponent of Zircaloy-4 at 1300°C with Oxygen Concentration. ANL Neg. No. 306-77-68 Rev. 1.

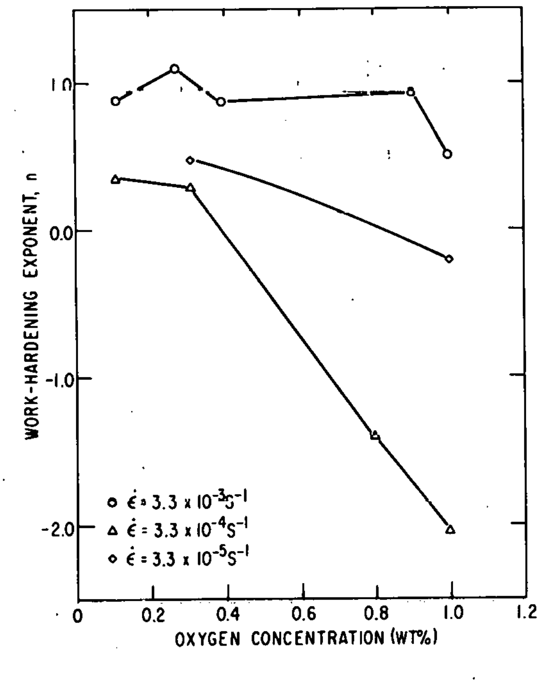

Fig. III.25

Work-hardening Exponent of Zircaloy-4 at 1400°C as a Function of Oxygen Concentration. ANL Neg. No. 306-77-53 Rev. 1.

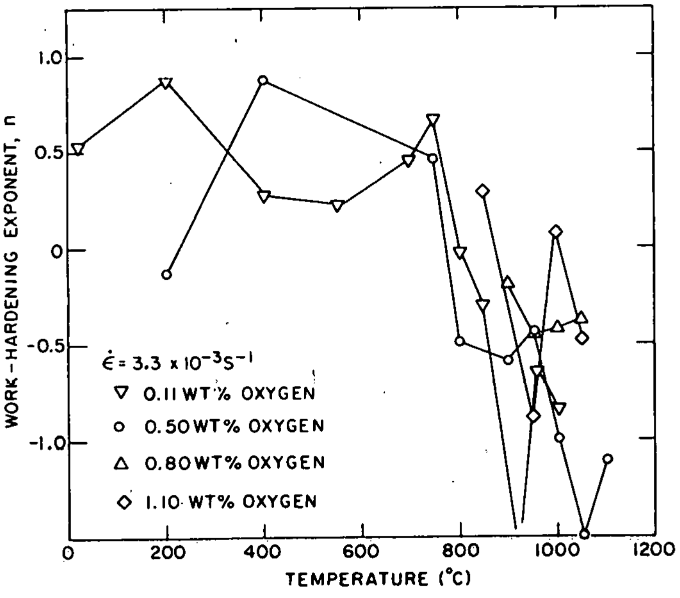

Fig. III.26

Temperature Dependence of Work-hardening Exponent of Zircaloy-4 with Several Oxygen Concentrations. ANL Neg. No. 306-77-77 Rev. 1.

homogenization anneal prior to the mechanical testing. Therefore, these specimens contained transformed β-phase nonequiaxed grains in which various degrees of oxygen (and probably other alloying elements) redistribution occurred.

The influence of oxygen on the work-hardening rate of Zircaloy depends on the microstructure of the alloy. Considering the Zircaloy-oxygen phase diagram[2] at a constant temperature above 1000°C, an increase in the oxygen concentration of the as-received Zircaloy-4 changes the microstructure of the alloy from β to $(\alpha + \beta)$. The data reported in Ref. 6 indicate that small additions of oxygen increase the work-hardening rate of β-phase Zircaloy for alloy compositions that are not close to the two-phase boundary. Near the two-phase boundary, the work-hardening rate shows a minimum (negative value of n).

Data in Figs. III.21 III.23 show a minimum value of n at intermediate oxygen concentrations, and the oxygen concentration at which the minimum occurs increases as the temperature increases from 1000 to 1200°C. In Figs. III.24 and III.25, the minimum is not readily apparent, since the oxygen-concentration range for the alloys is not near the $\beta/(\alpha + \beta)$ phase boundary at 1300 and 1400°C. With a higher work-hardening rate, the criteria for maximum load point on the load-elongation curve $d\sigma/d\epsilon = \sigma$ is satisfied at higher strain. Therefore, the previously observed[6] uniform strain behavior is consistent with Figs. III.23-III.25.

The influence of strain rate on the work-hardening rate is complicated by the concomitant grain growth that occurs during deformation. At slower strain rates, the grain-boundary-sliding component is expected to be more significant, and this may lead to a lower work-hardening rate. However, longer testing times associated with lower strain rates lead to significant grain growth and result in higher work-hardening rates. These two opposing factors operate to varying degrees and result in a complicated behavior. The data in Fig. III.26 refer to specimens that were oxygen-charged and homogenized in the α-phase region and therefore had an equiaxed grain structure at the start of deformation. Consistent with the phase diagram, the region of negative work-hardening exponent shifts to higher temperatures as the oxygen concentration increases.

2. Composite Specimens with Nonuniform Oxygen Distribution

Zircaloy-4 tensile specimens were oxidized in oxygen at reduced pressure under the following conditions: 700°C, 720 s; 800°C, 720 s; 800°C, 2700 s; and 900°C, 900 s; this resulted in total oxygen contents of ~0.4, 0.8, 1.1, and 1.9 wt %, respectively, in the specimens. The microstructures of the composite specimens showed significant differences for deformation temperatures above and below ~1000°C. In specimens deformed below ~1000°C, both the oxide and α layer showed significant cracking (Fig. III.27). In specimens deformed above ~1000°C, the oxide layer, in general, was absent and the α layer did not show cracking (Fig. III.28).

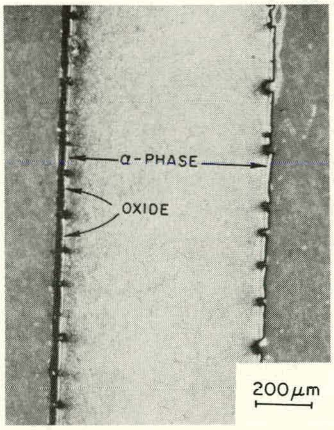

Fig. III.27

Microstructure of Zircaloy-4/Oxide Composite Specimen Deformed at 800°C, Showing Cracks in Oxide and α Layers. ANL Neg. No. 306-77-89 Rev. 1.

Fig. III.28

Microstructure of Zircaloy-4/Oxide Composite Specimen Deformed at 1100°C, Showing No Cracks in α Layer. ANL Neg. No. 306-77-88 Rev. 1.

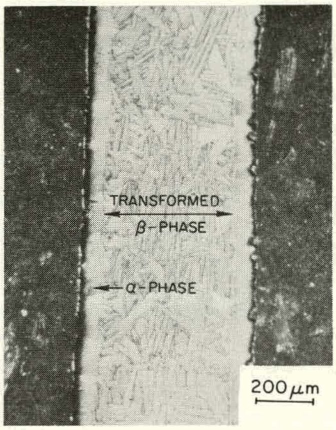

Figures III.29 and III.30 show the effect of total oxygen concentration in the composite on the yield stress, UTS, uniform strain, and total strain, respectively. Below 900°C, the yield stress (Fig. III.29) and UTS (Fig. III.30) are not sensitive to oxygen concentration. This is the result of two compensating factors. As the oxygen concentration increases, the oxide-layer thickness increases. This layer cracks during deformation and therefore the load-bearing area decreases.

On the other hand, the diffusion of oxygen into the material increases its strength. Above 950°C, both the yield stress and UTS increase as the oxygen concentration increases, since the α layer on the β phase does not crack significantly and it also carries some of the load. The effect of oxygen on the uniform strain is complicated (Fig. III.31), but, in general, oxygen decreases the uniform strain. As shown in Fig. III.32, oxygen also decreases the total strain of composites.

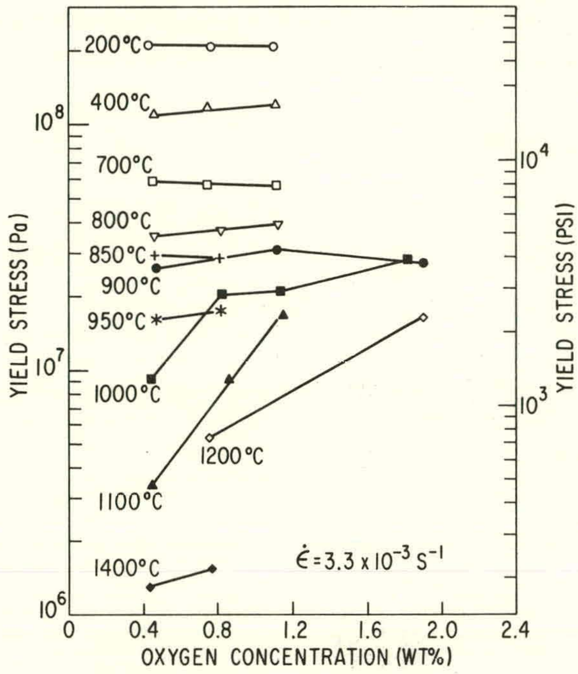

Fig. III.29

Oxygen-concentration Dependence of Yield Stress of Zircaloy-4/Oxide Composites at Several Temperatures. ANL Neg. No. 306-77-57 Rev. 1.

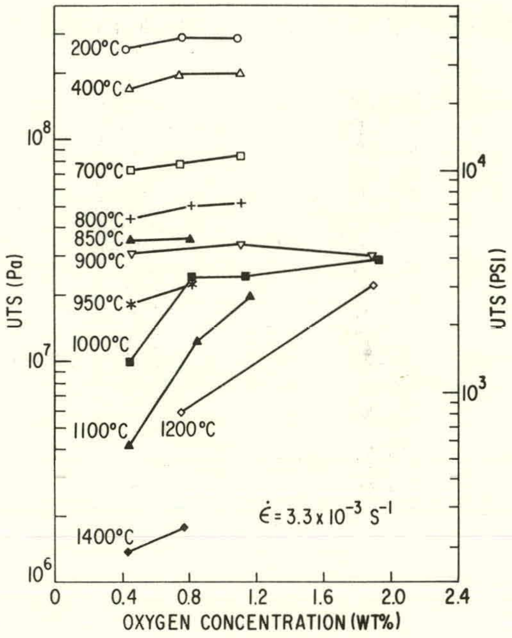

Fig. III.30

Ultimate Tensile Strength of Zircaloy-4/Oxide Composites as a Function of Oxygen Concentration at Several Temperatures. ANL Neg. No. 306-77-70 Rev. 1.

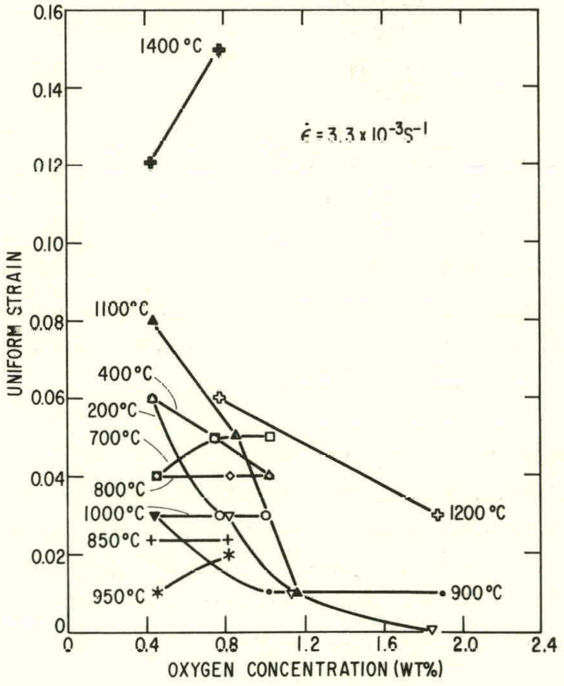

Fig. III.31

Effect of Oxygen Concentration on Uniform Strain of Zircaloy-4/Oxide Composites at Several Temperatures. ANL Neg. No. 306-77-52 Rev. 1.

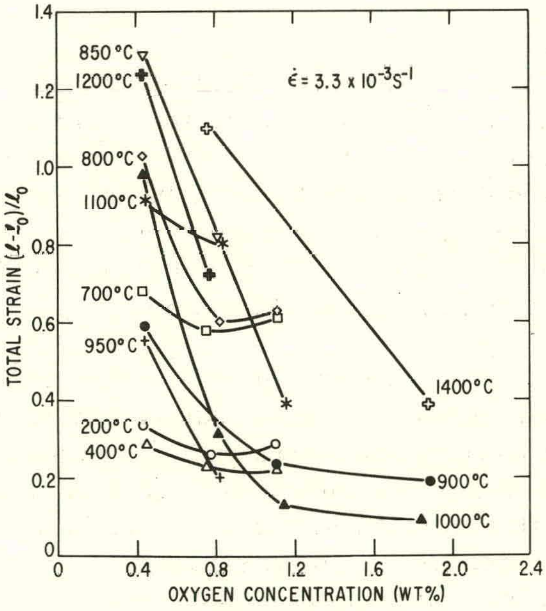

Fig. III.32

Variation of Total Strain of Zircaloy-4/Oxide Composites with Oxygen Concentration at Several Temperatures. ANL Neg. No. 306-77-72 Rev. 1.

The influence of oxygen on the work-hardening rate of composites is shown in Fig. III.33 and Table III.11. In general, oxygen decreases the

TABLE III.11. Least-squares Work-hardening Constants for Zircaloy-4 Oxide Composite Specimens, $\dot{\epsilon} = 3.3 \times 10^{-3}\ s^{-1}$

Temp., °C	Oxygen Concentration, wt %	Stage Number	Strain Interval	n	k, Pa	Average σ_0, Pa
200	0.43	2	0.008-0.02	0.87	1.3×10^9	2.0×10^8
		3	0.025-0.045	-1.40	-1.3×10^5	2.8×10^8
	0.77	2	0.0004-0.025	0.51	7.3×10^8	1.8×10^8
	1.10	2	0.0004-0.025	0.39	5.7×10^8	1.6×10^8
400	0.45	1	0.0004-0.0016	0.12	7.3×10^7	7.5×10^7
		2	0.002-0.015	1.10	3.2×10^9	1.1×10^8
		3	0.02-0.05	-1.40	-1.2×10^5	1.9×10^8
	0.75	2	0.0004-0.013	0.83	2.1×10^9	1.0×10^8
		3	0.014-0.04	-0.88	-1.4×10^6	2.3×10^8
	1.11	2	0.0004-0.011	0.41	7.4×10^8	6.5×10^7
700	0.45	2	0.008-0.04	-0.09	-6.2×10^7	1.6×10^8
	0.75	1	0.0004-0.008	0.55	2.8×10^8	4.9×10^7
		2	0.009-0.045	-0.36	-4.8×10^6	9.6×10^7
	1.12	1	0.0004-0.011	0.28	1.6×10^8	2.8×10^7
		2	0.012-0.045	-0.66	-1.2×10^6	9.7×10^7
800	0.45	2	0.0004-0.04	-0.05	-4.7×10^7	1.0×10^8
	0.82	2	0.0004-0.04	-0.09	-3.4×10^7	9.7×10^7
	1.12	1	0.0004-0.012	0.36	9.6×10^7	2.9×10^7
		2	0.013-0.035	-0.96	-9.6×10^4	5.5×10^7
850	0.45	2	0.0004-0.025	-0.23	-3.2×10^6	4.3×10^7
	0.81	2	0.0004-0.02	-0.12	-1.3×10^7	5.8×10^7
900	0.45	2	0.0004-0.025	-0.41	-6.6×10^5	3.5×10^7
	1.11	1	0.0004-0.007	-0.17	-4.6×10^6	4.4×10^7
		2	0.008-0.012	-2.50	-3.9×10^0	3.4×10^7
	1.89	1	0.0004-0.0012	0.36	1.5×10^8	1.2×10^7
		2	0.0012-0.004	-0.67	-7.7×10^4	3.2×10^7
		3	0.004-0.008	-2.50	-8.4×10^{-1}	3.0×10^7
950	0.45	1	0.0004-0.006	-0.42	-3.7×10^5	2.1×10^7
		2	0.007-0.013	-0.10	-2.4×10^6	2.2×10^7
	0.82	1	0.0004-0.0024	0.69	5.2×10^8	1.0×10^7
		2	0.0024-0.009	-0.71	-8.4×10^4	2.4×10^7
		3	0.009-0.015	-1.90	-1.4×10^2	2.3×10^7
1000	0.44	2	0.0004-0.03	-0.38	-1.5×10^5	1.1×10^7
	0.82	1	0.0004-0.0024	0.34	7.1×10^7	1.1×10^7
		2	0.0028-0.025	-0.59	-1.4×10^5	2.6×10^7
	1.14	2	0.0004-0.008	-0.25	-2.2×10^6	3.1×10^7
	1.84	2	0.0004-0.0036	-0.87	-4.7×10^3	2.9×10^7
1100	0.44	2	0.0004-0.07	0.05	7.4×10^6	-2.1×10^6
	0.85	1	0.0004-0.004	0.90	2.7×10^8	8.2×10^6
		2	0.005-0.05	-0.45	-3.1×10^5	1.4×10^7
	1.16	2	0.0004-0.012	-0.54	-1.3×10^5	2.1×10^7
1200	0.76	2	0.0004-0.05	-0.20	-5.3×10^5	7.1×10^6
	1.88	1	0.0004-0.0028	0.73	8.6×10^8	6.2×10^6
		2	0.0032-0.025	-1.10	-4.8×10^3	2.2×10^7
1400	0.43	2	0.0004-0.11	0.89	1.8×10^6	1.3×10^6
	0.77	1	0.0004-0.0028	-0.71	-1.1×10^3	1.6×10^6
		2	0.0032-0.11	0.50	1.6×10^6	1.5×10^6

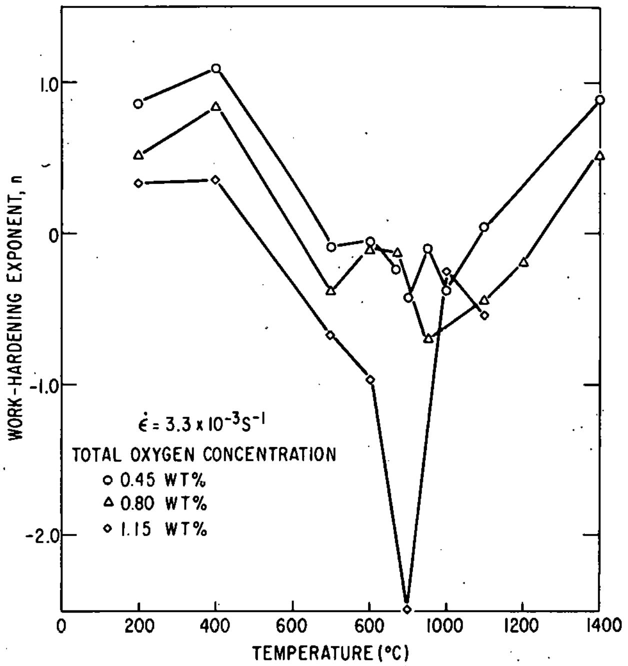

Fig. III.33

Temperature Dependence of Work-hardening Exponent of Zircaloy-4/Oxide Composites with Several Oxygen Concentrations. ANL Neg. No. 306-77-71 Rev. 1.

work-hardening rate of the major deformation stage. This observation is consistent with the data in Fig. III.31, which tend to show smaller uniform strains as the oxygen concentration increases.

D. Biaxial Deformation and Rupture Characteristics of Zircaloy-4 Cladding

During the present reporting period, the effect of circumferential temperature variations on the maximum circumferential strain of Zircaloy cladding was investigated at several heating rates. A radial strain-localization parameter was defined and evaluated from measurements of the cladding thickness at several positions along the circumference of the tube in the region of maximum circumferential strain. This parameter was used to correlate quantitatively the circumferential strain at failure with the circumferential temperature variation around the tube. Transient-heating tube-burst tests were also performed on longer lengths of Zircaloy cladding to determine whether this variable had a significant effect on deformation behavior.

1. Effect of Specimen Length on Rupture Characteristics of Zircaloy-4 Cladding

Results reported previously[4] on the deformation and rupture characteristics of 153-mm-long cladding at temperatures in the α-phase region (~800°C) indicated that axial contraction and bending of the tube occurred during the ballooning stage. To determine whether the specimen length had any effect on the deformation characteristics, several tube-burst experiments were performed on 300-mm-long tubes in vacuum and steam at heating rates of 5, 45, and 115°C/s. Figures III.34 and III.35 compare the circumferential strains as a function of burst temperature in vacuum and steam, respectively, for several of the 300-mm-long tubes with curves based on numerous tests with the 153-mm sample length. These results confirm the generally accepted criterion that, under otherwise identical conditions, the specimen length has no significant effect[7] on the tube-burst properties if the length-to-diameter ratio of the tube is >10.

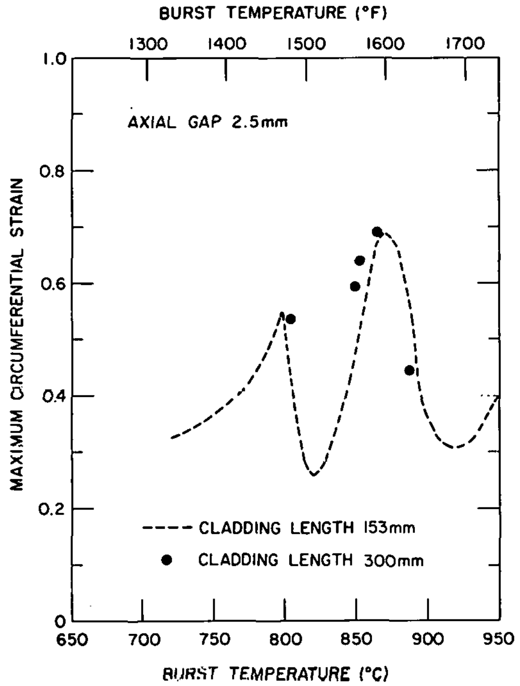

Fig. III.34

Comparison of Maximum Circumferential Strain vs Burst Temperature for 153- and 300-mm-long Axially Constrained Cladding at Heating Rate of 115°C/s In Vacuo. ANL Neg. No. 306-77-145.

2. Burst Characteristics of Zircaloy-4 Cladding Axially Constrained by Al_2O_3 Pellets

To investigate the effect of circumferential temperature variations in the cladding on the deformation behavior, the alumina rod, used to simulate the fuel column, was replaced by a stack of 10-mm-long high-purity recrystallized Al_2O_3 pellets. The average diametral gap between the cladding and the pellets was 0.075 mm, and the axial gap between the top of the pellet stack and the end plug was 2.5 mm, as for most of the tests with the alumina rod. As a result of the asymmetrical position of the pellets with respect to the inner-diameter surface of the cladding (Fig. III.36), large local temperature variations in the circumferential and axial directions developed in the cladding during the transient-heating tube-burst experiments.

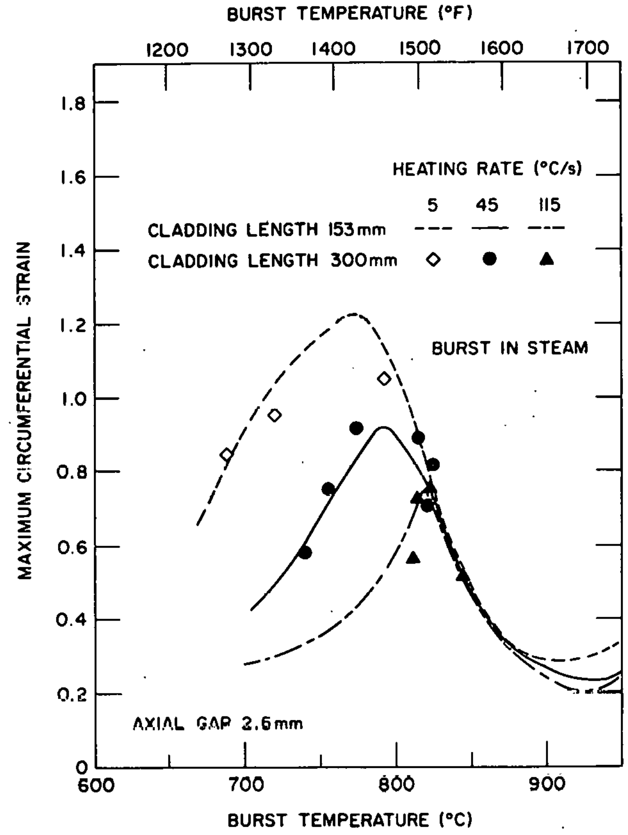

Fig. III.35

Comparison of Maximum Circumferential Strain vs Burst Temperature for 153- and 300-mm-long Axially Constrained Cladding at Heating Rates of 5, 55, and 115°C/s in Steam. ANL Neg. No. 306-77-149.

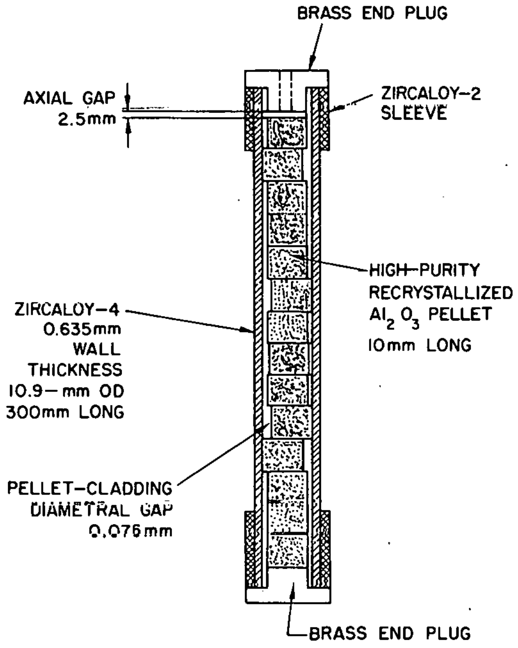

Fig. III.36

Schematic Diagram of Cladding Tube Containing Alumina Pellets. ANL Neg. No. 306-77-150.

Typical localized "hot" and "cold" spots on a cladding tube during the later stages of a burst test are shown in Fig. III.37 along with thermocouple locations in the vicinity of the burst region. Figure III.38 shows the temperature-time and pressure-time information from this test as well as the point at which the photograph in Fig. III.37 was taken. The maximum temperature difference between thermocouples 7 and 11 at the moment of burst was ~150°C. Because of the nonuniformity in the temperature, highly nonsymmetric ballooning and bending of the specimens was commonly observed in specimens that contained Al_2O_3 pellets (Fig. III.39).

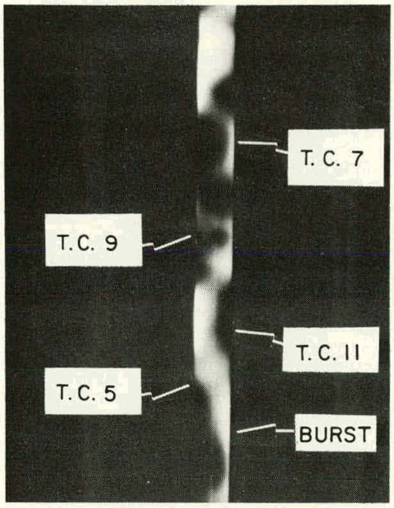

Fig. III.37

Nonuniform Brightness of Cladding Specimen Containing Al_2O_3 Pellets due to Axial and Circumferential Temperature Variations during Heating at 45°C/s. ANL Neg. No. 306-77-135.

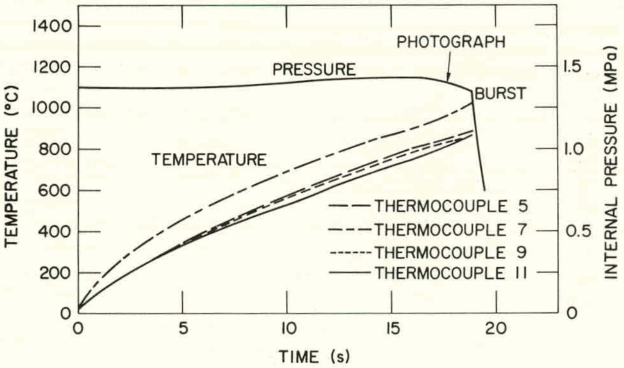

Fig. III.38

Temperature and Internal Pressure as a Function of Time for Cladding Specimen Described in Fig. III.37. ANL Neg. No. 306-77-141.

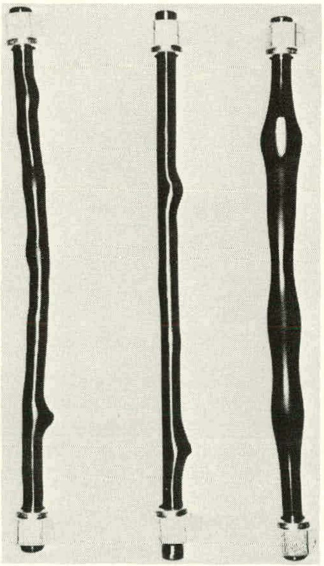

Fig. III.39

Cladding Constrained by Pellets after Burst. Multiple ballooning regions and irregular bends are a result of temperature nonuniformity. ANL Neg. No 306-77-134.

Since oxidation of the Zircaloy is not an important parameter in the deformation behavior of cladding that bursts in the α-, or predominantly α-phase region ($\lesssim$850°C), the temperature nonuniformity becomes the major factor in the localization of the strain. When compared with the previous results,[4,5,8] in which more uniform heating was achieved, plastic instability occurs at an earlier stage of ballooning and the circumferential strain is considerably smaller. Figures III.40-III.42 compare the maximum circumferential strain as a function of burst temperature in steam for Zircaloy cladding with the same degree of axial constraint that was produced by the alumina mandrel and pellet stack (2.5-mm gap). The data points for the tubes constrained by the pellets, in these figures, correspond to the maximum temperature, and the bars associated with each point represent the range of temperatures obtained from the four or five thermocouples in each test.

Except for the 5°C/s heating-rate data in Fig. III.40, the circumferential strain at failure is significantly lower for the tubes constrained by pellets at burst temperatures $\lesssim$850°C; i.e., the strain does not exceed a value of 0.4 for all cases. Within the uncertainty of the temperature measurements

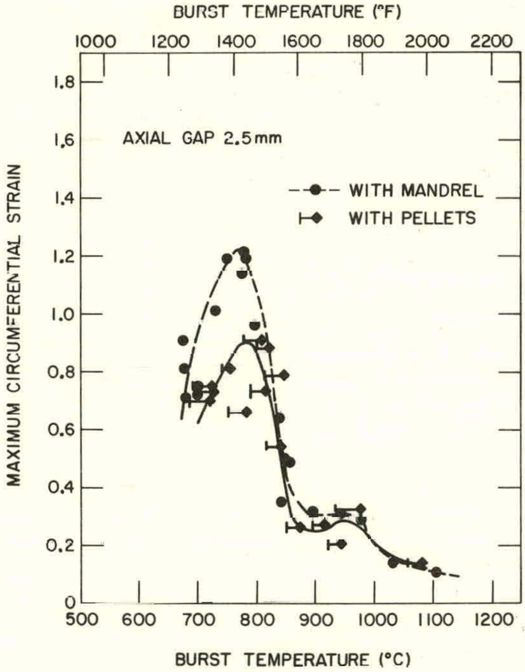

Fig. III.40

Maximum Circumferential Strain vs Maximum Burst Temperature in Steam at Heating Rate of 5°C/s for Cladding Constrained by Pellets. Maximum recorded temperature difference for each test is shown by a bar. Similar results for mandrel-constrained cladding are also shown for comparison. ANL Neg. No. 306-77-152.

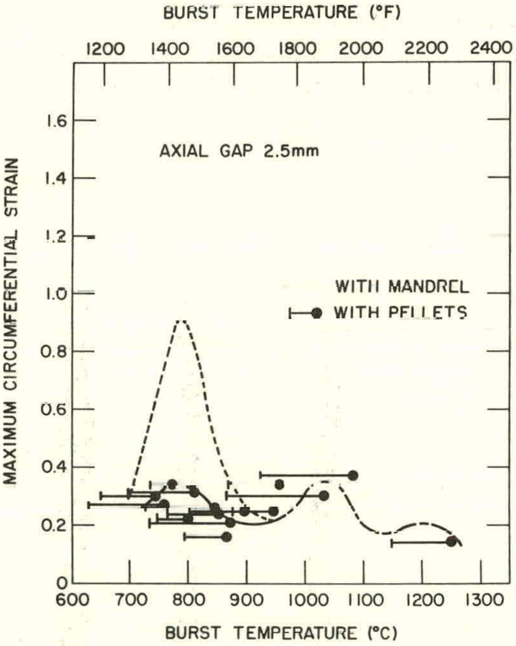

Fig. III.41

Maximum Circumferential Strain vs Maximum Burst Temperature in Steam at Heating Rate of 45°C/s for Cladding Constrained by Pellets. Maximum recorded temperature differences are shown by bars. Similar results for mandrel-constrained cladding are also shown for comparison. ANL Neg. No. 306-77-155.

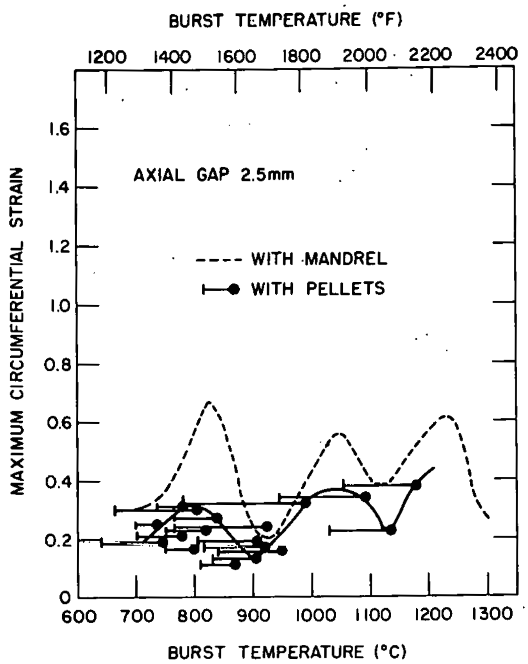

Fig. III.42

Maximum Circumferential Strain vs Maximum Burst Temperature in Steam at Heating Rate of 115°C/s for Cladding Constrained by Pellets. Maximum recorded temperature differences are shown by bars. Similar results for mandrel-constrained cladding are also shown for comparison. ANL Neg. No. 306-77-151.

in these experiments, the general features of the strain-burst temperature relationships obtained with the mandrel-constrained tubes are evident at the three heating rates.

Figures III.43-III.45 show the relationships between the maximum circumferential strain and the initial pressure, at different heating rates, for unconstrained cladding and for tubes axially constrained by the alumina mandrel and the pellet stack. The curves for the cladding constrained by the

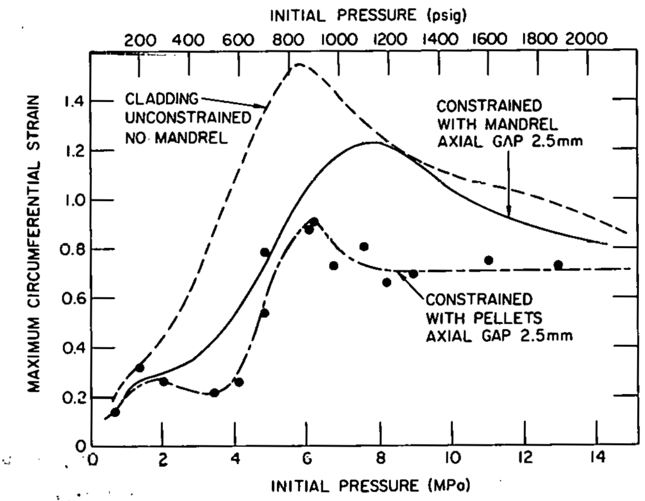

Fig. III.43

Comparison of Maximum Circumferential Strain vs Initial Internal Pressure for Unconstrained Mandrel- and Pellet-constrained Cladding at Heating Rate of 5°C/s in Steam. ANL Neg. No. 306-77-157.

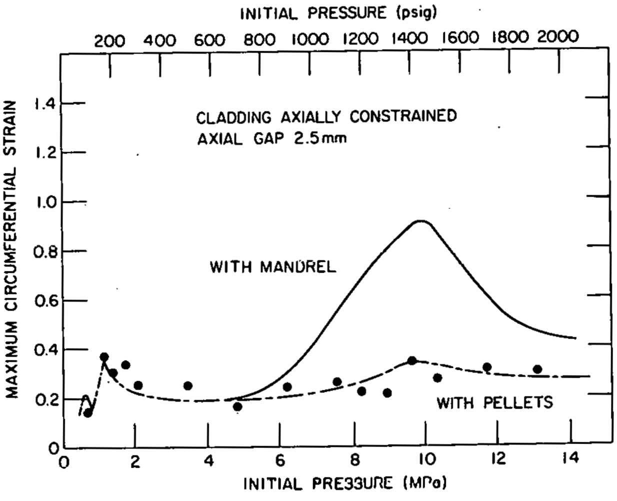

Fig. III.44

Comparison of Maximum Circumferential Strain vs Initial Internal Pressure for Mandrel- and Pellet-constrained Cladding at Heating Rate of 45°C/s in Steam. ANL Neg. No. 306-77-147.

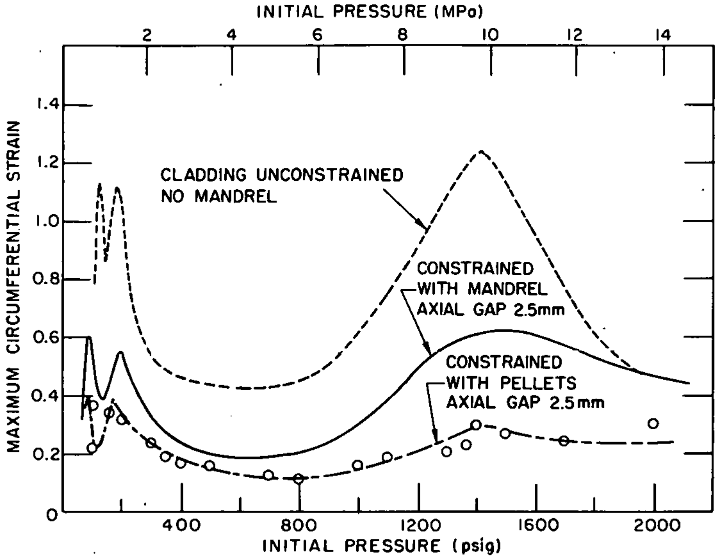

Fig. III.45

Comparison of Maximum Circumferential Strain vs Initial Internal Pressure for Unconstrained and Mandrel- and Pellet-constrained Cladding at Heating Rate of 115°C/s in Steam. ANL Neg. No. 306-77-153.

alumina pellets were used to generate the three-dimensional plot of the circumferential strain as functions of the initial pressure and heating rate shown in Fig. III.46. Similar results for mandrel-constrained tubes in steam and vacuum environments were reported in Ref. 8.

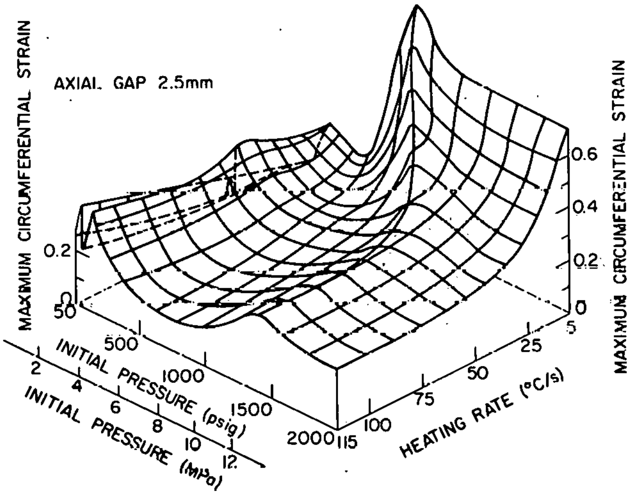

Fig. III.46

Effect of Initial Internal Pressure and Heating Rate in Steam on Maximum Circumferential Strain for Zircaloy-4 Cladding Constrained by Pellets. ANL Neg. No. 306-77-139.

3. Analysis of Local Fracture Strain and Development of a Strain-localization Parameter

In Ref. 5, the failure mode of Zircaloy cladding was classified in terms of a "rupture"- or "fracture"-type failure. The fracture edge of the former was sharp as a result of considerable thinning of the tube wall, whereas in the latter case, blunt edges characteristic of a shear process were typically observed. In a steam environment, "fracture"-type failures occurred invariably in α-phase material at temperatures $\lesssim$830°C and "rupture"-type failures were found at higher temperatures. Because of the blunt fracture edge, the local radial strain can be measured unambiguously in specimens that burst at the lower temperatures. The cross section at the location of maximum circumferential strain was examined for tubes that burst at temperatures ≤830°C under different combinations of heating rate, initial internal pressure, degree of axial constraint, cladding length, circumferential temperature nonuniformity, preoxidation, and test environment (i.e., vacuum or steam). The true local radial fracture strains were determined from thickness measurements at the fracture tips and the relation

$$e_r^0 = \ln(h_F/h_0), \tag{1}$$

where

e_r^0 = true fracture radial strain,

h_F = thickness of the fracture tip measured perpendicular to a centerline at the midwall position,

and

h_0 = initial undeformed cladding thickness.

The true fracture radial strain is plotted in Fig. III.47 as a function of the maximum temperature at burst for unconstrained and mandrel-constrained cladding at three heating rates in a steam environment. The results indicate that the radial strain decreases as the burst temperature increases (i.e., more wall thinning at the higher temperatures) and increases with heating rate. Figures III.48 and III.49 compare the fracture radial strain as a function of burst temperature for Zircaloy cladding constrained by the mandrel and the pellet stack at heating rates of 5 and ~55°C/s, respectively. At both heating rates, the radial strains for the pellet-constrained cladding

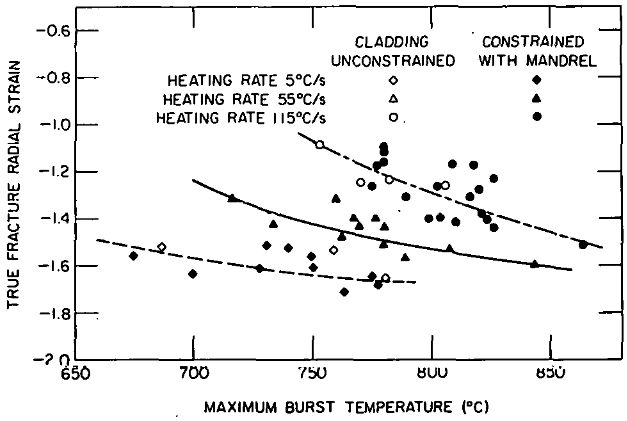

Fig. III.47

True Fracture Radial Strain vs Maximum Burst Temperature for Unconstrained and Mandrel-constrained Zircaloy-4 Cladding Burst in Steam at Heating Rates of 5, 55, and 115°C/s. For burst temperatures below ~850°C, the cladding is entirely or predominantly in the α phase. ANL Neg. No. 306-77-142.

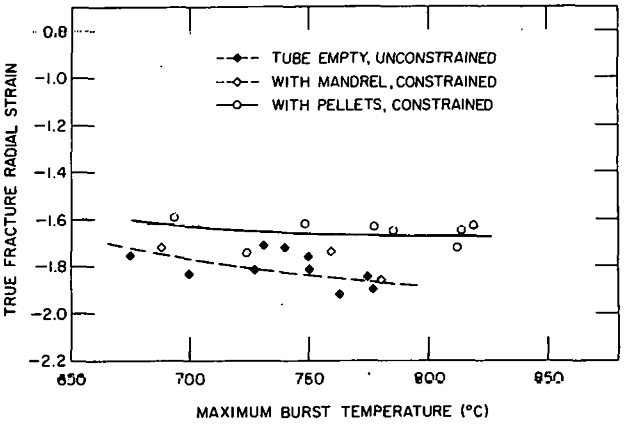

Fig. III.48

True Fracture Radial Strain vs Maximum Burst Temperature for Unconstrained and Mandrel- and Pellet-constrained Cladding Burst in Steam at Heating Rate of 5°C/s. ANL Neg. No. 306-77-158.

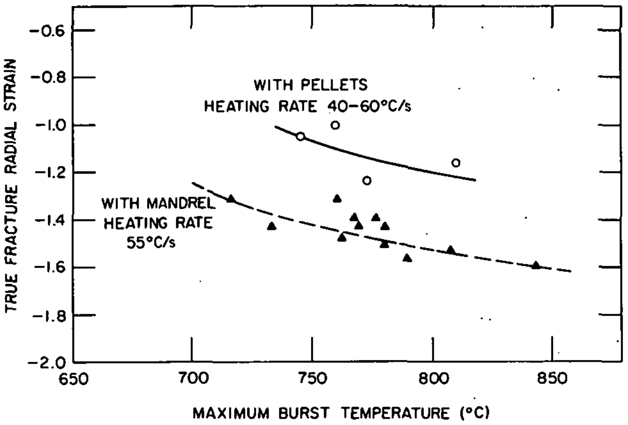

Fig. III.49

True Fracture Radial Strain vs Maximum Burst Temperature for Unconstrained and Mandrel- and Pellet-constrained Cladding Burst in Steam at Heating Rate of 40–60°C/s. ANL Neg. No. 306-77-146.

are higher (less thinning); this is a direct consequence of the more localized ballooning that occurs when the circumferential temperature variation is quite large. Since deformation is highly localized, the effective strain rate at the fracture tip is also greater than for the mandrel-constrained cladding.

Based on the results in Figs. III.40-III.42 and III.47-III.49, the radial strain at fracture can be correlated with the heating rate and the maximum circumferential temperature variation for the cladding at burst temperatures $\lesssim$830°C. Oxidation of the cladding is small at these temperatures during the transient-heating tests,[5] and differences in the amount of oxidation due to temperature variations are also quite small. It should therefore be possible to correlate the maximum circumferential strain with a quantitative measure of the extent of radial strain localization, such that the circumferential strain decreases as the radial strain becomes more localized.

For this purpose, a radial-strain-localization parameter W can be defined by

$$W = 1 - \frac{1}{2\pi} \int_0^{2\pi} \frac{e_r(\theta)}{e_r^0} d\theta, \tag{2}$$

where

θ = tangential angle from the fracture tip,

$e_r(\theta)$ = $\ln(h/h_0)$, i.e., the true local radial strain at different θ positions around the circumference of the cladding,

and

h = local thickness of the cladding cross section at the region of maximum circumferential strain.

Thus, the radial-strain-localization parameter can be calculated from measured values of the cladding thickness from each experiment. Figure III.50

shows micrographs of a cladding cross section and lists the e_r/e_r^0 values as a function of normalized angular position $\theta/2\pi$. It was assumed that

$$\theta/2\pi = \ell/L, \tag{3}$$

where

ℓ = distance from the fracture tip along the circumference of the tube,

and

L = outside circumference of the tube determined from the cross section.

The e_r/e_r^0 values, such as those shown in Fig. III.50, were plotted against $\theta/2\pi$ and integrated according to Eq. 2 with a planimeter. The results from several tubes are shown in Fig. III.51, where the shaded area for one of the experiments corresponds to the parameter W.

Figure III.52 is a plot of the maximum circumferential strain versus the parameter W for experiments that encompass a wide range of conditions such as heating rate, internal pressure, and degree of temperature

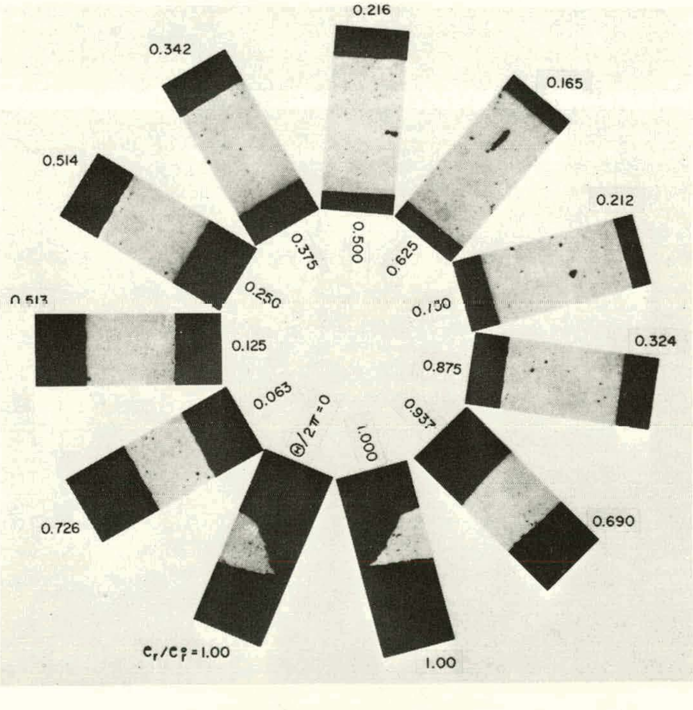

Fig. III.50. Calculation of Ratio of True Local Radial Strain to True Fracture Radial Strain at Different Tangential Angles in Cross Section of Maximum Circumferential Strain. ANL Neg. No. 306-77-133.

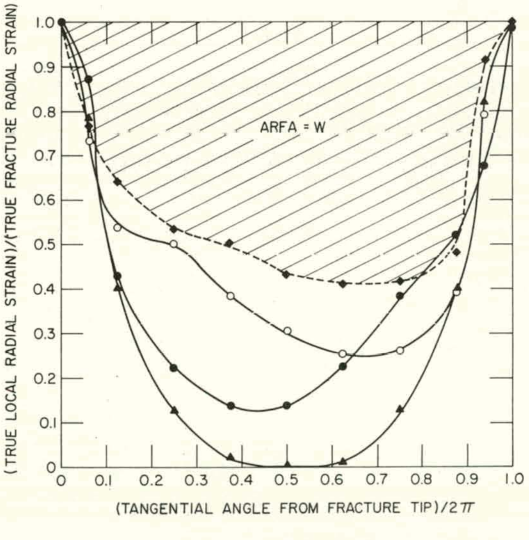

Fig. III.51. Method of Determining Radial-strain-localization Parameter W from Plots of Ratio of True Local Radial Strain to True Fracture Radial Strain as a Function of Normalized Tangential Angle. ANL Neg. No. 306-77-144.

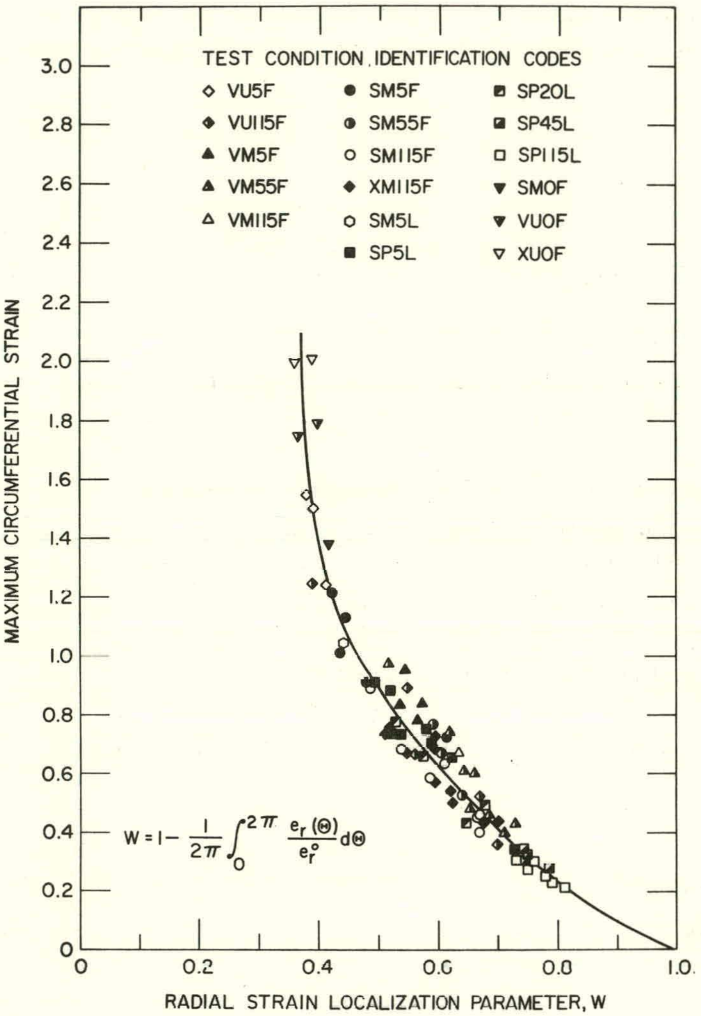

Fig. III.52

Maximum Circumferential Strain vs Radial-strain-localization Parameter for α-phase Cladding Burst under Different Test Conditions at Temperatures between 700 and 850°C. Test conditions can be identified from the following code abbreviations: V = vacuum environment, S = steam environment, X = preoxidized cladding in steam at a transient-heating rate of 115°C/s for 7 s and burst in vacuo, U = unconstrained cladding, M = mandrel-constrained cladding with a 2.5-mm axial gap, P = pellet-constrained cladding with a 2.5-mm axial gap, F = specimen length 153 mm, L = specimen length 300 mm, numerals denote the heating rate in °C/s, and 0 represents isothermal stress-rupture tests. ANL Neg. No. 306-77-143.

nonuniformity as well as other variables listed in the figure caption. A surprisingly good correlation between the circumferential strain and the radial-strain-localization parameter was obtained. For isothermal stress-rupture tests, the circumferential strain increases markedly as the W parameter decreases. It is expected that the theoretical limits for the curve in Fig. III.52 are

$$\lim_{W\to 0} \varepsilon_\theta^M = \infty, \tag{4}$$

and

$$\lim_{W\to 1.0} \varepsilon_\theta^M = 0, \tag{5}$$

where ε_θ^M is the maximum circumferential strain.

Figure III.53 shows the dependence of the W parameter on the maximum circumferential temperature difference ΔT_θ^M for pellet-constrained cladding in steam at four heating rates. The results in this figure are limited to experiments in which the burst temperature lies within ±25°C of the ~800°C strain peak (i.e., the maximum in the circumferential strain versus burst-temperature plot at ~800°C). Therefore, based on Figs. III.52 and III.53, we can predict, with reasonable accuracy, the maximum circumferential strain for burst temperatures near 800°C for pellet-constrained cladding in steam if the heating rate and temperature variation ΔT_θ^M are known.

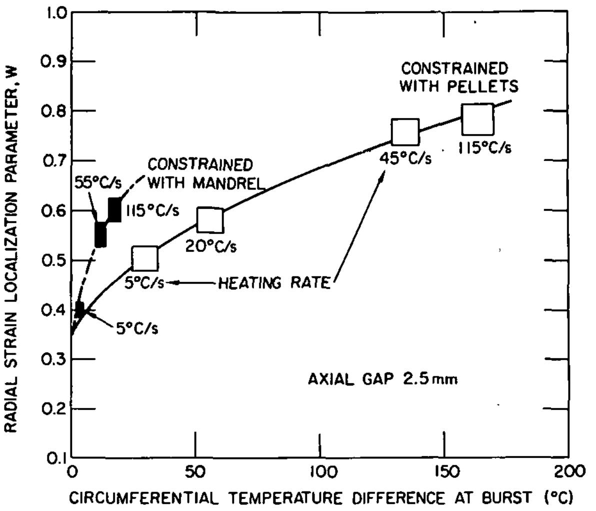

Fig. III.53. Radial-strain-localization Parameter as a Function of Maximum Circumferential Temperature Difference for Cladding Burst in Steam at Temperatures near 800°C Strain Maximum. ANL Neg. No. 306-77-140.

Similarly, from a knowledge of the heating rate, measurements of the maximum circumferential strain, and an evaluation of the W parameter from thickness measurements of the cladding cross section in the burst location, we should be able to evaluate the maximum temperature variation in fuel cladding from in-reactor and multirod-burst tests in which instrumentation is quite difficult.

Figure III.53 also shows a correlation between the W parameter and ΔT_θ^M for mandrel-constrained cladding. In these tests, the measured circumferential temperature nonuniformity does not exceed ~20°C for heating rates up to 115°C/s. For the same value of ΔT_θ^M, the W parameters for mandrel- and pellet-constrained cladding differ primarily because of the large difference in the effective strain rate at the fracture region that is associated with the different heating rates. (For example, for a ΔT_θ^M of ~20°C, the high strain rate for mandrel-constrained cladding at a heating rate of 115°C/s tends to localize the radial strain to a greater extent than that which occurs in pellet-constrained cladding at a heating rate of ~3°C/s.)

We believe that the relationships between the circumferential temperature difference, the radial-strain-localization parameter, and the maximum circumferential strain in the vicinity of ~800°C strain peak for Zircaloy cladding heated by UO_2 fuel under postulated LOCA conditions will be within the range of the data in Figs. III.52 and III.53 for mandrel-and pellet-constrained cladding. The present results will provide the basis for interpreting the deformation behavior of Zircaloy fuel cladding in nuclear-heated fuel rods tested in the Power Burst Facility at the Idaho National Engineering Laboratory and in the FR-2 reactor at the Karlsruhe Nuclear Research Center in the Federal Republic of Germany.

E. Embrittlement of Zircaloy-4 Cladding by Oxidation

A more quantitative cladding embrittlement criterion (than the present criterion that allows a total oxidation limit of 17% of the wall thickness and a peak cladding temperature of 1204°C) is required to establish the margin of performance of the emergency-core-cooling system in LWR's. For this purpose, the dynamic toughness of Zircaloy with different oxygen contents and distributions will be measured in the next reporting period. To better define the maximum degree of oxidation of the mechanical-test specimens for the toughness measurements, ~60 Zircaloy tubes were oxidized in air for time periods of 60-3660 s at temperatures of 1000-1500°C. The degree of embrittlement of these specimens under "normal handling conditions" was evaluated after cooling from the oxidation temperature at a controlled rate.

1. Embrittlement Tests in Air Atmosphere

Zircaloy-4 cladding specimens 254 mm long were induction-heated in air over the center 102-mm region.

A heating rate of 50°C/s was maintained to the oxidation temperature, and after various isothermal oxidation periods, the cladding was cooled at 5°C/s to 500°C and the power was turned off. The 5°C/s cooling rate to 500°C simulated cooling under film-boiling heat-transfer conditions, and the more rapid cooling below ~500°C represented the transition to nucleate boiling below the Leidenfrost temperature.

The temperature of the cladding was monitored by three Pt-Pt 10% Rh thermocouples (0.51-mm diameter) that were positioned 25.4 mm apart at the center of the tube. The thermocouples were attached to holes drilled in the cladding, slightly larger than the thermocouple junction, which permitted the ingress of air and oxidation of the inner surface of the tube. Both ends of the tube were sealed loosely to limit air circulation so that oxidation of the inner surface occurred to a lesser extent. No mechanical constraint or load was imposed on the tube during oxidation.

After cooling to room temperature, the capability of the cladding to remain intact by "normal handling" was determined by bending and twisting without excessive force. The open and closed data points in Fig. III.54 indicate whether the cladding remained intact or failed, respectively, under normal handling after the different oxidation times in air at the various temperatures.

2. Interpretation of Embrittlement-test Results

A computer program was written to calculate several oxidation parameters, listed in Table III.12, from the oxidation conditions, the solubilities of oxygen in the oxide, α, and β phases, and the observed layer thicknesses. The oxygen solubility and diffusivity values for the different temperatures are shown in Table III.13. Oxidation that occurred during

TABLE III.12. Summary of Embrittlement Test Conditions, Cladding-phase Thicknesses, and Various Calculated Oxidation Parameters[a]

Run No.	Temp., °C	t, s	ζ_{ox}^{o}, 10^{-2} mm	ζ_{α}^{o}, 10^{-2} mm	ζ_{β}, 10^{-2} mm	ζ_{α}^{I}, 10^{-2} mm	ζ_{ox}^{I}, 10^{-2} mm	ECR, %	F_W	C_{β}^{AVE}, wt %	C_{β}^{CEN}, wt %	$F_{\beta,C}^{SAT}$	$F_{\beta,L}^{(0.65)}$	$F_{0.65}$
25	1450	60	16.3	14.9	33.7	2.3	1.1	20.8	0.54	0.97	0.52	0.81	0.260	0.135
67	1450	90	24.8	18.1	21.7	4.5	1.4	30.6	0.35	1.13	0.77	0.95	0.000	0.00
63	1450	120	25.2	20.1	18.0	4.7	1.6	31.6	0.30	1.16	0.88	0.98	0.000	0.00
6	1450	168	34.4	32.4	0.0	6.5	1.6	39.5	0.00	-	-	-	-	0.00
62	1400	60	11.4	10.2	41.6	1.5	1.7	16.2	0.67	0.79	0.38	0.72	0.490	0.328
12	1400	90	19.0	15.0	33.5	4.3	1.2	22.8	0.51	0.93	0.52	0.84	0.324	0.165
13	1400	108	16.1	15.4	32.9	3.2	1.3	20.8	0.52	0.98	0.59	0.89	0.160	0.080
16	1400	120	20.8	19.7	21.9	5.1	1.5	26.6	0.36	1.04	0.72	0.95	0.000	0.000
15	1400	132	19.8	21.1	20.5	6.2	2.8	26.6	0.33	1.06	0.76	0.96	0.000	0.000
7	1400	180	21.3	21.0	23.7	5.2	1.9	26.1	0.36	1.07	0.78	0.97	0.000	0.000
17	1400	210	30.3	33.2	0.0	7.0	2.4	36.6	0.00	-	-	-	-	0.000
5	1400	240	15.7	33.2	0.0	9.5	1.9	24.3	0.00	-	-	-	-	0.000
18	1350	600	20.9	42.8	0.0	10.3	1.2	24.0	0.00	-	-	-	-	0.000
27	1300	60	6.9	8.4	49.2	0.9	0.3	9.0	0.78	0.48	0.19	0.54	0.791	0.616
24	1300	120	9.4	12.4	42.1	2.1	0.8	12.7	0.67	0.66	0.34	0.76	0.650	0.435
22	1300	180	10.1	13.5	39.0	2.9	1.0	14.1	0.62	0.76	0.45	0.87	0.550	0.341
41	1300	240	11.8	15.2	35.2	4.2	1.8	16.7	0.55	0.81	0.52	0.92	0.400	0.220
21	1300	264	17.1	15.9	29.8	6.0	2.2	22.6	0.46	0.84	0.57	0.95	0.311	0.142
44	1300	282	18.4	18.5	25.3	6.1	1.4	23.5	0.40	0.85	0.61	0.96	0.170	0.068
14	1300	288	42.5	8.8	24.1	6.5	1.0	44.5	0.36	0.85	0.61	0.96	0.168	0.060
43	1300	360	20.9	20.8	23.1	5.3	2.1	25.9	0.36	0.86	0.66	0.98	0.000	0.000
20	1300	480	29.4	31.0	6.1	6.0	2.2	34.2	0.10	0.88	0.82	1.00	0.000	0.000
19	1300	630	21.4	40.3	0.0	8.5	2.2	26.2	0.00	-	-	-	-	0.000
23	1230	120	8.2	10.4	45.0	2.0	1.2	11.4	0.71	0.46	0.22	0.63	0.900	0.639
28	1230	180	10.1	13.0	41.2	3.5	1.9	14.1	0.63	0.55	0.29	0.75	0.850	0.535
9	1230	240	9.9	11.7	42.2	2.8	1.4	13.7	0.66	0.61	0.34	0.82	0.820	0.541
8	1230	300	11.0	13.2	40.3	3.0	0.9	14.3	0.63	0.64	0.38	0.87	0.800	0.504
45	1230	360	11.3	13.8	38.5	4.9	1.0	15.0	0.59	0.67	0.42	0.91	0.760	0.448
52	1230	390	12.1	15.0	34.8	4.5	1.3	16.4	0.55	0.69	0.45	0.93	0.733	0.402
46	1230	420	12.2	14.9	37.1	4.8	1.3	16.1	0.57	0.69	0.45	0.93	0.730	0.416
48	1230	480	19.2	16.4	29.1	7.0	2.1	23.8	0.44	0.71	0.50	0.96	0.614	0.292
54	1230	780	15.1	19.8	27.8	6.3	1.8	19.7	0.43	0.73	0.56	0.99	0.540	0.232
68	1230	960	18.5	16.2	29.2	4.8	1.9	23.4	0.46	0.73	0.56	0.99	0.464	0.213
65	1230	1080	20.4	25.1	22.3	6.4	2.4	24.1	0.33	0.74	0.60	0.99	0.340	0.112
66	1230	1200	24.2	27.3	4.3	11.7	10.2	37.3	0.07	0.74	0.71	1.00	0.000	0.000
64	1230	1230	31.8	31.3	0.0	8.3	1.3	37.5	0.00	-	-	-	-	0.000
57	1220	840	16.5	21.9	25.0	6.0	2.3	21.3	0.38	0.71	0.56	0.99	0.878	0.339
56	1220	960	17.4	22.4	27.0	7.3	2.1	21.1	0.39	0.71	0.56	0.99	0.870	0.333
38	1200	120	8.2	8.3	48.9	2.0	1.1	10.8	0.75	0.38	0.18	0.57	0.973	0.729
26	1200	180	8.1	9.1	47.2	2.6	1.5	11.5	0.72	0.46	0.23	0.69	0.962	0.692
42	1200	240	8.5	10.6	44.1	1.8	1.6	12.2	0.70	0.52	0.29	0.78	0.954	0.667
29	1200	360	12.5	14.4	36.7	4.2	2.2	17.1	0.57	0.60	0.37	0.89	0.942	0.537

TABLE III.12 (Contd.)

Run No.	Temp., °C	t, s	ζ_{ox}^{o}, 10^{-2} mm	ζ_{α}^{o}, 10^{-2} mm	ζ_{β}, 10^{-2} mm	ζ_{α}^{I}, 10^{-2} mm	ζ_{ox}^{I}, 10^{-2} mm	ECR, %	F_W	C_{β}^{AVE}, wt %	C_{β}^{CEN}, wt %	$F_{\beta,C}^{SAT}$	$F_{\beta,L}^{(0.65)}$	$F_{0.65}$
49	1200	480	11.4	13.3	38.8	3.4	1.2	15.0	0.60	0.62	0.40	0.92	0.930	0.558
50	1200	540	14.3	16.3	31.9	5.8	2.9	19.7	0.49	0.64	0.44	0.95	0.922	0.451
51	1200	600	24.2	22.2	17.3	7.0	1.7	29.1	0.37	0.66	0.53	0.98	0.880	0.237
59	1200	1080	46.5	25.2	5.0	6.2	3.0	48.6	0.07	0.67	0.64	1.00	0.390	0.027
60	1200	1200	53.0	13.0	0.0	9.2	13.3	68.4	0.00	-	-	-	-	0.000
58	1200	1350	53.0	17.0	0.0	8.8	3.2	61.0	0.00	-	-	-	-	0.000
61	1200	1440	45.0	17.0	0.0	5.8	15.3	64.8	0.00	-	-	-	-	0.000
32	1150	180	6.3	6.2	51.4	1.1	0.4	8.2	0.82	0.34	0.11	0.61	1.000	0.800
31	1100	30	7.6	7.9	46.5	1.9	0.8	9.8	0.75	0.15	0.11	0.34	1.000	0.750
36	1100	60	4.2	4.1	55.0	0.9	0.3	5.5	0.87	0.19	0.11	0.41	1.000	0.870
35	1100	180	6.8	7.0	50.3	1.1	0.3	8.4	0.80	0.25	0.13	0.56	1.000	0.800
40	1100	450	8.3	8.2	45.7	2.8	1.0	11.3	0.73	0.36	0.21	0.79	1.000	0.730
30	1100	600	10.0	10.1	33.1	9.2	6.9	20.5	0.52	0.41	0.28	0.92	1.000	0.520
78	1100	2160	15.8	17.5	47.6	5.6	2.4	16.4	0.58	0.43	0.31	0.97	1.000	0.580
88	1100	3000	22.8	22.0	26.0	4.7	2.2	25.3	0.38	0.45	0.37	0.99	1.000	0.380
81	1100	3270	26.3	14.9	25.0	4.8	2.0	31.0	0.40	0.45	0.37	1.00	1.000	-
87	1100	3540	22.0	30.4	18.4	4.8	2.1	24.2	0.27	0.45	0.40	1.00	1.000	-
86	1100	3600	26.2	32.9	19.0	4.9	2.1	25.9	0.25	0.45	0.40	1.00	1.000	-
84	1100	3660	25.3	27.0	20.0	5.6	1.8	19.7	0.27	0.45	0.36	1.00	1.000	-

[a] Temp. = maximum isothermal oxidation temperature.

t = time at the isothermal oxidation temperature.

ζ_{ox}^{o} = outside-diameter oxide-layer thickness.

ζ_{α}^{o} = outside-diameter α-layer thickness.

ζ_{β} = β-layer thickness.

ζ_{α}^{I} = inside-diameter α-layer thickness.

ζ_{ox}^{I} = inside-diameter oxide-layer thickness.

ECR = equivalent cladding reacted

F_W = fraction of prior β layer of the original cladding thickness.

C_{β}^{AVE} = average oxygen concentration of β layer.

C_{β}^{CEN} = oxygen concentration at centerline of β layer.

$F_{\beta,C}^{SAT}$ = fractional saturation of β phase, C_{β}^{AVE}/C_S.

$F_{\beta,L}^{(0.65)}$ = fraction of β layer containing oxygen content <0.65 wt %.

$F_{0.65}$ = fraction of original cladding thickness containing oxygen content <0.65 wt %, $F_W \times F_{\beta,L}^{(0.65)}$.

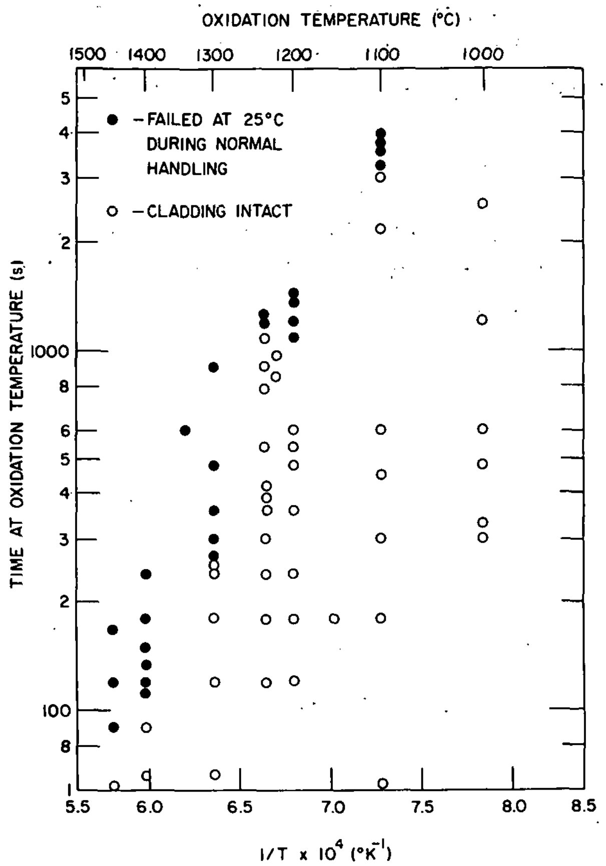

Fig. III.54

Capability of Zircaloy-4 Cladding to Withstand "Normal Handling" at Room Temperature without Fracture after Oxidation in Air at Temperatures between 1000 and 1450°C for Various Times. ANL Neg. No. 306-77-154.

TABLE III.13. Summary of Diffusion Coefficients and Equilibrium Phase-boundary Concentrations of Oxygen in Zircaloy-4[a]

Temp., °C	D_{ox}, 10^{-10} m^2 s^{-1}	D_α, 10^{-10} m^2 s^{-1}	D_β, 10^{-10} m^2 s^{-1}	C_{ox}^{II}, wt %	C_{ox}^{I}, wt %	C_α^{II}, wt %	C_α^{I}, wt %	C_S, wt %
1450	5.6	1.0	7.1	28.0	26.0	7.12	2.80	1.19
1400	4.1	0.66	5.5	28.0	26.0	7.00	2.75	1.10
1350	3.2	0.43	4.2	28.0	26.0	6.87	2.68	0.99
1300	2.2	0.25	3.2	28.0	26.0	6.80	2.62	0.88
1230	1.3	0.11	2.0	28.0	26.0	6.75	2.48	0.74
1220	1.2	0.10	1.9	28.0	26.0	6.75	2.46	0.72
1200	1.0	0.078	1.7	28.0	26.0	6.75	2.41	0.67
1150	0.64	0.042	1.2	28.0	26.0	6.75	2.27	0.56
1100	0.42	0.022	0.86	28.0	26.0	6.75	2.12	0.45

[a] D_{ox} = diffusion coefficient of oxygen in Zircaloy-4 oxide phase.

D_α = diffusion coefficient of oxygen in α-Zircaloy-4.

D_β = diffusion coefficient of oxygen in β-Zircaloy-4.

C_{ox}^{II} = oxygen concentration of Zircaloy-4 oxide at the oxide/gas interface.

C_{ox}^{I} = equilibrium oxygen concentration of the oxide at the oxide/α interface.

C_α^{II} = equilibrium oxygen concentration of the α phase at the oxide/α interface.

C_α^{I} = equilibrium oxygen concentration of the α phase at the α/β interface.

C_s = equilibrium oxygen concentration of the β phase at the α/β interface.

transient heating and cooling of the specimens was neglected in these computations. The room-temperature embrittlement results in Fig. III.54 have been examined in terms of the various oxidation parameters in Table III.12.

a. F_W Criterion

The results from Fig. III.54 are shown in a plot of the fractional thickness of the transformed β region F_W versus temperature in Fig. III.55, in which F_W was computed from

$$F_W = \frac{\zeta_\beta}{\frac{1}{R}\left(\zeta_{ox}^{O} + \zeta_{ox}^{I}\right) + \left(\zeta_\alpha^{O} + \zeta_\alpha^{I}\right) + \zeta_\beta}, \tag{6}$$

where

R = Pilling-Bedworth ratio, i.e., 1.54,

ζ_{ox}^{O} = outer-diameter (OD) oxide-layer thickness,

ζ_{ox}^{I} = inner-diameter (ID) oxide-layer thickness,

ζ_α^{O} = OD α-layer thickness,

ζ_α^{I} = ID α-layer thickness,

and

ζ_β = β-layer thickness.

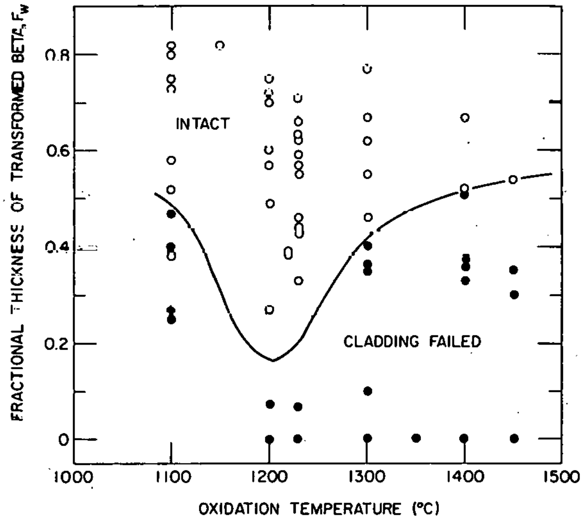

Fig. III.55

Failure Map for Zircaloy Cladding under "Normal Handling" at Room Temperature in Terms of Fractional Thickness of Transformed β Region F_W and Oxidation Temperature in Air. ANL Neg. No. 306-77-136.

No simple boundary between the intact and failed cladding is evident based on the F_W criterion.

b. Equivalent-cladding-reacted (ECR) Criterion

The equivalent-cladding reacted was calculated from the ID and OD oxide-layer thicknesses and the conversion of the oxygen content of the α and β phases to the equivalent oxide-layer thickness by

$$\mathrm{ECR} = \left\{\frac{1}{200}\left(C_{\mathrm{ox}}^{\mathrm{II}} + C_{\mathrm{ox}}^{\mathrm{I}}\right)\left[\frac{1}{R}\left(\zeta_{\mathrm{ox}}^{\mathrm{o}} + \zeta_{\mathrm{ox}}^{\mathrm{I}}\right) + \left(\zeta_{\alpha}^{\mathrm{o}} + \zeta_{\alpha}^{\mathrm{I}}\right) + \zeta_{\beta}\right]\right\}^{-1} \cdot \left[\frac{1}{2R}\left(C_{\mathrm{ox}}^{\mathrm{II}} + C_{\mathrm{ox}}^{\mathrm{I}}\right)\left(\zeta_{\mathrm{ox}}^{\mathrm{o}} + \zeta_{\mathrm{ox}}^{\mathrm{I}}\right) + I_{\alpha}^{\mathrm{o}} + I_{\alpha}^{\mathrm{I}} + 2I_{\beta}\right], \tag{7}$$

where

$$I_{\alpha} = \int C_{\alpha}(T, t, x)dx$$

and

$$I_{\beta} = \int C_{\beta}(T, t, x)dx.$$

The quantities C_{α} and C_{β} are the oxygen-concentration profiles in the α and β phases. The time- and temperature-dependent functional expressions of I_{α} and I_{β} have been reported elsewhere.[10]

The cladding-failure results are represented in a plot of the percent of the equivalent-cladding reacted versus the oxidation temperature (Fig. III.56). The results are in good agreement with the 17% ECR-failure criterion line in that no failures occurred for specimens within the 17% limit. The degree of conservatism of the present criterion at temperatures between ~1100 and 1300°C is evident from these results.

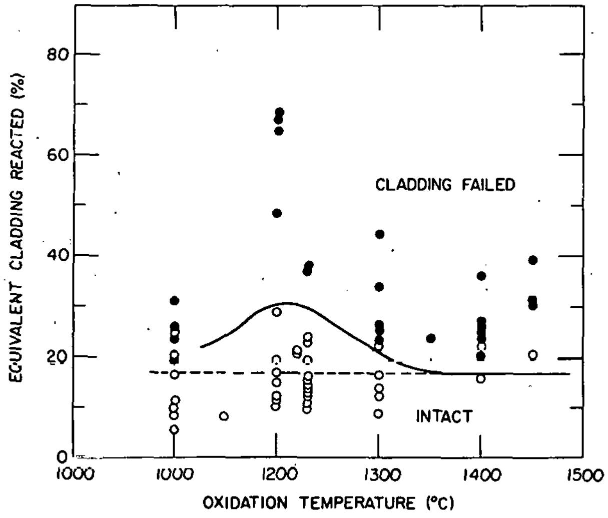

Fig III.56

Failure Map for Zircaloy Cladding under "Normal Handling" at Room Temperature in Terms of Equivalent-cladding-reacted Parameter ECR and Oxidation Temperature in Air. ANL Neg. No. 306-77-148.

c. Fractional β-phase Saturation (FBS) Criterion

The fractional saturation of the β phase by oxygen was calculated from

$$F^{SAT}_{\beta,C} = \frac{1}{C_S \zeta_\beta} \int_0^{\zeta_\beta} C_\beta(T_o, t_o, x)dx, \qquad (8)$$

where

T_o = oxidation temperature,

t_o = oxidation time,

and

$C_\beta(x)$ = β-phase oxygen distribution function.[1,9,10]

The cladding-failure data at the various temperatures are plotted in terms of the fractional saturation of the β phase in Fig. III.57. Zircaloy tubes with the saturated β phase invariably failed under normal handling. At temperatures ≳1200°C, the fractional saturation of the β phase required for failure decreases as the oxidation temperature increases. According to this criterion, virtual saturation of the β phase

$$\left(F^{SAT}_{\beta,C} \geq 0.99\right),$$

is the condition for failure at temperatures ≲1200°C.

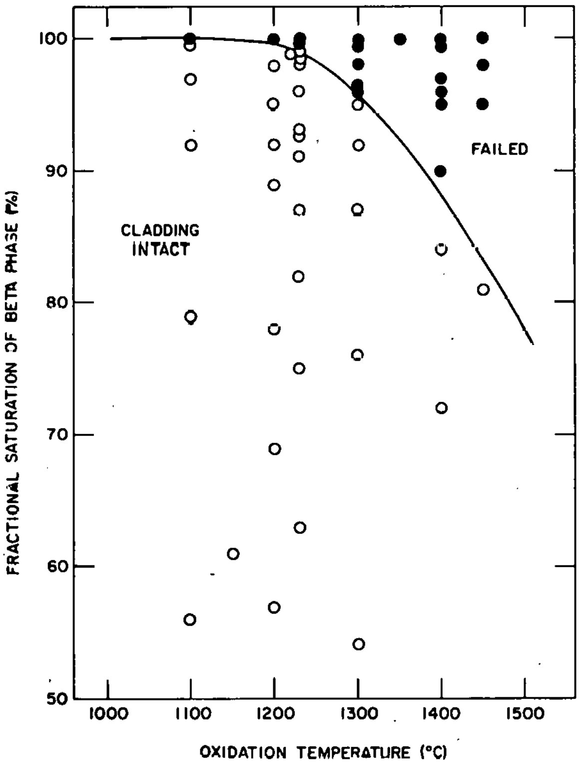

Fig. III.57

Failure Map for Zircaloy Cladding under "Normal Handling" at Room Temperature in Terms of Fractional Saturation of Central β-phase Region and Oxidation Temperature in Air. ANL Neg. No. 306-77-138.

d. $F_{0.65}$ Criterion

The $F_{0.65}$ criterion is based on the fraction of the original cladding thickness with an oxygen content <0.65 wt % after cooling the material to room temperature. The parameter can be computed from a product of the values from columns 10 and 14 in Table III.12, i.e.,

$$F_{0.65} = F_W \cdot F^{0.65}_{\beta,L}, \qquad (9)$$

where $F^{0.65}_{\beta,L}$ is the fraction of the β-layer thickness with <0.65 wt % oxygen, and can be evaluated from

$$C_{\beta}\left(T_O, t_O, \frac{\zeta_{\beta}}{2}\left[1 - F^{0.65}_{\beta,L}\right]\right) = 0.65. \qquad (10)$$

Figure III.58 shows the cladding-failure results at the various temperatures in terms of the $F_{0.65}$ thickness parameter. No exception was found to the criterion that predicts cladding failure when the thickness of the cladding with <0.65 wt % oxygen is <10% of the original wall thickness ($F_{0.65} \leq 0.1$) at temperatures above 1200°C. At lower temperatures, the solubility of oxygen in β-Zircaloy-4 is <0.65 wt %, and this criterion is therefore not applicable.

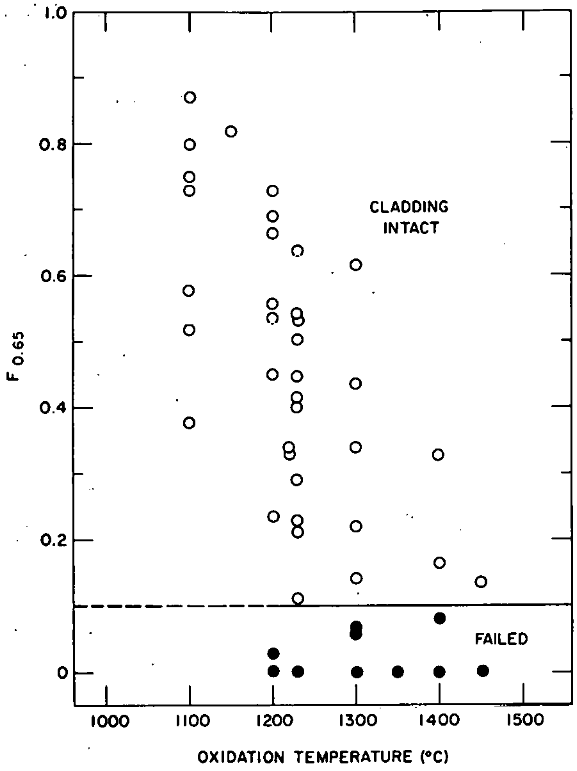

Fig. III.58. Failure Map for Zircaloy Cladding under "Normal Handling" at Room Temperature in Terms of Fraction of Original Cladding Thickness Containing <0.65 wt % Oxygen and Oxidation Temperature in Air. ANL Neg. No. 306-77-137.

Of the four criteria for the embrittlement of Zircaloy cladding by high-temperature oxidation in air and failure during normal handling at room temperature, the best representation of the results (least amount of conservatism) is given by the FBS and $F_{0.65}$ criteria for oxidation temperatures below and above 1200°C, respectively. None of the tests violated the combined criterion.

3. Future Embrittlement Studies

Additional oxidation experiments will be performed in a steam environment with a controlled cooling rate to the Leidenfrost temperature followed by a rapid water quench to room temperature. If the specimen remains intact after the transient heating, oxidation, and cooling cycle, a uniaxial tensile test will be performed on the tube, which will be held in the grips of a biaxial MTS testing system. Several specimens will be ruptured under internal pressure in the MTS machine during a simulated LOCA transient, and the residual strength and ductility of the tube will be determined in a tensile test. This information will supplement the dynamic toughness data that will be obtained on composite Zircaloy specimens at temperatures below ~600°C. The embrittlement studies in steam and air environments will also be extended to lower temperatures and longer oxidation times.

References

1. Light-water-reactor Safety Research Program: Quarterly Progress Report, April-June 1975, Sec. III, "Mechanical Properties of Zircaloy Containing Oxygen," ANL-75-58 (Sept 1975).
2. Light-water-reactor Safety Research Program: Quarterly Progress Report, January-March 1976, Sec. III, "Mechanical Properties of Zircaloy Containing Oxygen," ANL-76-49.
3. Light-water-reactor Safety Research Program: Quarterly Progress Report, October-December 1975, Sec. III, "Mechanical Properties of Zircaloy Containing Oxygen," ANL-76-15.
4. Light-water-reactor Safety Research Program: Quarterly Progress Report, April-June 1976, Sec. III, "Mechanical Properties of Zircaloy Containing Oxygen," ANL-76-87.
5. Light-water-reactor Safety Research Program: Quarterly Progress Report, July-September 1976, Sec. III, "Mechanical Properties of Zircaloy Containing Oxygen," ANL-76-121 (Dec 1976).
6. Light-water-reactor Safety Research Program: Quarterly Progress Report, July-September 1975, Sec. III, "Mechanical Properties of Zircaloy Containing Oxygen," ANL-75-72.
7. J. T. Venard, Stress-Rupture Properties of Type 304 Stainless Steel Tubing, ORNL-TM-535 (June 1963).
8. Light-water-reactor Safety Research Program: Quarterly Progress Report, October-December 1976, Sec. III, "Mechanical Properties of Zircaloy Containing Oxygen," ANL-77-10 (Mar 1977).
9. Light-water-reactor Safety Research Program: Quarterly Progress Report, January-March 1975, Sec. III, "Mechanical Properties of Zircaloy Containing Oxygen," ANL-75-28 (June 1975).
10. H. M. Chung, ANL, personal communication (Oct 1974).

IV. STEAM-EXPLOSION STUDIES

Responsible Section Manager:
R. E. Henry, RAS

A. Vapor Explosive Behavior at Elevated Ambient Pressure (R. E. Henry and L. M. McUmber, RAS)

Unstable bubbly growth from some infinitesimal perturbation over the critical size is determined by a combination of physical properties including surface tension, liquid inertia, liquid viscosity, liquid-to-vapor density ratio, liquid thermal conductivity, and latent heat of vaporization. The details of bubble growth and collapse have been formulated in Ref. 1. The results in Ref. 1 show that, from a first-order viewpoint, the bubble growth can be estimated from the two solutions shown in Fig. IV.1 in terms of radius versus time. The combination of the two solutions, i.e., the inertial solution early in time and the heat-conduction solution for larger radii, provides an upper bound on the actual growth behavior.

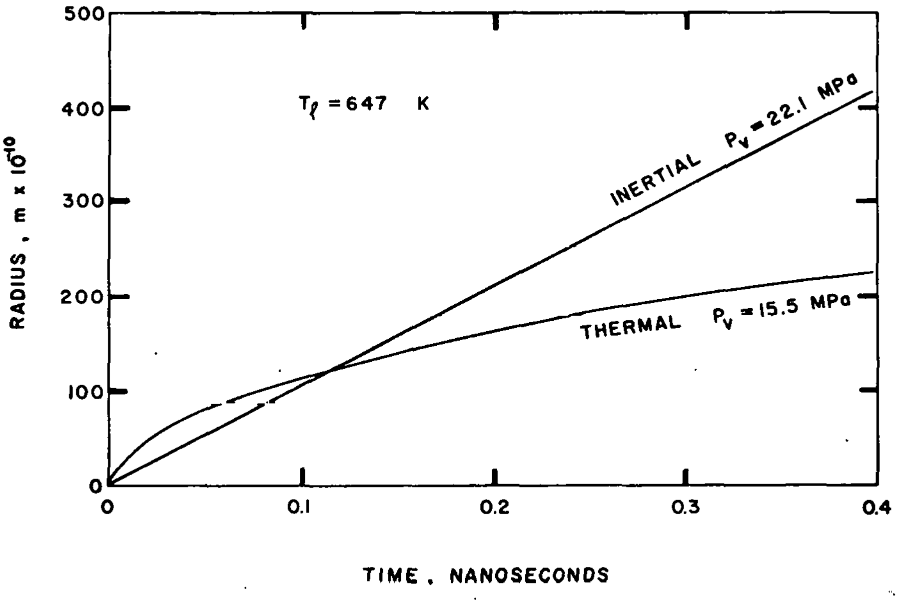

Fig. IV.1. Inertial and Thermal Bubble-growth Behavior for Water at 15.5 MPa. ANL Neg. No. 900-77-527 Rev. 1.

There is an important difference between the inertially and thermally dominated behavior. In the inertially dominated regime, the liquid and vapor are at the same temperature but different pressures. The vapor pressure is the saturation value corresponding to the liquid temperature; the liquid pressure far removed from the bubble is the ambient pressure. Under these conditions, the bubble radius versus time is given by the Rayleigh equation

$$r(t) = \frac{2}{3}\sqrt{\frac{P_v - P_\ell}{\rho_\ell}t}; \qquad (1)$$

i.e., the growth is limited by the rate at which the liquid can be pushed out of the way.

In the thermally dominated regime, the vapor and the liquid are at the same pressure, which is the ambient value; but the vapor temperature is the saturated value at the ambient pressure, while the liquid far removed from the bubble is at a higher (superheated) temperature. For such conditions, the growth is limited by the rate at which thermal energy, for formation of new vapor, can be conducted to the interface. A simple formation for this growth is given by Tong[2] as

$$r(t) = 2\sqrt{\frac{3}{\pi}}\,Ja\sqrt{\alpha_\ell t}, \qquad (2)$$

where the Jakob number is defined as

$$Ja = \frac{\rho_\ell c_\ell}{\rho_v h_{fg}}(T_{SUP} - T_{SAT}). \qquad (3)$$

To sustain a vapor explosion, nucleation sites must be provided, and as discussed in Ref. 3, these sites arise from spontaneous nucleation within the cold liquid. Table IV.1 lists the homogeneous nucleation potentials for an ambient pressure of 155 bars and for temperatures approaching the thermodynamic critical point. In these calculations, the surface tension was represented by

$$\sigma = 186.0(1 - T/T_c)^{1.18} \qquad (4)$$

as deduced from the data in Ref. 4.

TABLE IV.1. Homogeneous Nucleation of Water at 15.5 MPa

T, °C	P_v, MPa	σ, n/m	T_c, 10^{10}m	J, sites/cm^3·s
350	16.5	0.0038	73	4.14×10^{-11}
351	16.8	0.0036	58	1.63×10^{7}
352	17.0	0.0034	47	1.25×10^{17}
355	17.6	0.0029	27	2.71×10^{28}
360	18.7	0.0020	13	3.22×10^{32}

The lower limit of the homogeneous nucleation region is about 350°C. If the interface temperature between the hot and cold liquids is the thermodynamic critical temperature of the water, which is the maximum temperature that can be assigned to a vapor-liquid system, then the maximum vapor pressure is 22.1 MPa. Under these conditions, the inertially dominated growth is given as

$$r(t) = 1.06 \times 10^4 t, \tag{5}$$

where r(t) is in centimeters and t is in seconds. The Jakob number for these conditions is 4.1, and the resulting expression for thermally dominated bubble growth is

$$r(t) = 0.113\sqrt{t}, \tag{6}$$

where r(t) is in centimeters and t is in seconds.

These two growth characteristics are illustrated in Fig. IV.1. It is seen that, under these conditions, the bubble growth rate becomes thermally dominated at a radius of 1.2×10^{-10}m (120 Å), and the growth time to this radius is about 10^{-10} s. As listed in Table IV.1, the critical radius for the vapor nucleus is 0.53×10^{-10} m (53 Å). Consequently, the bubble growth, i.e., vapor production, is essentially thermally dominated from the critical size. This means that the vapor is produced at the ambient liquid pressure, and that there is no source of high pressure vapor to produce an explosive event.

This elevated ambient-pressure behavior can be contrasted to the growth characteristics at an ambient pressure of 1 atm (1×10^5Pa). For these conditions, the lower limit of the homogeneous nucleation regime is about 310°C, which corresponds to a vapor pressure of 9.87 MPa. If the liquid temperature is again assumed to be the thermodynamic critical point, the inertially dominated behavior is given by

$$r(t) = 2.16 \times 10^4 t, \tag{7}$$

which only differs from the elevated pressure behavior by a factor of two.

The thermally dominated growth has a Jakob number of 3524, which results in a radius-time dependence of

$$r(t) = 97.3\sqrt{t}, \tag{8}$$

where the radius and time are again given in centimeters and seconds, respectively. Under these circumstances, the inertially dominated growth is dominant until the radius is about 4 mm, as shown in Fig. IV.2, which is an increase of more than five orders of magnitude from the elevated-pressure case. This means that high-pressure vapor can indeed impose an increased pressure on the system as both an incipient shock wave and as a high-pressure source to provide propagation and escalation of the event.

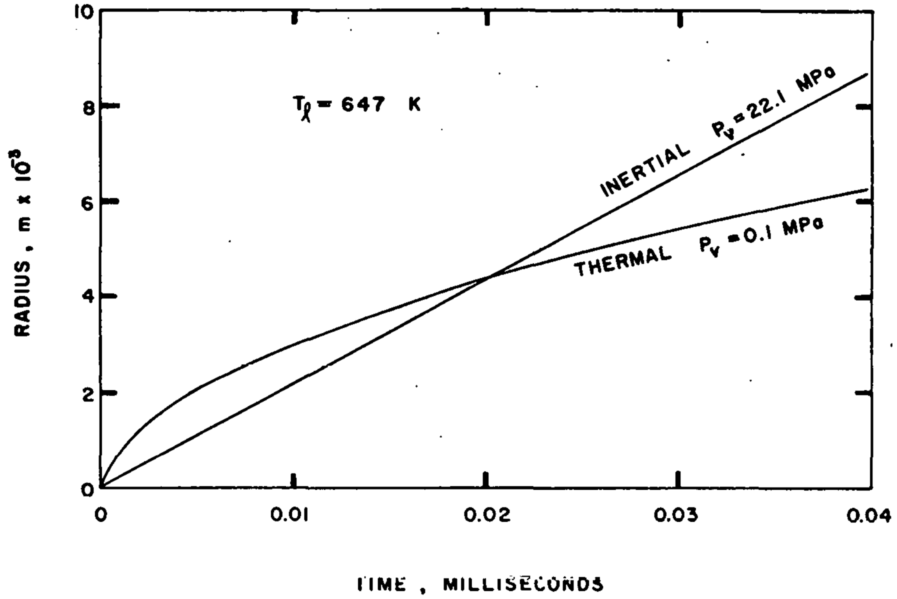

Fig. IV.2. Inertial and Thermal Bubble-growth Behavior for Water at 0.1 MPa. ANL Neg. No. 900-77-526 Rev. 1.

The above points outline the logic behind the initial contention that vapor explosions would not exist at system pressures typical of PWR operating conditions. Simulant-fluid experiments were conducted with Freon-22 and mineral oil, as well as Freon-22 and water, to determine if elevated ambient pressures did indeed suppress explosive interactions, even though all other known criteria for large-scale explosions were satisfied. These experiments demonstrated that energetic explosive events (explosive pressures of 2.0-2.5 MPa) would be obtained for an ambient pressure of 0.1 MPa, but for ambient pressures of 0.22 MPa, all explosions ceased.

These results agree with the model predictions. The initial prediction, as given in Ref. 5, related only to the inability to generate a vapor explosion when the bubble growth was thermally dominated. Consequently, it was initially stated that, at elevated ambient pressures, the energy-transfer rate would be greatly reduced and the propensity for film boiling would be increased. In addition, vapor explosions would be self-limiting to a pressure of about two-thirds of the critical pressure.

As stated above, the experiments revealed that an increase of 0.1-0.22 MPa in ambient pressure caused all explosions to cease. A possible reason for this sensitivity to the ambient pressure is the relationship between the capture diameter and the transition diameter between inertial and thermal growth and the resulting effect on the propagation potential for the system.

The capture diameter, as a function of interface temperature, was calculated in Ref. 3 and is graphically illustrated in Fig. IV.3. This prediction, which is for a 0.1-MPa ambient pressure, is not significantly affected by an

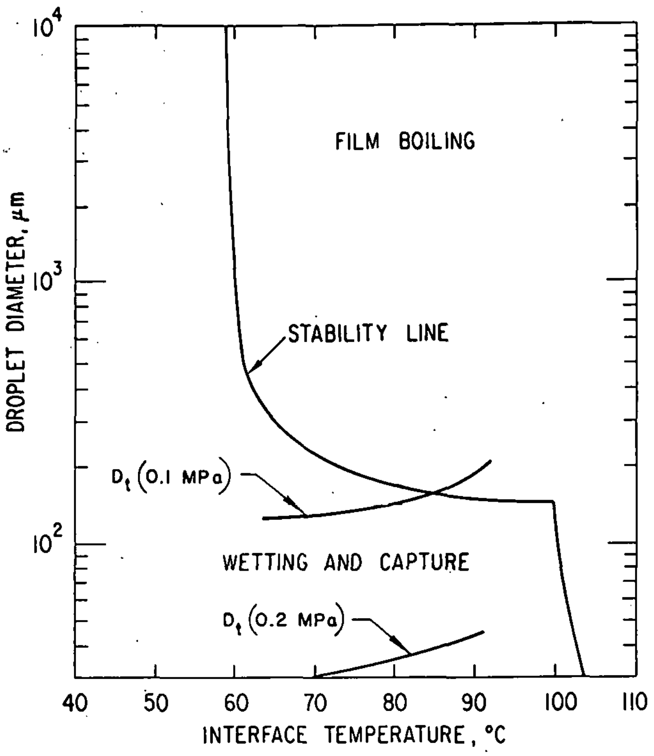

Fig. IV.3. Transition Radius and Capture Diameters for Freon-22. ANL Neg. No. 900-77-562 Rev. 1.

increase of 0.1 MPa in the ambient pressure. The predictions for the transition diameter are also included for the two system pressures of interest. For an ambient pressure of 0.1 MPa, the transition diameter exceeds the capture diameter. This means that vapor embryos can grow completely through the captured liquid mass with a pressure inside the vapor space that is higher than the surrounding system pressure.

Such behavior produces the unique, high-rate fragmentation mechanism illustrated in Fig. IV.4. As the high-pressure vapor bubble approaches the opposite boundary of the liquid drop, the liquid is violently fragmented into a spray and high-pressure vapor is released locally. This high-pressure vapor can be the incipient shock wave of the explosive event. More importantly, however, a fine liquid spray has been produced in which all the resulting drops lie in the capturable range and are much smaller than the transition diameter.

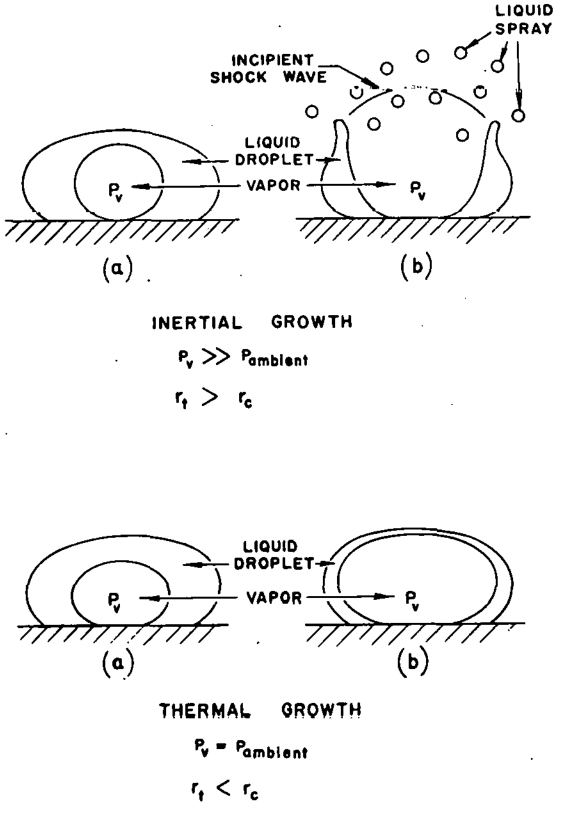

Fig. IV.4

Internal Fragmentation of Liquid Droplets by Inertial Bubble Growth. ANL Neg. No. 900-77-563.

Table IV. 2 includes estimates of the time required for growth to the transition condition, which occurs in about 1 μs. This internal fragmentation of the working fluid occurs on a time scale that is three orders of magnitude less than that of the overall event and thus is capable of supporting the propagation of a local event into a large-scale explosion.

TABLE IV.2. Transition Radius and Time

P = 0.1 MPa			
T, °C	P_v, MPa	r_t, m	t_t, s
70	3.0	68	1.5×10^{-6}
80	3.7	77	1.5×10^{-6}
90	4.4	94	1.5×10^{-6}
T = 90°C			
P, MPa	P_v, MPa	r_t, m	t_t, s
0.1	4.4	94	1.5×10^{6}
0.2	4.4	22	3.7×10^{-7}
2.5	4.4	3.3×10^{-2}	0.8×10^{-9}

On the other hand, the transition diameter for a system pressure of 0.22 MPa is about one-third of the capture diameter. For these conditions, the vapor growth that approaches the opposite liquid interface is at a pressure that is essentially equal to the ambient pressure. Consequently, there is no release of high-pressure vapor and no violent fragmentation of the liquid. With these conditions, initiation and sustained propagation would be difficult to achieve.

This proposed behavior is somewhat system-dependent in that it may be possible to provide an external trigger that prefragments the cold liquid to a size that is smaller than the transition diameter. In this case, the system can sustain the propagation. This is principally what happens in an explosive event; i.e., even though the system pressure is rising rapidly, the fragmentation mechanism has a much shorter time constant and can provide a fine liquid spray capable of sustaining the propagation at elevated pressures. However, there is a limit to the fragmentation mechanism, and this is reached when inertially dominated bubble growth is suppressed.

As discussed above, for Freon-22 the transition radius is essentially the critical radius for system pressures of about 2.5 MPa. If the system pressure were initially at this value, even an external trigger would be incapable of prefragmenting the cold phase to a size that could sustain the explosive event. This is a simple argument that can be used in assessing the behavior of postulated fuel failures at nominal operating pressures.

Pressurized-water-reactor system pressures of 15.5 MPa result in a transition radius essentially equal to the critical size. Consequently, this system should be independent of any external triggering mechanism. For boiling-water-reactor systems having a pressure of 7.0 MPa, the inertial growth for a temperature of 370°C would be

$$r(t) = 14{,}427t \tag{9}$$

and the thermal growth is given by

$$r(t) = 0.45\sqrt{t}, \tag{10}$$

where r and t are again given in centimeters and seconds, respectively.

These equations result in a transition radius of 1.4×10^{-5} cm, which is much less that the characteristic coolant dimensions. Consequently, energetic interactions would again seem to be essentially impossible, even with an energetic external trigger.

B. Combined Physical-Chemical Explosions (D. R. Armstrong, RAS)

The effort during this quarter has been directed toward improving the exploding-wire-triggered aluminum drop. Several test photographs have been taken at 200,000 frames/s using a 1.7-kJ flashlamp mounted in a parabolic reflector. This has been used in a back-lighting mode, which silhouettes both the aluminum and the surrounding water vapor. Thus, for these test films, the progress of the explosion can only be followed by tracing the motion of the aluminum envelope, which may be either the water/aluminum or the water/water-vapor interface.

For a typical run, the film shows the aluminum pooled on the bottom of the water tank in a thin bubble 5-10 cm in diameter. Several frames after the wire explosion, the portion of the puddle interface closest to the wire begins to move as if the vapor layer between the aluminum and water were collapsing. With succeeding frames, portions of the puddle farther from the exploding wire begin to collapse and those closer to the wire show a motion reversal and start to expand. This collapse motion propagates along the surface of the aluminum puddle with a velocity of 0.5-1.5 km/s. The correlation of pressure measurements with the films has been prevented by an erratic pulse noise appearing in the data-recording system.

Several runs have been made to determine the triggering threshold for an aluminum/water explosion in this system. For 800°C aluminum and

30°C water, the maximum output from one capacitor unit (40 J max) gave a peak pressure of 0.25 MPa, which was insufficient to trigger an explosion. The minimum output from a second capacitor unit (380 J min) giving a peak pressure of 2.5 MPa was always enough to initiate an explosion. A third capacitor unit will be built covering the discharge-energy range of 40-400 J and will be used to determine the threshold-trigger characteristics for this experiment.

References

1. T. Theofanous, L. Biasi, H. S. Isbin, and H. Fauske, A Theoretical Study on Bubble Growth in Constant and Time-Dependent Pressure Fields, Chem. Eng. Sci. 24, 885-897 (1969).
2. L. S. Tong, Boiling Heat Transfer in Two-Phase Flow, John Wiley & Sons, Inc., New York-London-Sydney (1965).
3. R. E. Henry and H. K. Fauske, Energetics of Vapor Explosions, ASME Paper No. 75-HT-66 (1975).
4. J. G. Collier, Convective Boiling and Condensation, McGraw-Hill, London-New York (1972).
5. R. E. Henry and H. K. Fauske, "Nucleation Characteristics in Physical Explosions," Proc. Third Specialists Meeting on Sodium/Fuel Interaction in Fast Reactors, Tokyo, Japan (Mar 1976).